PREDICTION OF GROUND DEFORMATIONS CAUSED BY UNDERGROUND CONSTRUCTION OF THE TREN URBANO IN RIO PIEDRAS

by

Angela L. Alba-Carbó

B.S., Civil and Environmental Engineering
University of Puerto Rico, 1995

Submitted to the Department of
Civil and Environmental Engineering in Partial Fulfillment of
the requirements for the Degree of

MASTER OF SCIENCE
in Civil and Environmental Engineering
at the Massachusetts Institute of Technology

February, 1998

Signature of Author_____
Department of Civil and Environmental Engineering
December day, 1997

Certified by_____
Professor Andrew J. Whittle
Thesis Supervisor

Accepted by_____
Professor Joseph M. Sussman
Chairman, Departmental Committee on Graduate Studies

PREDICTION OF GROUND DEFORMATIONS CAUSED BY UNDERGROUND CONSTRUCTION OF THE TREN URBANO IN RIO PIEDRAS

by
ANGELA L. ALBA-CARBO

Submitted to the Department of Civil and Environmental Engineering on December 1st, 1997 in partial fulfillment of the requirements for the Degree of Master of Science in Civil and Environmental Engineering

ABSTRACT

One of the principal factors affecting the design of deep excavations in cohesive soils is the control of ground deformations, in order to minimize damage to adjacent facilities and mitigate the costs of underpinning. The goal of this thesis is to estimate the magnitudes of ground movements for Section 7 of the Tren Urbano project in San Juan, Puerto Rico, and to relate these movements to the stratigraphy of the surrounding alluvial soils and proposed methods of construction.

The area around the proposed Río Piedras Station is underlain by thick alluvial deposits comprising the Hato Rey formation. A review of the site investigation data has led to a simplified interpretation of complex stratigraphy at the site. Predictions of excavation-induced ground movements are made by non-linear finite element analyses, incorporating a relatively simple effective stress, elasto-plastic soil model (HS). Input stiffness and strength parameters for this model are estimated from available laboratory test data, while (Darcian) groundwater flow is controlled by field permeability measurements. Finite element calculations of real-time coupled flow and deformation are performed using the PLAXIS, a commercially available PC based code. The calculations focus on a simplified geometry, based on preliminary designs for cut-and-cover approaches to the Río Piedras Station, supported by a diaphragm wall and cross-lot bracing. The analyses evaluate the effects of selected input parameters (wall embedment length, soil stiffness and permeability properties) on predicted wall deflections and ground deformations. The predictions of maximum wall deflections and maximum surface settlements are in very good agreement with published empirical data, for excavations in similar types of soil.

However, predictions of settlement distributions are unrealistic and do not match empirical case history data. In principle, the calculations of ground movements can be improved by using soil models which replicate more closely the non-linear stiffness properties of Hato Rey soils. The application of these more complex analyses can only be justified if there is sufficient test data for selecting model parameters. The thesis recommends specific types of laboratory and field test that should be carried out for this purpose.

Thesis Supervisor: Prof. Andrew J. Whittle
Title: Associate Professor of Civil and Environmental Engineering

ACKNOWLEDGMENTS

I wish to express appreciation to those individuals and organizations that made this thesis possible:

First of all, I would like to thank Dr. Antonio González for involving me with the Tren Urbano project. Ever since we met at the University of Puerto Rico, he has been a source of support and inspiration.

My advisor, Professor Andrew J. Whittle, for his careful review of this thesis. He was always very encouraging and supportive of my work. It has been a great experience working with him.

I should also like to thank Professor Charles C. Ladd and Professor Herbert Einstein for been extremely generous of their time and giving me their input during several stages of my thesis.

I would like to thank the Tren Urbano GMAEC for providing the financial support of this research. The Tren Urbano research experience has been very rewarding in many different aspects.

Special thanks to my office mate, Lucy Jen, for all her help and good advises.

Mary and Carolyn for their kind words and interesting conversations.

My family in Puerto Rico for being so loving and supportive. *Papi y Mami, los quiero mucho.*

Ramón, my husband, friend and companion. Thanks for sharing with me all my experiences. *Mi Vida,*
eres mi inspiración divina.

Angela L. Alba-Carbó

TABLE OF CONTENTS

LIST OF TABLES

LIST OF FIGURES

1. Introduction

Tren Urbano is a high-capacity, rapid transit regional rail system to be constructed in the metropolitan area of Puerto Rico. Phase I of Tren Urbano consists of an L-shaped route, extending from Bayamón east to Río Piedras and north from Río Piedras to Santurce and includes approximately 14 kilometers of double track guideway and 15 stations (Figure 1.1). The Río Piedras Alignment, Section 7, is entirely underground, consisting of 1500 meters and will be constructed by cut-and-cover excavations and tunneling techniques.

One of the principal factors affecting the design of these sections is the control of ground deformations, in order to minimize damage to adjacent facilities and mitigate the costs of underpinning. This is especially true for construction in congested areas where the potential for damage to adjacent buildings, utilities, etc., can lead to very expensive remedial measures because of uncertainties in predicted deformations. The design specifications address these problems by requiring stiff pre-stressed bracing of cut-and-cover excavations, and installation of a permanent tunnel canopy by pipe jacking ('umbrella' construction method). However, there remain large uncertainties in the prediction of ground movements and the effectiveness of these construction procedures.

The aim of this project is to estimate the magnitudes of ground movements for Section 7 of the Tren Urbano project, and to relate these movements to the stratigraphy of the surrounding alluvial soils and proposed methods of construction.

1.1 Overview of Tren Urbano

The Tren Urbano project is divided into several phases: Phase I, Phase IA, Phase II, Phase III, and Phase IV. Figures 1.1 and Figure 1.2 shows the Tren Urbano Phase I and the final system configuration, respectively. Phase I of Tren Urbano is an independent viable project that does not depend on any future extensions of the system. However, the planning and design of Phase I anticipates these future actions and nothing in the design of this phase will preclude these extensions in the future. The Phase I Alignment of Tren Urbano can be described as follows (Figure 1.2):

1. From the Bayamón River to PR-21 and the De Diego Ave. Interchange (Sta. 182+60), the alignment runs slightly above existing grade through the 65th Infantry Expressway corridor.
2. From PR-21 (De Diego Station) to PR-3 at Río Piedras, the alignment is elevated and proceeds through highly developed areas such as Villa Nevárez, Veteran's Hospital Area, Centro Médico, etc.
3. From PR-3 at Río Piedras up to Central Ave. (PR-17), the route descends underground as it proceeds through the downtown area of Río Piedras.
4. From Central Ave. to the end of the trackway at Sagrado Corazón, an elevated structure is proposed crossing the Hato Rey center and "Milla de Oro" area.

Approximately 40% of the alignment is at or near grade. The remainder of the alignment, aside from short below-grade sections in the Jardines de Caparra, Centro Médico, and Las Lomas areas and the underground section through Río Piedras, is generally elevated above roadway rights-of-way.

1.2 Overview of Río Piedras Section

Section 7 alignment of the Tren Urbano involves approximately 1,500 meters of underground tunnels and two stations: Río Piedras Station and University of Puerto Rico Station. It connects to the Villa Nevárez (Section 6) on the south, and the Hato Rey (Section 8) to the north. The alignment passes Barriada Venezuela, crosses PR-3 near station 219, proceeds to go underground at Calle Julián E. Blanco and continues under Río Piedras until Station 231 near Calle Mariana Bracette (Figures 1.3a-d). Much of the Río Piedras alignment runs beneath (or slightly to the east of) and parallel to the Ponce de León Avenue. This section will be all constructed within deep alluvial deposits of interbedded stiff clays and silts referred to as the Hato Rey formation. This alignment was developed to optimize service to the traditional town center of Río Piedras and the University of Puerto Rico (UPR). The section also includes a junction to accommodate a future extension of the system to Carolina Centro (Phase II of Tren Urbano), which runs due east from Río Piedras Station along an elevated alignment parallel to PR-3.

The Río Piedras Station will be sited beneath existing buildings and utilities adjacent to the Commercial Center Historic District, along Ponce de León Avenue. The existing buildings consist of old masonry structures, which could be very sensitive to deformations. The approaches to the station will be constructed by cut-and-cover excavations, with a maximum depth of approximately 23 m, while the station itself will be excavated by tunneling techniques. To minimize subsidence impacts, the preliminary design proposes a very strong and stiff "roof" of jacked pipes to be installed between the station and the buildings. The microtunnel arch will provide a continuous shield, supporting and protecting the crown of the excavation. The underground mined station

work will occur between Sta. 219+90 and Sta. 221+15. The overburden depth over the crown of the station varies between 7m and 5m. The station opening, approximately 14m high by 19m wide will be arch shaped. Figures 1.4 and 1.5 illustrate typical cross-sections of the Río Piedras Station and North Approach Cut and Cover Sections, based on preliminary designs.

1.3 Methods for Predicting Ground Movements

Existing techniques for predicting ground movements fall into two categories: semi-empirical methods and finite element methods. Semi-empirical methods, which are based on field data collected from case histories, provide a useful guide for estimating a likely wide range of movements, but cannot be used reliably for site specific predictions. Figure 1.6 shows empirical charts of the distribution of ground surface settlements for braced excavations in: a) stiff to very hard clays; and b) design chart for wall movements after Clough et. al. 1989. As a first approximation, ground conditions along the Río Piedras alignment can be classified as stiff clays. Hence, the results in figure 1.6a show that maximum expected ground settlements for a 20 m deep excavation are $\delta_v \cong 6$ cm (2.5").

More reliable predictions can be achieved by using advanced finite element analyses that incorporate realistic modeling of soil behavior, proper definition of the site stratigraphy and relevant soil properties, and realistic simulation of all pertinent construction activities, which occur during the excavation process. Finite element analyses were first applied to braced excavations by Clough et. al. (1972), Christian and Wong (1973) and have now gained widespread acceptance through their capability to

model complex construction sequences, and to incorporate detailed site-specific properties of the structural system and surrounding soils. In principle, the finite element method offers a comprehensive tool for analyzing multiple facets of excavation performance ranging from the design of the wall and supporting system, to predictions of ground movements and the effects of construction activities such as dewatering, ground improvement, etc. The MIT geotechnical group has extensive experience in applying these advanced numerical simulations for excavations and has reported results from two detailed case studies at well instrumented sites: 1) Post Office Square garage in Boston (Whittle et. al., 1993a), and the World Trade Convention Center in Taipei (Whittle et. al., 1993b). In both cases, the finite element predictions were performed using site characterization data provided prior to construction, while the simulated excavation sequence was based on the actual record of construction activities. The analyses were compared with all available field monitoring data (i.e., wall deflections, vertical and lateral soil deformations, strut loads, pore water and lateral earth pressures) in order to assess all aspects of the prediction. No attempt was made to correlate or adjust input parameters to improve agreement with the measured data. Appendix A summarizes these case studies. The results show very good agreement with the measured excavation performance and provide strong support for further applications of these methods for Tren Urbano project.

1.4 Selection of Finite Element Program

The recent studies of excavation performance at MIT have used the ABAQUS^{TM} program, a commercial workstation based finite element program. The stress-strain-

strength properties of soft clays were described using the MIT-E3 effective stress soil model (Whittle and Kavvadas, 1994; Whittle et. al., 1994). In contrast, the current study uses PLAXIS™, a commercially available PC-based finite element program, together with much simpler soil models. The reasons for this choice are as follows:

1. Soil conditions at Río Piedras comprise alluvial deposits of clays, sands and clayey sands, which are highly overconsolidated. There is limited laboratory data on these materials and no existing documentation to show the advantage of using sophisticated soil models. The lack of laboratory data also makes parameter selection difficult even for relatively simple soil models.
2. ABAQUS is a very general finite element program that is widely used in the aerospace, defense and oil industries. However, its application within the geotechnical community is mainly for research purposes, and it is not widely used in the construction industry. In contrast, PLAXIS is designed as user-friendly software for geotechnical problem solving and has many features similar to ABAQUS for the purpose of modeling excavation behavior: i) It models concurrently the soil deformation and flow of groundwater, and hence can model the effects of partial drainage during construction. Excavation and dewatering activities alter the groundwater regime in the soil, which sets up a transient flow condition (partial drainage) and induces time dependent deformations of the soil mass. ii) PLAXIS includes a range of simple elasto-plastic models (EP) of soil behavior. This research uses the Hard Soil model (Schanz and Vermeer, 1996), which was originally developed to describe the behavior of sand, gravel, and heavily overconsolidated (stiff) cohesive soils. This model follows the logic of the Duncan-Chang model (HS:

Schanz and Vermeer, 1996), but also incorporates plasticity theory. The key characteristics of the Hard Soil model are:

1. Stress dependent stiffness, according to a power law.
2. Hyperbolic relationship between strain and deviatoric stress.
3. Distinction between primary deviatoric loading and unloading/reloading.
4. Failure behavior according to the Mohr-Coulomb model.

These features represent a set of reasonable assumption for modeling soil conditions at the Río Piedras site.

1.5 Objectives and Scope

The aim of this project is to estimate the magnitudes of ground movements for Section 7 of the Tren Urbano project, and to relate these movements to the stratigraphy of the surrounding alluvial soils and proposed methods of construction. This project involves three main tasks:

1. Characterization of the site stratigraphy, ground water conditions and engineering properties of the principal soil layers along the Section 7 alignment in Río Piedras
2. Development of numerical analysis models to represent a typical cross-section of the project, simulate the proposed construction sequence and represent the deformation and flow properties of the soils
3. Interpretation of the predicted ground movements

No previous geotechnical engineering studies were conducted specifically for the Río Piedras Section of the Tren Urbano prior to those conducted through Tren Urbano/GMAEC. However, there have been previous studies of local soil conditions

(Deere, 1959; Kaye, 1959; and Monroe and Pease, 1977). The site characterization is based on geotechnical exploration programs already carried out for Section 7 alignment (GMAEC, GDR 1996). The geotechnical field investigations consisted of two phases:

1. Phase One, which included 6 borings along the present Río Piedras alignment between Sta. 217+00 and Sta. 225+00 (current alignment). Six additional borings were drilled east of the Río Piedras alignment near Highway PR-3.

2. Phase Two, which included 10 borings along the revised proposed tunneled section between Sta. 217+00 and Sta. 230+00.

Additional field and laboratory tests were performed during Phase Two investigation, index tests[1], unconfined compression tests, borehole permeability (9) and pressuremeter tests (3). Also, supplemental geotechnical investigations for Río Piedras were conducted from August through the first week of October 1996.

The analyses focus on two typical cross-sections of the cut-and-cover braced excavations at the North and South approaches of the Río Piedras Station. Special consideration is given to the representation of soil properties in the numerical analyses. The predicted ground deformations are compared with published data from projects using similar construction techniques and available empirical correlations.

[1] The tests include Atterberg limits, particle size gradation, etc. However, there is no information given on typical unit weights.

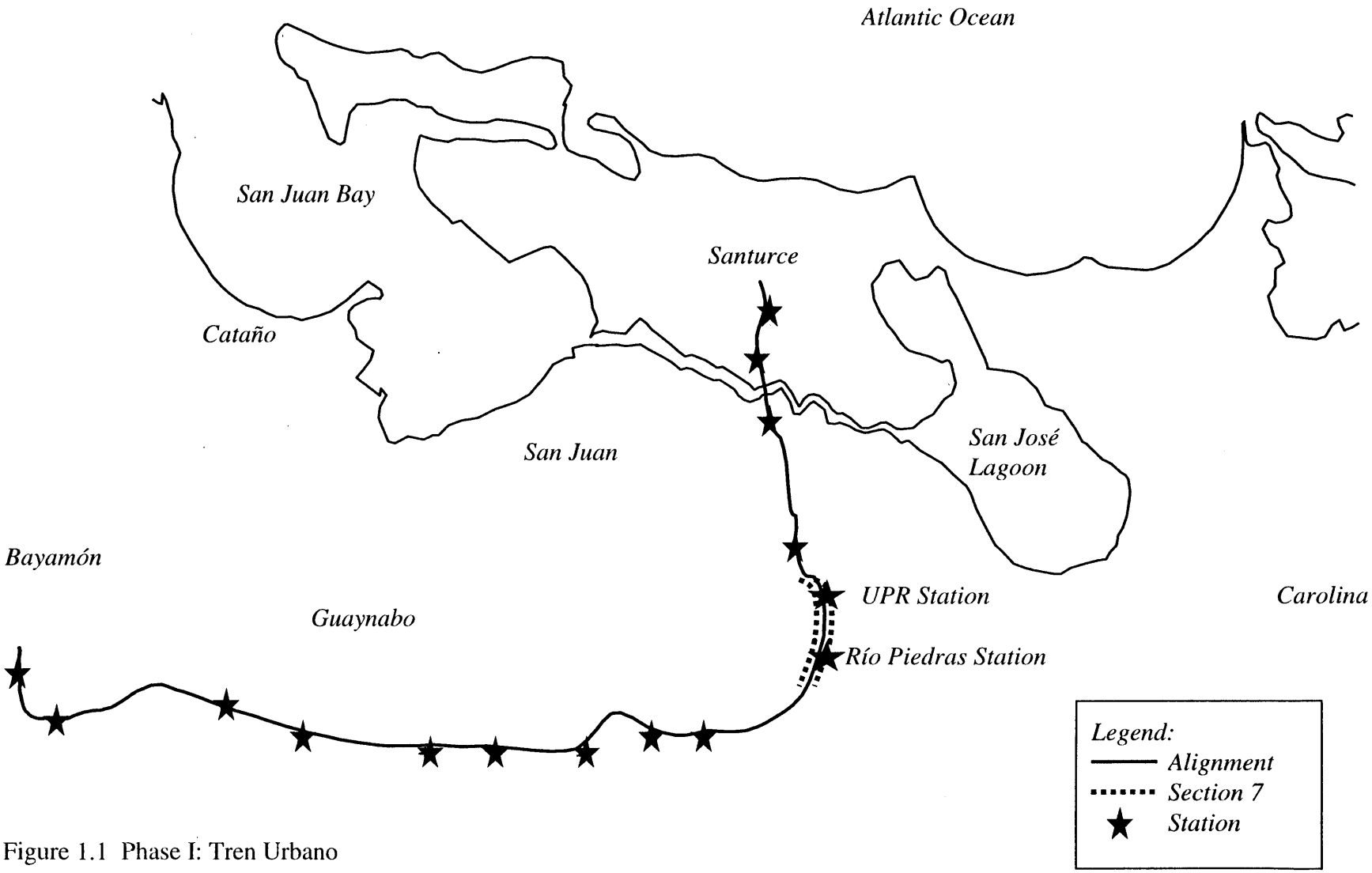

Figure 1.1 Phase I: Tren Urbano

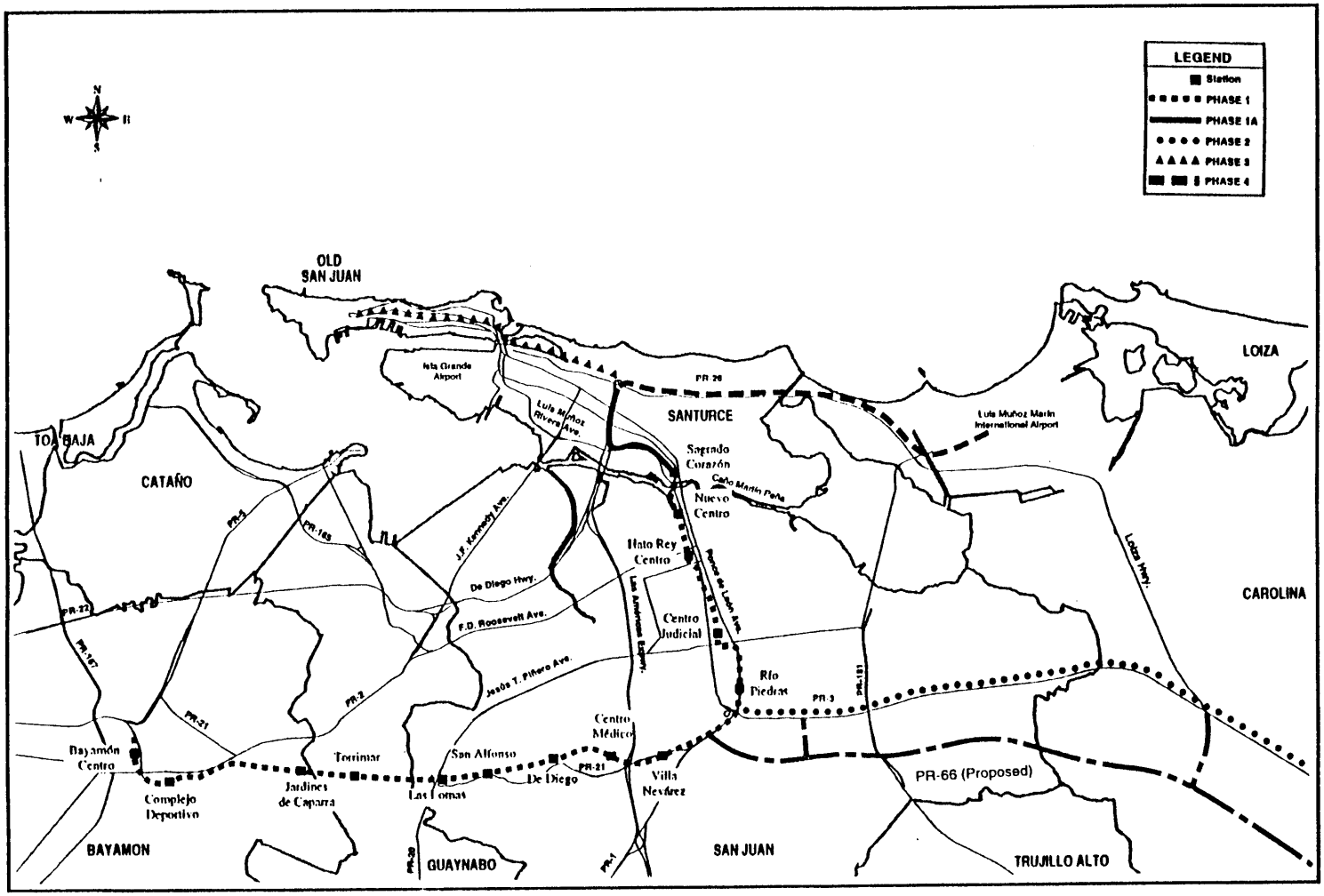

Figure 1.2 Final System Configuration

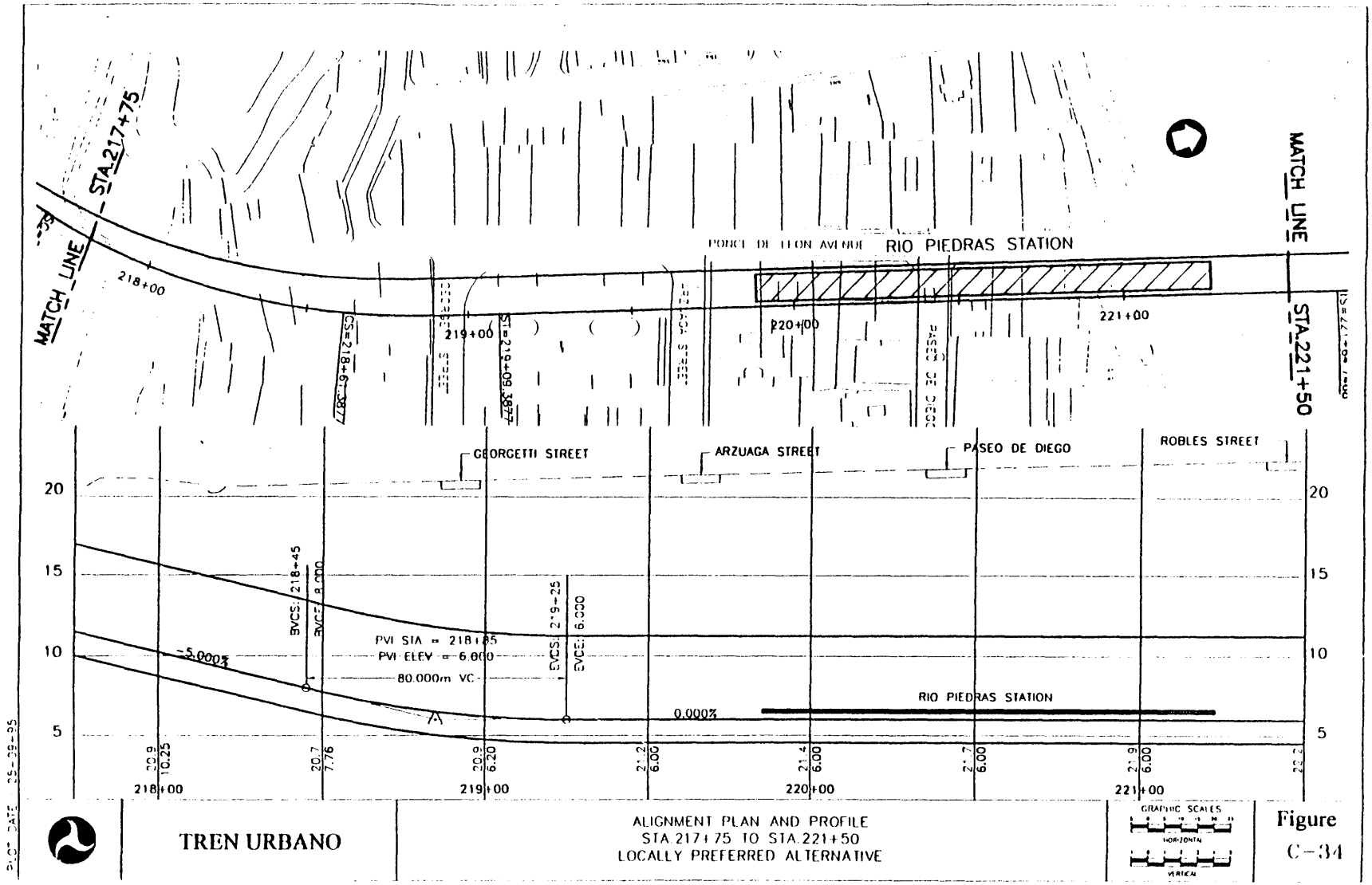

Figure 1.3a Section 7 Alignment

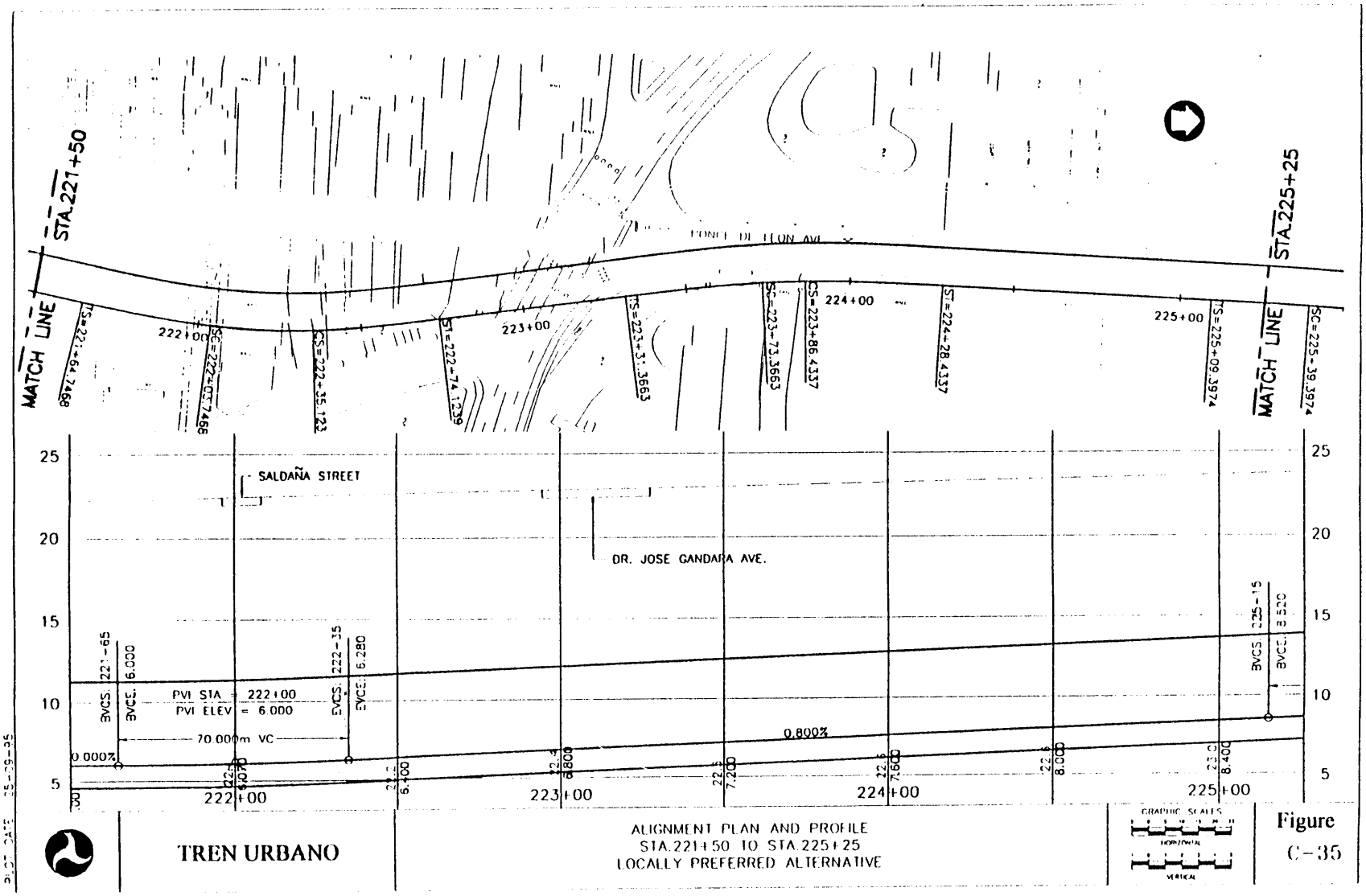

Figure 1.3b Section 7 Alignment

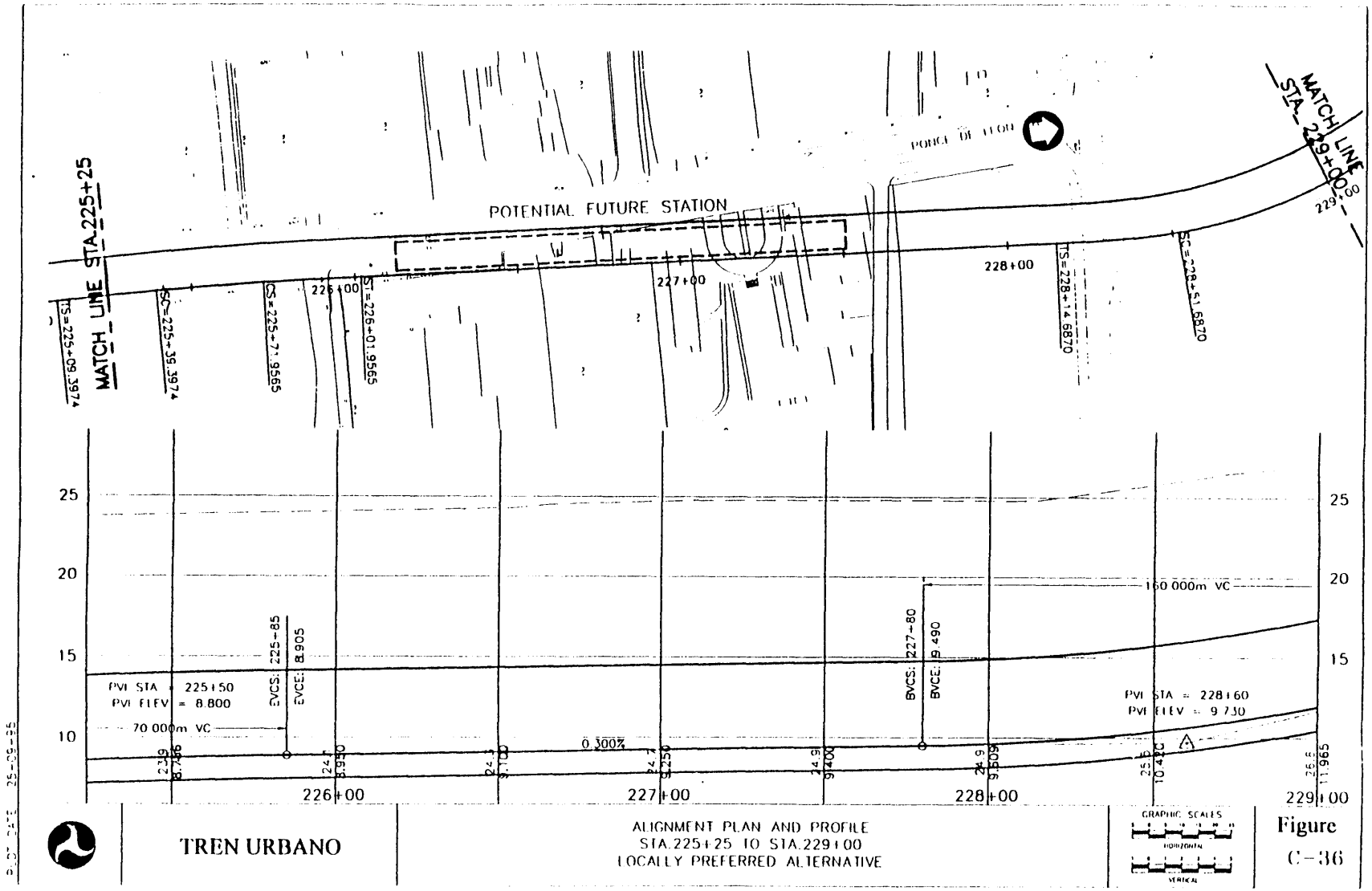

Figure 1.3c Section 7 Alignment

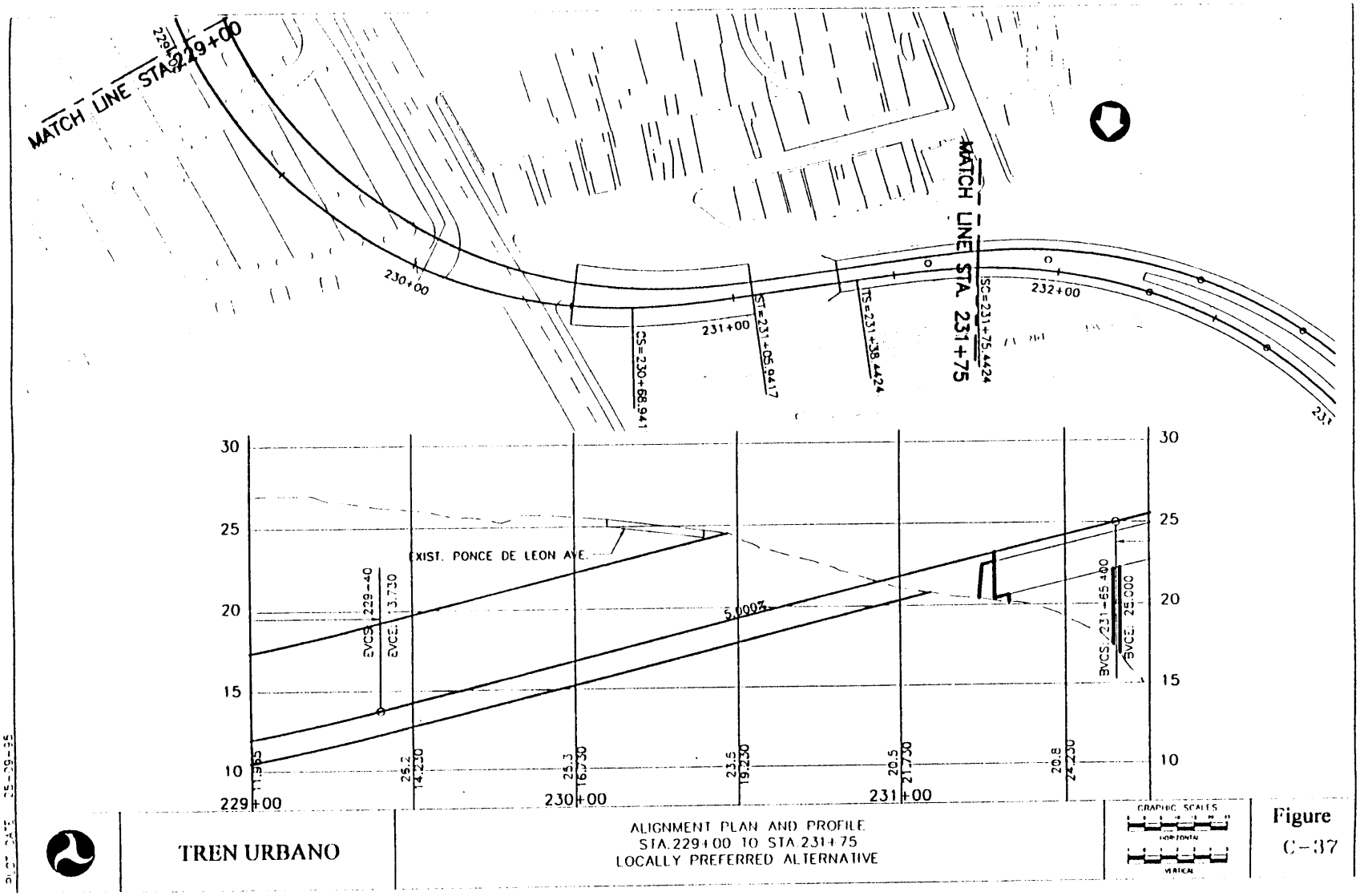

Figure 1.3d Section 7 Alignment

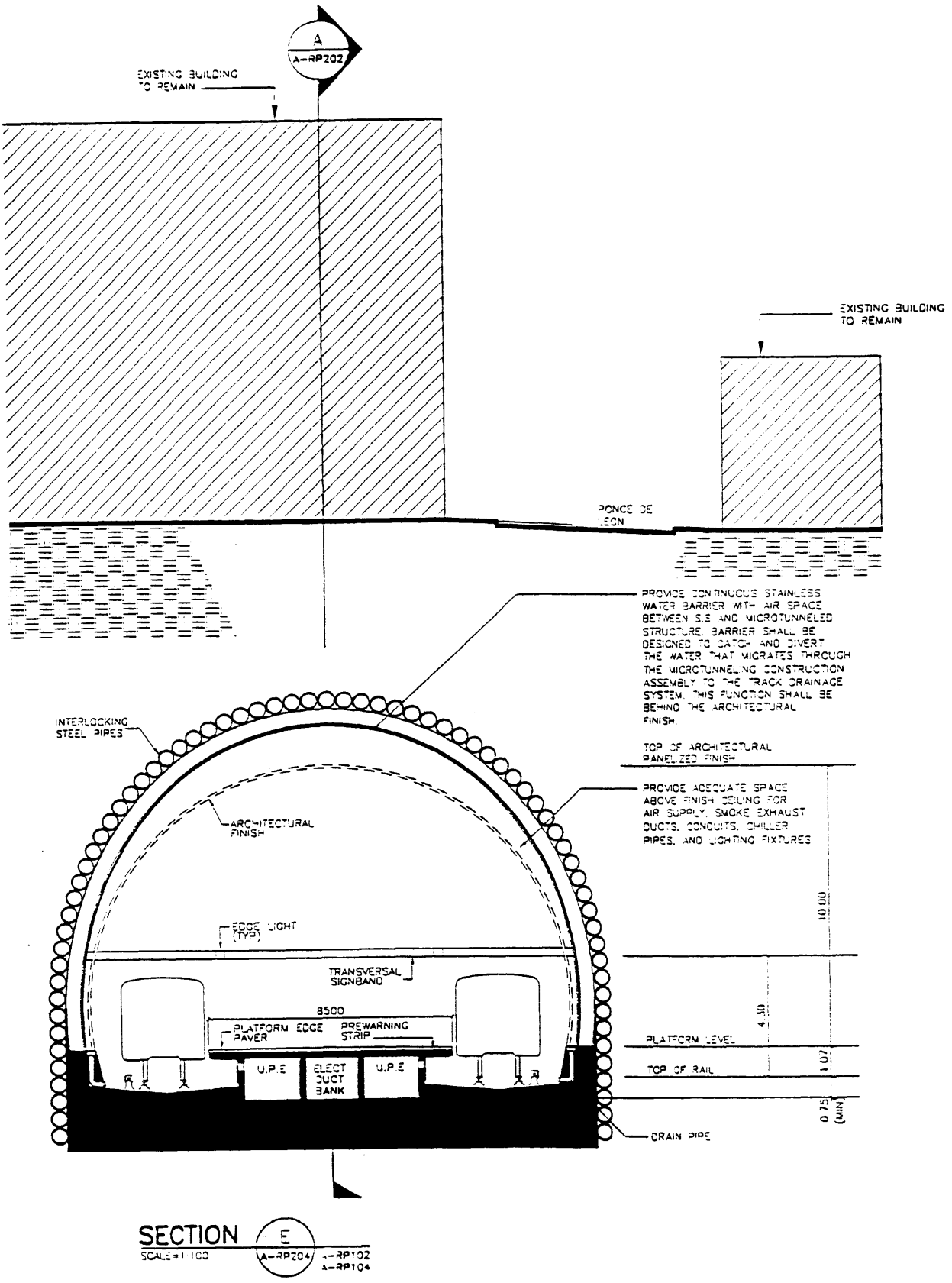

Figure 1.4 Río Piedras Station Section- Microtunnel

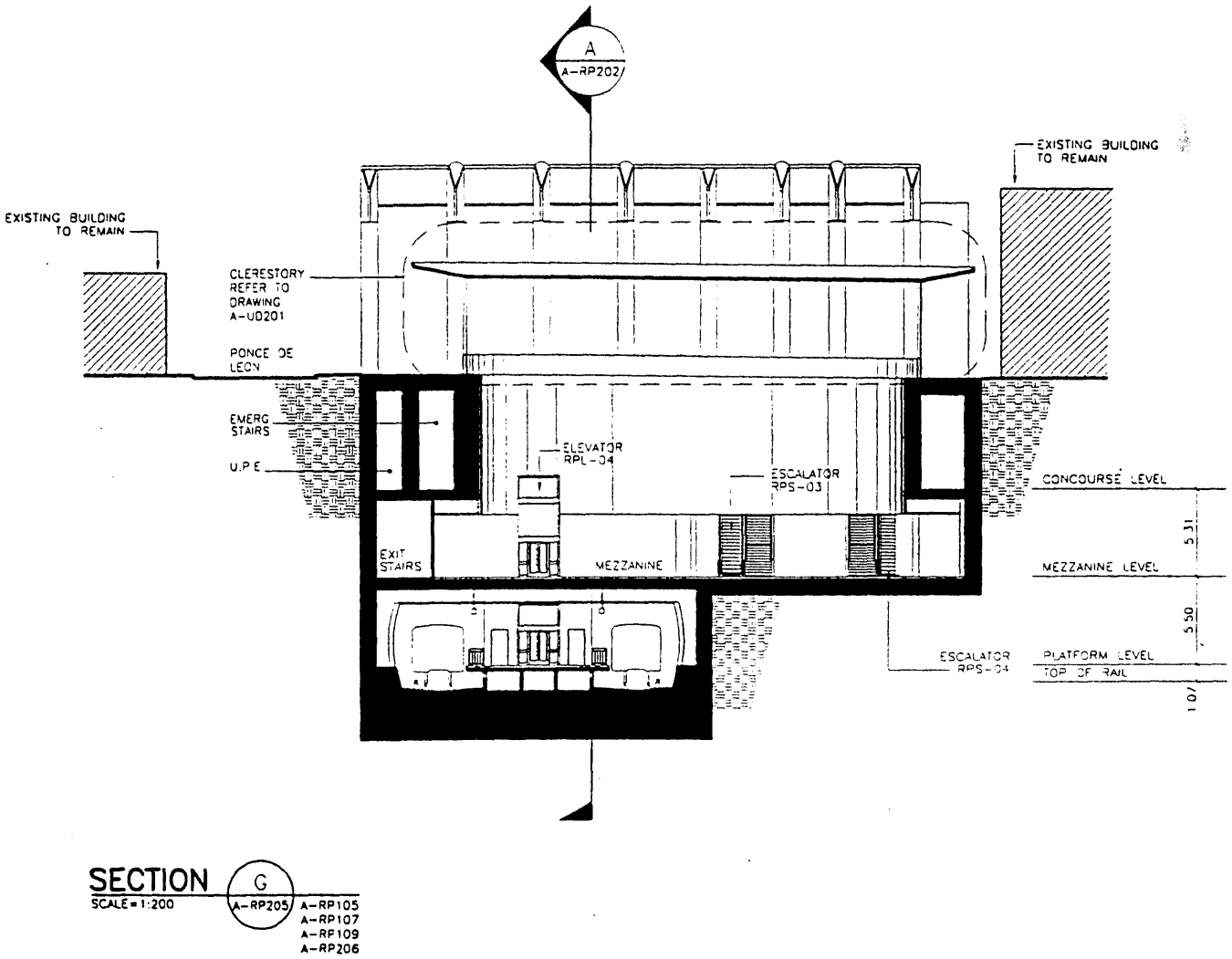

Figure 1.5 Río Piedras Station Transversal Section North- Cut and Cover

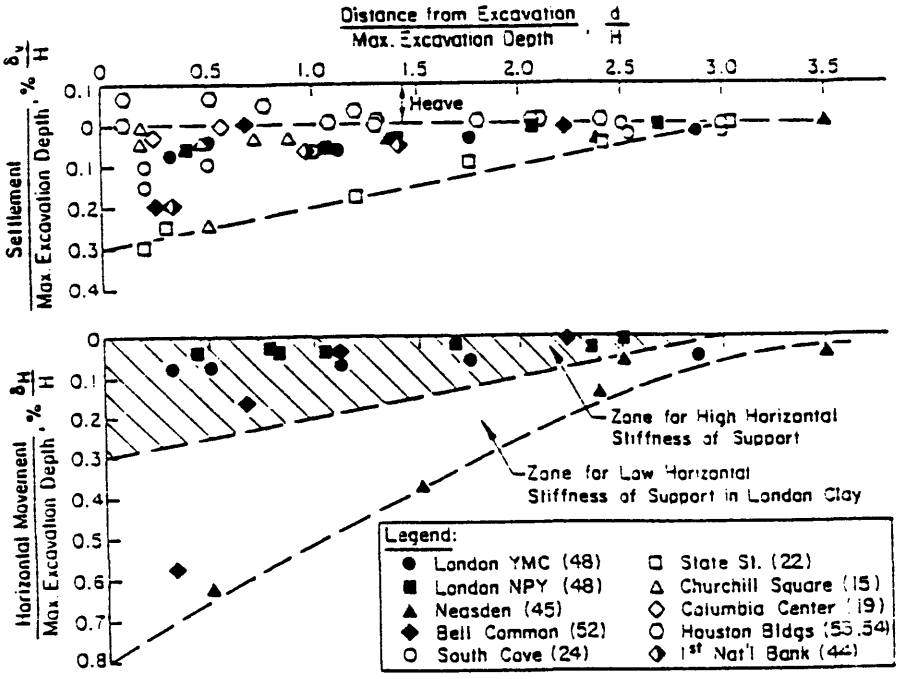

Summary of Measured Settlements and Horizontal Displacements Adjacent to Excavations in Stiff to Very Hard Clay.

(a)

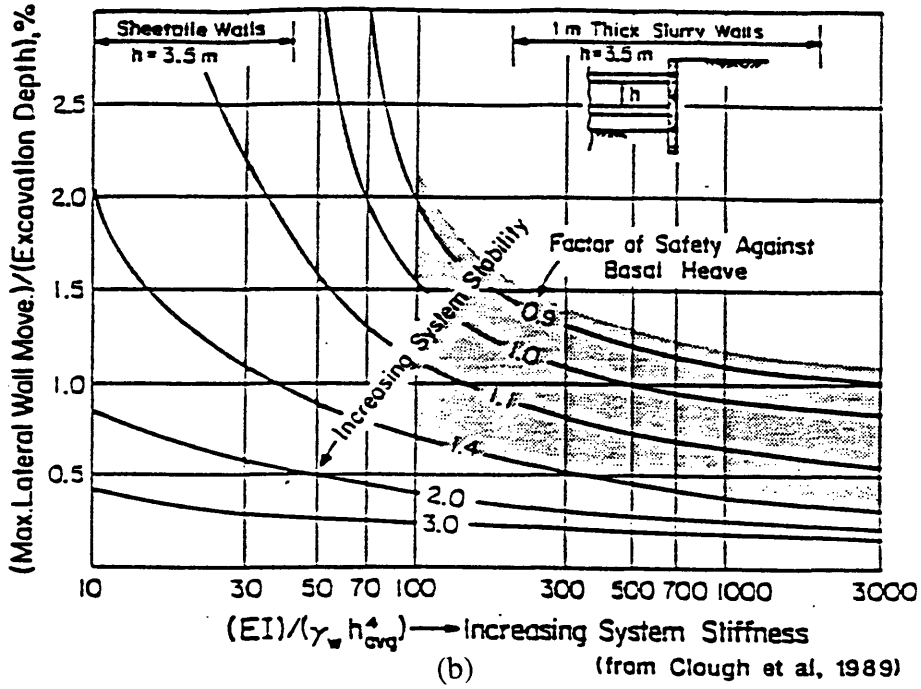

(b) (from Clough et al, 1989)

Figure 1.6 Examples of Semi-Empirical design Charts

2. Geology of Section 7 Alignment

The island of Puerto Rico is the easternmost and smallest of the Greater Antilles (Figure 2.1), a chain of large islands that comprises, from west to east, Cuba, Jamaica, Haiti, Dominican Republic, and Puerto Rico. The islands are bounded on the north by the Atlantic Ocean and on the south by the Caribbean Sea. Puerto Rico is roughly rectangular in shape, measuring approximately 110 miles from east to west and 37 miles from north to south. Puerto Rico is approximately 1,000 miles southeast of Miami, Florida, and 425 miles north of Venezuela. The climate of Puerto Rico is subtropical marine; and it lies in the zone of the trade winds which blow steadily from the northeast (Kaye, 1959). The city of San Juan is located on the eastern part of the north coast of Puerto Rico (See Figure 2.2).

2.1 Stratigraphy of the San Juan Metropolitan Area

The following is a summary of the geologic units of the San Juan Metropolitan area , based on three main sources of information Deere (1955), Kaye (1959), and Monroe (1976). The stratigraphic sequence can be summarized as follows (from oldest to youngest):

(1) Bedrock

The bedrock is comprised of Cretaceous[1] rocks and Tertiary[2] formations. No rocks older than Upper Cretaceous have been recognized in Puerto Rico (Deere, 1955). The rocks of Upper Cretaceous age consist of a great range of pyroclastic, sedimentary, extrusive, and intrusive igneous rocks. The Tertiary formations can be subdivided into the basal Río Guatemala group

[1] The Cretaceous period took place from 144 to 66.4 millions of years ago (total duration of 78 millions of years).
[2] The tertiary formations are 66.4 to 1.6 millions of years of age.

(middle to upper Oligocene), the Aguada limestone (lower Miocene), and the Aymamón limestone (lower Miocene).

(2) Quaternary Formations[3]

These sediments were deposited during the Pleistocene and Recent epochs; and they include, from oldest to youngest:

(a) Old Alluvium (Hato Rey Formation); which consists of thick deposits of clay, sand, clayey sand, sandy clay, and occasional beds of gravel.

(b) Santurce Sand; which is comprised of red and tan clayey silty sand, pure white quartz sand, partially cemented calcareous sand and quartz sand, and stiff red and gray mottled sandy clay.

(c) San Juan Formation; consisting of calcareous sandstone

(d) Floodplain Sediments; comprising mostly silty clay

(e) Lagoonal Sediments

(f) Sand Covered Lagoonal Sediments

2.2 Bedrock

The older rocks, that is to say, those of Cretaceous and early Tertiary age, are highly deformed and faulted. They comprise a sequence of volcanic flows, pyroclastics, and sedimentary rocks, but many of the latter consist largely of reworked volcanic material. Into these rocks have been intruded plugs, dikes, sills, and larger subjacent bodies that range in composition from granodiorite porphyry to diabase (Kaye, 1959).

[3] Quaternary is the name for recent deposits (not older than 1.6 millions of years ago).

Unconformably overlying the Upper Cretaceous and lower Tertiary complex in the San Juan area is a sequence of sands, clays, marls, and limestones of early Miocene age, which have been tilted to the north and faulted on a small scale but which are otherwise undeformed. These rocks probably underlie most of the coastal plain alluvium (Kaye, 1959).

Section 7 alignment: In the northern part of this section of the alignment, the top of decomposed and weathered calcareous limestone was encountered. The Geotechnical Data Report (GMAEC[4], GDR, April 1996) also states that at the southern limits of the project, the alluvial soils may also be underlain by the Eocene and Paleocene Río Piedras siltstone (sedimentary & volcanic rocks). This formation may be what Kaye (1959) refers to as the Fajardo Formation. Near the old town's plaza, the Río Piedras siltstone was found at about 35m of depth. The contact between the Cretaceous siltstone and the Tertiary calcareous limestone has not been established even though the evidence is that it should lie at depths below 40 m within the town of Río Piedras.

2.2.1 Cretaceous Rocks

Cretaceous rocks comprise the bedrock only along the southern boundary of the San Juan Metropolitan area. In general, no particular problem has been associated with the Cretaceous rocks. The upper part of the rock has been weathered to soft decomposed rock and residual soil. There exists a gradational and often irregular contact between residual soil, soft decomposed rock, and sound rock.

[4] General Management Architectural and Engineering Consultant

2.2.2 Tertiary Formations

The major portion of the San Juan area is underlain by the Tertiary rock formations ranging from zero to more than 100 ft. The great irregularity in depth to rock is due to erosion and solution. The character of the Tertiary formations is also extremely variable.

2.2.2.1 Fajardo Formation

At the southern limits of Section 7 Alignment, the alluvial soils may be underlain by the Eocene and Paleocene Río Piedras siltstone (GMAEC, GDR, April 1996). This formational unit could be what Kaye (1959) refers to as the Fajardo Formation (early Eocene or late Paleocene). Most characteristic of the Fajardo formation is a relatively soft, very well bedded, light colored, non-fissile aphanitic[5] rock of rather low density. The color is light yellow, light tan, white, pink, and various shades of red. The beds are generally about 2 inches thick. Thin intercalations, usually less than 1 inch thick, of light-gray to white kaolinitic clay are common between siltstone beds. The rock is everywhere well jointed, and it breaks readily into rhomboidal-shaped flagstones and blocky fragments bounded by smooth joints and bedding planes. Despite the fact that the rock seems to be deeply weathered, it does not decompose readily to soft clay but retains its cohesive strength and form even when wet. This peculiarity probably accounts for the fact that in the San Juan area its outcrops generally form prominent topographic highs. Most of the Montes de Hatillo, south and east of Río Piedras are cuestas of these rocks. Besides the rather soft ashy siltstone there is also cream-colored to white thin bedded chert and a siliceous siltstone.

[5] A rock in which individual crystals are too small to be identified without the aid of a microscope.

No fossils have been found in the Fajardo formation and it is judged to be late Paleocene or Eocene in age (Kaye, 1959). No formational unit of the older complex[6] higher than the Fajardo formation has been recognized in the San Juan area. Between the time it was deposited, probably in the Paleocene or Eocene, and the onset of the deposition of the next youngest rocks in the early Miocene, a profound revolution took place during which occurred most of the folding, faulting, and intrusion of igneous material that characterizes the older complex.

2.2.2.2 Aguada Formation

The basal Tertiary formation in the San Juan area is the Aguada formation that lies directly upon the eroded surface of the Cretaceous rocks. Because of its depth it normally is not of concern in foundation work.

The formation consists predominantly of non-carbonate rocks (Kaye, 1959). It is composed of sands, gravels, shale, marl, and interbedded limestone[7]. It outcrops in the middle and southern portion of the San Juan Metropolitan area (Deere, 1955). The beds assigned to the Aguada formation crop out as soil-covered round slopes and tepee-shaped hills east and west of Río Piedras. This topographic form is in contrast with that developed on the overlying dense Aymamón limestone, which generally forms karst hills with steep rocky slopes. The Aguada formation possesses the following characteristics: 1) It underlies the dense limestone of the Aymamón formation; 2) it possesses a fauna of Miocene aspect like the overlying Aymamón formation; and 3) it consists essentially of interbedded pure limestone and softer chalky to marly

[6] Older complex: consist of an unknown thickness of sedimentary and volcanic rocks of late Cretaceous to Paleocene or early Eocene age.
[7] Limestone, and particularly dense limestone, occurs only sparsely and generally as thin lenses (Kaye, 1959).

limestone, although up to 10m of basal sand, gravel, and shale occur where the formation rests directly on the Cretaceous rocks.

The Aymamón limestone, which overlies the Aguada formation, is the formation that forms the bedrock throughout the majority of the San Juan Bay area.

The Aymamón limestone was originally a hard, finely crystalline, dense limestone. However, during the period that it was subjected to sub-areal erosion, extensive solution reduced it to karst topography characterized by caverns, fissures, and sinkholes. Collapse of many of the openings took place, causing brecciation of the limestone. Clay filled many of the channels and caverns and became mixed with the limestone fragments. Because of the modified character of the rock, the term bedrock in the San Juan Bay area does not necessarily designate a firm sound rock into which piles cannot be driven. Normally erratic driving resistance is encountered (Deere, 1955).

The entire San Juan area was at one time covered by these formations (Aguada & Aymamón) but they have been almost completely removed by solution and erosion. The remnants show collapse structures, clay-filled fissures and cavities, and in general the effects of solution.

2.3 Quaternary Deposits

The last one million years of geologic time (from the end of Tertiary to present), have been characterized by: a) severe climatic changes; and b) formation of glacial ice-sheets covering large areas. Four main advances of the glaciers separated by periods of warmer climate took place.

During the glacial stages, the precipitation was largely retained by the glaciers. Consequently, the amount of water in the ocean decreased and as a result, there was a general

lowering of the sea level throughout the world {e.g., last glacial age: lowering of 70m to 100m}. Stream gradient and energy increased resulting in downcutting through and reworking up previously deposited coastal plain sediments.

Each of the advances of glaciers was followed by a period of warmer climate, probably of much longer duration than the periods of glacial condition. The sea level rose to a position even higher than it is now (from 20m to 50m above the present sea level) and finer grained deposition generally occurred.

In Puerto Rico, nearly every deposit along the coast has a direct relationship with the change in sealevel corresponding to the various glacial and interglacial ages.

Volcanic Activity and Crustal Stability: At present there are no active volcanoes in Puerto Rico or the Virgin Islands (since 60 million years ago). However, the frequent earthquakes, which occur throughout the island, are evidence of continued crustal instability. Puerto Rico is located within an active seismic area with major fault zones located in the Puerto Rico trench between the Caribbean and North American plates. There are four major tectonic features near Puerto Rico capable of generating a major earthquake, these are the Puerto Rico Trench, Mona Passage, the Anegada Trough, and Los Muertos Trough.

Recent uplift: Meyerhoff (1933) concludes that the uplift has been differential with perhaps 1.5m to 3.1m uplift in the northeastern part of the island and 4.6m to 9.1m along the western and southern coasts. The differential uplift in Puerto Rico is probably a combination of the general lowering of sea level and slight uplift and tilting. This has been of immense importance from the foundation engineering viewpoint because the lowered water table has allowed soil above the ground water level to dry out, forming a stiff desiccated crust several feet in thickness.

2.4 Near Surface Deposits

In San Juan and its suburbs (Santurce, Hato Rey and Río Piedras) the hills and the adjacent lowlands, which are not covered by more recent lagoonal or flood plain sediments, show exposures of thick deposits of clay, sand, clayey sand, sandy clay, and occasional beds of gravel. These soil deposits are commonly referred to as the old alluvium, the blanket sands of Puerto Rico, and/or the *Hato Rey formation* (Figure 2.3). The formations are striking in appearance with colors ranging from white to reddish brown, often in a mottled pattern. The light brown, brown, and reddish brown color comes from oxidation. The sand is mostly quartz sand, a product of older Cretaceous bedrock in the interior of the island. Secondary structure is commonly present in the form of joints, concretions, and occasional slight cementation by iron oxides. These deposits are noted to be of variable thickness, but probably less than 100m. The presence of occasional stratification, sand pockets, and lenses; the lack of marine fossils; and the areal relationship with the definitively fluvial type of deposit where the Hato Rey formation overlaps the Cretaceous rocks to the south, suggest very strongly the fluvial origin of the deposits, probably been deposited as a piedmont alluvial plain.

The Hato Rey formation is quite extensive and can be traced westward along the north coastal plain for more than 50 miles. In that area it blankets the eroded Tertiary rocks, although solution remnants of limestone (haystack hills, "mogotes") potrude above the general level of the coastal plain as hills of "circumalluviation" (Deere, 1955).

The sediments rest unconformably upon the eroded and weathered surface of the Tertiary formations in most of the area but south of the Tertiary-Cretaceous boundary they overlap the Cretaceous rocks a short distance. The gravels are present only near the Cretaceous boundary. Away from the Cretaceous boundary, in the area of the Tertiary formations, the sediments are

predominantly clay and quartz sand which have been derived from the Tertiary rocks. The Aguada formation (lower Miocene) in particular contains many beds of quartz sands and was no doubt an important source of sediments.

Age: The Hato Rey formation is younger than the erosion surface (eroded Caguana peneplane) of the Tertiary and Cretaceous rocks upon which it rests, and older than the cemented dune sands, floodplain sediments, and lagoonal deposits which in many areas overlie it. It pre-dates the period of erosion in which valleys were carved through the Hato Rey deposits and were infilled with floodplain sediments. These valleys were eroded during the time of lowered sealevel of middle Wisconsin[8] and the floodplain and lagoonal sediments were deposited with the rising sealevel, of late Wisconsin time. Therefore, the Hato Rey formation must be at least pre-middle Wisconsin (Deere, 1955). Meyerhoff (1927) dates the Caguana peneplane as late Pliocene, and the uplift and dissection of the peneplane as early Pleistocene. The Hato Rey formation could have been deposited contemporaneously with and following the dissection, then it is reasonable to date the Hato Rey formation as early Pleistocene.

Section 7 alignment: The entire Río Piedras alignment consists of *Older Alluvial* (i.e. Hato Rey) deposits that are Pleistocene and Pliocene silty and sandy clays with interbedded sands. The predominant soil types encountered during the site investigation were clays and silts with variable amounts of sand typical of cut-and-fill structures in floodplain areas. The silty clays and clayey silts both contain some sand and are highly pre-consolidated by desiccation. The sand grains are fine to medium in size and consist almost entirely of clear quartz, although the grains are often stained tan or red by iron oxide. The sequence of the different types of soil is present in an erratic fashion. The sediments are normally in a dense or compact stage. The soil

[8] Late Pleistocene

deposits along this section of the alignment rest unconformably over the bedrock at depths estimated from 30 to 100m.

2.5 Ground Water Conditions

Local experience indicates that the limestone underlying the clayey coastal plain sediments comprises a confined bedrock aquifer that, locally, contains ground water under artesian pressure. In these areas, considerable ground water inflow can occur into excavations. However, there are no artesian conditions expected in the vicinity of Río Piedras according to Capacete (*personal communication*, 1997).

An unconfined watertable aquifer resides within the soil deposits overlying the limestone bedrock. Perched ground water conditions are also possible within the highly variable, discontinuous, lenticular sand layers that are found within the alluvium (which is generally more clayey in nature). Some ground water monitoring data (GMAEC, GDR, April 1996) show large variations over time and could be caused by leaking sewer and water utilities in the vicinity.

2.6 Seismic Considerations

Puerto Rico is located within an active seismic area with major fault zones located in the Puerto Rico trench between the Caribbean and North American plates. There are four major tectonic features near Puerto Rico capable of generating a major earthquake, these are the Puerto Rico Trench, Mona Passage, the Anegada Trough, and Los Muertos Trough. Figure 2.4 shows the location of Puerto Rico with respect to major geographic and tectonic features. Approximately 300 earthquakes are registered in Puerto Rico each year, but only a few are felt by people (GMAEC, GDR, April 1996). The earthquake activity in the Caribbean strongly suggests

that the main sources of possible damaging earthquakes are active and that although no predictions can be made, this area is susceptible to future earthquake shocks of the same or higher magnitude than those experience in the past, such as the ones in the years 1844, 1867, 1906 and 1918. The strong earthquakes of 1943 (magnitude 7.5) and 1946 (magnitude 8.1), whose epicenters were located in the Puerto Rico Trench Fault Zone, did not cause any damage on the Island due to the high attenuation that took place due to their location (GMAEC, GDR, April 1996). Figure 2.5 shows the seismic hazard map (1987) for Puerto Rico (Earth Scientific Consultants and W. McCann and Associates, Inc., 1994). Figure 2.6 shows maps of acceleration for 50, 100 and 250 year exposure (Earth Scientific Consultants and W. McCann and Associates, Inc., 1994). Most of the island has values in excess of 0.25g (Earth Scientific Consultants and W. McCann and Associates, Inc., 1994).

2.7 Overview of Engineering Properties of Hato Rey Deposits

There are two main sources of information on the physical, index and engineering properties of the Hato Rey deposits: i) PhD thesis at University of Illinois by Deere (1955); and ii) Geotechnical Data Reports (GDR) of GMAEC for Tren Urbano Section 7 (GDR, 1996a,b). The following paragraphs summarize the main observations made by Deere (1995) and highlight some similarities and differences reported from the Section 7 site investigation.

Water contents measured on 70 samples from typical borings in the Hato Rey formation ranged from 15 to 48 %. The great majority of the values are in the range from 30 to 35%. Deere (1955) explains that the wide spread in values is due primarily to variations in texture of the samples, which range from clayey sands to clays. Beneath the water table, the materials are

generally saturated. The GDR data (Table 2.2) show less scatter with water content equal to approximately 29 ± 7%.

Deere (1955) performed a limited number of Atterberg limits tests (15 samples) showing more uniform results. The liquid limit ranges from w_L=78 to 105%, (with an average of 92%) while the plastic limit, w_p= 31 to 47% (ave. 38%). Hence, the plasticity index I_p= 41 to 62%. The majority of the samples plot close to or slightly above the A-line in the Casagrande classification chart (Casagrande, 1955) and are classified as high plasticity clays (CH) while some samples below the A-line are silts of high compressibility. The GDR data (Table 2.2) show less scatter and lower values with w_L= 53 ± 17 % and w_p= 24 ± 7%, where most of the data plot above the A-line in the Cassagrande classification chart.

The activity ratio was determined on 4 samples and ranges from A=0.95 to 1.60, and hence are classified as normal to active sediments. Two samples were studied by X-ray diffraction and differential thermal methods to determine their clay mineralogy. One of the samples showed poorly associated kaolinite with some illite[9]. The other, which was studied by X-ray diffraction method[10], gave indications of being a member of the kaolin family but not kaolinite. This could possibly be poorly associated kaolinite, or perhaps halloysite.

The cohesive sediments of the Hato Rey formation are normally of stiff to very stiff consistency. Unconfined compressive strengths of over 70 samples from typical borings range from 1.0 to 5.5 TSF and average 2.9 TSF. The lower values were associated with sand pockets or joints in the sample that caused local failure during testing. The N-values obtained from the standard penetration test range from 15 to over 100. However, the samples normally fall in the

[9] Work by Dr. E. Grim, (Deere, 1955)
[10] Work done by the Laboratorio Industrial in Puerto Rico, (Deere, 1955)

range N= 20 and 40. This would indicate a consistency of very stiff to hard, with unconfined compressive strengths on the order of 2.0 to 4.0 TSF or greater.

The wide scattering of the values is said to be caused by joints, the wide range in textural composition, and the random sand pockets all typical properties of the Hato Rey sediments. Since settlements are not a serious problem, the compressibility characteristics of the sediments have not been extensively investigated at the time of Deere's thesis and the results of only a few consolidation tests were available. A review of these data shows that the applied consolidation stresses were significantly smaller than the pre-consolidation pressure (there is no well defined yield in the e-logσ_v' data). By using the empirical relationship, C_c=0.009(w_L-10) (Terzaghi and Peck, 1948), to estimate the compressibility of normally consolidated clays, Deere (1955) estimates C_c=0.72. By doing curve fitting to the measured data he estimates a preconsolidation pressure, σ_p'= 20 TSF. Other test results suggest much lower values than this, σ_p'= 3-5 TSF.

Deere also suggests that the sediments of the Hato Rey formation possess many characteristics that are normally associated with swelling clays. Terzaghi (1955) states that clays which have been investigated with relation to heave phenomena have a plasticity index greater than 30 and a liquidity index close to or below zero, are intensively jointed, and have a water table located at a depth of 15' or more below the surface. The author argues that the Hato Rey formations meet these conditions in most respects with the exception in some areas of the deep water table and intense jointing. Deere (1955) states that no heave phenomena have been observed to date, but the probability that swelling could be of importance under certain conditions should be realized. Swelling properties may be of particular importance for proposed deep excavations in the Hato Rey deposits associated with Section 7 of the Tren Urbano.

Table 2.1 Bedrock Formations in San Juan Metropolitan Area

Stratigraphic unit	*Description*	*Thickness, feet*	*Age*
Fajardo Formation	Light colored ashy siltstone, siliceous siltstone and chert, interfingering graywayke, conglomerate, and impure limestone.	3,000+	early Eocene? or late Paleocene?
Aguada Formation	Friable sandstone, clay, and concretionary limestone	325	early Miocene
Aymamón Formation	Thick-bedded, light colored, dense limestone	950+	early Miocene

Table 2.2 Comparison of Index Properties for Hato Rey Alluvial Sediments

Property	Deere (1955)	GDR (1996a)	GDR (1996b)
Water Content, w (%)	15 - 48	29 ± 7	29 ± 8
Plastic Limit, W_p (%)	31 - 47	24 ± 7	23 ± 5
Liquid Limit, w_L (%)	78 - 105	53 ± 17	52 ± 14
Compressibility Index, C_c* (of N.C. clay)	0.72	0.38	0.38

* Estimated from empirical relation, $Cc=0.009(w_L-10\%)$ after Terzaghi and Peck (1948)

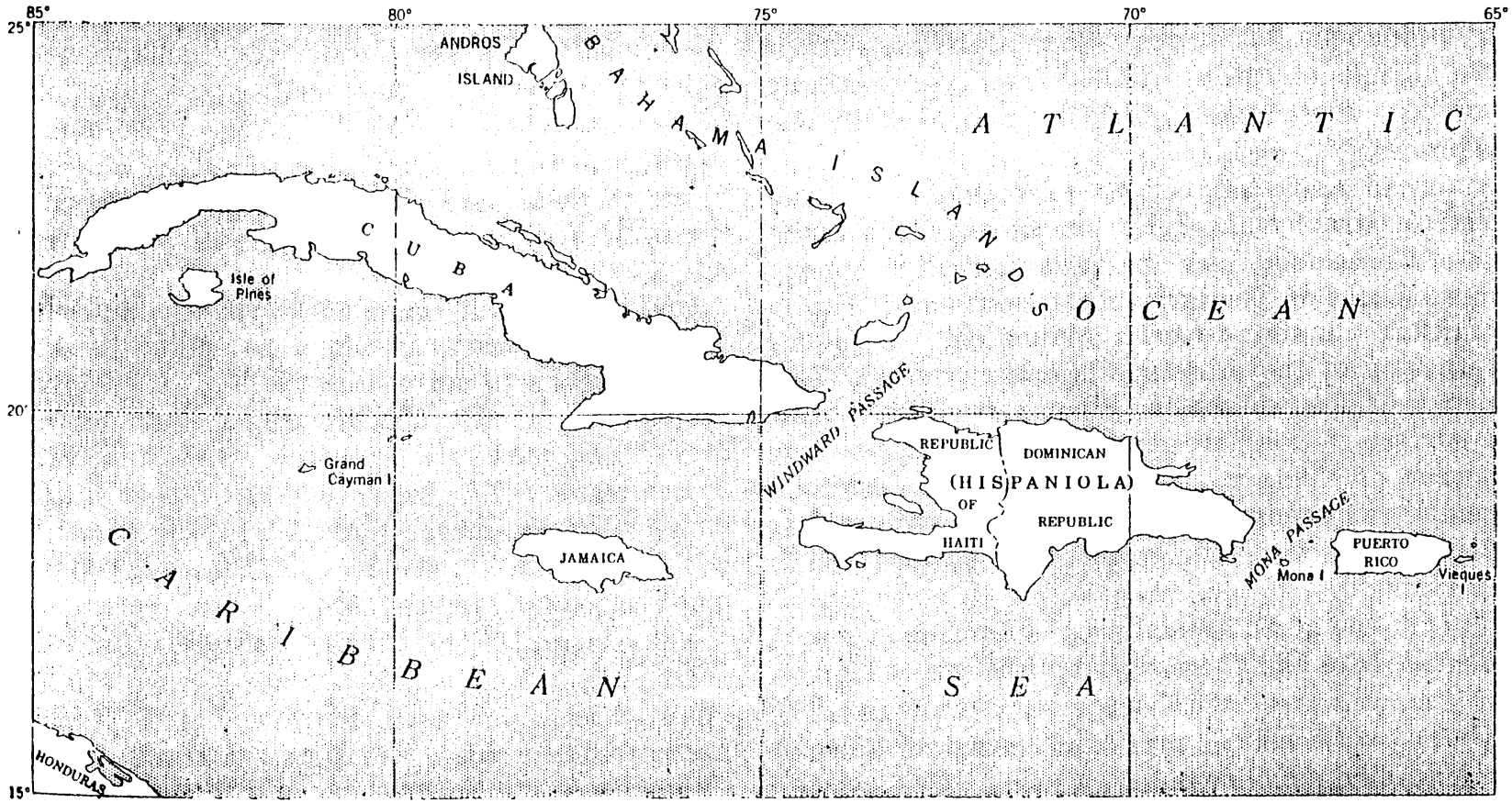

Figure 2.1 Map of the Greater Antilles

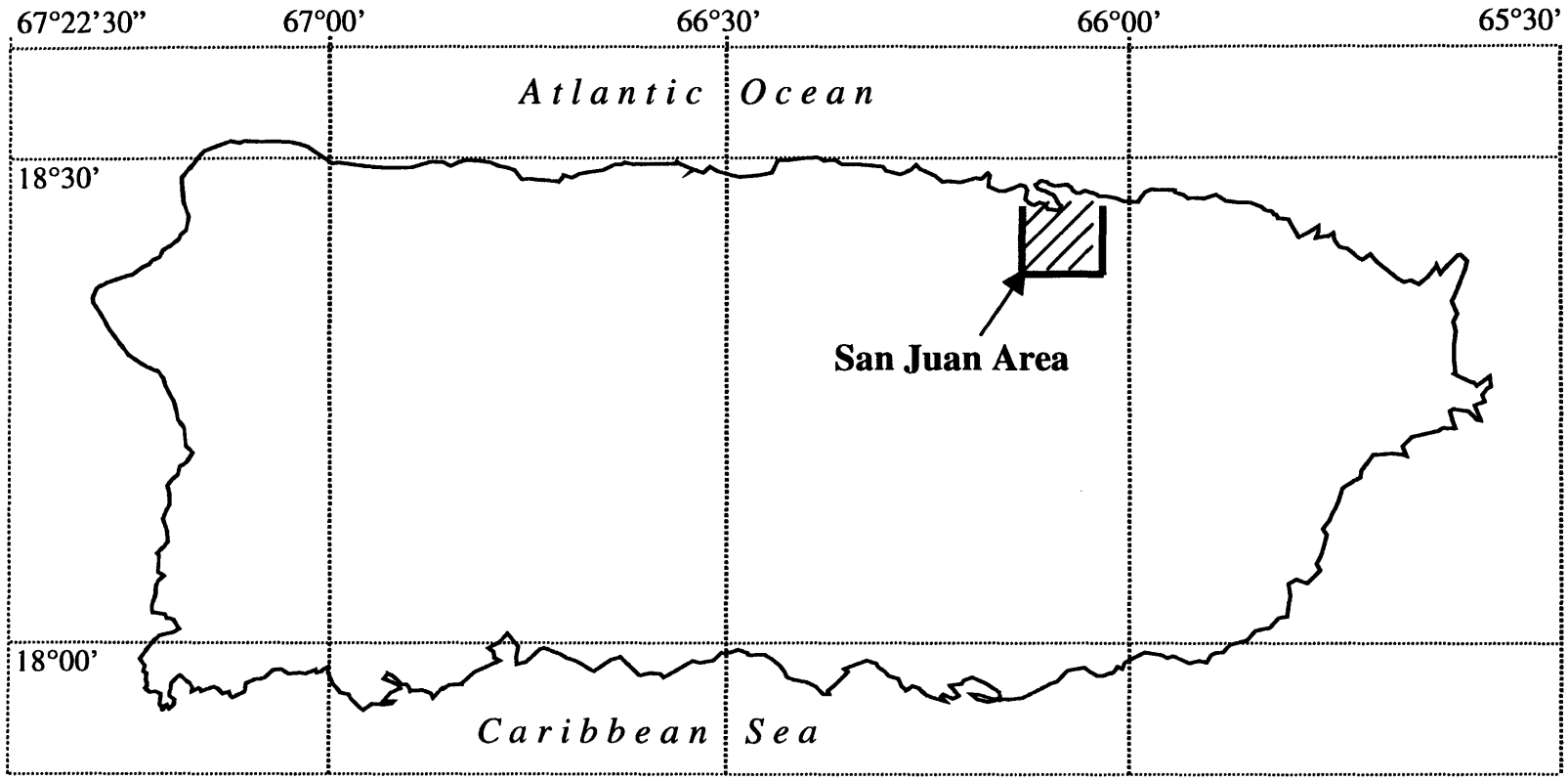

Figure 2.2 Map of Puerto Rico

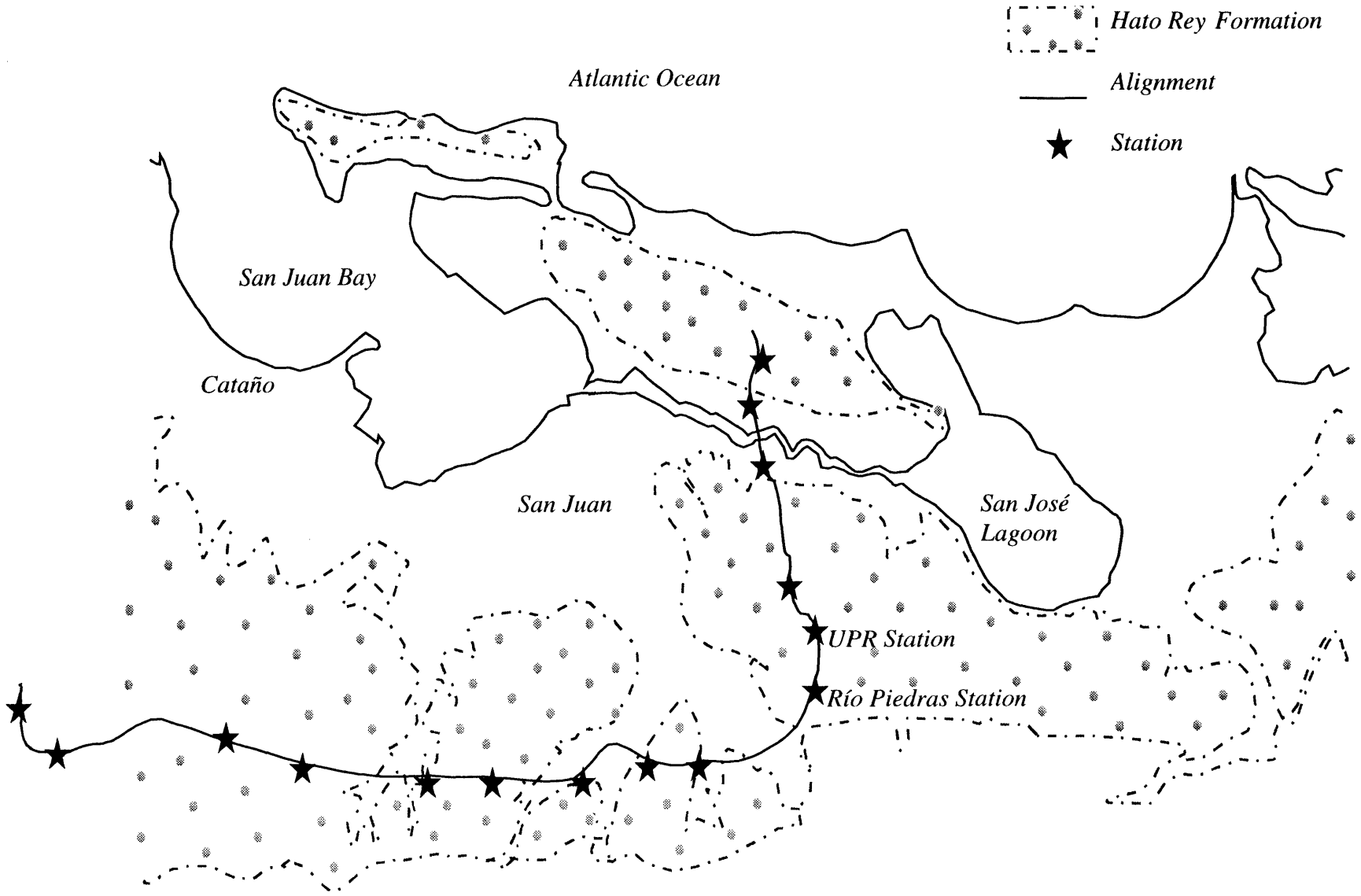

Figure 2.3 Hato Rey Formation

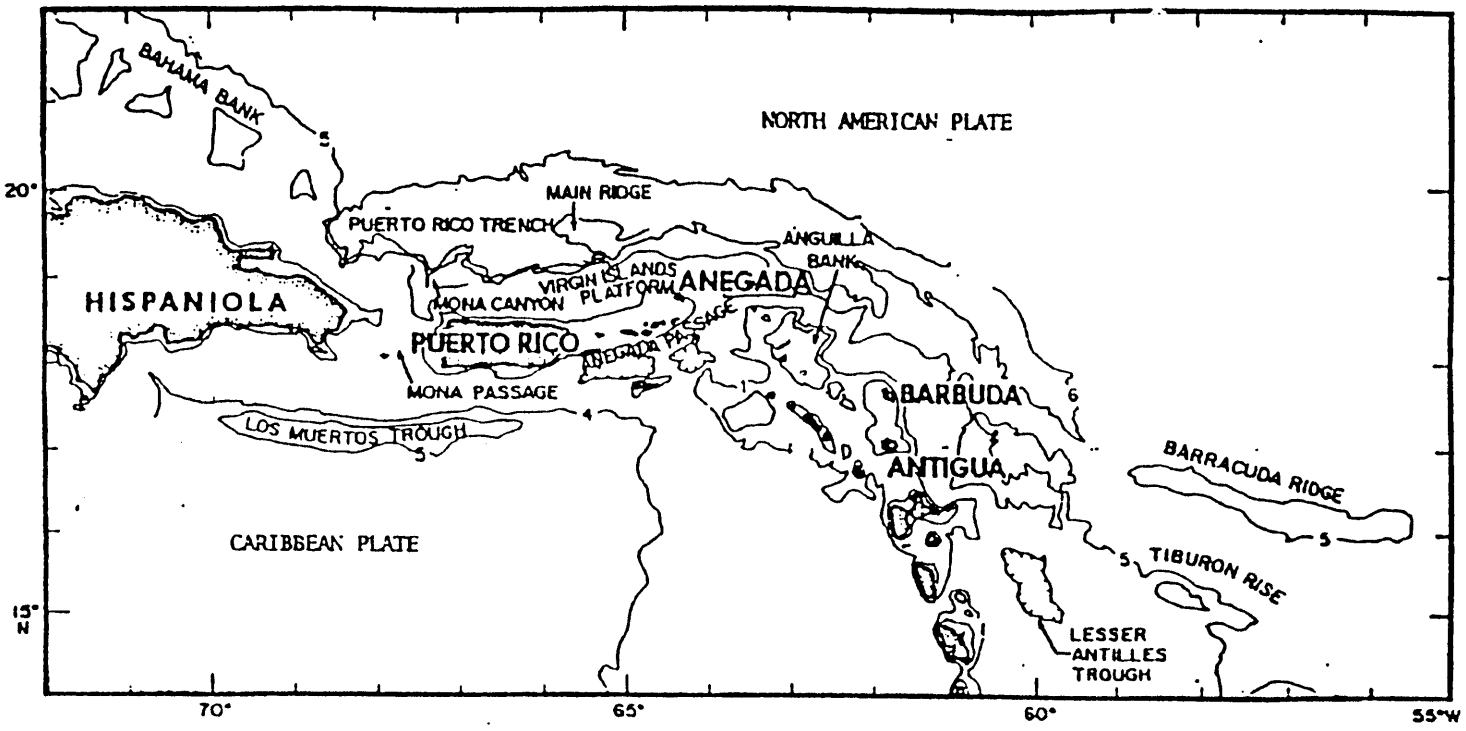

. Location of Puerto Rico with respect to major geographic and tectonic features. The Caribbean Plate extends to the east of the Lesser Antilles and to the north to Puerto Rico and Hispaniola. The oceanic deeps flanking the island such as the Puerto Rico Trench. Los Muertos Trough and Anegada Passage are all geologically active features and are the principal causes of the island's earthquake hazard (after McCann and Sykes, 1984).

Figure 2.4 Location of Puerto Rico with Respect to Major Geographic and Tectonic Features

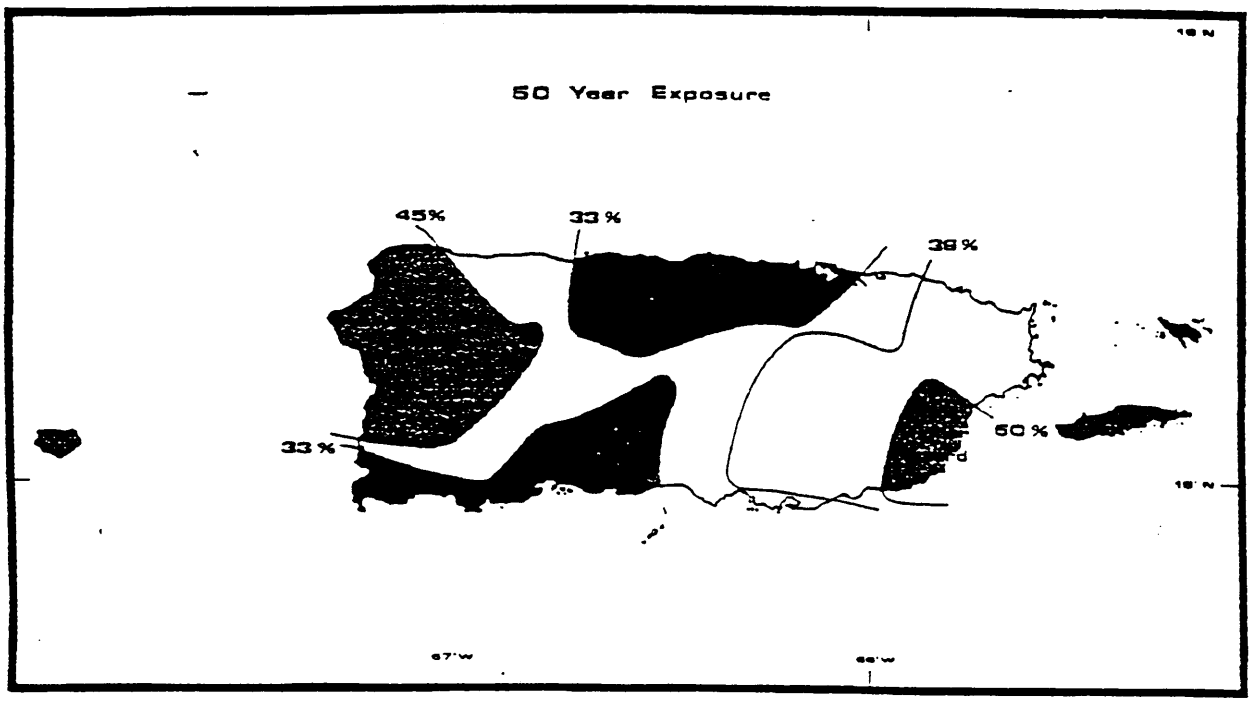

Calculated probabilities that any given area will experience ground accelerations exceeding 0.1g in a 50 year period.

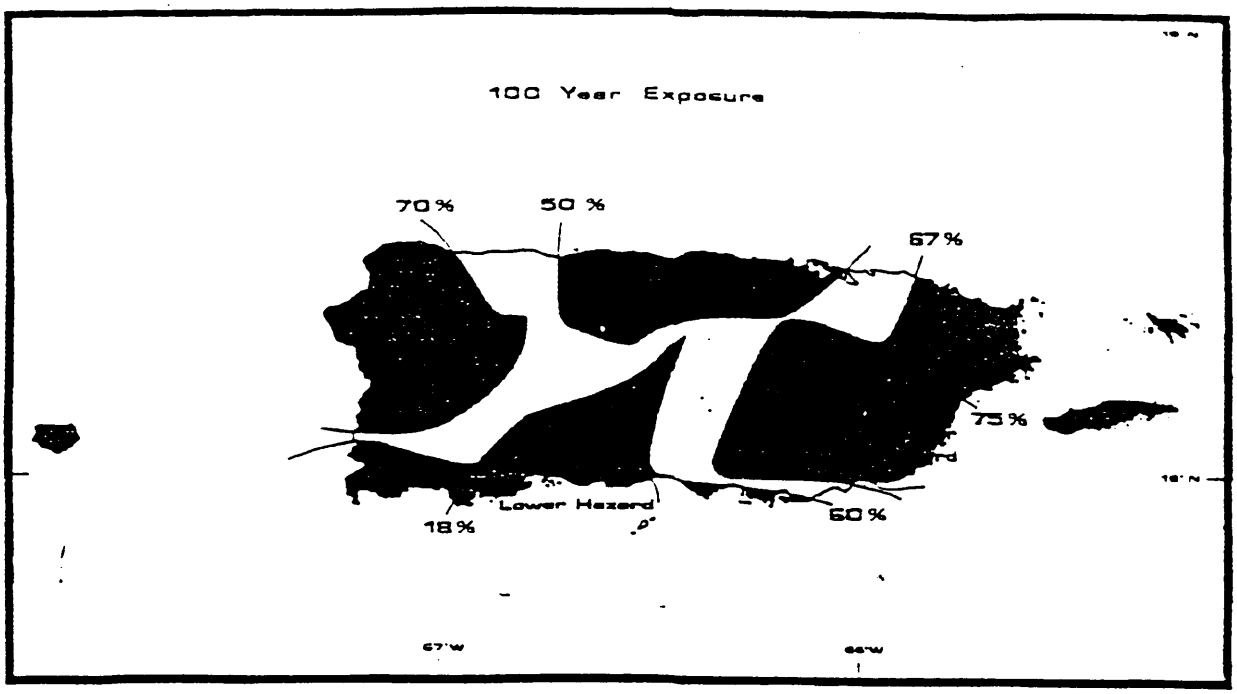

Calculated probabilities that any given area will experience ground accelerations exceeding 0.1g in a 100-year period.

Figure 2.5 Seismic Hazard Map of 1987 for Puerto Rico (Earth Scientific Consultants and W. McCann and Associates, Inc., 1994).

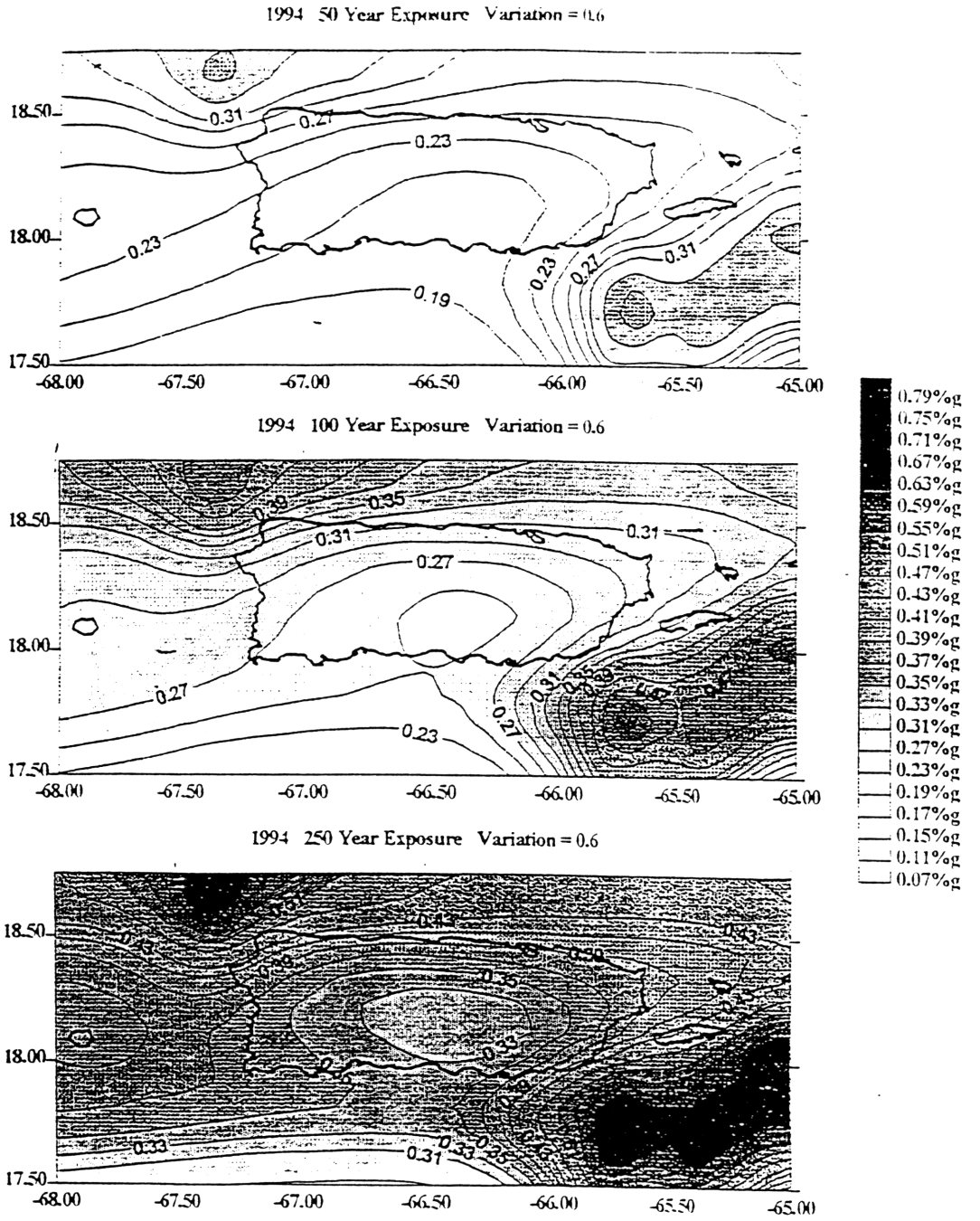

Map of acceleration not to be exceeded at a probability of 90 % as calculated by the program seisrisk III and the parameters described above. In this case the recommended ground variability of 0.6 is used. Note that most of the island has values in excess of .25, and that extreme values clearly exceed 0.30 on the island of Puerto Rico and 0.35 on Vieques

Figure 2.6 Maps of Acceleration for 50, 100 and 250 Year Exposure (Earth Scientific Consultants and W. McCann and Associates, Inc., 1994).

3. Site Investigation for Río Piedras Station

3.1 Introduction

The site characterization is based on geotechnical exploration programs already carried out for Section 7 alignment, that were intended for final design and construction of the section as a design-build contract (GDR 1996a, 1996b). Additional geotechnical evaluations and design, possibly including additional geotechnical field investigations and laboratory testing, will necessarily be required to complete the project (GDR, 1996a).

3.2 Scope of Site Investigation

Geotechnical investigations for the Río Piedras Section were started in March 1995 as part of the preliminary geotechnical field investigation for the Tren Urbano. No previous geotechnical engineering studies were conducted specifically for the Río Piedras Section of the Tren Urbano prior to those conducted through Tren Urbano/GMAEC. However, there have been previous studies conducted for other reasons near the Río Piedras alignment (Deere, 1959; Kaye, 1959; and Monroe and Pease, 1977). Geotechnical field investigations were completed in two phases (I and II) ending during February 1996 (GDR, 1996a). Also, a final phase (III) of supplemental geotechnical investigations for Río Piedras were conducted during August, September and the first week of October 1996 to obtain additional information for prospective bidders (GDR, 1996b).

The purpose of the Phase I investigation was to study the general subsoil conditions in the Río Piedras area in order to recommend possible underground construction techniques for the Río Piedras. The Phase II investigations included field and laboratory tests, such as, pocket

penetrometer tests on all samples, limit and grading tests for detailed soil classification, unconsolidated-undrained (UU) triaxial compression tests, and slug tests to estimate the hydraulic conductivity (test performed in standpipe piezometers installed in nine borings). The Phase III investigations include further laboratory testing (UUC, CIUC triaxial shear and consolidation tests), Ménard type pressuremeter tests, piezometer installations and two additional pumping tests.

The Phase I investigation program included 6 borings along the present Río Piedras alignment drilled to depths varying from 15 to 40m (Table 3.1), between Sta. 217+00 and Sta. 225+00 (see Figures 3.1a-b). Six additional borings were drilled east of the Río Piedras alignment at and near Highway PR-3 in order to investigate the possibility of a future extension of the alignment to the town of Carolina (Phase I borings are identified by the number of the station closest to each boring).

Phase II consisted of drilling ten borings along the revised proposed tunnel section between Sta. 217+00 and Sta. 230+00. These borings were drilled to depths well below the proposed top of rail along this section of the alignment, typically in the order of 30m. These borings are identified as P-borings (P-1 to P-11). Continuous sampling was done in the P-borings from above the proposed tunnel crown to below the rail elevation.

The Phase III investigation program included six additional geotechnical test borings to augment the previous studies. The borings (designated B101- B107) were drilled at midpoints between previous borings (Phase I and II) at areas of interest based on subsurface conditions encountered in the previous borings, and at the locations of important underground construction elements such as tunnel station and shafts. The borings were drilled to depths of 20.3 to 30.6m below existing grade and included continuous sampling from approximately 3m above crown

elevations to 2m or greater below invert grades. Table 3.1 gives a brief description of borings done for all investigations.

The test borings were made using conventional truck-mounted CME geotechnical drill rigs 83mm hollow stem continuous flight auger casing. In this method the borings are advanced by turning the auger into the ground a desired amount distance. Sampling below the bottom of the auger is attained by inserting the sampling apparatus within the auger, eliminating the need for casings. Two types of samples were taken: 1) standard (Terzaghi) 35mm I. D. split spoon (disturbed) samples, and 2) 75mm inside diameter, thin-walled, stainless-steel, Shelby tube samples ("undisturbed"). The undisturbed samples were obtained by forcing the Shelby tube samples into the ground using a static force or downward pressure and was pulled out also using a static pull. The Shelby tube samples were sealed in the field with wax, end caps and tape and shipped to soil laboratories for testing.

3.3 Stratigraphy

3.3.1 Section 7

Figures 3.2 and 3.3 show the stratigraphy for the entire Section 7 Alignment. This figure confirms the erratic nature of the deposits, which comprise a series of erratic layers of clays, silts sands and sandy clays. The composition of the predominant elements of the alluvial deposits can be described as follows: 32% clayey sand, 24% clay, 13% sandy clay and 11% sand. The clayey layers, which are heavily overconsolidated, contain considerable amount of silts and sands. In general, there is great scatter in the data due to the wide range in textural composition of the Hato Rey deposits. Since a lot of spatial variability exists it is not possible to identify

characteristic continuous horizontal layers. In the following sections the groundwater conditions and index and engineering properties are discussed.

3.3.2 Río Piedras Station

Figure 3.4 illustrates the stratigraphy near the Río Piedras Station. About 26% of the stratigraphy are comprised of clays, 13% sandy clays, 2% silty clays and 2% gravelly clays (total: 43% of clayey material). Approximately 3% are sands and 44% clayey sands, totaling about 47% sands. Also, included are 5% silts, 2% fill and 1% organic.

The subsequent numerical calculations approximate the complex stratigraphy by a single (homogenized) layer using average properties of a sandy clay (or clayey sand).

3.3.3 Index Properties

In order to classify samples according to the USCS and refine visual-manual soil classifications on the boring logs, selected samples were used for Atterberg Limits (ASTM D4318), natural moisture content (ASTM D2226), gradation or sieve (ASTM D422 and D1140), and hydrometer (ASTM D422) analyses. The Atterberg Limits are very useful for soil identification and classification (Lambe and Whitman, 1969). They describe the consistency of fine-grained soils with varying degrees of water content. The limits can be used for quick estimates of engineering properties through empirical correlations.

There is some scatter in natural water content but it decreases with depth (see figure 3.5), with w= 29± 7%. More scatter is shown the measured liquid limits (Figure 3.6), which range from w_L=53 ±17%. In general w_L decreases with depth. The plastic limits of the alluvial

deposits (Figure 3.7) exhibit similar degree of scatter as the natural water content, with w_p=24 ±7%. In all Atterberg limits plots there is wide scattering of values that might be due to the broad range in textural composition of the deposits. There is wide scatter in the plasticity index (Figure 3.8), with I_p=29± 15%.

Figures 3.9 and 3.10 show the Casagrande classification chart for Phases I, II and III. The majority of the data plot close to or above the A-line with most of the samples plotting as clays of low plasticity (about 50%) and clays of high plasticity (about 50%).

Figure 3.11 illustrates how the Liquidity Index varies with depth. A great amount of scatter is evident, with a Liquidity Index equal to 0.17± 0.26.

Figure 3.12 shows dry and saturated unit weight values from several tests (GDR 1996b). Average saturated and dry unit weight of 17.85±0.94 kN/m^3 and 13.35±1.1 kN/m^3, respectively, were selected.

3.4 Groundwater Conditions

During the field investigations, piezometers were installed in two of the Phase I borings and in nine of the Phase II borings along the alignment. The ground water levels in general were monitored during the period from March 1995 to March 1996. During Phase III investigation piezometers were installed in all six borings. The piezometers were screened at various depths to monitor piezometric ground water levels in sandy strata encountered at various depths in the borings. The installations used open standpipe piezometers (50mm diameter) with slotted screens and filter packs, were set up as monitoring points along the length of the alignment.

Additional piezometers were installed as part of the groundwater pumping tests carried out during the three phases of geotechnical investigation. Locations of the piezometer installations are listed on Tables 3.2 and 3.3.

A pumping test was performed during October 18 through 21, 1995 next to boring 226.3, near Sta. 225+00. It was performed to obtain preliminary indication of the difficulty of creating a drawdown given the erratic characteristic of the soil deposits that will be encountered in tunneling. The results from that pump test were included in GDR (1996a). The test consisted of drilling a pumping well to a depth of 30.4 meters. The well casing was perforated and wrapped with filter fabric from 5m below the ground surface to a depth 1m above the base of the borehole. The annular space was packed with sand instead of gravel. Three piezometer clusters were installed at 2.3m (226.3-P1), 4.6m (226.3-P3) and 9.2m (226.3-P2) radial distance from the well (Figure 3.13). These piezometers were installed at depths of 15.8, 21.0 and 26.8 meters at the 226.3-P1 monitoring well; 21.3 and 25.9 meters depths at the 226.3-P3 monitoring well and at 15.8, 19.8 and 26.8 meter depths at the 226.3-P2 monitoring well. A submersible pump with intake at 28 meters deep was used. A maximum drawdown was created in the well to a depth of 26.8 meters and pumping was continued for 80 hours.

The results of the tests (see Figure 3.14) are only applicable in the immediate vicinity of the test. Test well pumping produced only a small drawdown in the adjacent, approximately 0.67m and the following conclusions were reported in GDR (1996a):

1. The computed permeability of $3x10^{-3}$ cm/sec is equal to the highest values obtained in the small-scale falling head tests in the piezometers of the exploration program. Under the

condition of a very small drawdown, the permeability computation is highly unreliable[1] and a value exceeding 10^{-3} cm/sec probably represents only a minor portion of the overburden soils.

2. The very small drawdown and the substantial flow to the test well suggest that there may have been local recharge directly into the well, presumably rainfall on the surface and from leaking shallow utilities seeping toward the water table that affected the test.

Two supplemental pumping tests were performed as part of the Phase III geotechnical investigation during 3 September through 4 October 1996. The two new pumping test locations were selected to investigate aquifer conditions in the vicinity of relatively sandy soils encountered near the intersection of Ponce de León and Gándara Avenue (supplemental Pump Test No. 1), and in the vicinity of the south shaft area for the proposed mined Rio Piedras Station (supplemental Pump Test No. 2). The tests were performed to evaluate the impact of groundwater on the construction, so that appropriate construction methods can be chosen, and groundwater control schemes designed and estimated.

Pump Test No. 1 was performed within the section of twin mined tunnels at about Station 223+24, just north of where the tunnel alignment passes under Dr. Jose Gándara Ave (Figure 3.15). Test Well PW-1 was installed at Station 223+23.95. Pump Test No. 2 was performed at the south end of the proposed Rio Piedras Station at about Station 219+61 (Figure 3.16). Test Well PW-2 was installed in Calle Arzuaga at Station 219+81.49.

Both tests were designed with 30m deep, fully screened, 150mm diameter pumping wells, installed to maximize potential yield from the formation strata. Both tests included

[1] It was also stated that the borings logs indicate the presence of SP lenses, and that in that case, an average of 10^{-3} cm/sec would not be unreasonable.

multiple piezometers screened at "shallow", "middle", and "deep" horizons in monitoring wells at 3 m and 9 m radii from the pumping wells in relatively sandy strata. The pumping wells were installed using a Mobile B90 drill rig equipped for mud rotary drilling. The holes were advanced using a 35.6 cm (14") diameter tricone drill bit attached to an approximately one foot diameter by ten foot long drill rod stabilizer. Development was accomplished by a combination of airlifting, swabbing, surging, and pumping.

The piezometers were installed using Acker AD2 and BK 50 drill rigs using 8.26cm (3-1/4") hollow stem auger casing. Shallow, intermediate and deep screened piezometers are referred to by the designations A, B, and C, respectively, at given radii from the test wells.

Both tests were intended to create maximum stress on the alluvial aquifer system by pumping at the highest possible rates, thereby creating maximum possible drawdown. Pump Test No. 1 took place during 27-30 September 1996 and was initially pumped at a rate of approximately 100 gpm. During the first hour of the test the rate had to be throttled back to a constant 70 gpm (to maintain pump operations), for a total test duration of 72 hours. The sustained drawdown in the pumping well at 70 gpm was equivalent to a drawdown of approximately 24m in the pumping well (i.e. approximately 5m above the pump intake). Test No. 2 took place during 1-3 October 1996 and was initiated at the same maximum pumping rate of about 100 gpm. But the pumping rate was quickly throttled back after casing storage was depleted. Maximum drawdown was maintained to the pump intake at approximately 29m depth without pump operation problems during this test. After several hours the test maintained a more or less constant rate of approximately 20 to 25 gpm in contrast to the higher rate of the first test.

The results of these two pumping tests, shown on Figures 3.17 and 3.18, were included in GDR (1996b). The conclusions reached in the report were the following:

1. That a properly constructed and developed well in the area of the test at Gándara Ave.(pump test No.1) will give good yield, and produce significant drawdown.
2. That a properly constructed and developed well in the area of the test at the Rio Piedras Station (pump test No.2) will provide low to moderate yield, and produce drawdown. Tighter well spacing and more extended pumping time will probably be necessary for groundwater control than in the area of the pump test at Gándara Ave.
3. The two supplemental pump tests show well yields moderately greater than would be anticipated from the soil descriptions and laboratory tests. The drawdowns observed during the tests indicate greater communication horizontally than would be expected from the soil data. In both tests, the screened horizons exhibited different responses to pumping. The maximum drawdowns measured at r= 3m Test No.1 at (78.5 hrs.) were 2.1m, 7.8m and 11.7m, for the shallow, intermediate and deep piezometers, respectively. Equivalent drawdowns due to Test No.2 (at r= 3m, 53 hrs.) were about 0.5m, 2.9m and 1.0m, respectively.
4. From a dewatering viewpoint, the soils above and below the tunnel and station construction present a complex series of heterogeneous, anisotropic strata of erratic continuity.
5. Because of the anisotropic nature of the soils, distinct vertical gradients have been observed. Typically, the higher the piezometer screen, the higher the water level observed. It appears that the source of recharge is shallow, from infiltration, leaking utilities and possibly from flow off the hills in surficial aquifers. This vertical component to the groundwater flow may result in perched water conditions that could impact construction operations.

The report states that it is not feasible to fully design an effective dewatering system in advance because of the variability of the soil and groundwater conditions along the alignment of

Section 7 of the Rio Piedras Contract of Tren Urbano, and in view of vertical flow and other departures from conventional dewatering assumptions. The observational approach is strongly recommended along with installation of additional wells for further testing.

3.4.1 Water Table and Equilibrium Pore Water pressures

Figure 3.19a shows the ground surface and groundwater elevations for all three of site investigations (data from the pumping tests are also included). It can be seen that for most cases there is variability within five meters. Within the Río Piedras Station area (see Figure 3.19b), which has an average ground elevation of El.+26m[2], the water table elevation changes from 13.41m to 18.59m, with an average elevation equal to El.+16m.

Figure 3.20 shows the initial stress profile using the dry unit weight above the water table and the saturated unit weight below the water table. In-situ effective vertical stresses (σ'_{vo}) were calculated using the following equation: $\sigma'_{vo} = \sigma_{vo} - u_o$, were σ_{vo} is the vertical total stress, and u_o is the pore water pressure. (Note: at the Río Piedras Station, the ground elevation is approximately 26m and the groundwater averaged an elevation of 16m).

3.4.2 Hydraulic Conductivity

3.4.2.1 Field Test Data

During Phase II, permeability tests were performed in each of the nine P-series borings where piezometers were installed on clayey and sandy soils. Both rising head and falling head slug tests were performed. The tests were carried out using the following procedures: i) the rising

head test consisted of bailing out water within the piezometer down to an elevation close to or slightly below the screened section (to the base of the piezometer, if possible), and then measuring the time taken for the water pressures to rise to the static level. ii) The falling head test consisted of adding water to the piezometer up to the ground elevation or top of the piezometer and measuring the time taken for this level to return to the static water elevation. The results from these tests (Figure 3.21) shows an average hydraulic conductivity, k=3 $x10^{-4}$ cm/sec, with maximum and minimum values equal to 1.3 $x10^{-3}$ cm/sec and 2.7 $x10^{-6}$ cm/sec, respectively. In general higher values of k are measured in falling head tests. Most of the high k results correspond to silty and clayey sand. The permeability computed in the first pumping test (Phase I and II), k=$3x10^{-3}$ cm/sec, is very similar to the maximum value for slug tests. Additional slug tests were performed during the Phase III investigations as part of a future addendum, but were not available at the time of this study.

3.5 Strength and Deformation Properties

3.5.1 Test Procedures

3.5.1.1 Field Tests

Field tests performed on Section 7 include Menard Pressuremeter (PMT) and Standard Penetration Test (SPT). Standard Penetration Tests (SPT) were performed in conjunction with split spoon samples in accordance with ASTM D1586. Each test consists of recording the number of blows required to drive the sampling spoon a distance of 30 cm into the ground using a 64kg hammer falling 75cm. The Standard penetration N-value were recorded as the number of

[2] Mean Sea Level elevations

blows required to advance the sampler 30cm beginning 15cm below the top of the sample interval.

In order to obtain in-situ stress-strain characteristics of soil with depth, three pressuremeters were successfully completed during the Phase III investigations. Strength measurements were obtained in terms of pressuremeter modulus (E) and the pressure limit values. The designations for these borings are PM-1, PM-3 and PM-P6. PM-1 was drilled adjacent to boring B106 near the middle of the proposed UPR Station (see Figure 1.3). PM-3 was drilled adjacent to GDR Phase Two boring P-2 at the south shaft area for the Río Piedras Station. PM-P6 was drilled next to GDR Phase Two boring P-6 near the twin mined tunnels at the intersection of Ponce de León and Gándara Avenue.

The pressuremeter borings were advanced using similar hollow stem auger drilling equipment as described above for the sample borings. After drilling to the target test interval, a clean, smooth-walled borehole test interval was established by pushing a Shelby tube. If the soil stratum was too stiff to advance the Shelby tube then the test interval was accomplished by slow rotary drilling fluid ahead of the auger casing. After creating a smooth borehole wall below the casing, the pressuremeter was lowered into position and the expansion test conducted. Pressuremeter tests were performed at 3m intervals in each of the three pressuremeter borings (GDR, 1996b). The pressuremeter used was a Menard G-AM Pressuremeter. In this type of test, the loading component is a dilatable cylindrical probe set in place within the soil at the desired level of testing in a previously drilled borehole. Once installed, the probe is submitted to an increasing pressure applied in equal increments. At each pressure stage the volume changes of the probe are recorded at specific time intervals. The pressure-volume relationship is then drawn up for subsequent determination of material properties.

3.5.1.2 Laboratory Tests

A combination of split spoon and Shelby tube samples were used for laboratory testing in order to determine strength characteristics of soil strata encountered in the borings. In general, the same types strength tests were performed in the three Phases of investigations. However, based on requests from prospective bidders, additional testing were performed in Phase III with emphasis on CIUC and UUC triaxial testing. The tests were performed in accordance with referenced ASTM specifications.

During Phases I and II, the laboratory strength tests performed consisted of Pocket Penetrometer (PP), Unconfined Compression (UC) tests, and Unconsolidated-Undrained (UU) triaxial tests. The laboratory strength tests performed in Phase III include unconfined compressive strength (UC) tests (ASTM D2166), unconsolidated-undrained (UU) triaxial tests (ASTM D2850), consolidated undrained (CU) triaxial tests (ASTM D4767), and laboratory vane shear tests (ASTM D4648). Shelby tube samples were tested both in Puerto Rico by Jaca & Sierra (UU, consolidation and laboratory vane shear) and in Miami by Ardaman & Associates (CIU).

Penetrometer tests were performed on cohesive split spoon samples that exhibit certain amount of cohesion. The unconfined compression test (ASTM D 2166-72) was performed on the best quality sample recovered in the split spoon sample[3]. The unconfined strength values measured from the split-spoon samples are used to compare relative strengths and as an additional index property for classification and identification purposes. More accurate values of strength are obtained from thin-walled Shelby tubes. Shelby tube samples were sent to Ardaman

& Associates, Inc., in Florida for triaxial testing. The UU tests were performed in order to obtain information helpful for the design and construction of the tunnels.

The CIU triaxial tests were only performed on several samples from the first two borings drilled, B106 at UPR Station and B102 near the middle of Rio Piedras Station, because of the long turnaround time for this type of test (GDR, 1996b). The tests were performed in order to provide supplemental triaxial compression information for the design and construction of the stations and tunnels in accordance with requests from prospective bidders. The CIU and UU tests were run on tube samples taken from depths of interest related to the vertical tunnel alignment (i.e., near the crown, springline or invert elevations).

3.5.2 Undrained Strength, S_u

Results from measured Standard Penetration Tests are included in Figure 3.22a, and show the following main features:

1 Above El.+10m, N remains relatively constant, varying between N=10 to 30.

2 Much more scatter exits below El.10m. SPT N increases with depth, with high values, $N \geq 190$, and low values $N \cong 10$.

Undrained shear strength, s_u, can be estimated from SPT N values using two empirical correlations, i) $s_u = 0.13N$ (ksf) (Terzaghi and Peck, 1948); and ii) $s_u = 4.4N$ (KPa) (Simpson, B. et al., 1979). Based on these correlations, $s_u \approx$ 100kPa above El.+10m, Figure 3.22b, $s_u \approx$ 200kPa at El.+10m increasing to $s_u \approx$ 600kPa at El.-8m[4].

---

[3] At best these samples are highly disturbed due to the hammering process by which they were obtained.

[4] Pocket Penetrometer results show great scatter (see Figure 3.23), with s_u = 25 to 240 kPa (q_u=50 to 480 kPa; and can be classified as medium to hard clays)

Figure 3.24 shows the undrained strength, s_u, from the pressuremeter tests estimated from the following empirical correlations:

1 Baguelín et al 1978:

$$s_u(TSF) = \frac{P_l - P_o}{12}$$

2 Amar and Jezequel, 1972:

$$s_u(KPa) = \left(\frac{P_l - P_o}{10}\right) + 25$$

3 Centre d'Etudes Menard, 1967:

$$s_u(TSF) = \frac{P_l - P_o}{5.5}$$

The first two of these correlations tend to give approximately constant s_u with depth, with an average s_u= 140 KPa.

Figure 3.25 summarizes the undrained strength results from all the laboratory tests and correlations for field tests. Although the results show a large scatter, $s_u \leq 200$ kPa above El.+10m. Below this elevation, the principal source of scatter are SPT-N data points, and these may reflect stratigraphic variations not seen in laboratory tests on small samples of soil.

The selection of the undrained strength is highly influenced by the quality of the samples and test procedures. The conventional practice of conducting shear tests tends to be highly empirical and often unreliable because it neglects to account for the following three principal factors that affect the measured s_u: i) anisotropy, ii) strain rate (or time to failure), and iii) sample disturbance. Pocket penetrometer tests (PP) and Unconfined compression (UC) tests were performed on highly disturbed samples (split-spoon samples). The pocket penetrometer tests give a rough approximation of the strength of a cohesive soil and should be used as an additional

index property for classification and identification purposes. Standard Penetration tests give very poor measure of s_u in low overconsolidated soils and can only be used in stiff, overconsolidated soils. The Ménard pressuremeter test results are similarly affected by the influence of stress release that is associated by the pre-bored hole of the test.

More accurate values of strength are obtained UUC and CIUC triaxial tests performed on thin-walled Shelby tubes. The use of UUC testing to estimate s_u depends on the following compensating errors: i) increased s_u due to neglecting anisotropy and rate of failure; and ii) decreased s_u due to sample disturbance. Better estimates of undrained strength may be attained using CIUC test results. In order to select s_u, the values of the laboratory vane were not included because they were too low compared to the rest of the undrained tests. Also excluded are the results from the SPT N correlations because below El. +10m the data show large scatter and a trend different from that of the undrained tests. Selection of undrained strength, shown on Figure 3.26, involves UUC and CIUC tests, since these tests were performed on the best samples available. There is some degree of scatter, with an average s_u= 150 kPa (147±48 kPa)

3.5.3 Drained Strength Parameters

Based on the estimates of undrained shear strength, s_u, it is possible to the preconsolidation pressures, σ'_p, by invoking the SHANSEP[5] equation for normalized soil shear strengths:

$$\frac{s_u}{\sigma'_{vo}} = S\left(\frac{\sigma'_p}{\sigma'_{vo}}\right)^m$$

where s_u is the undrained strength and σ'_{vo} is the in situ vertical effective stress. Typical values for S and m ranges from 0.22±0.03 and 0.8±0.1, respectively. Values of S=0.25 and

[5] Stress History And Normalized Soil Engineering Properties, (Ladd and Foott, 1974).

m=0.8 were chosen. Results (Figure 3.27) show maximum σ'_p= 1000 kPa and minimum σ'_p= 300 kPa (average 600 kPa). Backcalculated overconsolidation ratio (OCR), shown on Figure 3.28, vary mostly from OCR= 8 to 1.5 (few samples at El.+25m plot with OCR>>8).

The undrained cohesion, c', can be estimated using an empirical correlation developed by Mesri&Adel-Ghaffar (1993), shown on Figure 3.29. By previously selecting an average σ'_p= 600kPa, two values of cohesion, c', are determined from Figure 3.29: 1) an upper bound value of c' equal to 60 kPa ($2 \leq OCR \leq 5$); and 2) a lower bound value of 16 kPa ($10 \leq OCR \leq 20$). The average from the two estimates c'= 40 kPa was selected and used in the analyses described in chapter 4.

Effective stress measurements in CIUC triaxial tests provide the only source of information on drained strength parameters for Hato Rey soils. Figure3.30a, report drained friction angles ϕ'= 30.3°, 32.9° and 35.8°. The cohesion intercept (c') is very difficult to estimate from these limited CIU data.

Once the drained cohesion intercept (c'), was selected, an estimate of the drained friction angle, ϕ' cann be made from CIU effective stress data. Figure 3.30b shows results at maximum σ'_1-σ'_3 using an intercept of c'=40 Kpa[6]. The interpreted drained friction angle varies from ϕ'=24.6° to 24.9°.

3.5.4 Compressibility and Shear Stiffness

Figure 3.31 shows compression data from conventional incremental load oedometer tests on Shelby tube samples from Phase III site investigations. The data are plotted in conventional e-$\log_{10}\sigma'_{vo}$ space. Results show how compressibility of samples varies as a function of the

vertical confining effective stress. The data show a characteristic non-linear response, but no well-defined yield point corresponding to a pre-consolidation pressure (i.e., σ'_p larger than maximum σ'_{vo}).

Figure 3.32 shows the compressibility, m_v, of the soil specimens at the in-situ vertical effective stress σ'_{vo}, as functions of the initial void ratio and water content (Appendix C shows the calculations of m_v from the measured data). In general m_v increases as w (or e_o) increase with typical values ranging from $m_v \approx 0.0002 m^2/kN$ at e0 ≈ 0.6 to $m_v \approx 0.005 m^2/kN$ at $e_o = 1.0$. These values correspond to the range expected for very stiff overconsolidated clays (see table 3.7)

Young's Modulus, E, can be calculated from results of: i) pressuremeter expansion tests, ii) CIUC tests (conventionally reported at 50% strength), and/or iii) oedometer tests.

$$m_v = \frac{d\varepsilon_v}{d\sigma'_v} \text{ and } E' = \frac{(1+\upsilon')(1-2\upsilon')}{(1-\upsilon')} \frac{d\sigma'_v}{d\varepsilon_v}$$

In this third case, the drained Poisson's ratio must be assumed, while cases 1 and 2 are assumed undrained ($\nu_u = 0.5$). Results from all of these tests are shown in Figure 3.33. Note that the minor principal stress σ'_3 in figure is equal to the cell pressure at the end of consolidation, σ'_{cell} in the CIUC tests. For the Ménard pressuremeter and oedometer tests $\sigma_3' = \sigma'_{vo}$. The highest values correspond to the pressuremeter tests followed by the CIUC tests. The oedometer data give very low moduli compared to the CIU and Ménard pressuremeter tests.

[6] a' = c'cosϕ'=33.5KPa; tanα' = sinϕ'

3.5.5 Consolidation Properties

The vertical coefficient of consolidation can be calculated from laboratory oedometer tests using two methods: log-time and square-root time method. Appendix B shows log-time (B1-B7) and square-root time/ settlement (B8-B14) curves for all tests. It was difficult to determine c_v since in most cases (even for clays) the curves were of the form corresponding to clayey silts or silts (Head, 1980).

For clayey silts, the initial convex-upwards portion of the primary curve was passed before any readings could be taken. This indicates that settlements would occur quite rapidly and would not be expected to cause long-term problems. For silts, a typical log-time/ settlement curve is concave-upwards from the start (t_{50} <0.1 min). This indicates very rapid consolidation. The d_{100} (100% primary) point cannot be determined by the conventional method, and the square-root-time curve is of little use for determining the d_o (0% primary) point because there is no linear portion evident. For more details on how to estimate c_v for these types of soil refer to Head (1980).

There is large scatter in results (Figure 3.34[7]), and significant differences between values from the two methods. Much lower results are obtained from the square-log-time method, with c_v varying from 0.35 to 6.3 m²/y. Approximately 90% of data can be classified as clays of medium plasticity (Table 3.7). However, more scatter and much higher results are determined from the log-time method with c_v varying from 0.28 to 130 m²/y. Approximately 55% of data can be classified as clays of low plasticity, 27% as medium plasticity clays, 9% as high plasticity clays, and 9% as silts (Table 3.7).

[7] c_v values are reported for the last two load increments in each test.

Table 3.1 Description of Borings

Boring	Station	Ground Elevation m, MSL	Offset from Center Line	Maximum Depth, m
219	217+35	22.93	2R	15.4
P-1	218+34	25.16	6L	24.85
220.6	218+97	28.43	12R	38.41
B101	**219+00**	**27.55**	**6.35L**	**30.5**
P-2	219+61	27.02	11.5L	33.49
B102	**220+22**	**25.47**	**12.03L**	**27.3**
P-3	220+51	25.2	15.5L	26.11
P-4	221+45	24.19	5L	35.01
P-5	222+02	23.14	4L	27.57
224.9	222+84	22.32	6R	30.64
B104	**223+28**	**21.84**	**5.95L**	**23.5**
P-6	223+42	21.05	24L	24.54
225.8	224+06	20.34	2R	35.98
226.3	224+93	21.11	19.5L	30.43
B105	**225+08**	**21.49**	**0.2R**	**20.3**
P-8	226+23	25.23	3L	27.59
B106	**226+56**	**26.12**	**11.94L**	**30.6**
P-9	227+36	27.5	17.5L	24.49
B107	**227+77**	**29.73**	**1.01L**	**22.9**
P-10	228+30	28.34	16.5L	24.54
P-11	229+17	27.48	13L	26.07

On bold: Phase III Investigation
Not on bold: Phases I and II

Table 3.2 Piezometer Locations: Phases I, II and III Investigations

Boring	Station m	Ground elevation m, MSL	Location Elevation m	USCS Classification	Time Period[1] Months	GWT, Elevation Average, m
219	217+35	22.93	7.73	SC	9	13.16
P-1	218+34	25.16	6.87	CL	1	17.09
B101	219+00	27.55	-1.406	SP to SP-SC	1	13.41
P-2	219+61	27.02	2.63	CH	1	14.66
B102	220+22	25.47	7.53252	SM-SC	1	14.33
P-4	221+45	24.19	4.37	SC	1	18.59
P-5	222+02	23.14	9.42	SC	1	17.23
224.9	222+84	22.32	5.02	SM	7	17.91
B104	223+28	21.84	2.3328	SC	(5 days)	18.34
P-6	223+42	21.05	8.25	SC	1	18.17
226.3	224+93	21.11	-4.79	SP-SM/SP-SC	9	15.64
226.3*	224+93	21.11	-0.19	SP-SM/SP-SC	9	14.83
226.3(p1)*	224+95	21.11	5.26		5	16.41
226.3(p1)*	224+95	21.11	0.08		5	16.04
226.3(p1)*	224+95	21.11	-5.72		5	13.86
226.3(p2)*	225+02	21.11	5.26		5	16.27
226.3(p2)*	225+02	21.11	1.29		5	15.024
226.3(p2)*	225+02	21.11	-5.72		5	14.19
B105	225+08	21.49	11.2792	SM	(5 days)	16.77
P-8	226+23	25.23	4.8	SC	1	15.47
B106	226+56	26.12	-2.836	ML	1	12.32
P-9	227+36	27.5	10.84	SM-SC	1	13.88
B107	227+77	29.73	18.6048	SC	1	23.08
P-10	228+30	28.34	12.18	SC	1	19.55
P-11	229+17	27.48	12.24	SC	1	18.79

*: Piezometers of Pumping Test for Phases I and II

[1] Time period of averaged groundwater elevations

Table 3.3 Piezometer Locations Phase III Pumping Tests

well/ piezometer	Station m	Elevation Screen Interval,m from	to	Elevation Average,m	Static Water Level,m	USCS
PW-1	223+24	16.91	-8.54	4.185	17.97	
PW1-3A	223+24	9.46	8.24	8.85	19.06	SM-SC
PW1-3B	223+24	3.14	1.61	2.375	18.73	SM
PW1-3C	223+24	-5.83	-8.57	-7.2	14.52	SP-SM
PW1-9A	223+29	9.34	8.12	8.73	18.89	NO-SAMPLE
PW1-9B	223+28	2.95	1.73	2.34	18.57	SC
PW1-9C	223+30	-5.89	-8.63	-7.26	14.45	SM
P-6	223+42	11.05	8.05		18.59	
PW-2	219+81	21.97	-3.48	9.245	13.45	
PW2-3A	219+62	13.13	11.91	12.52	17.27	SC-ML/SM-SC
PW2-3B	219+61				16.1	SC-CL
PW2-3C	219+61	-1.95	-3.17	-2.56	13.63	SM
PW2-9A	219+56	13.28	12.07	12.675	17.44	SM-SC
PW2-9B	219+57	10.1	6.88	8.49	14.46	SM
221.2						
B101	219+00	-2.93	-0.12	-1.525	13.61	SP/SP-SC

Table 3.4 Consolidation Tests

Reference Name	Boring	Station	Elevation of Sample (m) From	To	σ'_{vo}, (kPa)	UCSC
C1	B101	218+99.76	19.63	19.02	147	CL
C2	B102	220+21.65	19.22	18.61	117	SM
C3	B102	220+21.65	9.01	8.55	221	CL
C4	B104	223+28.12	17.27	16.66	87	SC-SM
C5	B104	223+28.12	13.92	13.31	117	SM
C6	B106	226+56.41	19.41	18.8	125	SC
C7	B107	227+77.31	17.54	17.49	165	CL

Table 3.5 Description of Triaxial Tests

Reference Name	Boring	Station	Elevation of Sample, m		UCSC	σ'_{vo} (kPa)	σ'_{cell} (kPa)
			From	To			
T1A	B102	220+21.65	17.39	16.78	SC	149.6	68.7
T1B	B102	220+21.65	16.17	15.75	CH	163.0	137.3
T1C	B102	220+21.65	17.39	16.78	SC	149.6	207.0
T2A	B102	220+21.65	10.23	9.62	CH	211.6	103.0
T2B	B102	220+21.65	10.23	9.62	CH	211.6	206.0
T3A	B106	226+56.41	22.16	21.55	SC-CH	76.1	34.3
T3B	B106	226+56.41	22.16	21.55	SC-CH	76.1	68.7
T3C	B106	226+56.41	22.16	21.55	SC-CH	76.1	138.3

Table 3.6 Permeability Results

Boring	Station m	Falling Head		Rising Head		USCS	Permeability, k,	
		From, (m)	To, (m)	From, (m)	To, (m)		Rising Head (cm/sec)	Falling Head (cm/sec)
P-1	218+34	15	18	15	18	CH	2.86×10^{-4}	2.56×10^{-4}
P-2	219+61	21	24	21	24	CL	2.64×10^{-4}	1.6×10^{-4}
P-4	221+45	17	20	17	20	SM	6.7×10^{-5}	3.7×10^{-4}
P-5	222+02	11	14	11	14	SC	3.9×10^{-5}	8.1×10^{-4}
P-6	223+42	10	13	10	14	SC	4.2×10^{-4}	1.3×10^{-3}
P-8	226+23	19	20	19	20	SC	5.6×10^{-4}	7.4×10^{-4}
P-9	227+36	15	17	15	16	SM	3.2×10^{-4}	5.4×10^{-4}
P-10	228+30	13	16	13	16	ML	2.7×10^{-6}	7.5×10^{-6}
P-11	229+17	12	15	12	15	CL	1.7×10^{-5}	2.1×10^{-4}

Pumping Test (Phase I and II) $k=3 \times 10^{-3}$ cm/sec

Table 14.5. SOME TYPICAL VALUES OF COEFFICIENT OF VOLUME COMPRESSIBILITY

Description of compressibility	*Coefficient of volume compressibility, m_v* (m^2/MN)	*Clay types*
Very high	Above 1.5	Very organic alluvial clays and peats
High	0.3–1.5	Normally consolidated alluvial clays (e.g. estuarine clays)
Medium	0.1–0.3	Fluvio-glacial clays Lake clays Upper 'blue' and weathered 'brown' London Clay
Low	0.05–0.1	Boulder clays Very stiff or hard 'blue' London Clay
Very low	Below 0.05	Heavily overconsolidated 'boulder clays' Stiff weathered rocks

Table 14.6. TYPICAL RANGE OF VALUES OF COEFFICIENT OF CONSOLIDATION AND COMPRESSION INDEX FOR INORGANIC SOILS

Soil type	*Plasticity index range*	*Coefficient of consolidation c_v (m^2/year)*		*Compression index C_c*
		undisturbed	remoulded	
Clays — montmorillonite				Up to 2.6
high plasticity	Greater than 25	0.1–1	About 25–50% of undisturbed values	
medium plasticity	25–5	1–10		0.8–0.2
low plasticity	15 or less	10–100		
Silts		above 100		

From Lambe and Whitman (1979)

Table 14.7. TYPICAL VALUES OF C_{sec}

Soil type	C_{sec}
Normally consolidated clays	0.005–0.02
Very plastic clays	0.03 or higher
Organic clays	0.03 or higher
Overconsolidated clays (Overconsolidation ratio greater than 2)	Less than 0.001

From Lambe and Whitman (1979)

Table 3.7 Typical Range of Values of Vertical Coefficient of Consolidation

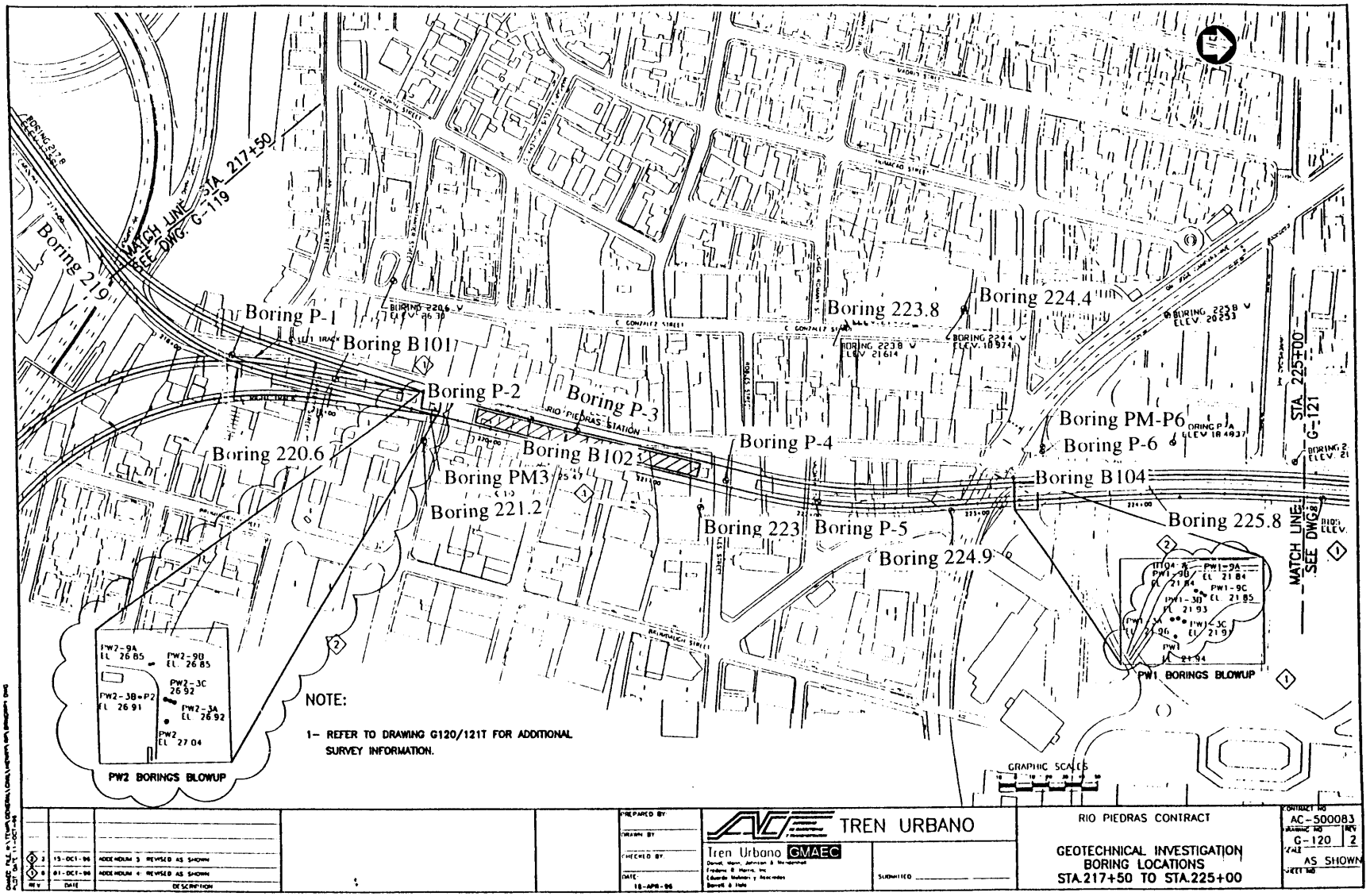

Figure 3.1a Boring Locations of Geotechnical Investigations

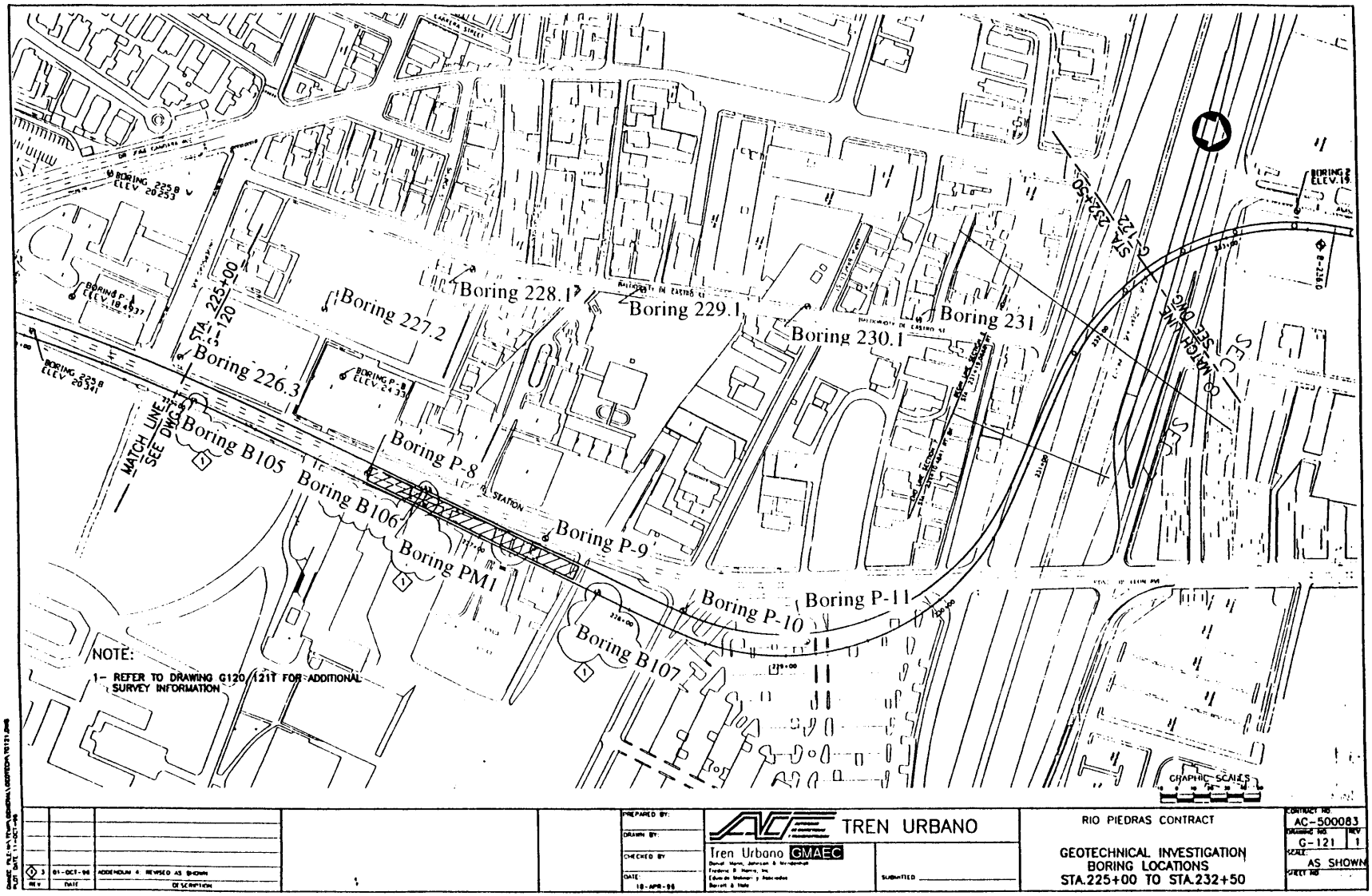

Figure 3.1b Boring Locations of Geotechnical Investigations

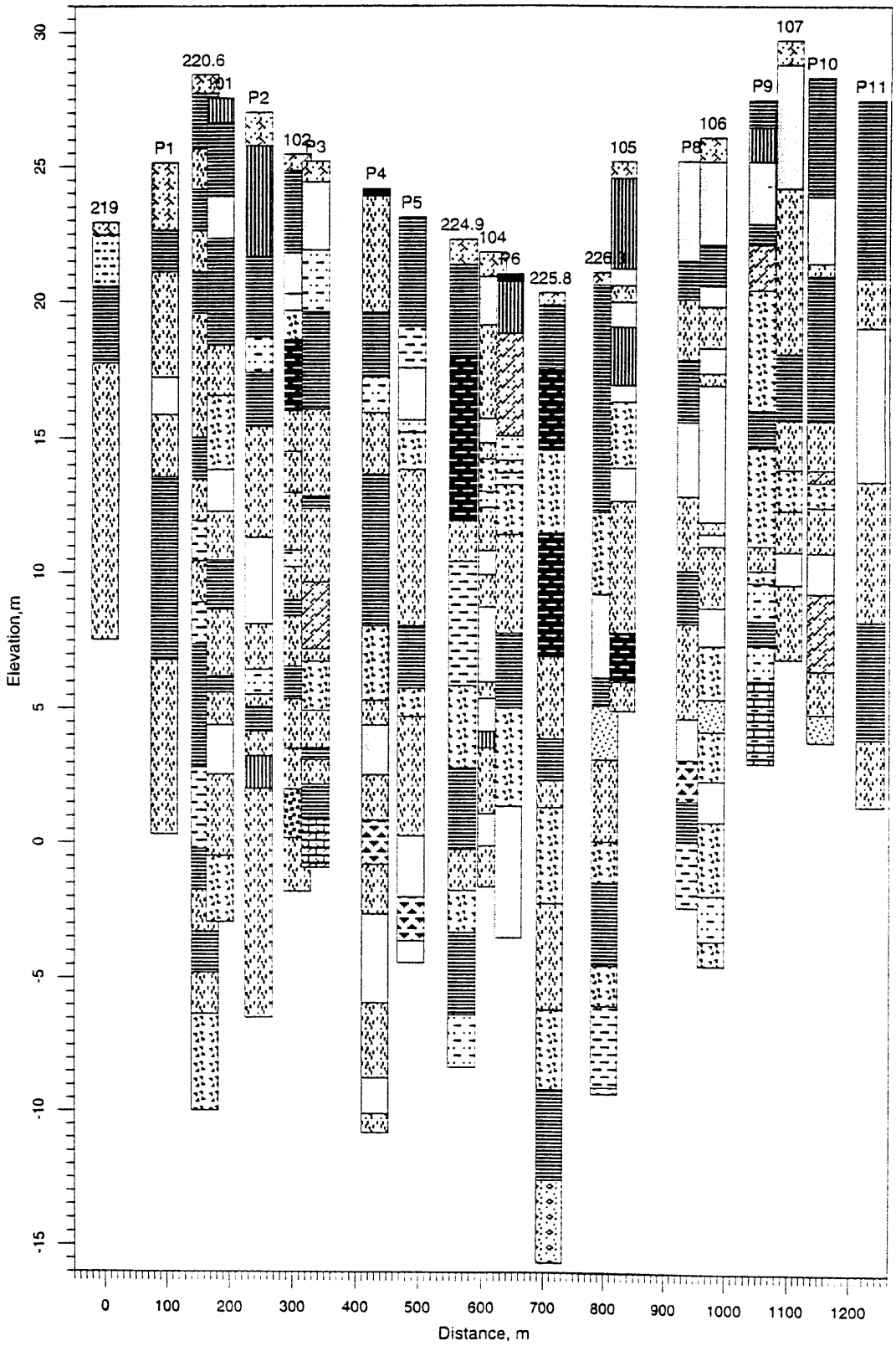

Figure 3.2 Geoprofile of Section 7: from boring 219 (Sta. 217+35) to boring P11 (Sta. 229+17)

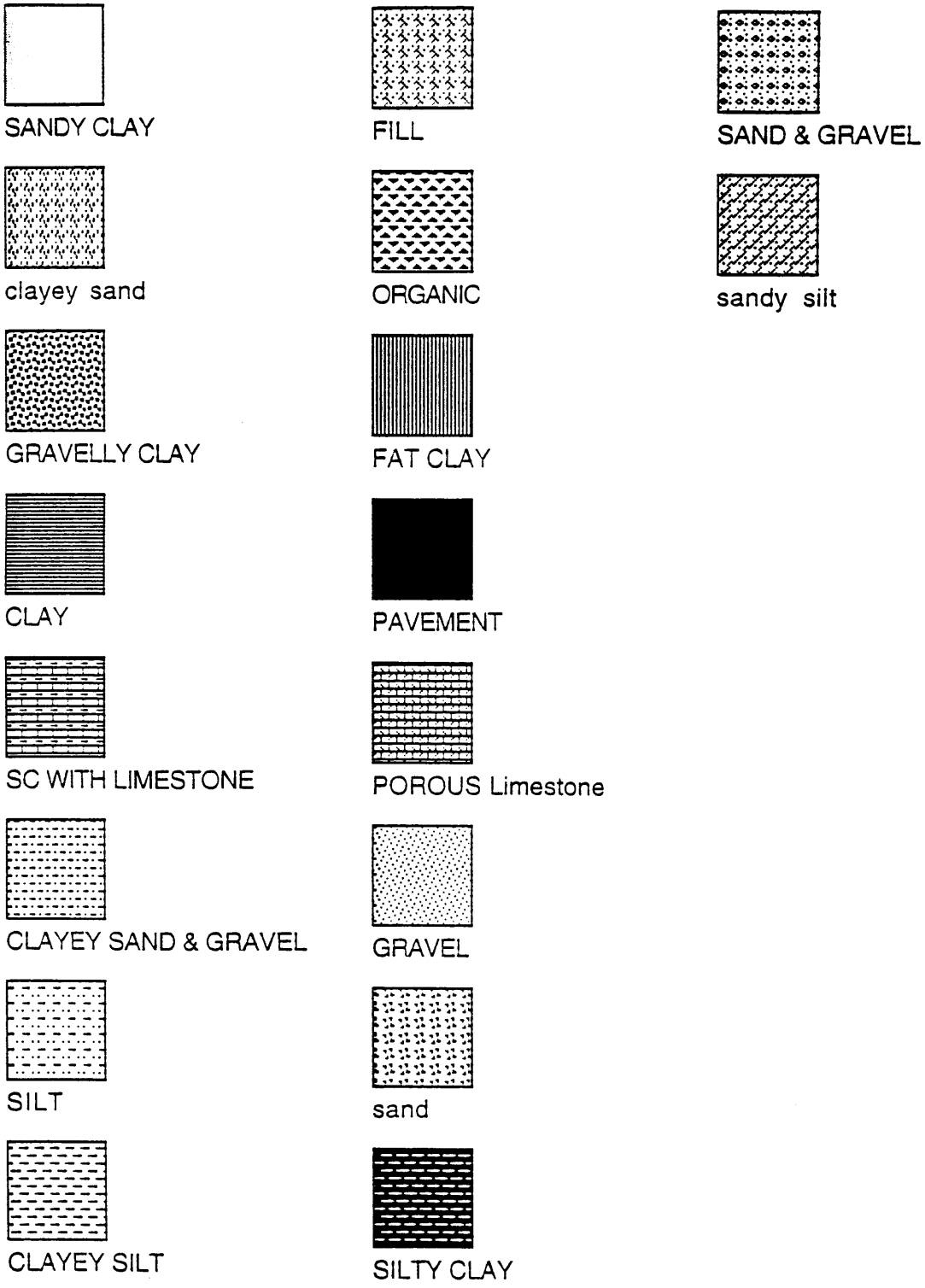

Figure 3.3 Legend of Geoprofile

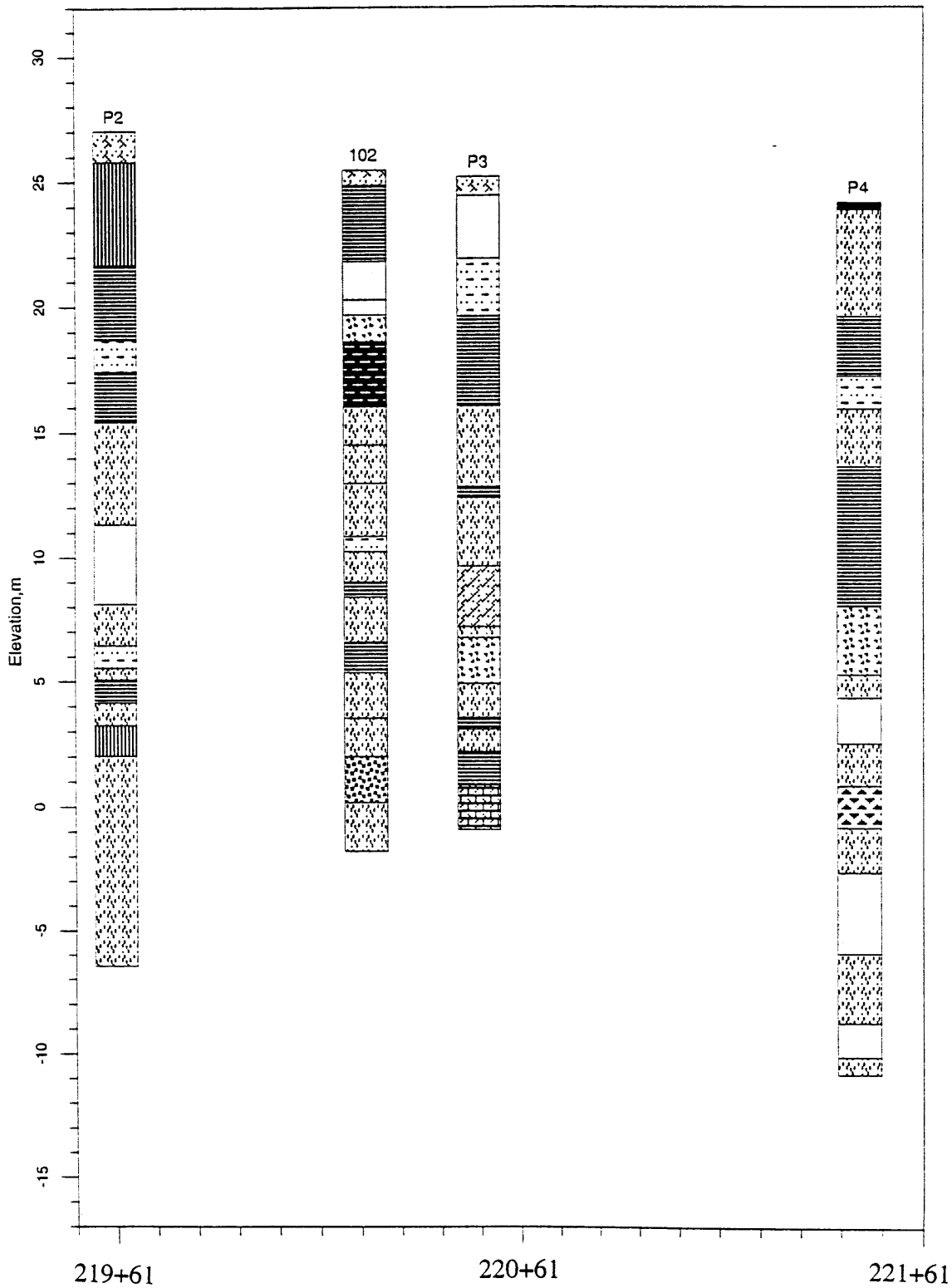

Figure 3.4 Stratigraphy of Río Piedras Station

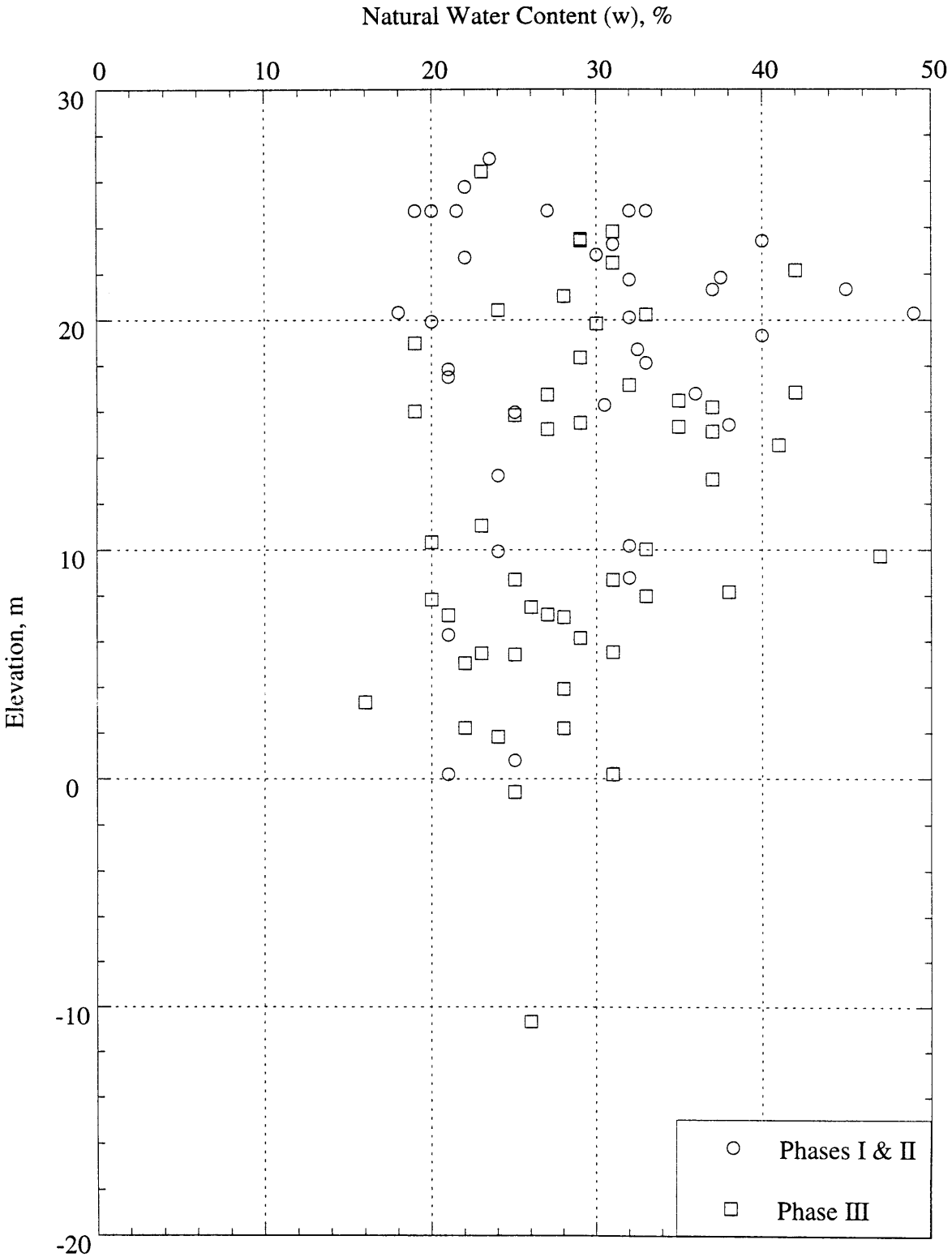

Figure 3.5 Natural Water Content, w

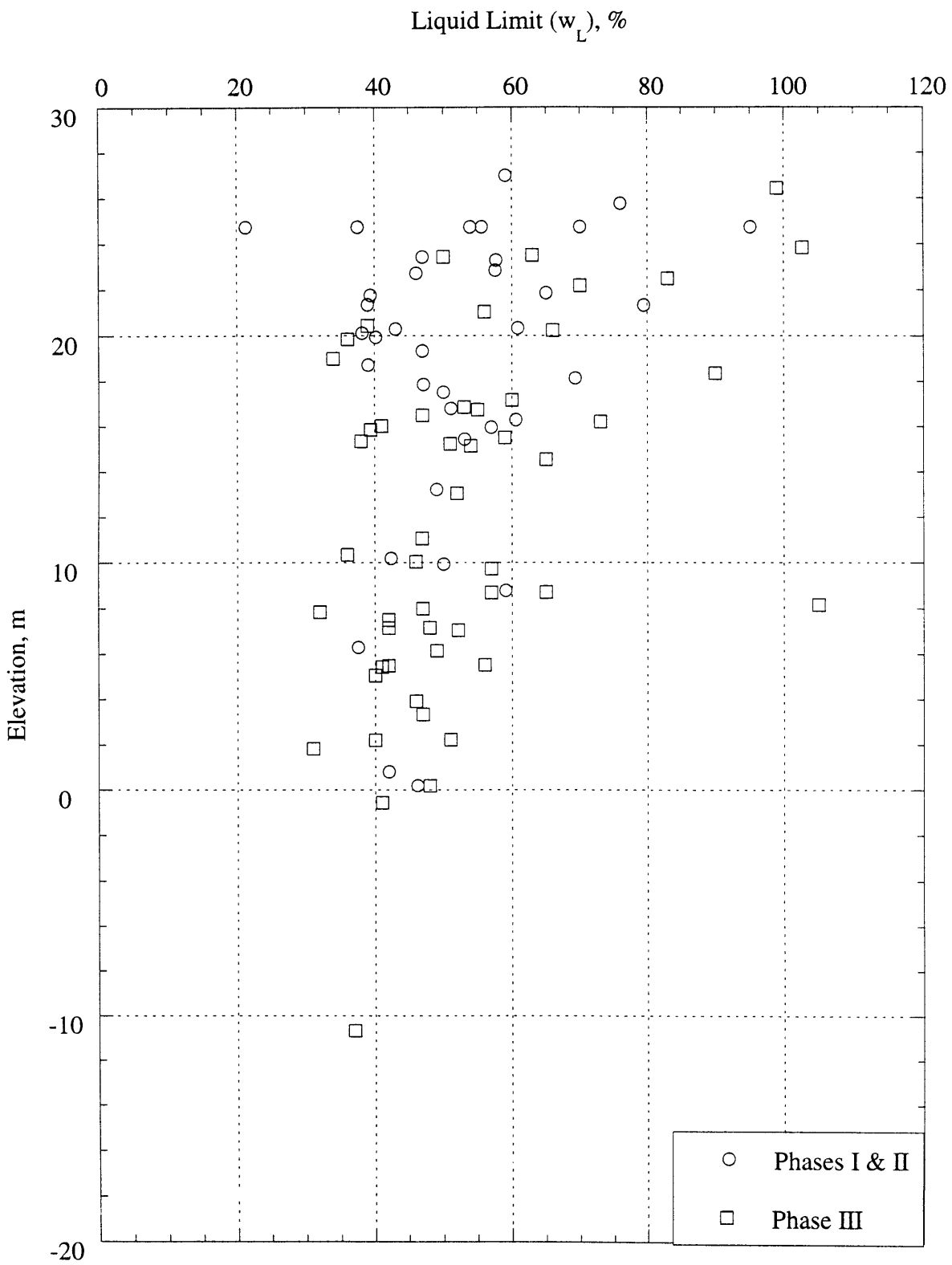

Figure 3.6 Liquid Limit, w_L

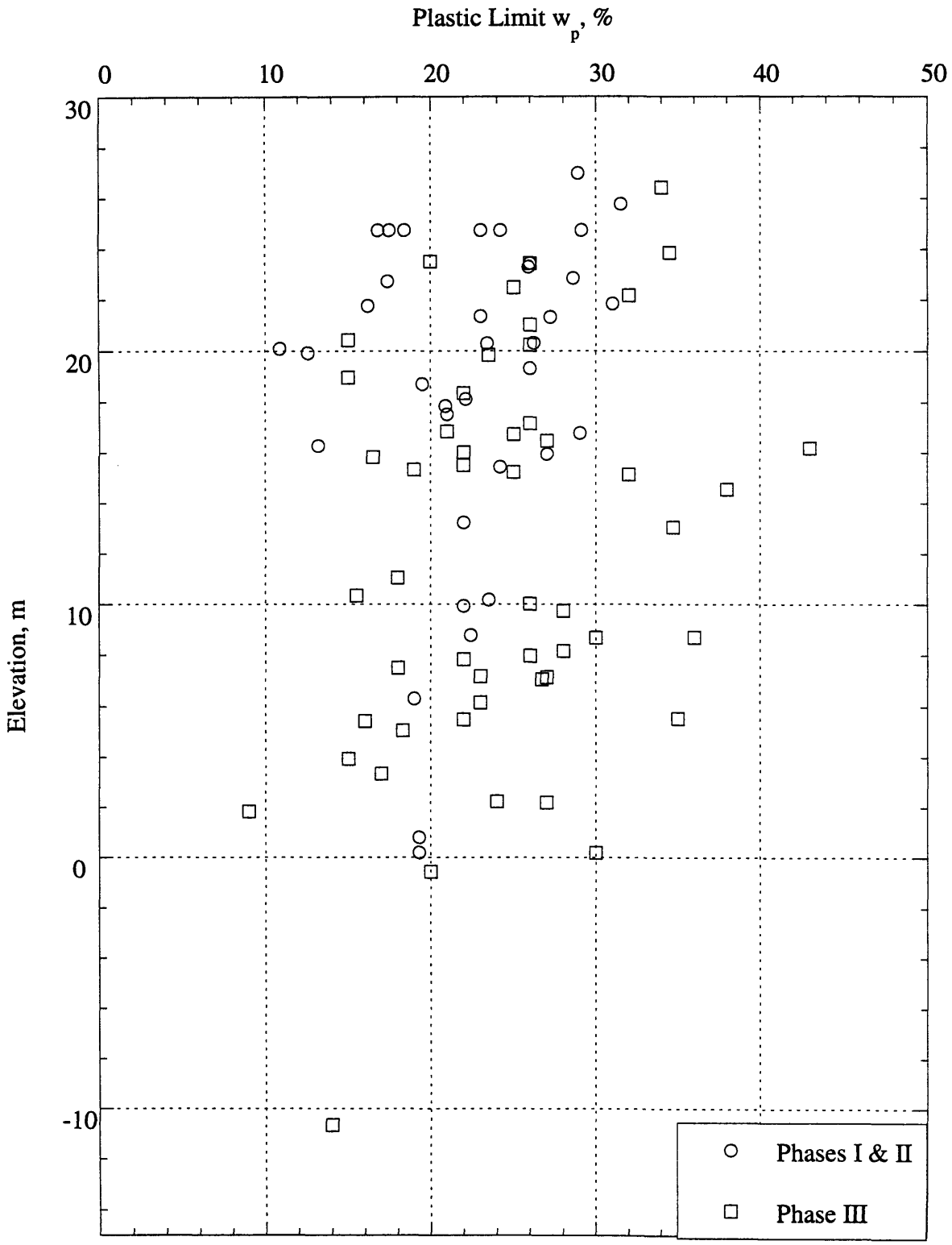

Figure 3.7 Plastic Limit, w_p

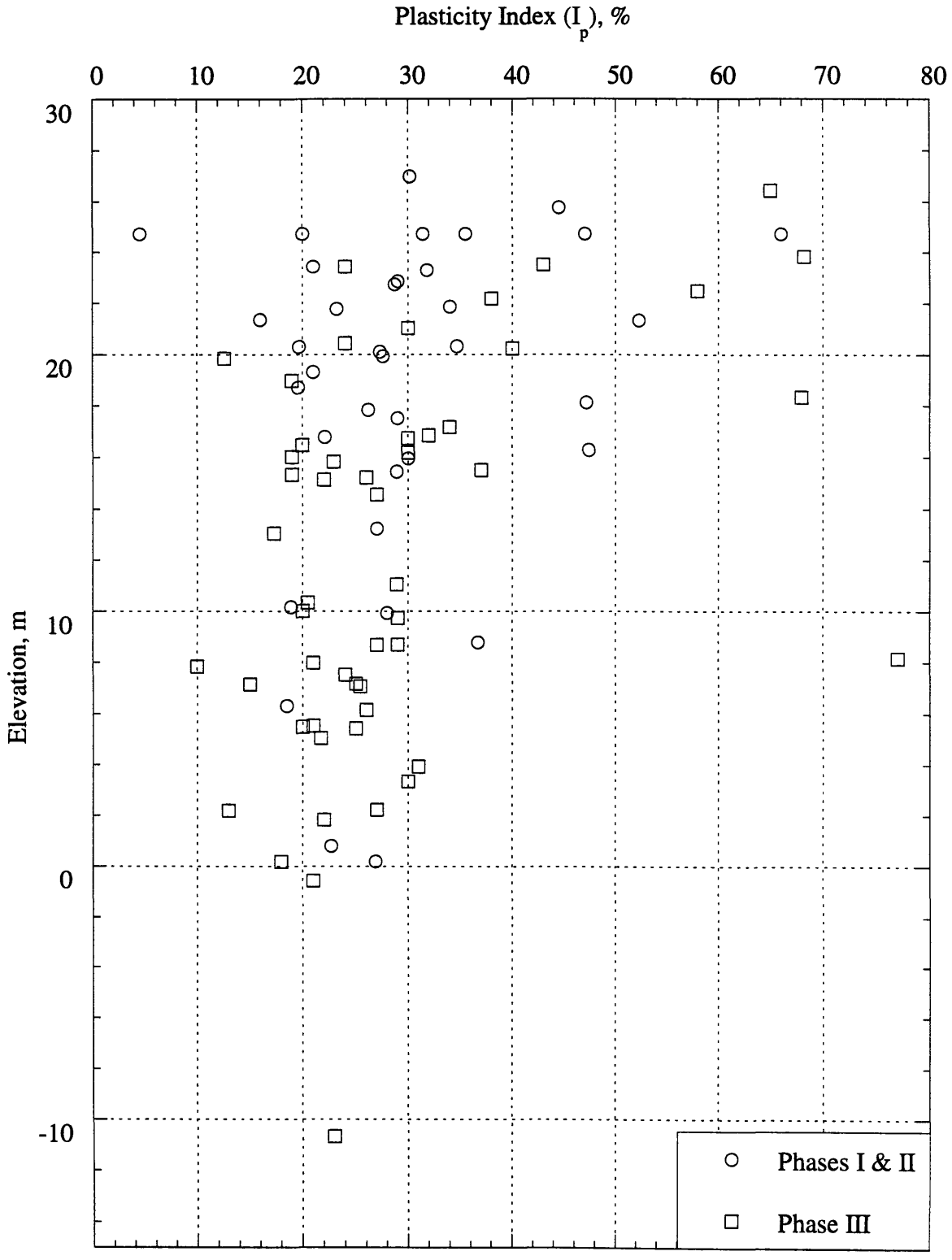

Figure 3.8 PLasticity Index, I_p

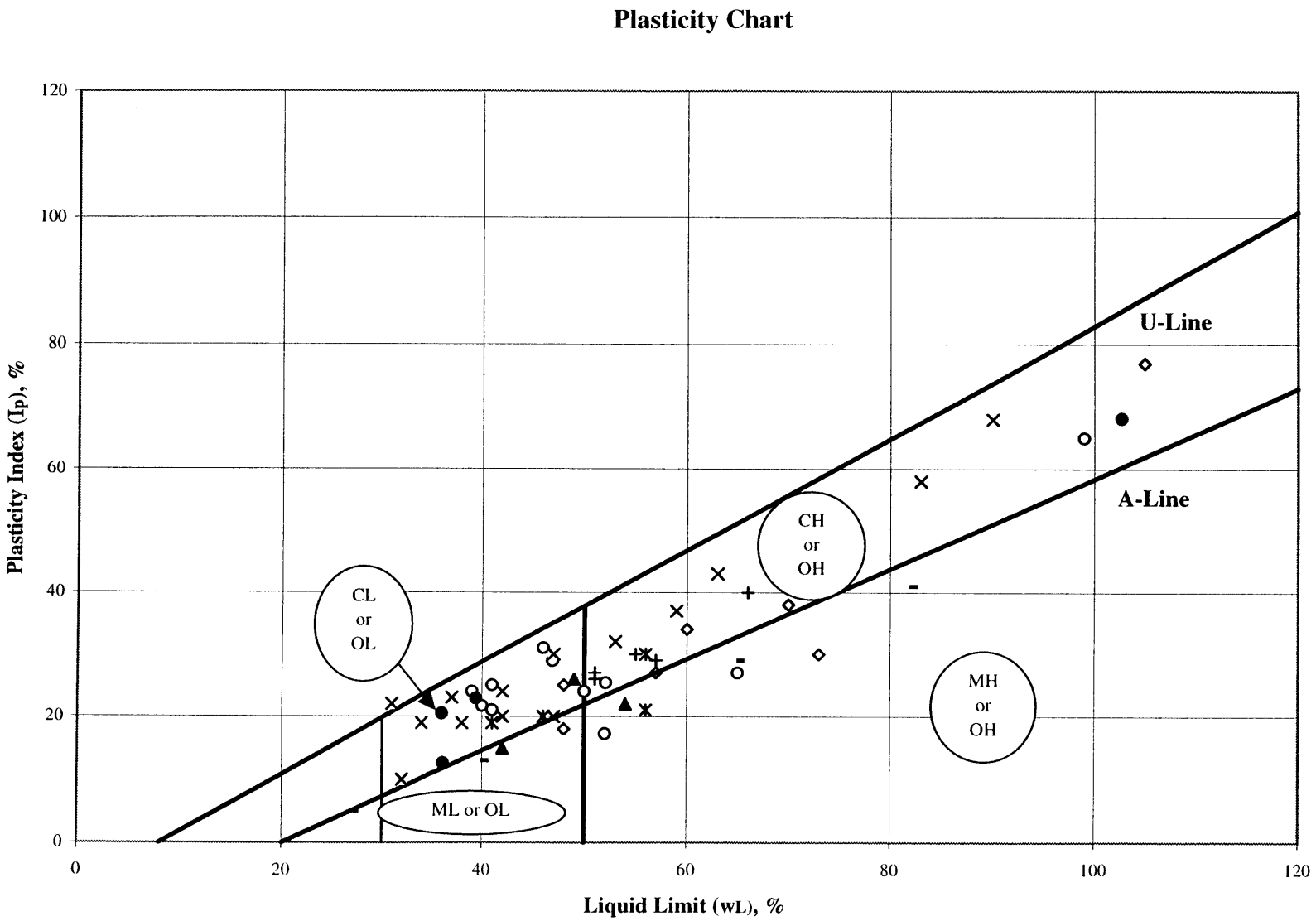

Figure 3.9 Plasticity Chart for Phases I and II

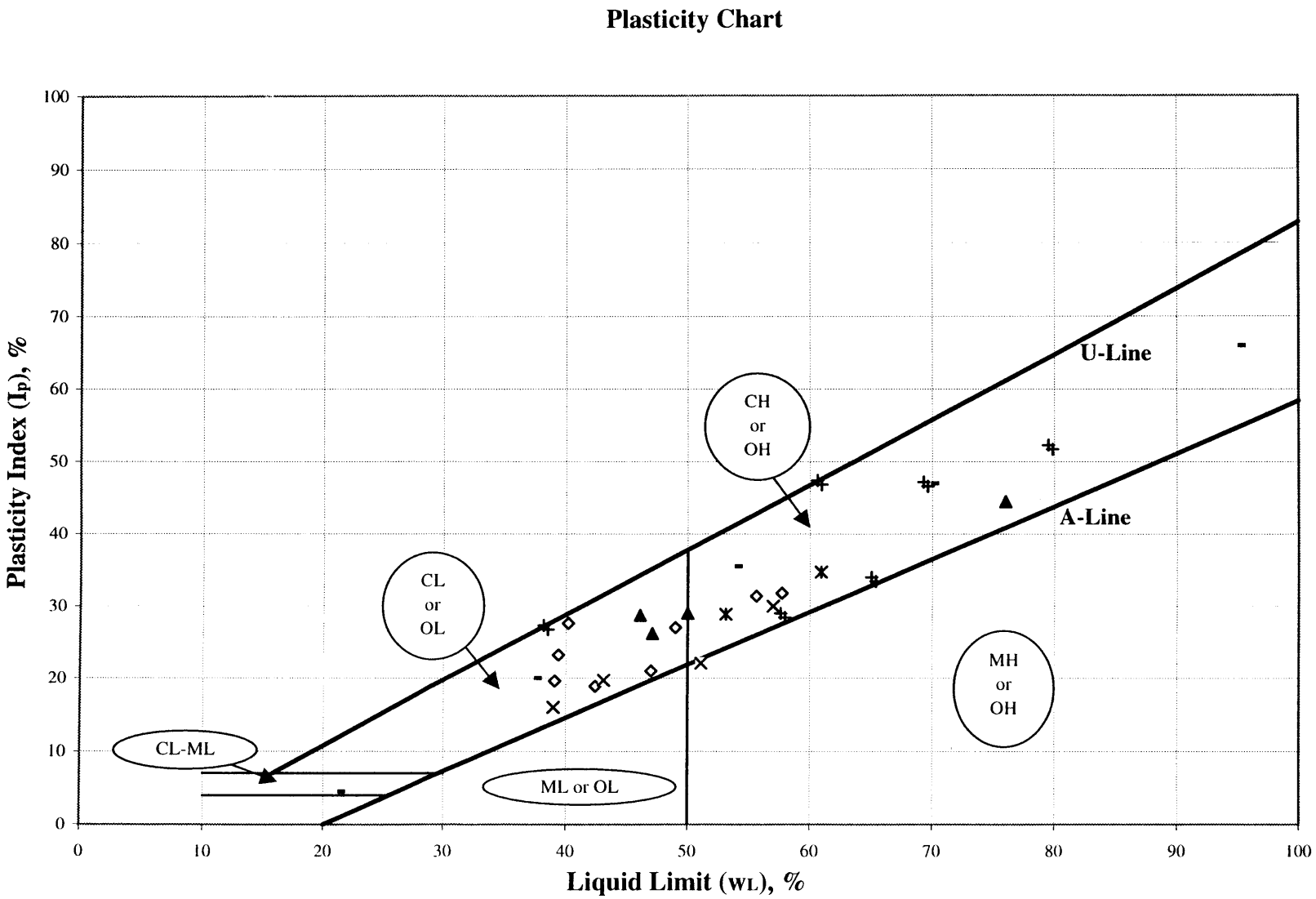

Figure 3.10 Plasticity Chart for Phase III Investigation

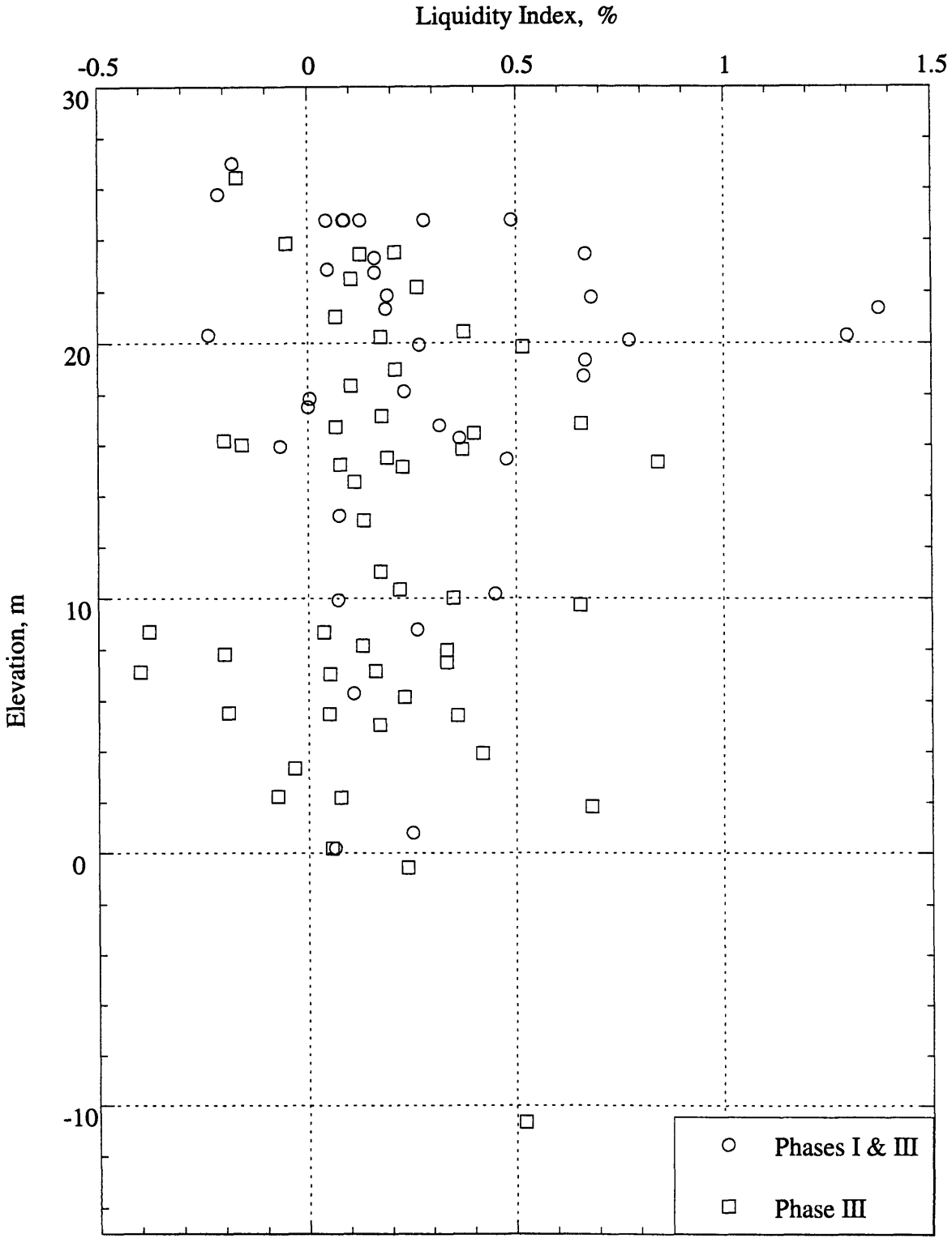

Figure 3.11 Liquidity Index

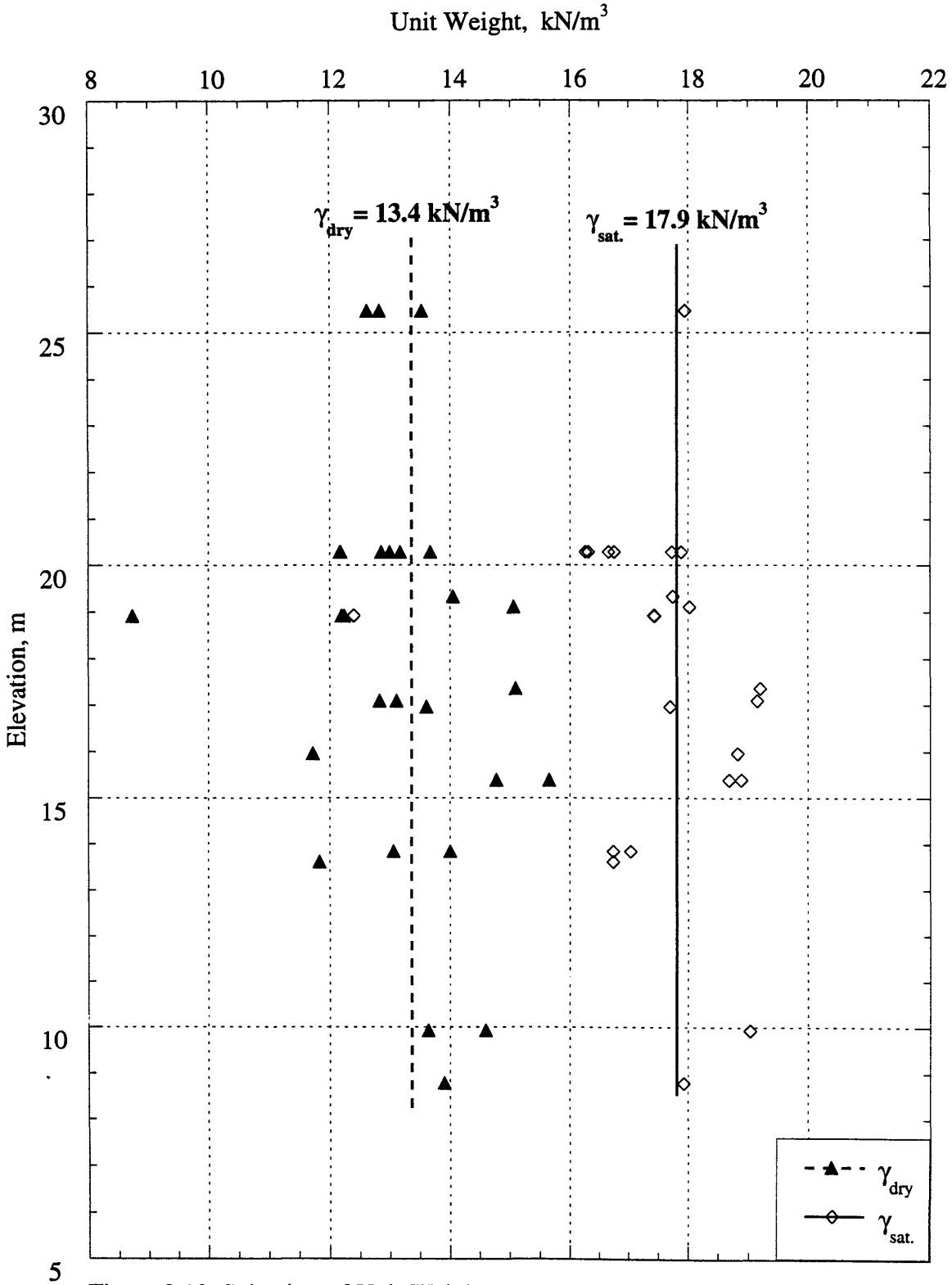

Figure 3.12 Selection of Unit Weight

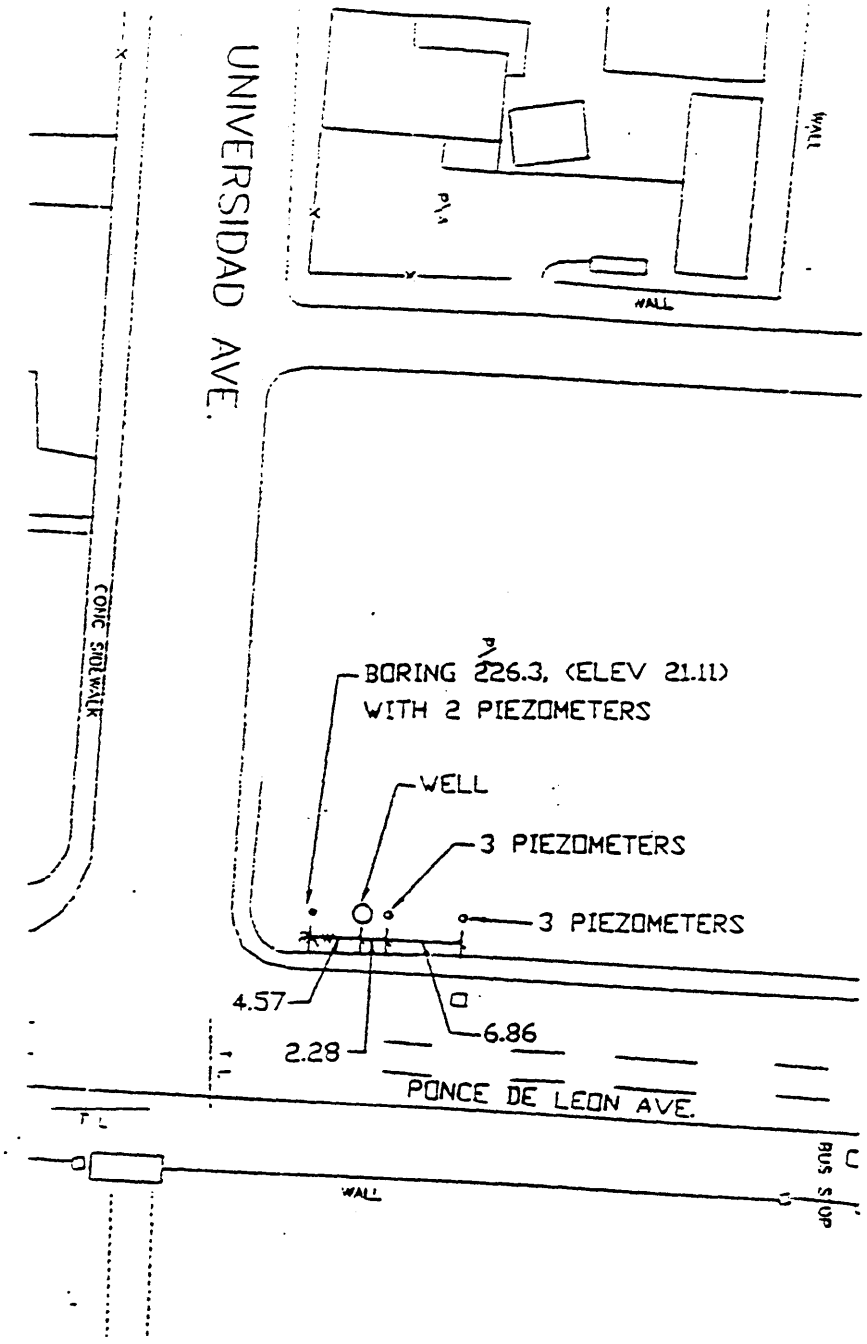

Figure 3.13 Site Layout of Pump Test (Phases I and II)

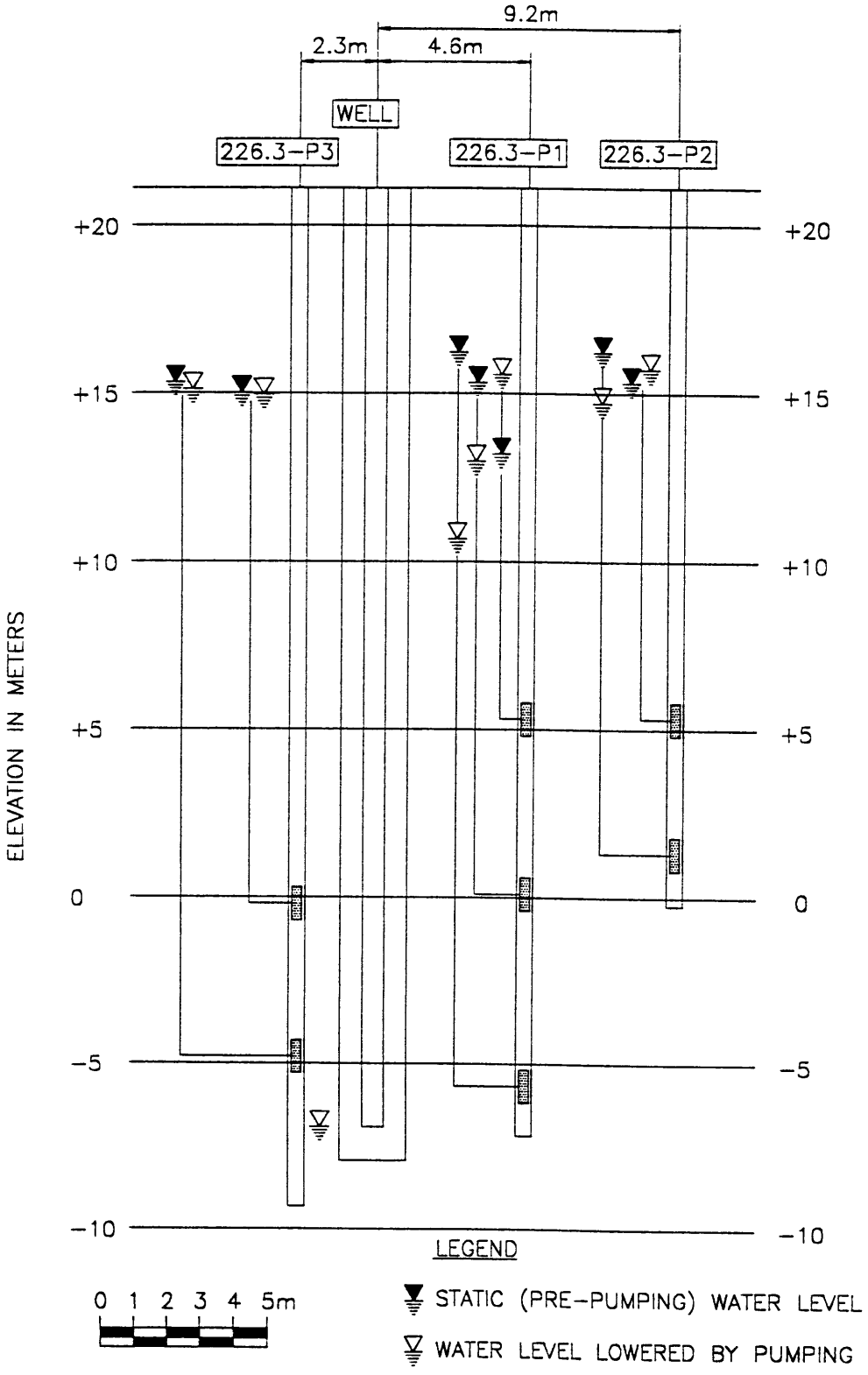

Figure 3.14 Results of Pump Test (Phases I and II)

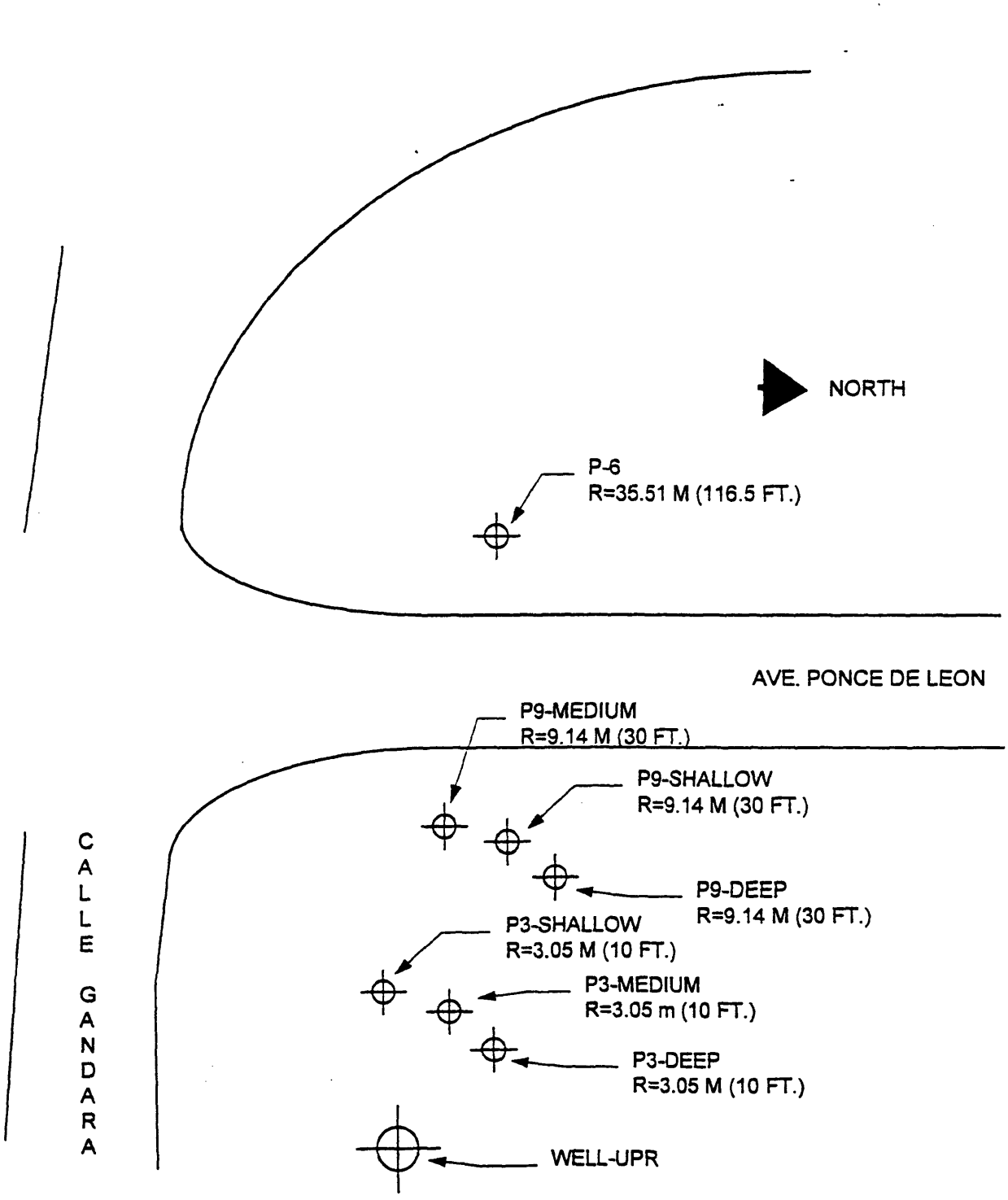

Figure 3.15 Site Layout of Pump Test No. 1 (Phase III)

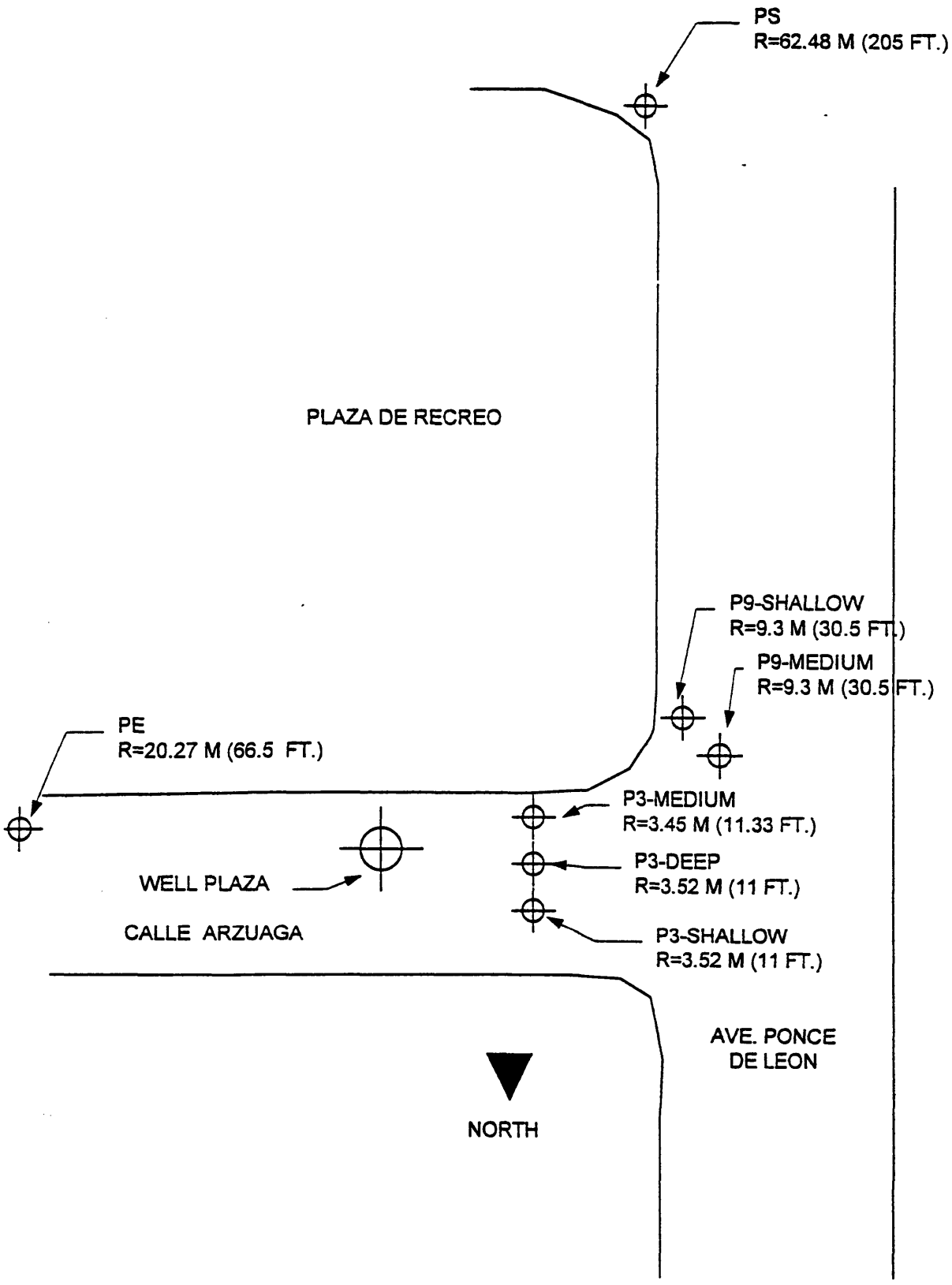

Figure 3.16 Site Layout of Pump Test No.2 (Phase III)

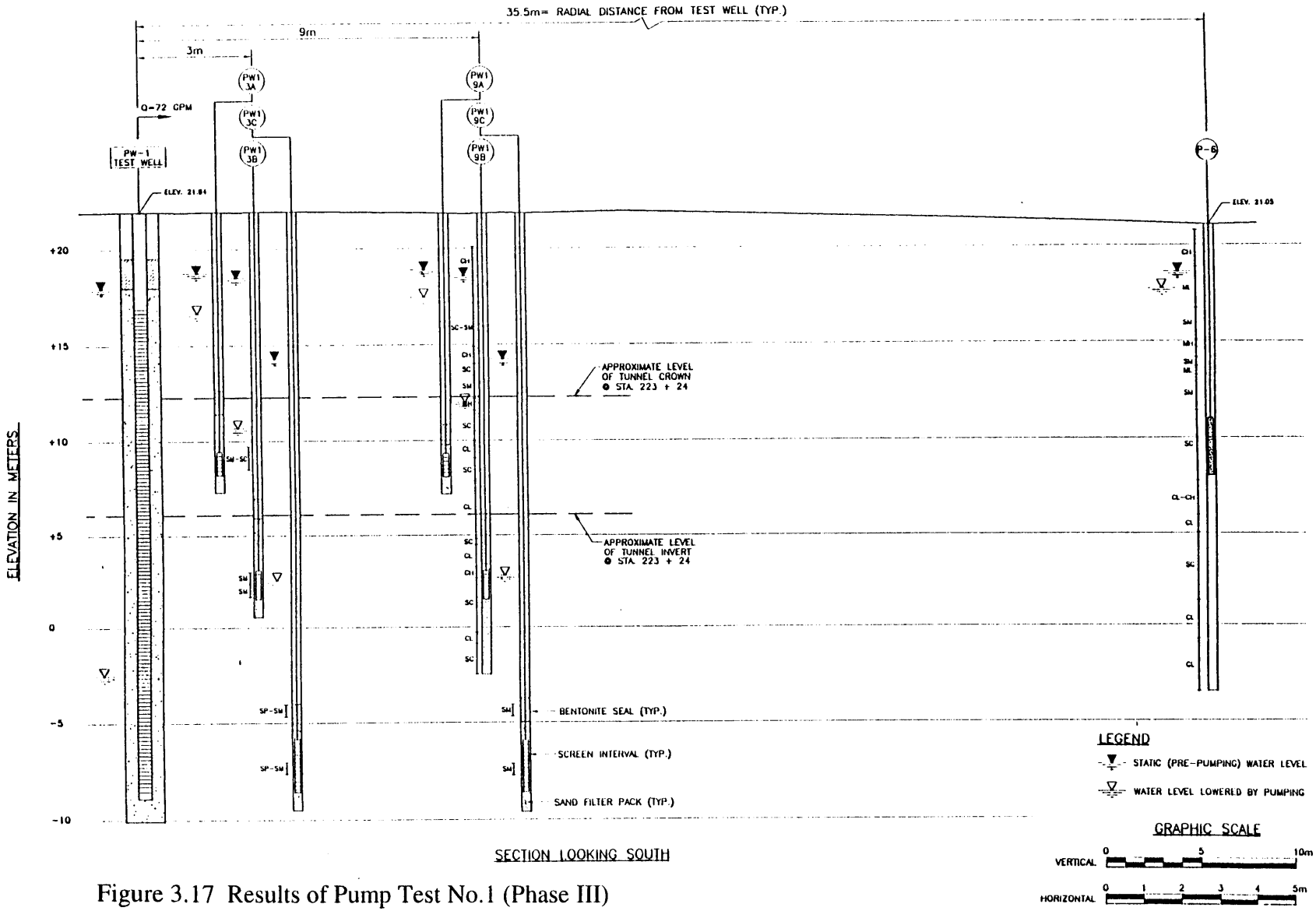

Figure 3.17 Results of Pump Test No.1 (Phase III)

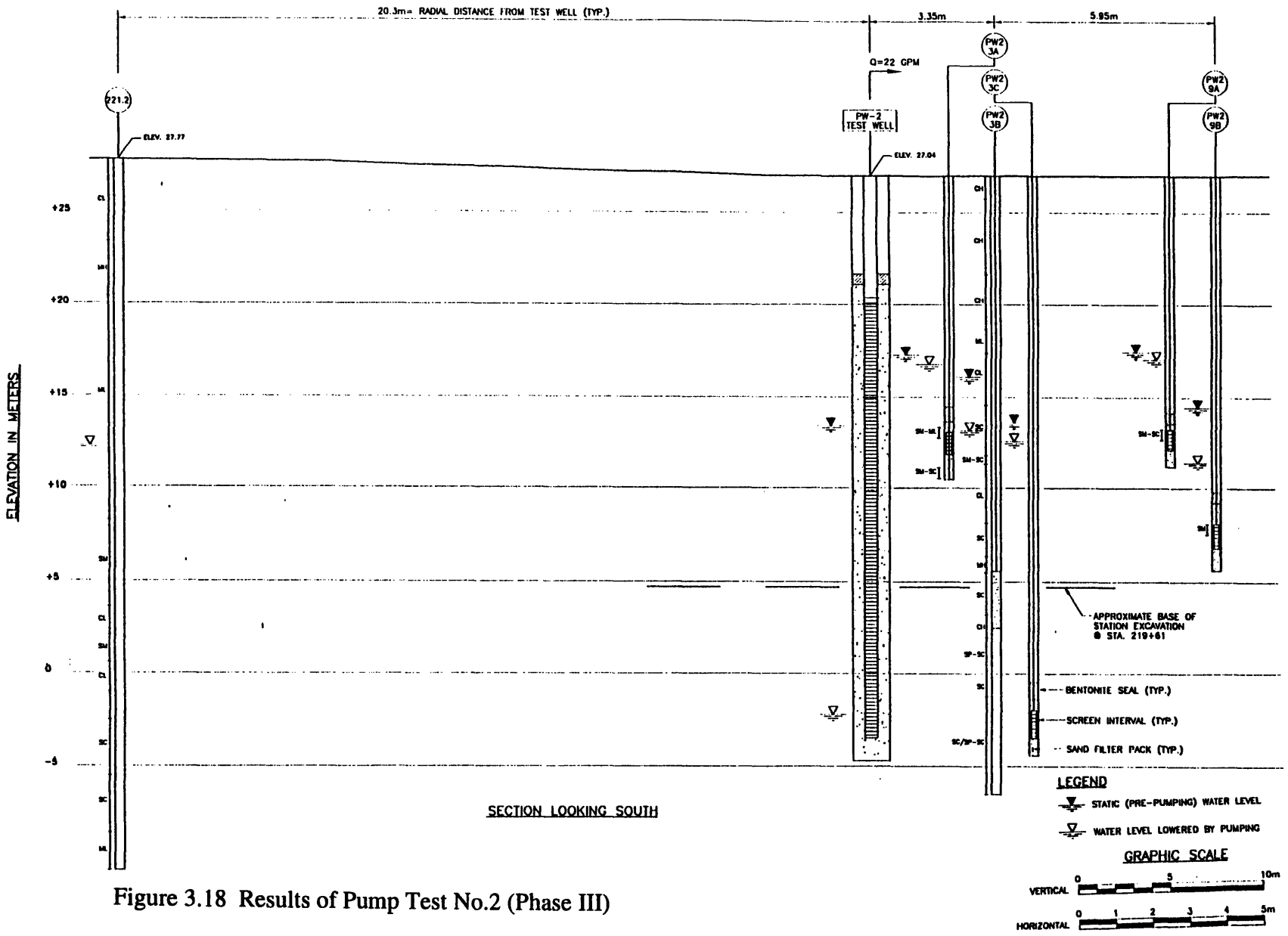

Figure 3.18 Results of Pump Test No.2 (Phase III)

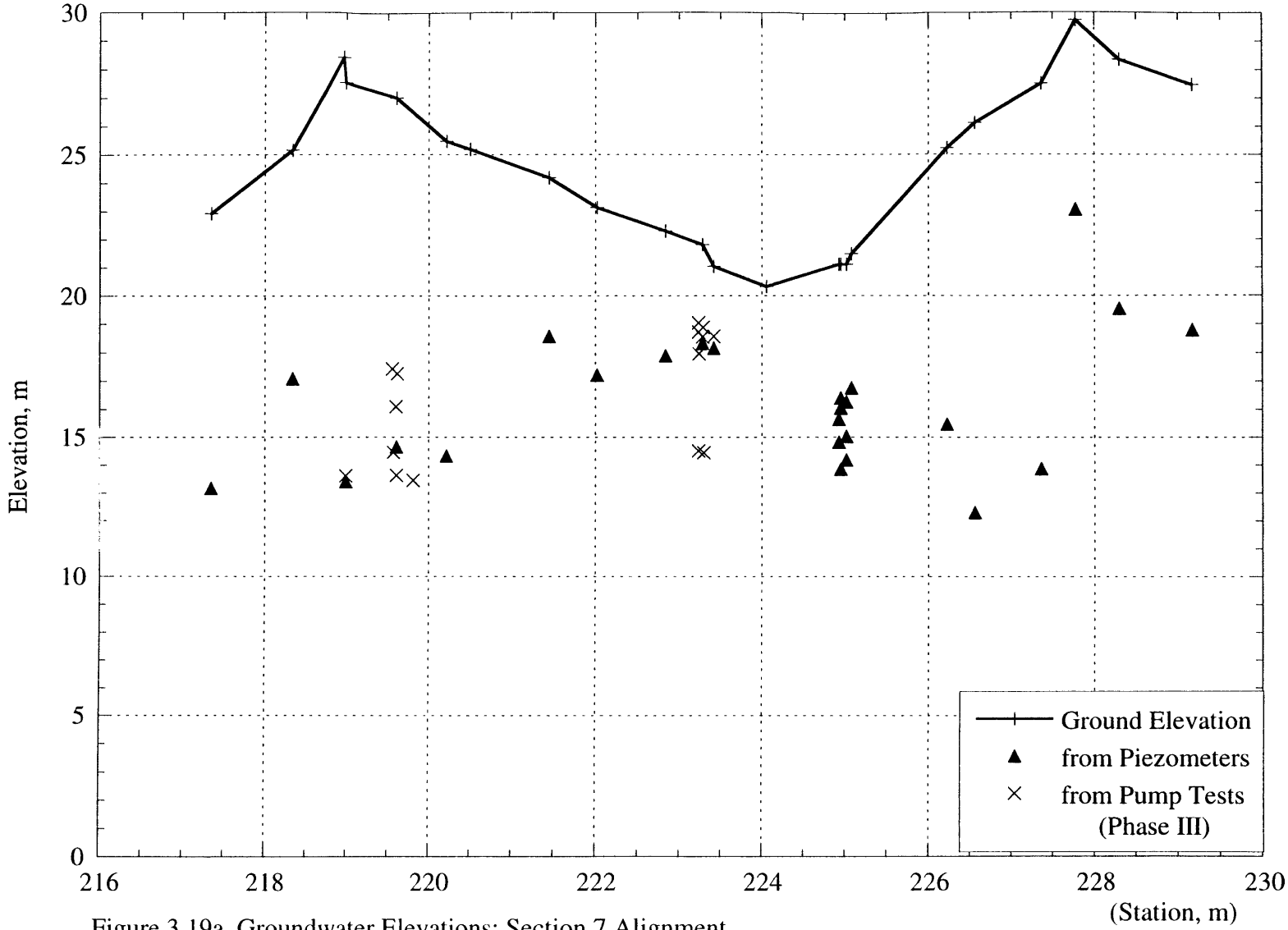

Figure 3.19a Groundwater Elevations: Section 7 Alignment

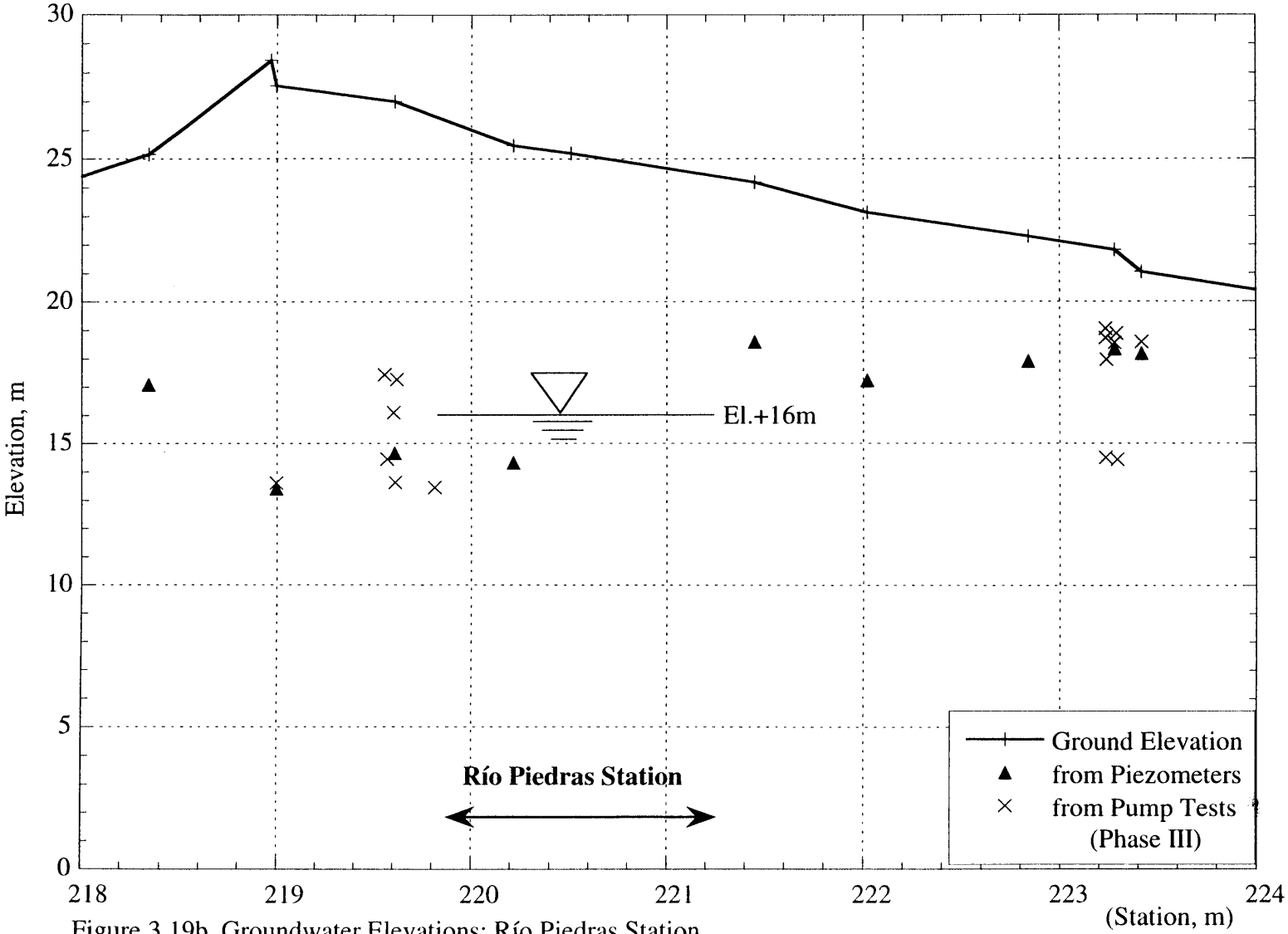

Figure 3.19b Groundwater Elevations: Río Piedras Station

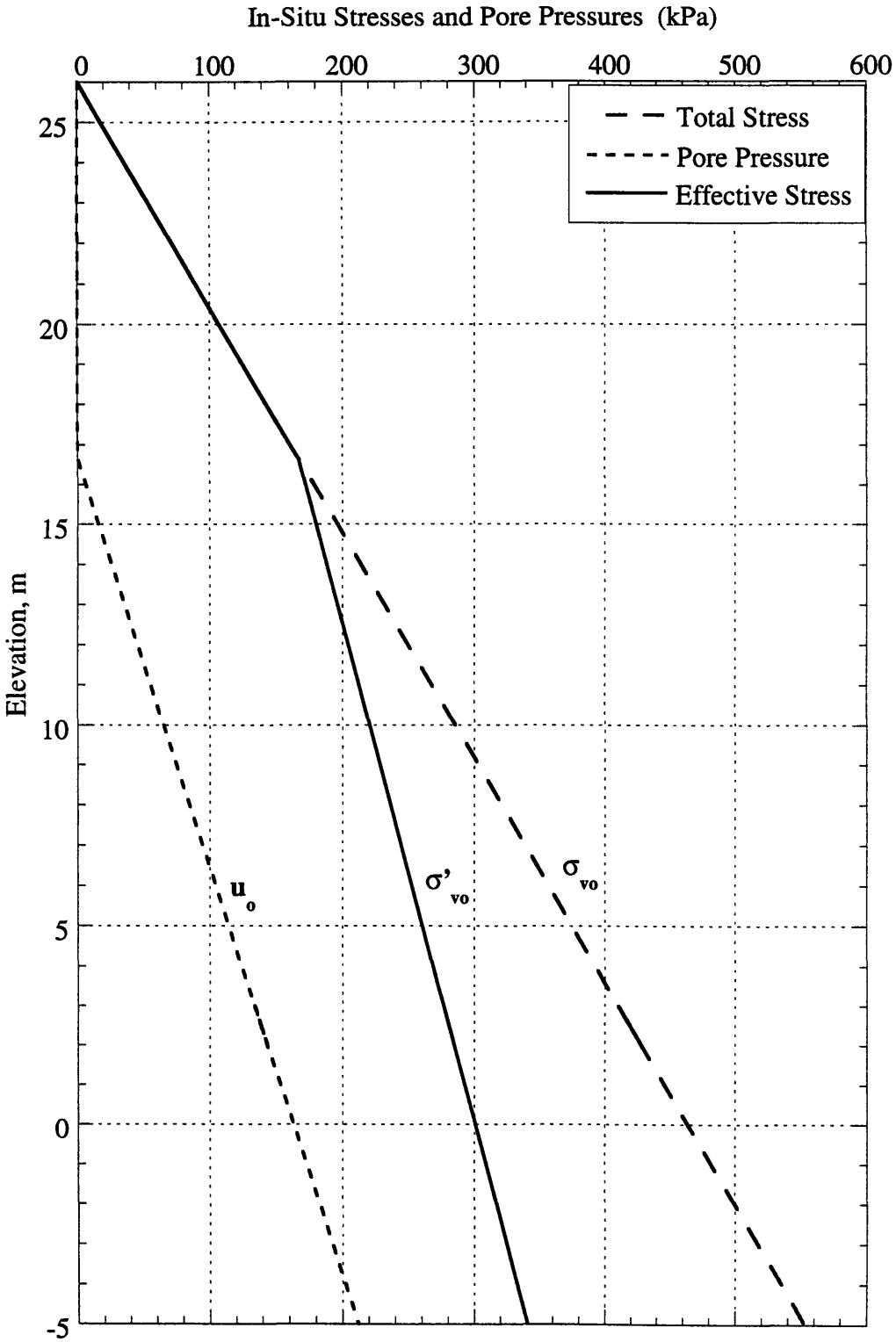

Figure 3.20 Initial Stress Profile

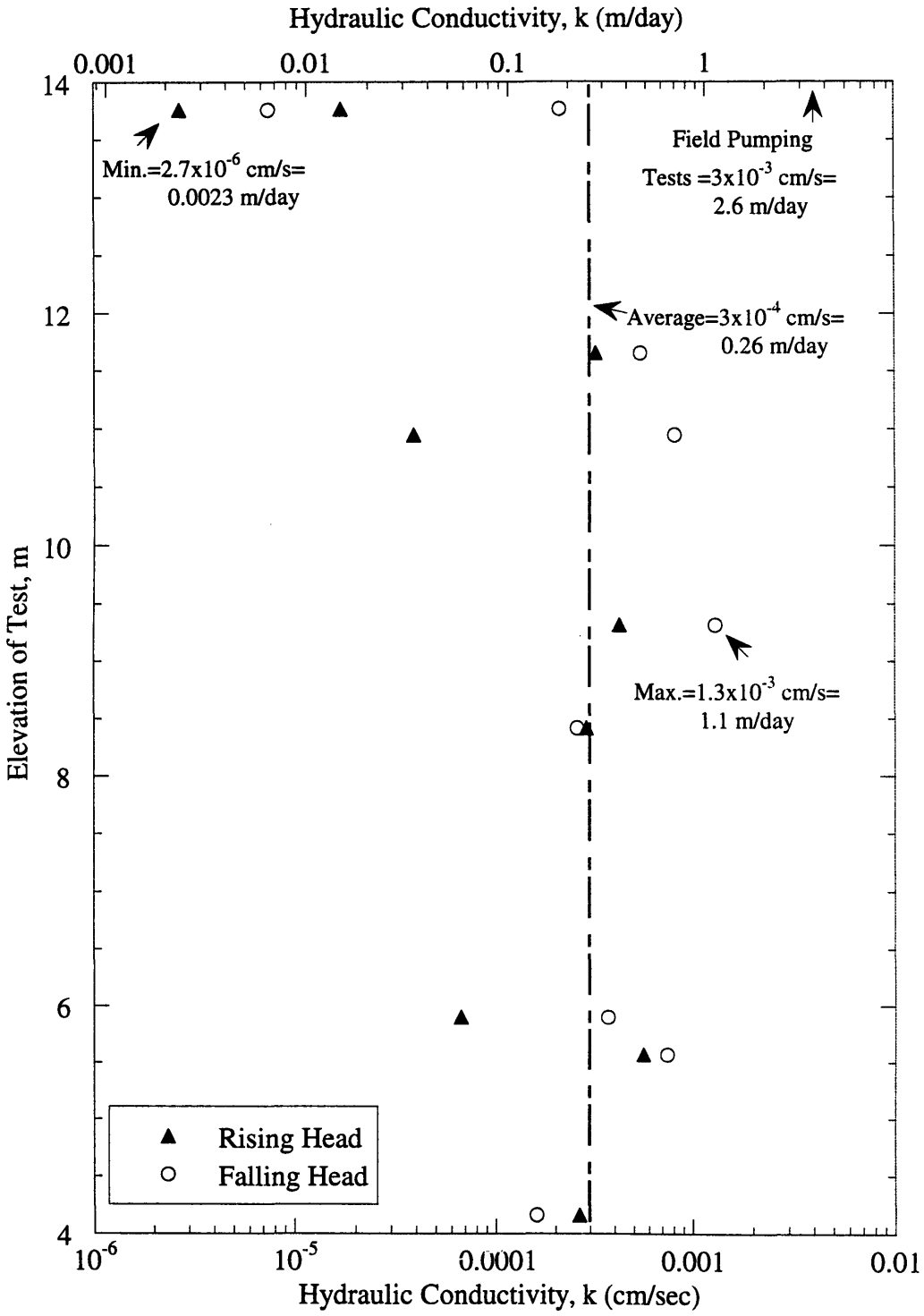

Figure 3.21 Permeability Results from Slug Tests

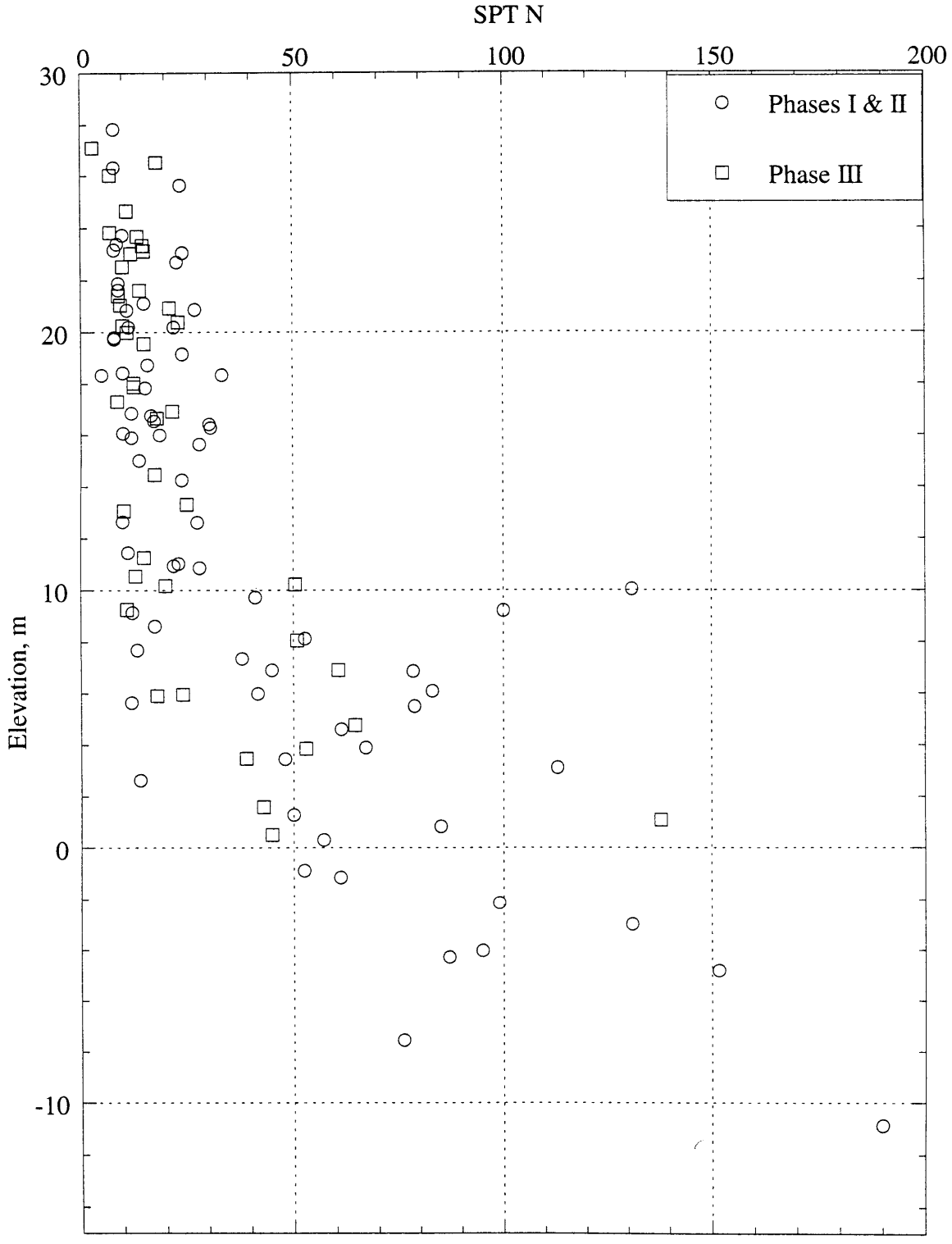

Figure 3.22a Measured Standard Penetration Test N-Value

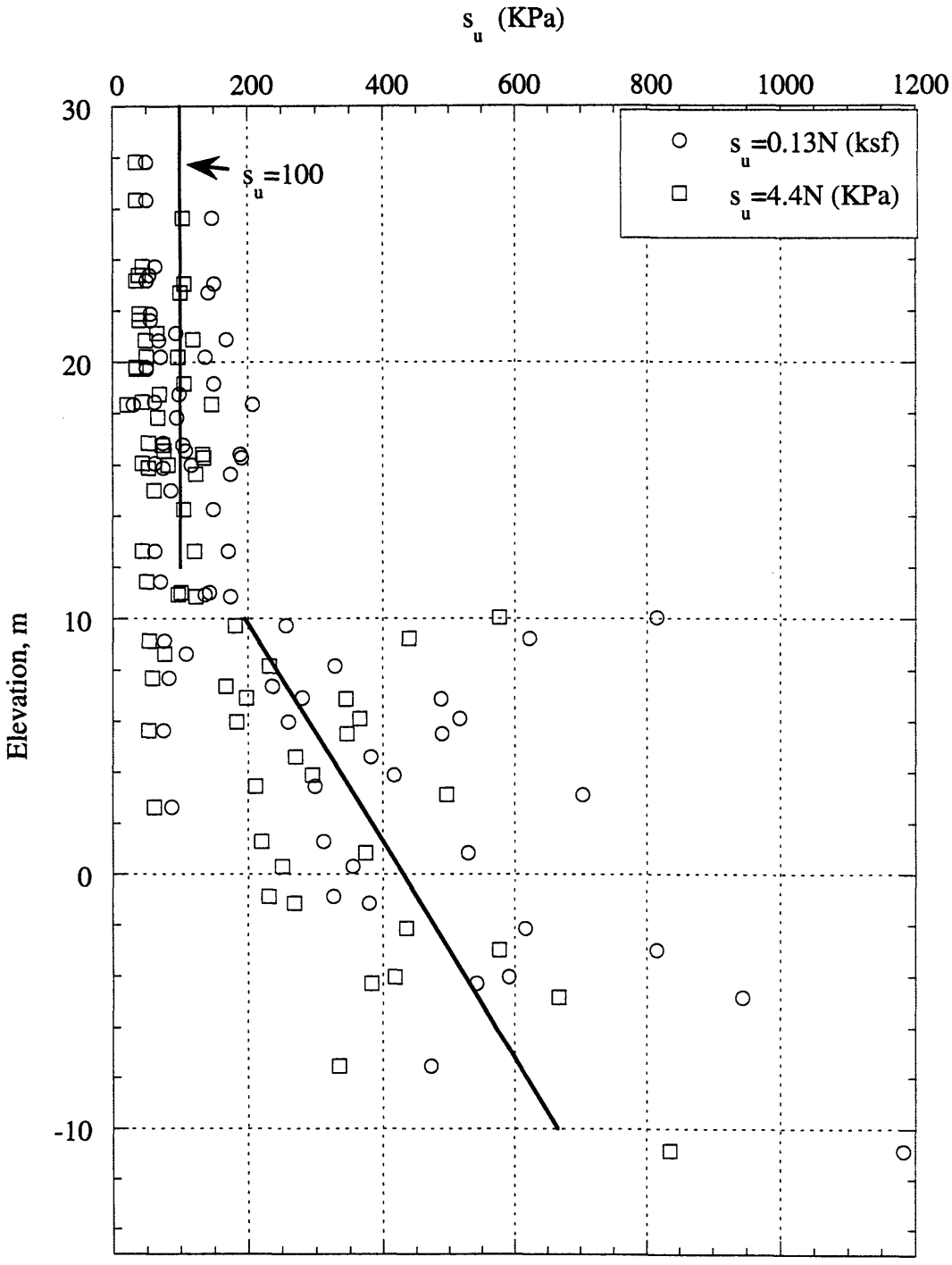

Figure 3.22b Undrained Strength from Measured Standard Penetration Test

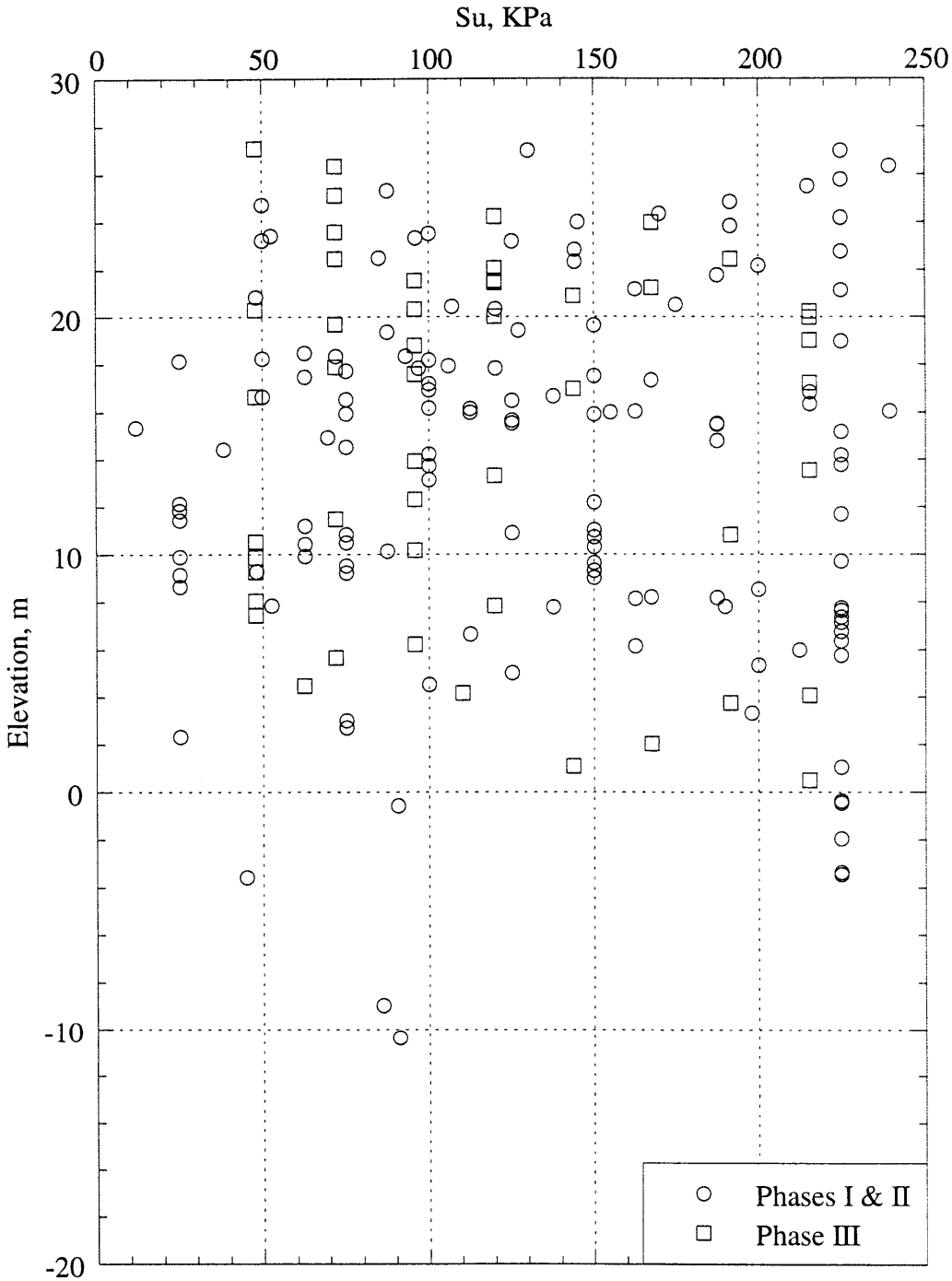

Figure 3.23 Pocket Penetrometer Results

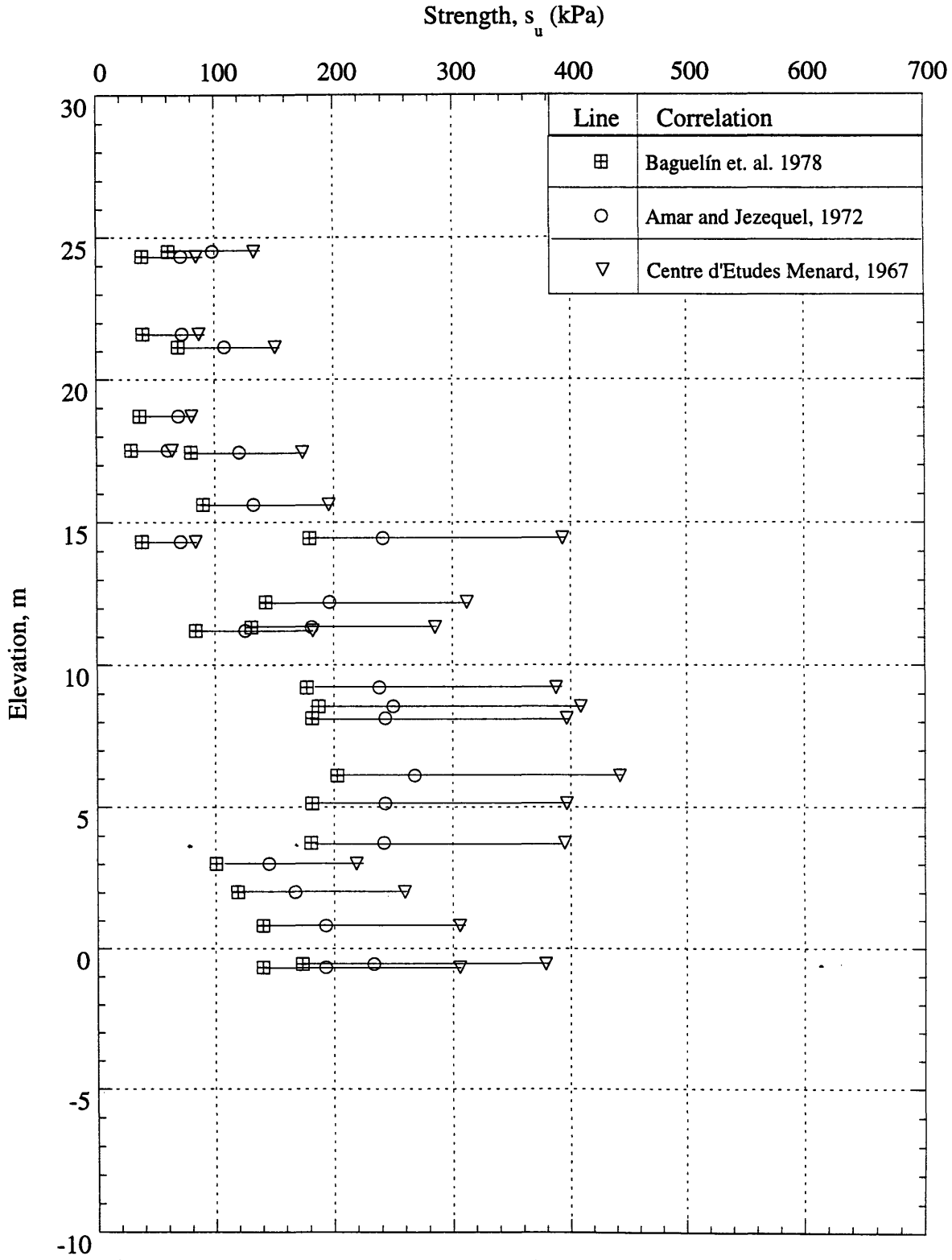

Figure 3.24 Pressuremeter Strength Results using Correlations

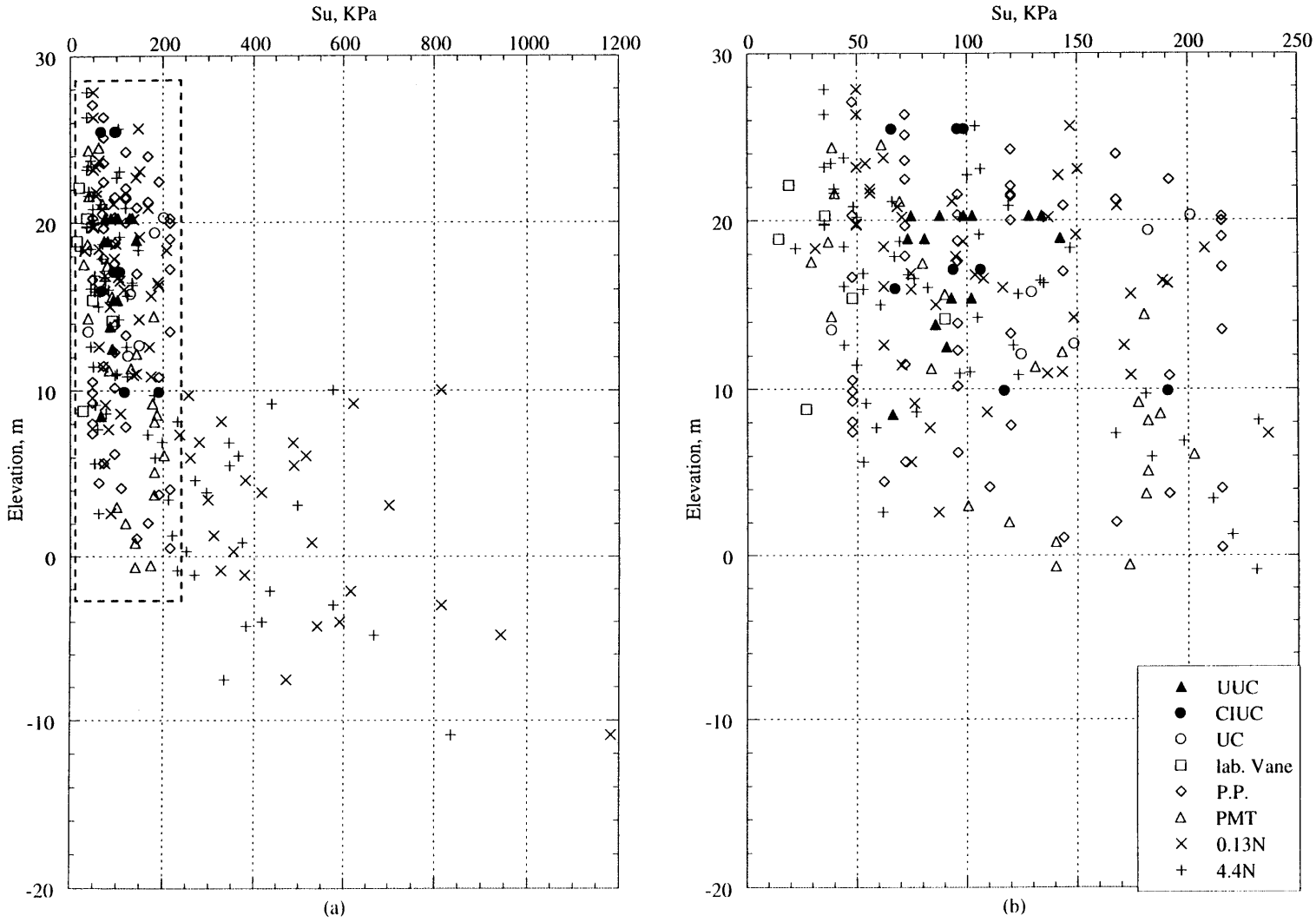

Figure 3.25 Undrained Strength Results from Laboratory and Field Tests

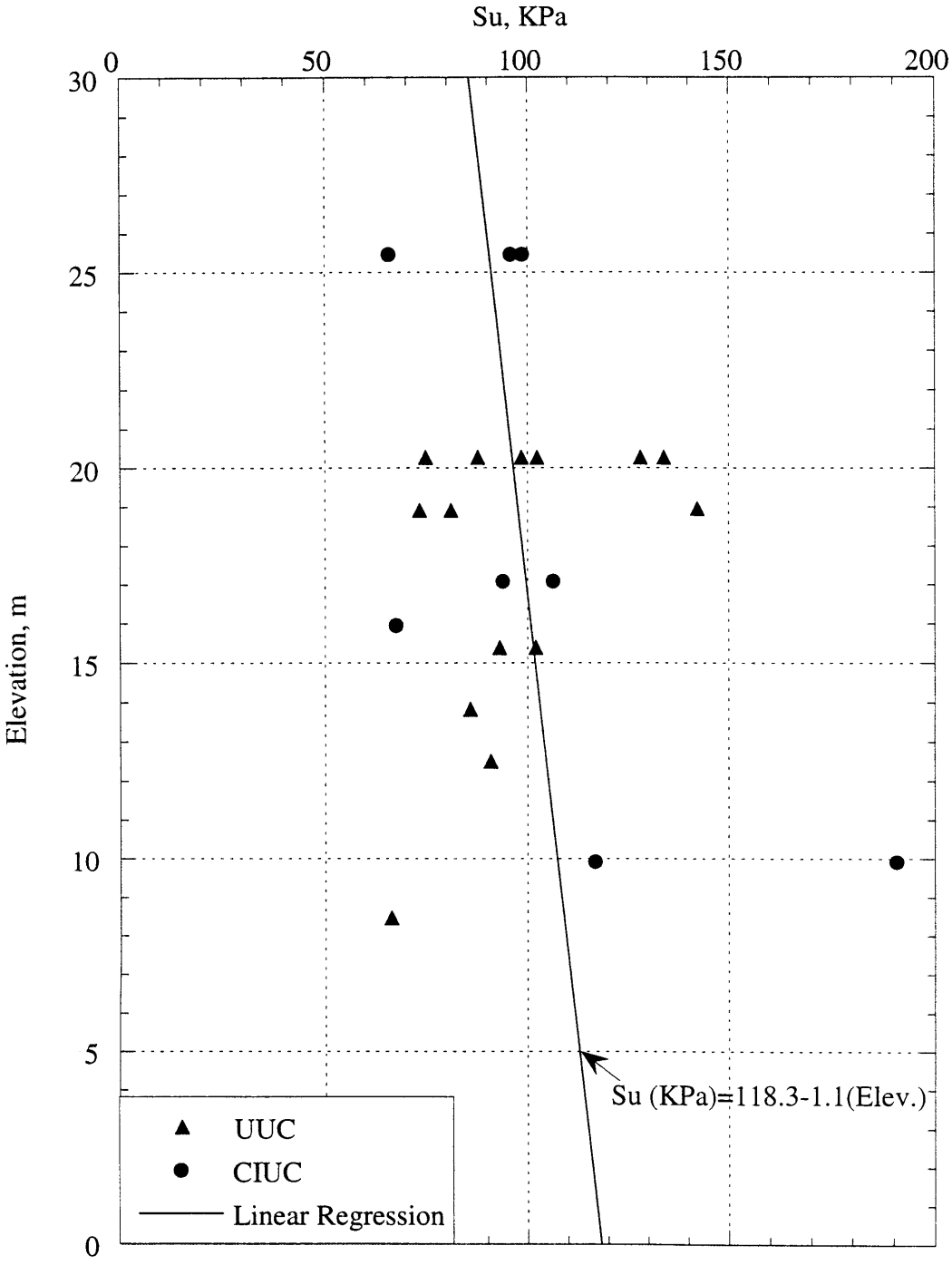

Figure 3.26 Undrained Strength Results from UUC and CIUC Tests

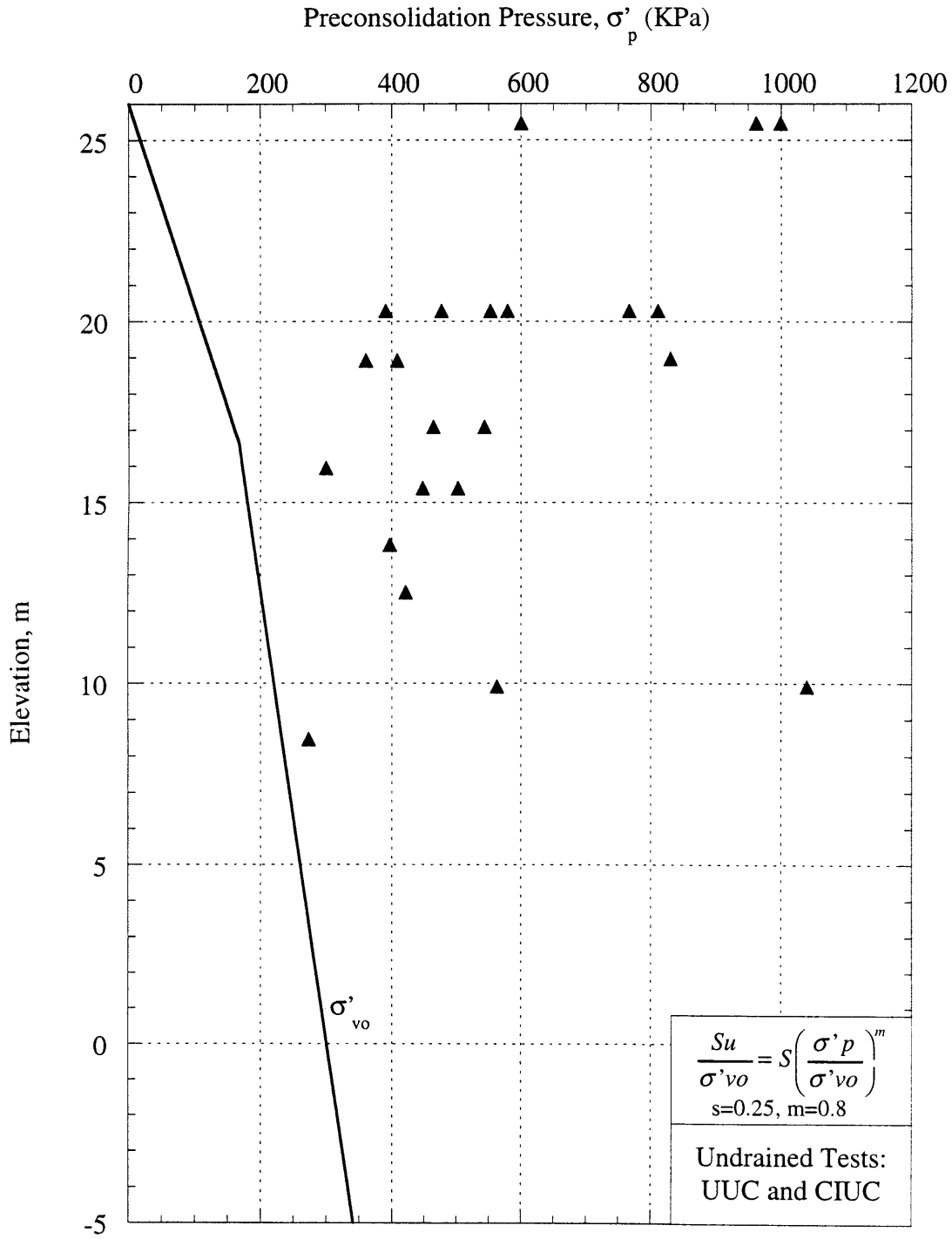

Figure 3.27 Backcalculation of Preconsolidation Pressure for Hato Rey Soils

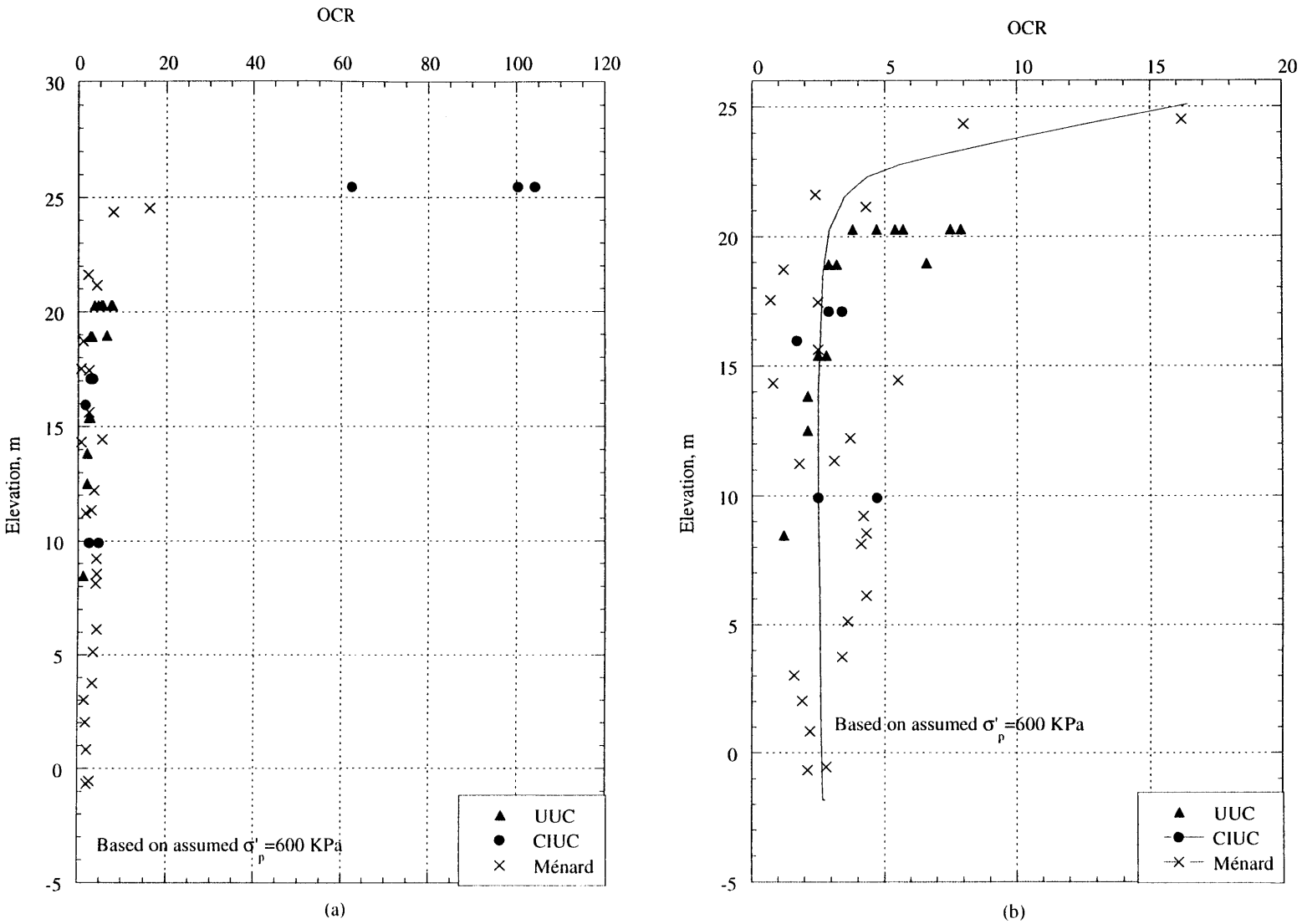

Figure 3.28 Backcalculation of Overconsolidation Ratio, for Hato Rey Clay:

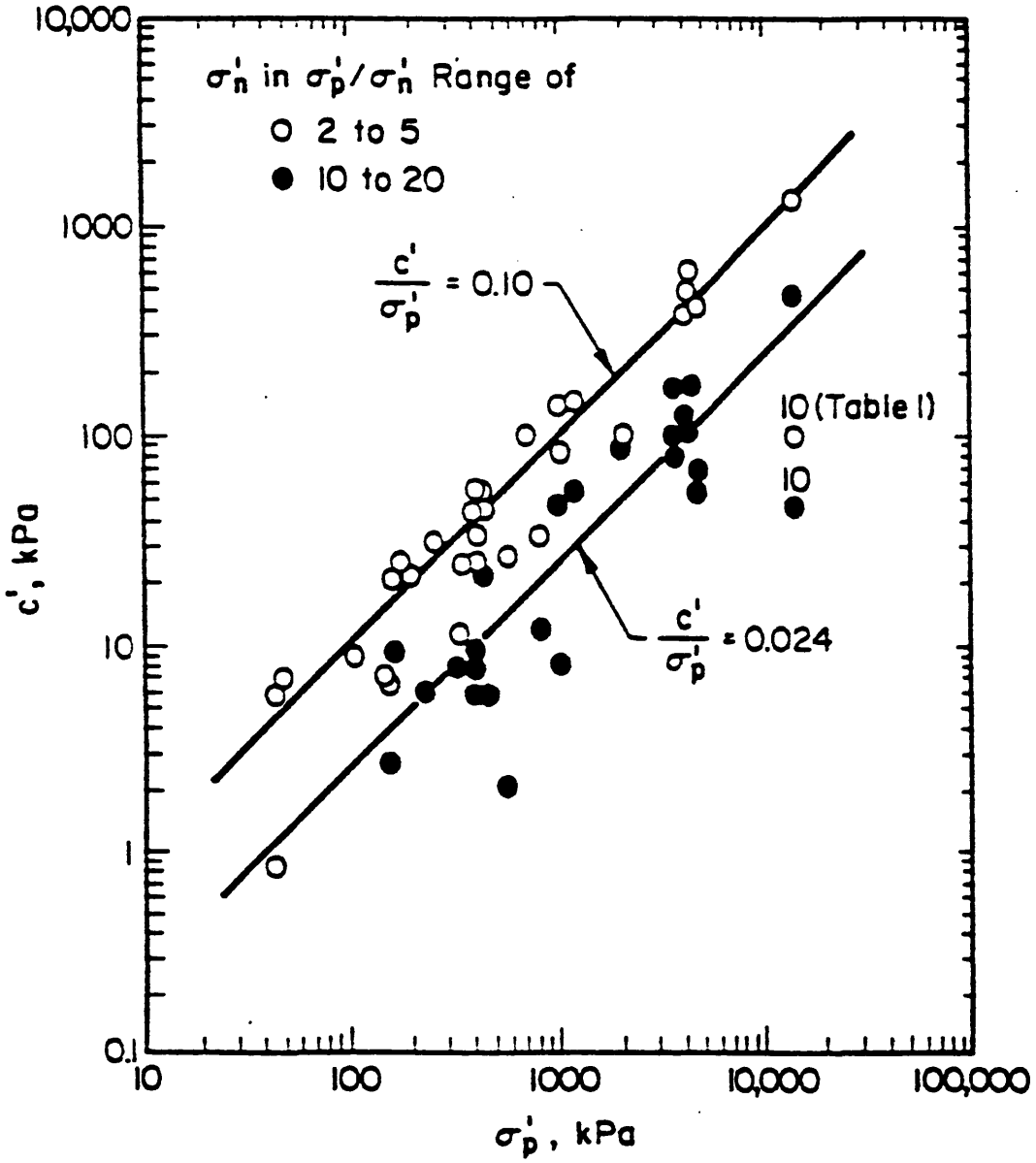

Figure 3.29 Relationship between Cohesion Intercept and Preconsolidation Pressure (Mesri and Adel-Ghaffar, 1993)

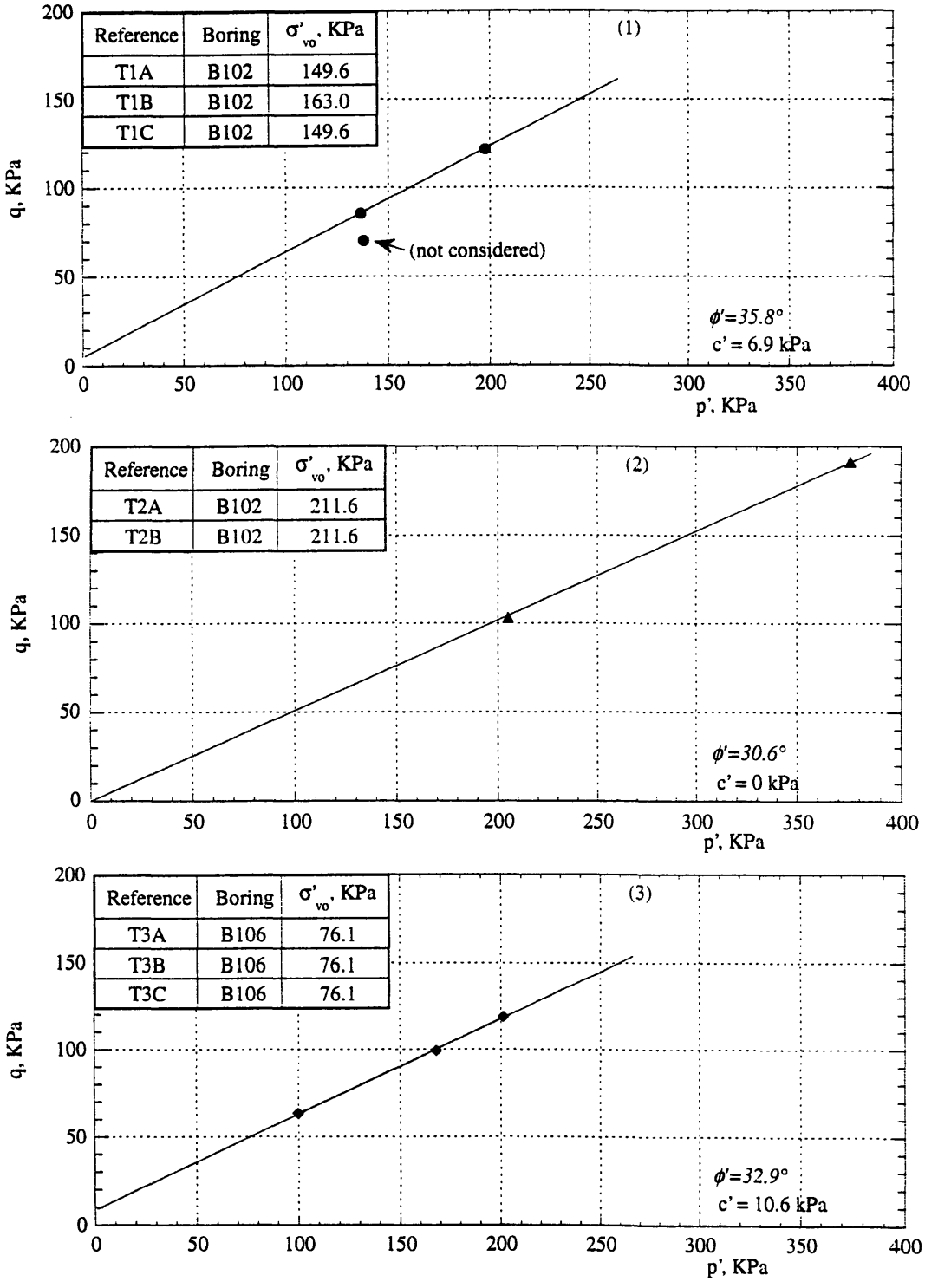

Figure 3.30a Estimation of Friction Angle for Mohr-Coulomb Failure Criterion

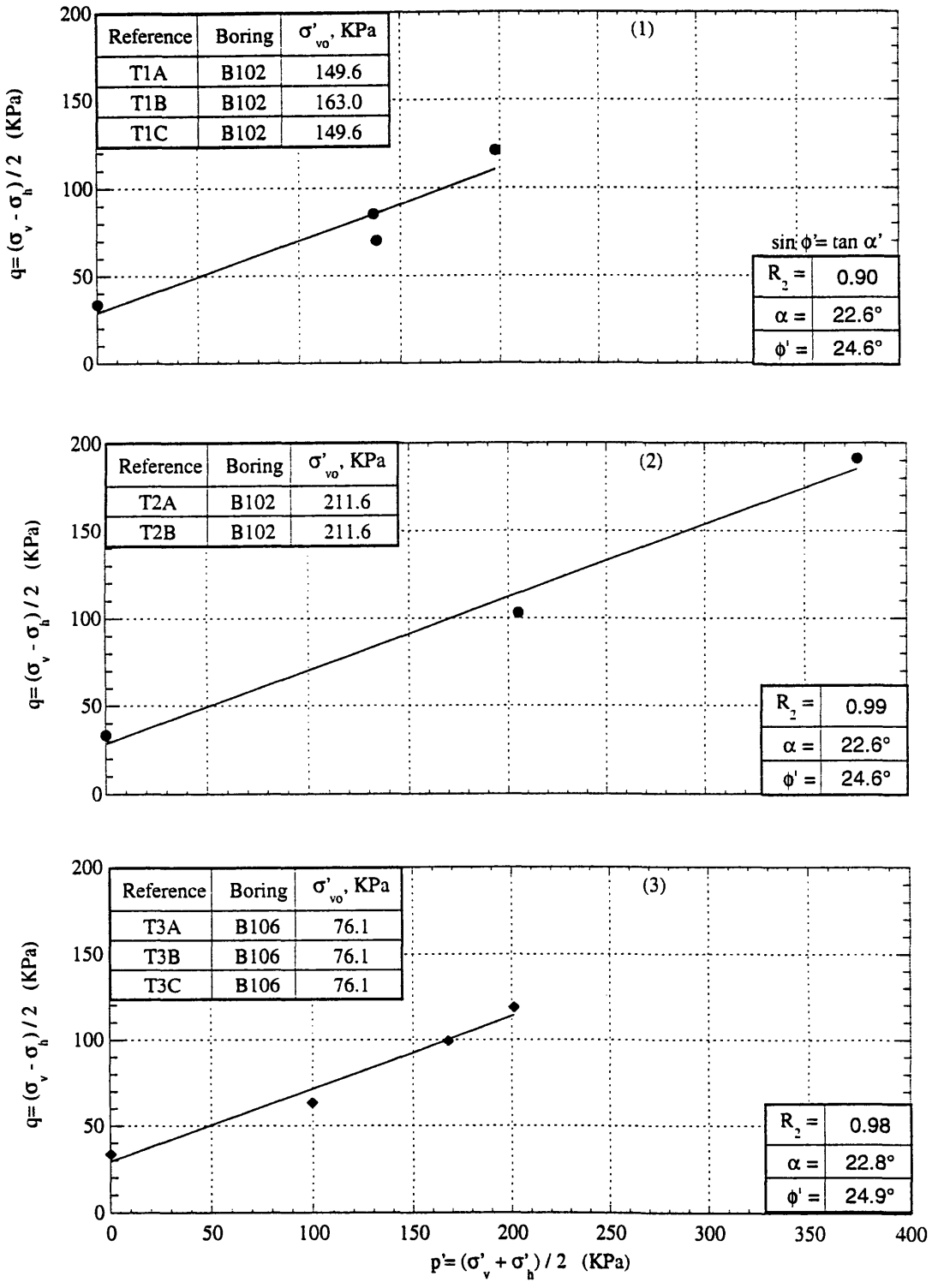

Figure 3.30b Estimation of Friction Angle for Mohr-Coulomb Failure Criterion

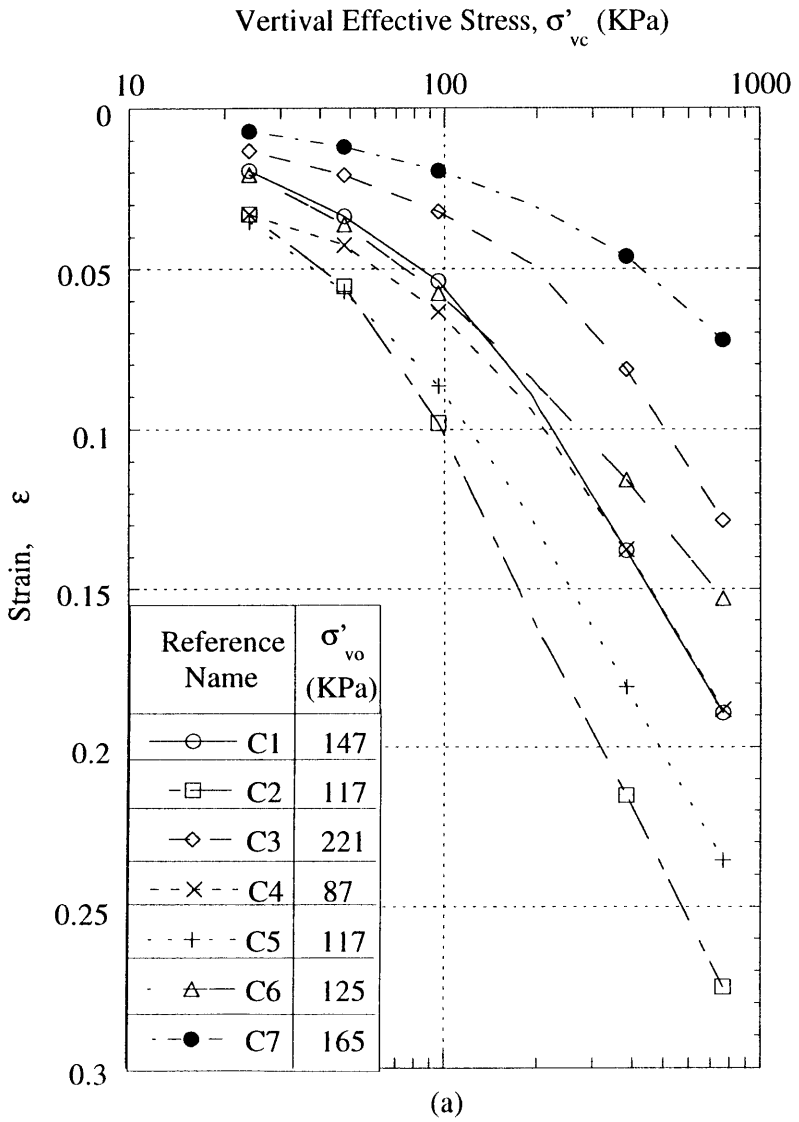

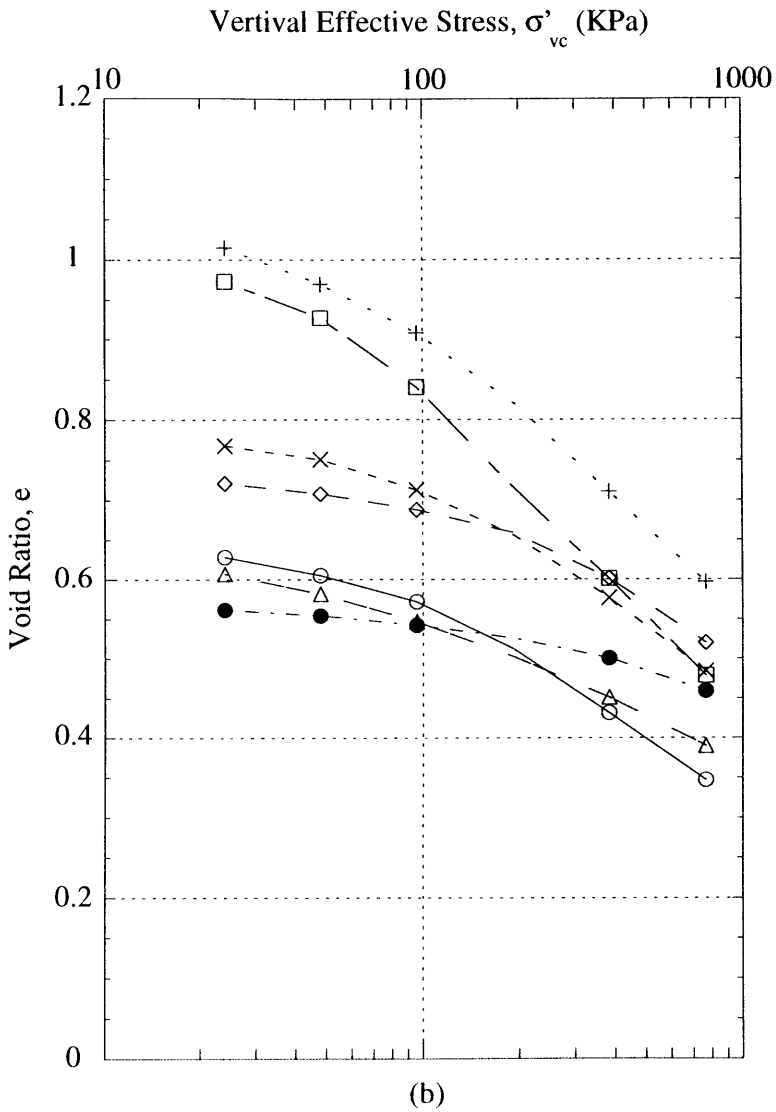

Figure 3.31 Consolidation Curves

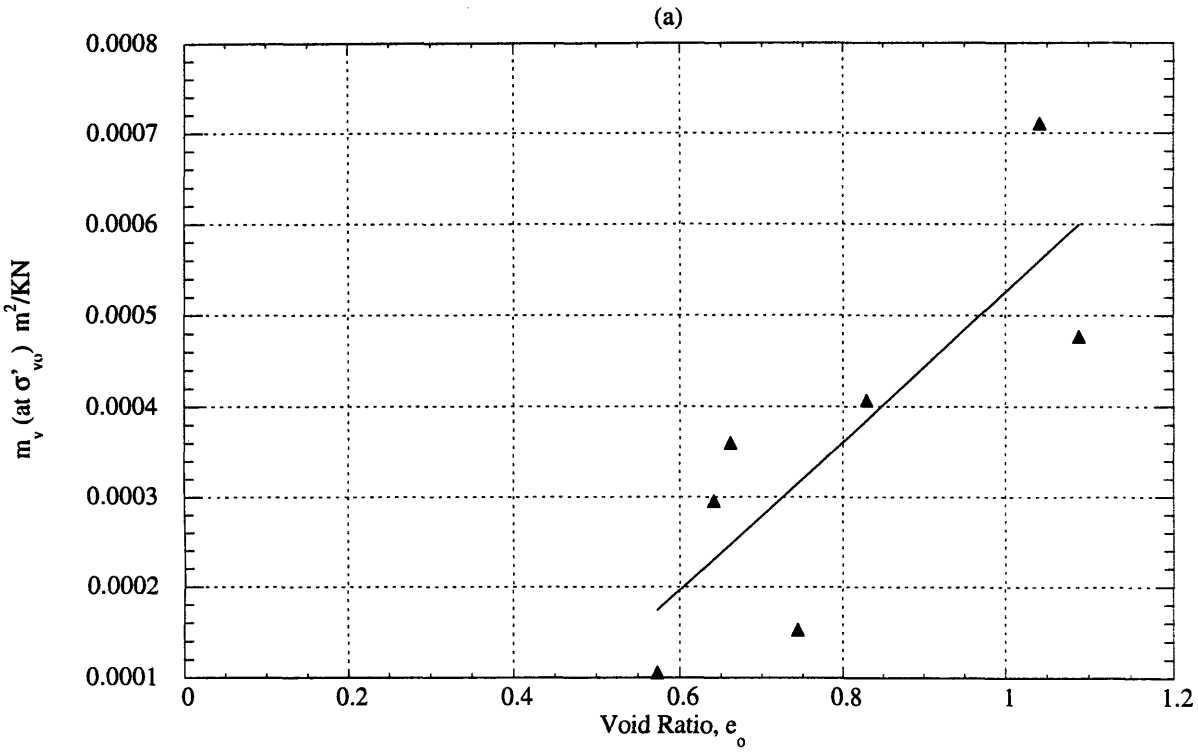

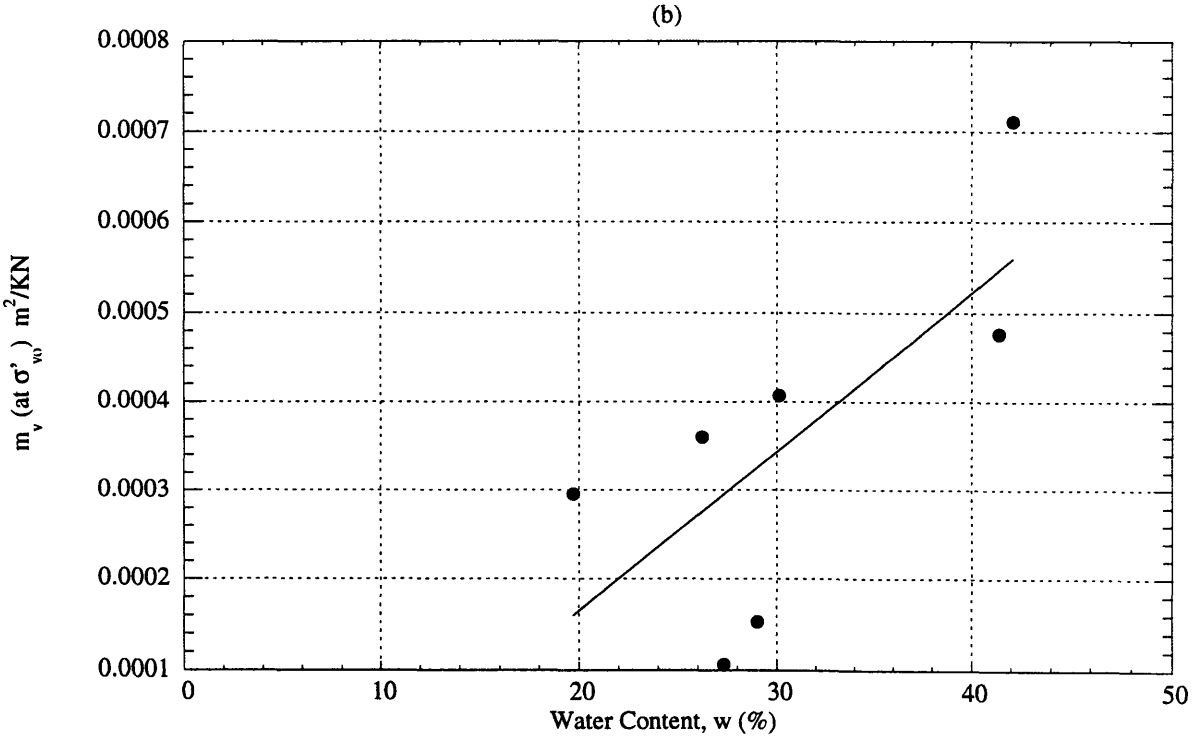

Figure 3.32 Compression as a function of Water Content (w) and Void Ratio (e_o)

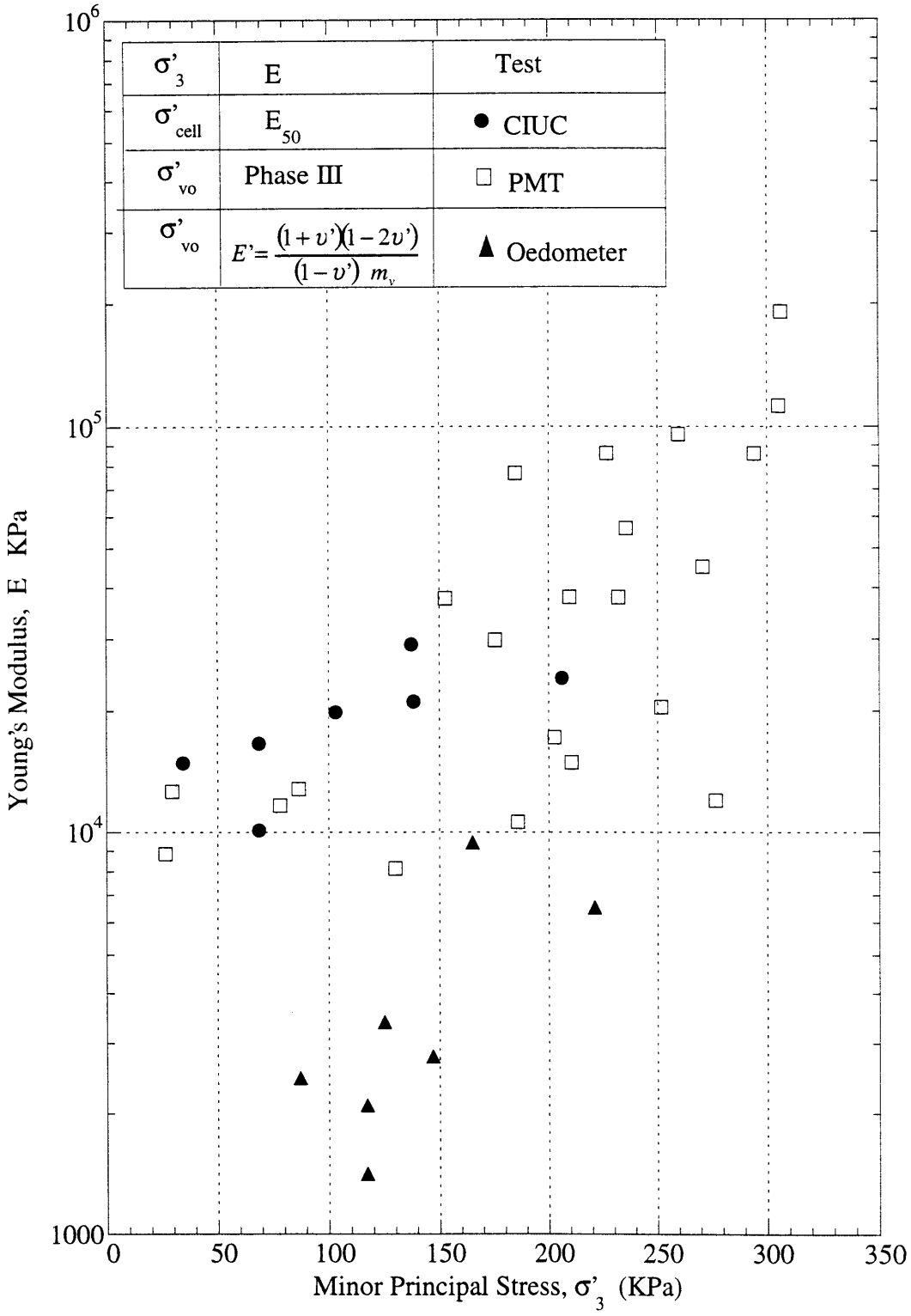

Figure 3.33 Young's Modulus from CIUC, Menard Pressuremeter and Oedometer

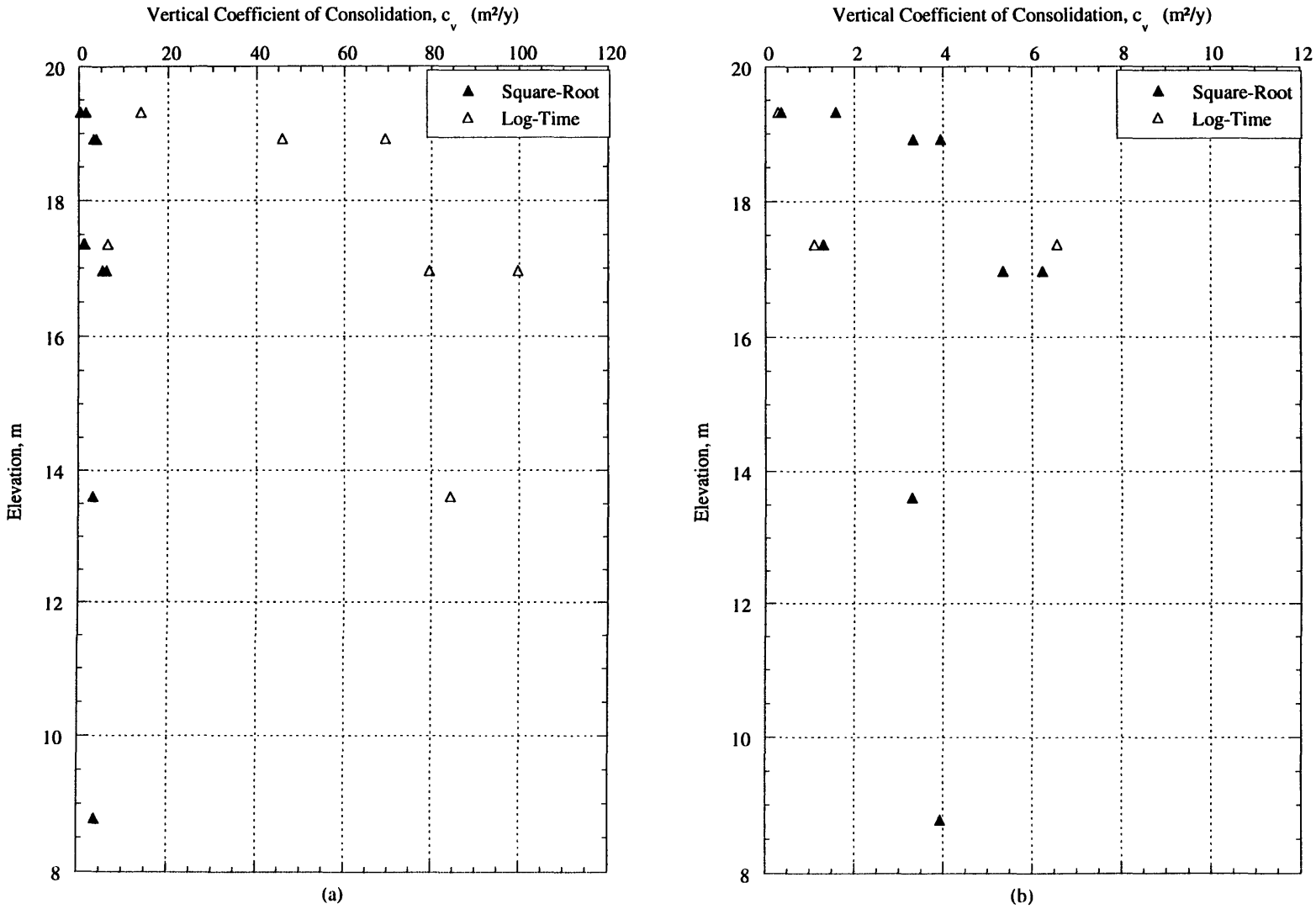

Figure 3.34 Vertical Coefficient of Consolidation (c_v) Profile

4. Finite Element model for Río Piedras Excavation

4.1 Introduction

This chapter describes the development of a finite element model for simulating the performance of braced excavations within typical Hato Rey soil conditions expected in the vicinity of the Río Piedras Station. Development of the model focuses mainly on the representation of soil behavior in the finite element analysis through selection of input parameters for simplified elasto-plastic models. Complete predictions of wall deflections and ground movements are presented for an idealized braced excavation whose dimensions approximate the cut-and-cover sections at the north and south approaches to the Río Piedras Station. The predictions are evaluated through comparisons with empirical data for excavation in similar stiff soil conditions.

4.2 The Hard Soil (HS) Model

Calculations of ground movements were accomplished using the PLAXIS[1] program, which models concurrently the deformation of the soil and flow of groundwater, and hence, can simulate the effects of partial drainage during construction.

Due to the lack of laboratory test data from which to estimate material properties, a simple elasto-plastic model, referred to as the 'Hard Soil' (HS) Model, is used to describe soil behavior (a sophisticated soil model is only appropriate when high quality input data are available). The HS model provides a simple framework for characterizing the behavior of almost incompressible soils like sand, gravel, and heavily overconsolidated (stiff) cohesive soils.

[1] A commercially available PC based non-linear finite element program supplied by A.A. Balkema, Rotterdam, Netherlands.

Shear stress-strain properties are based on the well known Duncan-Chang model (Duncan and Chang, 1970), but HS also includes formal definitions of loading based on plasticity theory. The basic characteristics of the HS model and their relevance to the Río Piedras conditions are as follows:

1. Stiffness is a non-linear (power law) function of confining pressure. This enables the model to describe stiffness variations with depth in a single soil unit.

2. Hyperbolic relationship between shear strain and deviatoric stress. This attribute more reliable predictions of ground movement distribution around excavations, compared to linear elastic models.

3. Distinction between primary deviatoric loading and unloading/reloading. This is essential for excavation problems where parts of the soil mass unloads while other regions undergo loading.

4. Failure is described by the Mohr-Coulomb criterion. This is the simplest representation of shear strength for a cohesive-frictional material.

As discussed in chapter 3, the Río Piedras Station area consists of erratic layers of overconsolidated clays, silts, sands, and sandy clays, which are not horizontally connected continuously. In order to conduct the numerical calculations, an averaged soil profile is needed. As a consequence, a profile consisting of one layer of overconsolidated material is used as a simplified solution.

4.2.1 Summary of Formulation

One of the most important characteristics of the HS Model is the hyperbolic relationship between the vertical strain, ε_1, and the deviatoric stress, q, in primary triaxial loading (Duncan & Chang, 1970):

$$\varepsilon_1 = \frac{1}{E_i}\left[\frac{q}{1-q/q_a}\right] \qquad \text{for } q<q_f \qquad (4.1)$$

This relationship is presented in Figure 4.1, where the parameter E_i is the initial Young's modulus for primary loading, and can be obtained from the following expression:

$$E_i = E_i^{ref}\left(\frac{c'\cot\varphi' - \sigma'_3}{p^{ref}}\right)^m \qquad (4.2)$$

Where:

1. E_i^{ref} is a reference Young's modulus corresponding to a reference pressure, p_{ref}
2. σ'_3 is the minor principal stress, which is the confining pressure in a triaxial test.
3. m is a constant exponent that determines the variation of stiffness with confining pressure. For stiff clays PLAXIS (1997) recommends a default value, m=0.5.

For unloading and reloading stress paths, the stiffness is linear with secant modulus, E_{ur}, given by:

$$E_{ur} = E_{ur}^{ref}\left(\frac{c'\cot\phi' - \sigma'_3}{p^{ref}}\right)^m \qquad (4.3)$$

where E_{ur}^{ref} is the reloading modulus at a reference pressure p_{ref}. The Plaxis manual recommends a default value, $E_{ur}^{ref} = 4E_{50}^{ref}$, where E_{50}^{ref} is the secant modulus in first loading at $q/q_f=0.5$.

4.2.2 Input Parameters for Hato Rey Soils

A list is given below of the material parameters used by the Hard Soil model (values in brackets correspond to recommended values):

1. c', drained cohesion
2. φ', drained angle of internal friction
3. Ψ, dilatancy angle (for stress states at failure)
4. E_{50}^{ref}, Secant Young's Modulus for primary loading at $q/q_f = 0.5$.
5. ν_{ur}, Poisson's ratio for unloading/reloading ($\nu_{ur} \approx 0.1$)
6. E_{ur}^{ref}, Unloading/reloading Young's Modulus ($E_{ur}^{ref} \approx 4E_{50}^{ref}$)
7. m, exponent controlling pressure dependency of stiffness ($m \approx 0.5$)
8. R_f, is the failure ratio which relates the asymptotic limit of the hyperbolic stress-strain law q_a and the maximum shear stress, q_f defined by Mohr-Coulomb ($R_f = q_f/q_a \approx 0.9$)

Table 4.1 summarizes the 7 input parameters selected for the HS model to represent the Hato Rey soils at Río Piedras:

1. Cohesion (drained), c': Due to the lack of tests, the cohesion intercept, c', was estimated based on correlations relating c' to σ'_p, the pre-consolidation pressure (Mesri&Adel-Ghaffar,1993), shown in Figure 4.2. As there is no reliable pre-consolidation pressure data for the Hato Rey soils, an approximate value is estimated indirectly from lab. measurements of undrained shear strength, using the SHANSEP[2] equation (after Ladd and Foott, 1974):

$$\frac{s_u}{\sigma'_{vo}} = S\left(\frac{\sigma'_p}{\sigma'_{vo}}\right)^m \qquad (4.4)$$

[2] Stress History And Normalized Soil Engineering Properties

where s_u is the undrained strength and σ'_{vo} is the in situ, vertical effective stress. Typical values of the constants, S = 0.22±0.03, and m = 0.8±0.1. Figure 4.3 shows the values of σ'_p computed from CIUC, UU and Ménard pressuremeter strength measurements using average values (S=0.25 and m=0.8). There is large scatter in the data and no well defined trend with depth. For the selected σ'_p, the correlations of Mesri and Adel-Ghaffar (Figure 4.2) bound the drained cohesion, $16 \leq c' \leq 60$ KPa. The average from the two estimates, c'= 40 Kpa was selected for the Río Piedras analysis.

2. The drained angle, φ' is estimated from the CIUC triaxial data, together with the empirical estimate of cohesion, c'= 40 kPa. Figure 4.4 shows the linear correlations used to estimate ϕ' from three sets of CIU triaxial tests. Linear regression analyses give ϕ'= 24.6° - 24.9°, with regression coefficients R^2= 0.90- 0.99. An average value ϕ'=24.6° is used in the finite element model.

3. Dilatancy angle, Ψ

   Figure 4.5 compares CIU measurements from one test with, σ'_3 = 100 kPa (Test T2A) with single element simulations of undrained shearing using the HS model, with Ψ = 0°- 3°. Figure 4.5b shows that the measured stress-strain shear response can be well described by the HS model with Ψ = 3°. However, there are large discrepancies between the computed and measured effective stress paths (for all 4 values). This result reflects limitations of the HS model in characterizing shear induced pore pressures at small strains.

4. The primary loading stiffness (secant) parameter, E_{50}^{ref}, is estimated by comparing results from CIUC tests, Ménard Pressuremeter (MPM) tests, and Oedometer data (Section 3.5.5). Figure 4.6 shows linear correlations through each of these data sets as function of the

confining pressure. Assuming a reference pressure p_{ref} = 100 kPa, the parameter E_{50}^{ref} = 20 MPa[3] is well defined from both CIU and MPM data sets.

5. Unloading/reloading Poisson's ratio , ν_{ur}

   Figure 4.7 compares the computed and measured CIU (T2A) shear behavior at a cell pressure, σ'_3 = 100 KPa using ν_{ur} = 0.1, 0.2, 0.25.

   The best approximation of the laboratory results was accomplished with a Poisson's ratio of 0.1.

6. Unloading/reloading stiffness , E_{ur}^{ref}

   Figure 4.8 compares the triaxial results at σ'_3= 100 kPa (Test T2A) with the single element calculations using the HS model and $E_{ur}^{ref}/E_{50}^{ref}$= 2, 3, 4 and 6. A ratio $E_{ur}^{ref}/E_{50}^{ref}$= 2 provides the best match to the measured stress-strain behavior and also significantly improves the prediction of the effective stress path.

7. Power stiffness law, m

   The Plaxis manual recommends a default value, m= 0.5 for overconsolidated, stiff clays. This parameter can also be estimated from laboratory triaxial tests as follows:

   The non-linear stiffness function for the Hard Soil model is given by

$$E_{50} = E_{50}^{ref}\left(\frac{\sigma'_3 + c'\cot\phi'}{p'_{ref} + c'\cot\phi'}\right)^m \qquad (4.5)$$

   when $\sigma'_3 = p'_{ref}$, then $E_{50} = E_{50}^{ref}$. Hence, by taking logs on both sides of this equation we can also get:

$$\log\left(\frac{E_{50}}{E_{50}^{ref}}\right) = m\log\left(\frac{\sigma'_3 + c'\cot\phi'}{p'_{ref} + c'\cot\phi'}\right). \qquad (4.6)$$

[3] Results from the Oedometer tests were not considered due to the reasons already explained in section 3.5.4.

Hence, m can be computed directly from the triaxial test data as shown in Figure 4.9. The linear correlation in this case gives m= 0.86, but with a relatively low regression coefficient R^2= 0.735. Figure 4.10 compares the computed and measured values of E_{50} as functions of confining pressure σ'_3 for m= 0.5 and 0.86. Given the large scatter in the measured data there is little to support the selection of either value of m. Hence, m= 0.5 is used in all subsequent calculations.

8. The Failure ratio, R_f = 0.9 is used in accordance with Plaxis recommendations.

Using the input parameters listed on Table 4.1, single element calculations were performed using the following cell pressures: 50, 75, 100, 150, 200 and 300 kPa. A comparison of the single element calculations and all the triaxial tests (T1a through T3C) is shown in Figure 4.11. In general, there are more similarities between the shear stress-strain paths than the effective stress paths. However, this similarity only occurs at low axial strain levels ($\varepsilon_a < 5\%$) and the shear stress-strain paths become very different as the axial strain increases ($\varepsilon_a > 5\%$)[4].

4.3 Idealized Braced Excavation

Figure 4.12 summarizes the initial conditions considered in the finite element model. The Río Piedras site has a level ground surface. The groundwater table is located at a depth of 10m, and initial pore pressures are assumed hydrostatic. The analysis uses saturated unit weight of 17.84 kN/m^3, both, above and below the water table, as Plaxis does not consider the capillary stresses above the water table. The analyses recognize that hydrostatic conductivity represents one of the least certain properties at the site and hence, the base case analysis assumes k = 3×10^{-3} cm/sec (2.6m/day), corresponding to the maximum expected permeability at the site.

[4] For finite element excavation calculations, characteristic shear strain levels are expected to be less than 5%.

The idealized geometry comprises a plane strain excavation with half width, B/2 = 11 m, (similar to that expected at Río Piedras Station approaches), and is supported by a 0.9 m thick diaphragm wall. The analysis assumes that the reinforced concrete diaphragm wall has elastic properties (Table 4.2), and is wished-in-place (i.e., the installation of the wall has no effect on stresses or pore pressures in the surrounding soil). The wall has a total length, L = 33m, such that at the maximum excavation depth, H = 22m, the embedment ratio L/H = 1.5. In order to minimize the effects of the boundaries on predicted ground movements, the finite element mesh extends far from the excavation to a total depth of 100 m and laterally to a distance of 200 m from the centerline. The Plaxis code limits the total number of 15-noded and 6-noded triangular elements that can be solved in a given analysis[5]. Hence the selection of the mesh must be carefully tailored to the proposed excavation sequence. Figure 4.13 shows the mesh (1,739 nodes and 782 6-noded elements) which models an excavation sequence with 2.75m vertical steps. The excavation is braced internally by rigid supports equally spaced at intervals of 2.75m vertically (nominal properties of the supports are given in Table 4.3).

The analyses assume a simplified construction sequence, (Figure 4.14) comprising the following steps: 1) The soil is initially excavated unsupported to a depth h_u= 2.75m; 2) the wall is propped at the surface and excavation proceeds to a depth h equal to 2.75 m; 3) a second level of support is installed at a spacing of 2.75m; and 4) step 3 is repeated until the excavation reaches a total depth H equal to 22 m. At each excavation stage partial drainage can occur over a specified time period related to the total expected construction duration, t= 240 days. The following paragraphs discuss these assumptions in more detail:

1. Plane Strain Model

[5] For 6-noded elements the number of elements in the mesh was restricted by a limitation of the maximum element number available in Plaxis equal to 800 elements.

Although most real excavations have geometries that are three dimensional, the current calculations consider a simplified planar geometry. Plane strain assumptions apply for situations where cross section, soil properties, and loading scheme are approximately uniform over a significant length such that displacements in this direction are assumed to be zero. Plane strain analyses can be a good approximation for linear excavations (such as those for transit lines), but will overestimate movements at the corners of an excavation. This type of analysis gives similar settlements to 3-D analyses but greater horizontal deformations (Hashash, 1992).

2. Material Models

The Hato Rey soils are simulated using HS model, with input parameters described in section 4.1. The diaphragm wall has linear elastic properties and is modeled using two rows of solid (6-noded triangular) elements were used because wall thickness is non-negligible compared to other dimensions in the excavation problem. The wall is non-porous[6] and has a unit weight, γ= 23.6 kN/m^3. A rough interface[7] is assumed in the analyses. This assumption is only significant for excavations approaching collapse (Desai 1988, Bakker and Vermeer, 1986).

3. Initial Conditions

The initial, in-situ state of stress is computed in the program input sub-menu. After entering a coefficient of lateral earth pressure, K_o, for all soil layers Plaxis computes and shows the initial stress state. This stress state is characterized by an initial vertical stress σ'_{vo} and an initial σ'_{ho} which are related by K_o in the following way:

$$\sigma'_{vo} = (\gamma_{ave} \cdot z) - P_i$$
$$\sigma'_{ho} = K_o \cdot \sigma'_{vo} \qquad (4.7)$$

[6] Non-porous elements have only displacements degrees of freedom in Plaxis.
[7] i.e. strength at the interface is identical to the strength of the adjacent soil.

where γ'_{ave} is the average weight above the stress point, z is its depth below the surface and P_i is the initial pore pressure in the stress point. The analyses assume K_o=1, this represents a reasonable average value given the lack of experimental data, erratic layering and geological history of the Hato Rey soils.

4. Groundwater Conditions

Plaxis distinguishes three types of pore pressures states: initial P_i, ultimate P_u and excess P_e. The initial pore pressure state (or initial steady-state pore pressures) represents the pore pressures in the undeformed (initial) situation. The ultimate pore pressure state (or ultimate steady-state pore pressures) may be used to study the influence of lowering or rising water tables on the deformation and stability of the soil body. In general, it can be used to study soil response due to a change from one pore pressure state to another pore pressure state. In this way, the steady state pore pressure, P_s, can be defined by:

$$P_s = P_i + C(P_u - P_i) \qquad (4.8)$$

where C=0 implies that pore pressures are set to the initial level, while C=1, corresponds to ultimate conditions. The distribution of steady-state pore pressures is determined by the boundary conditions, the geometries, and permeabilities of the different soil layers. Both pore pressure distributions are independent of deformations. In contrast, excess pore pressures are caused by deformation itself and represent pore pressures due to undrained soil response and consolidation. The active pore pressures, P_a, are defined as follows:

$$P_a = P_s + P_e \qquad (4.9)$$

The pore pressures can be imposed in two ways: 1) phreatic line input, or 2) groundwater calculations. When pore pressures are entered by means of a phreatic line, the pore pressures at a stress point are simply calculated by multiplying its depth below the phreatic line by the unit

weight of water. For many geotechnical problems, steady-state pore pressures are nearly hydrostatic and it is not necessary to performed detailed pore pressures calculations. Instead, a phreatic surface is specified and the pore pressure is taken to be hydrostatic along vertical lines beneath the phreatic surface. The alternative approach using a groundwater flow module enables any steady state flow field to be imposed. The Plaxis groundwater flow module is needed in order to simulate the lowering of the water table within the excavation. Boundary conditions in these calculations are:

1. Prescribed piezometric head[8], H, referred to as 'open node'.
2. Zero flux ('closed node')

Figure 4.15 indicates the flow boundary conditions used at each stage of the excavation. The Plaxis program assumes P= 0 at the excavated grade in each step of the analysis.

5. Bracing System

The bracing system is modeled as an elastic-plastic spring. One end of the spring is connected to a node in the mesh and the other end is fixed. The input parameters in Table 4.3 correspond to an approximation of an incompressible, non-yielding bracing system.

6. Calculation Sequence

The following calculation steps are performed to simulate the construction sequence of the excavation:

1. Unsupported excavation: A undrained analysis[9] is carried out in which the soil elements at the top of the excavation are removed (switched off). At this stage, the total excavation depth H= 2.75 m.

[8] $H= P/\gamma_w + y$, where y is elevation.
[9] 'plastic calculation'

2. After equilibrating the stresses at H= 2.75m a consolidation[10] analysis is performed, in order to allow for partial drainage. Assuming a total construction time t= 240 days, each stage of excavation is allowed to consolidate for 30 days.
3. Excavation and installation of strut 1 & 2: A plastic calculation is performed to model the excavation of another 2.75 m, so the total excavation reaches a depth of 5.5 m. The first anchor (0m depth) is activated as well as the second anchor (2.75m depth).
4. Consolidation: Same as step 2
5. Excavation and installation of strut 3: A third plastic calculation is performed to model the excavation of another 2.75 m, so the total excavation reaches a depth of 8.25 m. The third anchor (8.25m depth) is activated.
6. Consolidation: Same as step 2
7. Excavation and installation of strut 4: A plastic calculation is performed to model the excavation of another 2.75 m, so the total excavation reaches a depth of 11.0 m. The fourth anchor (11m depth) is activated.
8. Groundwater calculation: The water inside the excavation is lowered 1 m. A flow calculation is carried out to determine the pore pressures for the second groundwater situation. A plastic calculation is done to activate this groundwater situation.
9. Consolidation: Same as step 2
10. Steps 7, 8 and 9 are repeated until the excavation reaches 22m of depth.

[10] The governing equations as used in Plaxis follow Biot's theory

4.4 Results

4.4.1 Base Case Analysis

This section presents results from numerical analyses of the idealized excavation in Río Piedras. Using the base case input parameters listed in Table 4.1, with k = 2.6m/day and E_{ur}^{ref} = 80 MPa ($4E_{50}^{ref}$) as recommended in the Plaxis manual. Figure 4.16 presents the wall displacements for the base case analysis at each stage of excavation as a function of the excavated depth. During the first, unsupported excavation phase, the wall deforms in a cantilever mode with maximum deflections at the top (δ_{wmax} = 4mm). Thereafter, movements are constrained by the rigid bracing system and maximum wall deflections develop below the current grade level (i.e., the wall deforms by bulging below the excavation level). Table 4.6 (Case 1) presents the ratio of maximum wall movements and total excavation depth, δ_{wmax}/H. Maximum lateral wall deflections increase from δ_{wmax}/H = 0.1 - 0.16% at early stages of the excavation to 0.24% (5.2 cm) at H = 22m. Surface settlements around the excavation are of great practical importance in estimating potential damage to surrounding facilities. Figure 4.17 illustrates the settlements at the various excavation stages. The analysis also predicts that the wall itself moves upward by almost 3 cm at the final excavation grade. Maximum ground settlement increase from δ_{vmax}/H = 0.08 - 0.04% at early stages of the excavation to 0.15% at H = 22m (Table 4.7), which is comparable with field data reported in literature. The analyses predict settlements of approximately 45% of the maximum value (Figure 4.17) occurring at locations very far from the excavation (x ≈ 200m). The inward horizontal surface displacements towards the excavation are presented in Figure 4.18. Maximum lateral displacements equal to 80% of maximum surface settlements occur approximately 60m from the wall.

Bending moments in the wall can be estimated by curve fitting the wall deflection profile using power law series (see figures 4.19a - h). After a mathematical expression[11] is obtained by curve-fitting, the bending moments of the wall are calculated using the following equation:

$$M = -y'' EI \qquad (4.10)$$

$$y'' = \frac{\partial^2 y}{\partial x^2} \qquad (4.11)$$

where y is the wall displacements at an elevation x and EI ≈ 1,400 MN m²/m.

Figure 4.20 shows the bending moment distributions for each excavation stage. At H = 22m, maximum moments occur at a depth of approximately 8m (El.+18m) and below the excavated grade at El.+2m, with $M_{max} \cong 700$ kNm/m.

These predicted bending moments are approximately one-third of the plastic moment expected for a heavily reinforced 0.9m thick concrete diaphragm wall (Mp = 2.0MNm/m; Hashash and Whittle, 1992). Therefore it is unlikely that the wall will fail during excavation at Río Piedras.

Figures 4.21, 22, and 23 compare earth and pore water pressures on both the inside and outside faces of the diaphragm wall at the beginning and end of excavation (H = 22m). The effective lateral earth pressures (Figure 4.21), σ'_v, decrease on the excavated side, while σ'_v tend to increase from El.+22m to El.+7.5m. Below El. 7.5m the final vertical effective stresses are lower than the initial vertical effective stresses. The total lateral earth pressures (Figure 4.22) show similar trends than the effective lateral earth pressures. At the end of excavation (H = 22m) the maximum flow velocity at the excavated grade, v = 1.6 m/day. The predicted inflow of water into the excavation[12] is 17.5 m^3/d/m.

[11] $y = m_0 + m_1 * x + \ldots + m_8 * x^8 + m_9 * x^9$; y = wall displacement and x = elevation.
[12] Q = Velocity*Area; Area = B/2*1m.

4.4.2 Effects of individual parameters

A series of parametric analyses were conducted in order to evaluate the effects of individual soil properties on the predicted excavation performance. The following paragraphs investigate of the unloading modulus E_{ur}^{ref}, Poisson's Ratio ν_{ur}, anisotropic hydraulic conductivity and wall embedment length. The undrained analyses are listed numerically in Table 4.4.

4.4.2.1 Effects of Unloading Modulus E_{ur}^{ref}

Figures 4.24 - 4.26 compare predictions for analyses with E_{ur}^{ref} = 40, 120 MPa ($E_{ur}^{ref}/E_{50}^{ref}$ = 2, 6), respectively, with results for the base case parameters. Figure 4.24 shows that the deflected wall mode shapes are similar, however, the unloading stiffness has a major influence on the magnitudes of the initial cantilever deflections (at H = 2.75m). At the final excavation depth, H = 22m, maximum wall deflections occur below the excavated grade (at El.+0m) and range from δ_{wmax} = 4.9 - 5.6cm (15% variation for all three cases). There is large effect of reducing the unload modulus on the predicted vertical movements of the wall for H ≤ 8.25m (Figure 4.25). The Case 2 analysis shows ground surface heave extending throughout the retained soil at H = 8.25m. While results for Case 3 (E_{ur}^{ref} = 120 MPa) predict much smaller wall uplift with heave extending less than 40m. At later stages of the excavation, the effects of E_{ur}^{ref} are relatively small, such that at H = 22m maximum surface settlements range from δ_{vmax} = 3.2 - 3.7cm (the largest settlements occurring for Case2). The unload modulus has a major impact on the far field settlements (at x = 200m) where, δ_v decreases from 1.7cm (Case 3) to 0.7cm in the Case 2 analyses (i.e., more than 59% reduction). On the other hand, there is very limited impact on vertical wall movements when unload stiffness is increased above the base

case value. In all three cases, maximum settlements tend to occur at a lateral distance of 40 to 60 m from the wall. The effects of varying the soil stiffness on horizontal surface displacements are shown on Figures 4.26. By decreasing the unload modulus (Case 2), maximum horizontal displacements are reduced but they also occur further from the excavation (at about 80 m from the wall), while increasing E_{ur}^{ref} (Case 3) has the opposite effect. At H = 22m, the maximum δ_{hmax} range from 2.5cm to 2.7cm and are thus little affected by uncertainties in the unload modulus.

4.4.2.2 Effects of Poisson's Ratio ν_{ur}

Analysis Case 4 assumes a Poisson's ratio, ν_{ur} = 0.25, a value which is more typical of measured effective stress paths in K_o-swelling experiments (Pestana, 1994), than the value (ν_{ur} = 0.1) recommended and used in the base case calculations. Figure 4.27 shows how the wall deflections change with ν_{ur} (Cases 1 and 4). There is no impact on deflections at the early stages of the excavation, however, during the last 4 excavation stages of excavation the maximum movements decrease by about 5%. There is also no effect on the settlement predictions for H $\leq$ 11m, Figure 4.28. However, increases in ν_{ur} are linked to a 13% to 20% reduction in δ_{vmax} at H = 16.5 - 22m. There is also a decrease in wall uplift and in horizontal surface displacements (Figure 4.29) by about 10%.

4.4.2.3 Effects of Permeability Anisotropy

As discussed in Chapter 3, there is a discrepancy in hydraulic conductivity measured in small-scale, slug tests and the large-scale field pumping tests. The base case analysis considers an upper bound estimate of k, which corresponds to the worst case situation in terms of wall

stability and inflow rates. Analysis Case 5 considers the situation where the hydraulic conductivity is anisotropic with $k_h = 10k_v = 2.6$m/d (i.e., $k_v = 0.26$m/day similar to slug test data). Figure 4.30 compares the predicted wall deflections for the base case and Case 5 analyses. There is no effect on maximum wall deflections during the first 5 stages of excavation ($H < 13.5$m). However, for $H \geq 16.5$m, anisotropic flow causes larger subgrade wall movements than the base calculation. At $H = 22$m, Case 5 predicts $\delta_{wmax} = 6.5$cm ($\delta_{wmax}/H = 0.3\%$). In general, anisotropic flow reduces the predicted ground surface settlements (about 50% during the last 5 stages of excavation) however, there is a corresponding increase in predicted uplift of the wall 20% to 70% higher than the base case calculations (Figure 4.31). Figure 4.32 shows a 20% decrease in predicted horizontal surface displacements with anisotropic permeability.

4.4.2.4 Effects of Wall Length

This section considers the effects of increasing the length of the wall from L= 33 to L= 44m (Case 6). Results were compared up to an excavation depth of 19.25m (7 stages of excavation). Figure 4.33 shows that the wall length has very limited impact on the predicted wall defections. Wall length does reduce the maximum surface settlements and all far field settlements by approximately 15%, while the uplift of the wall decreases by 30% (Figure 4.34). Wall length has minimal effects on the horizontal surface displacements (Figure 4.35).

4.4.2.5 Summary of Results

Tables 4.5 - 4.8 summarize movement predictions for the Río Piedras excavation for all cases that were evaluated. Figure 4.36 summarizes the predicted maximum lateral deflection ratio, δ_{wmax}/H as function of the excavation depth for all six analysis cases (Tables 4.1, 4.4). In all

cases, the deflection to depth ratio increases from a minimum δ_{wmax}/H = 0.05 - 0.1% at H = 5m to 0.22% - 0.30% at H = 22m. The minimum wall deformation occurs for Case 2 using a low unload modulus, while the highest value is predicted in Case 5, with anisotropic permeability. Overall, the individual factors considered in these parametric studies have little influence on the predicted wall deflections. Figure 4.37 shows the maximum soil settlements ratios, δ_{vmax}/H as function of the excavation depth for H > 8m, reaching a maximum range δ_{vmax}/H = 0.07 - 0.17% at H = 22m. Contrary to the effect on wall deflections, decreasing soil stiffness increases maximum soil settlements, while increasing the stiffness has no effect on settlements. Anisotropic permeability has a major effect, showing much lower settlement ratios than the other five analyses.

Figure 4.38 compare the uplift ratios of the wall with excavation depth, H. The largest wall uplift is predicted for Case 5, with anisotropic permeability, while the smallest uplift occurs when the embedment of the wall increases (Case 6). It is very important to emphasize the uplift predictions are not very realistic and are a result of the limitations of the Hard Soil model. Further discussion on how these predictions compare with data published in literature is discussed in the next section

4.5 Practical Interpretation of Results

4.5.1 Measured Soil Movements Published in Literature

Semi-empirical design charts provide a useful guide for estimating a likely range of movements, based on ground deformation data collected from specific excavation histories. Clough and O'Rourke (1990) provide a through review of the available techniques for estimating

soil movements including data from excavations supported by diaphragm walls. Figure 4.39[13] shows their summary of maximum wall movements and soil settlements for excavations in stiff clays, residual soils, and sands. The data can be summarized as follows:

1. The horizontal movements tend to average about 0.2% of the excavation depth.
2. The vertical movements tend to average about 0.15% of the excavation depth.
3. No significant correlation was found between maximum movements and different types of wall.

There is a lot of scatter in the data, especially for the more extensive database of wall deflections. Figure 4.40 shows the distributions of soil surface settlements and horizontal displacements for excavation sites in stiff to very hard clays, involving horizontally supported concrete diaphragm and soldier pier walls, and other support systems. The settlements are only a small percentage of excavation depth, ($\delta_{vmax} \leq 0.3\%$), but are distributed over three times the excavation depth from the wall ($d/H \leq 3$). Records of horizontal ground movements are more variable, and show two distinct zones of movement. The majority of the horizontal displacements fall within a triangular boundary with the same dimensions as those pertaining to the settlements. The second zone includes excavations affected by their support systems. In general, the horizontal movements will tend to equal or exceed their vertical counterparts, with an upper bound of 2.5 times the vertical movements.

4.5.2 Comparison between Predicted and Empirical Data

Figure 4.42 compares the predicted maximum lateral wall deflections for the Río Piedras

[13] The cases reported in the charts are due to the basic excavation and support process. Displacements caused by ancillary construction activities were removed.

excavation with the empirical range proposed by O'Rourke and Clough (1990). All six analyses predict $\delta_{wmax}/H = 0.25 \pm 0.3\%$, which is in good agreement with measured data in the literature. Maximum soil settlements (Figure 4.43) also match published data, with an average ratio $\delta_{vmax}/H = 0.13\%$. From Figure 4.40 it can be estimated that the expected maximum settlement for stiff clays suggested by Clough and O'Rourke (1990) is 0.3% H (i.e. for H = 22m, δ_{vmax} = 6.6 cm). For Río Piedras, all finite element analyses settlement results are below 3.7 cm, with an average of 2.8 ± 0.8 cm. These results are also below the allowable maximum settlement specified in the Tren Urbano contract, which is 3.8 cm (Capacete, 1997; Personal Communication).

According to Clough and O'Rourke (1990), maximum horizontal movements are below 0.3% of the excavation depth (i.e. 6.6 cm at H = 22m). The numerical experiments show that horizontal surface movements are 2.5 ± 0.2 cm.

Figure 4.41 compares the distribution of surface settlements and horizontal movements as proposed by Clough and O'Rourke for design purposes. Their recommendations show a triangular distribution with zero settlement at a lateral distance of d = 3H (d = 66m at Río Piedras). The finite element analyses predict maximum ground settlements and horizontal surface movements at d = 40 to 60m (1.8H - 2.7H) from the wall. At boundaries far from the excavation, 200m (9 H), significant amount of settlement develops. Figure 4.44 show the predicted heave inside the excavation for Río Piedras. Although, significant heave is to be expected at the base of an excavation in this type of stiff soil, the amounts of heave estimated represent an upper bound.

In general, it seems that the finite element results give reasonable estimates of wall deflections, ground settlements and horizontal surface movements. However, the distribution of the settlements and horizontal surface movements tend to be unrealistic. A more realistic

distribution of deformations can be obtained by improving the modeling of soil behavior (Whittle and Hashash, 1994). Though the role of the constitutive model is very important, the use of a more sophisticated soil model is only justified when high quality input data are available. This is why more refined and sophisticated laboratory tests are highly recommended if more reliable predictions are needed.

Table 4.1 Hard Soil model parameters

Input Parameter	Hato Rey Formation	Base Case Analysis
Cohesion, c'	40 kPa	40 kPa
Angle of Internal Friction, φ'	24.6°	24.6°
Dilatancy, ψ	3°	3°
Primary Loading Stiffness, E_{50}^{ref}	20,000 kPa	20 MPa
Unloading/Reloading Poisson's Ratio, ν_{ur}	0.1	0.1
Unloading/Reloading E_{ur}^{ref}	40,000 kPa[1]	80 MPa[2]
Power Stiffness Law, m	0.5	0.5
Failure Ratio, R_f	0.9	0.9
Hydraulic Conductivity, k	k = 0.26 - 2.6 m/d,	$k_h = k_v = 2.6$m/d

Table 4.2 Diaphragm Wall Parameters[3]

Input Parameter	Diaphragm Wall
Young's Modulus, E	2.3×10^7 KPa
Poisson's Ratio, ν	0.1
Total Unit Weight, γ_t	23.6 KN/m^3

Table 4.3 Anchors Parameters

Input Parameter	Fixed-end Anchors
Stiffness, K[4]	1.15×10^8 KN
Ultimate Force	1,000 KN/m

[1] E_{ur}^{ref} recommended in Plaxis version 6.31 is equal to 4 E_{50}^{ref}=80,000 KPa

[2] E_{ur}^{ref} recommended in Plaxis version 6.31 is equal to 4 E_{50}^{ref}=80,000 KPa

[3] Material Model: elastic and Type of material: non-porous

[4] $K = \frac{EA}{L \cdot D}$ where: L= effective Length=B/2; and D= distance between struts

Table 4.4 Parametric Study

Case	Parameter Change
1	Base case, table 4.1
2	E_{ur}^{ref} = 40 MPa
3	E_{ur}^{ref} = 120 MPa
4	ν_{ur} = 0.25
5	k_h= 10k_v; k_v = 0.26m/day
6	L = 44m

Table 4.5 Ground Movement Predictions for Río Piedras Excavation at H = 22m[5]

Case	δ_{vmax}, mm	δ_{wmax}, mm	δ_{hmax},[6] mm	H, m	Uplift, m	Heave, m	δ_{vmax}/H, %	δ_{wmax}/H, %	Uplift/H, %	Heave/H, %
Case 1	33.1	52.2	26	22	27.9	166	0.15	0.24	0.13	0.75
Case 2	37.2	48.8	25	22	18.7	199	0.17	0.22	0.09	0.90
Case 3	32.1	56.1	27	22	31.5	162	0.15	0.26	0.14	0.74
Case 4	27.5	49.6	23	22	27.3	141	0.13	0.23	0.12	0.64
Case 5	16.4	65	22	22	50.9	458	0.07	0.30	0.23	2.08
Case 6	21.3	42	19	19.25	21		0.11	0.22	0.11	

[5] Except Case 6, which is at H = 19.25m
[6] Maximum horizontal surface displacements

Table 4.6 Comparisons of Wall Deflections δ_{wmax}/H, (%) at Each Excavation Step

Excavation Depth, m	Case 1	Case 2	Case 3	Case 4	Case 5	Case 6
(1) 2.75	0.160	0.080	0.160	0.160	0.160	0.240
(2) 5.50	0.120	0.040	0.120	0.120	0.120	0.120
(3) 8.25	0.107	0.080	0.133	0.107	0.107	0.107
(4) 11.0	0.140	0.100	0.140	0.140	0.140	0.140
(5) 13.75	0.176	0.128	0.176	0.160	0.176	0.176
(6) 16.50	0.200	0.160	0.200	0.187	0.200	0.200
(7) 19.25	0.217	0.194	0.229	0.206	0.240	0.229
(8) 22.0	0.240	0.220	0.260	0.230	0.300	

Table 4.7 Comparisons of Ground Settlements δ_{vmax}/H, (%) at Each Excavation Step

Excavation Depth, m	Case 1	Case 2	Case 3	Case 4	Case 5	Case 6
(1) 2.75	0.080	0.000	0.080	0.080	0.080	0.080
(2) 5.50	0.040	0.000	0.040	0.040	0.040	0.040
(3) 8.25	0.027	0.000	0.027	0.027	0.027	0.027
(4) 11.0	0.040	0.020	0.060	0.040	0.020	0.040
(5) 13.75	0.080	0.064	0.080	0.064	0.032	0.064
(6) 16.50	0.107	0.107	0.107	0.093	0.040	0.093
(7) 19.25	0.126	0.137	0.126	0.103	0.057	0.114
(8 22.0	0.150	0.170	0.150	0.130	0.070	

Table 4.8 Comparisons of Uplift $\delta_{uplift\ max}/H$, (%) at Each Excavation Step

Excavation Depth, m	Case 1	Case 2	Case 3	Case 4	Case 5	Case 6
(1) 2.75	0.080	0.080	0.080	0.080	0.080	0.000
(2) 5.50	0.160	0.240	0.120	0.120	0.160	0.080
(3) 8.25	0.187	0.267	0.160	0.160	0.187	0.107
(4) 11.0	0.180	0.240	0.180	0.160	0.220	0.120
(5) 13.75	0.176	0.192	0.176	0.160	0.224	0.112
(6) 16.50	0.160	0.160	0.173	0.147	0.227	0.107
(7) 19.25	0.149	0.126	0.160	0.137	0.240	0.114
(8) 22.0	0.130	0.090	0.140	0.120	0.230	

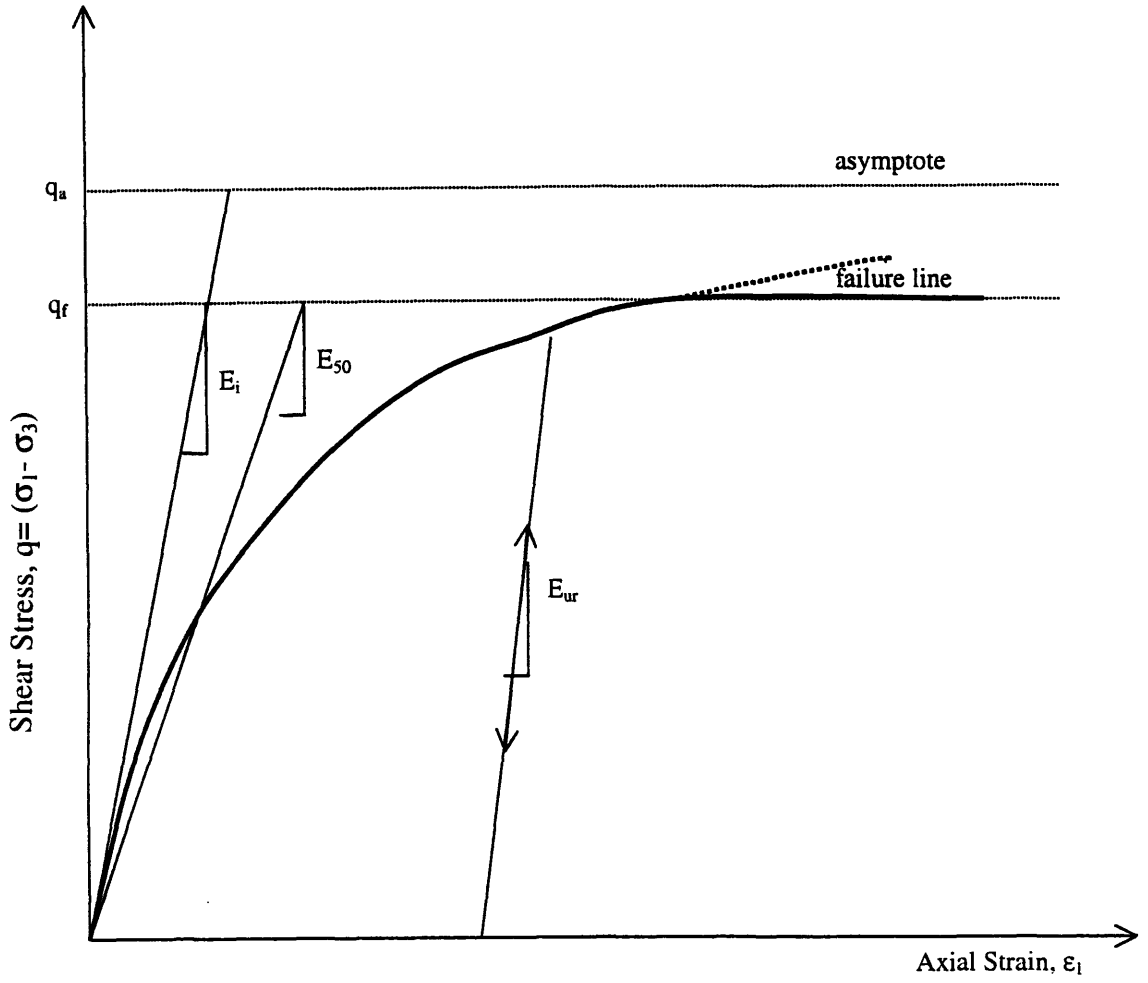

$$q_f = (c'\cot\varphi' - \sigma'_3)\frac{2\sin\phi'}{1-\sin\phi'}$$

$$q_a = \frac{q_f}{R_f}$$

Where:

- q_f is the ultimate deviatoric stress, which is derived from the Mohr-coulomb failure criterion. As soon as $q=q_f$, the failure criterion is satisfied and perfectly plastic yielding occurs according to the Mohr-Coulomb model.
- R_f is the failure ratio ($R_f \leq 1$).
- c' is the cohesion
- φ' is the drained angle of internal friction

Figure 4.1 Hyperbolic stress-strain relation in primary loading for a standard drained triaxial test

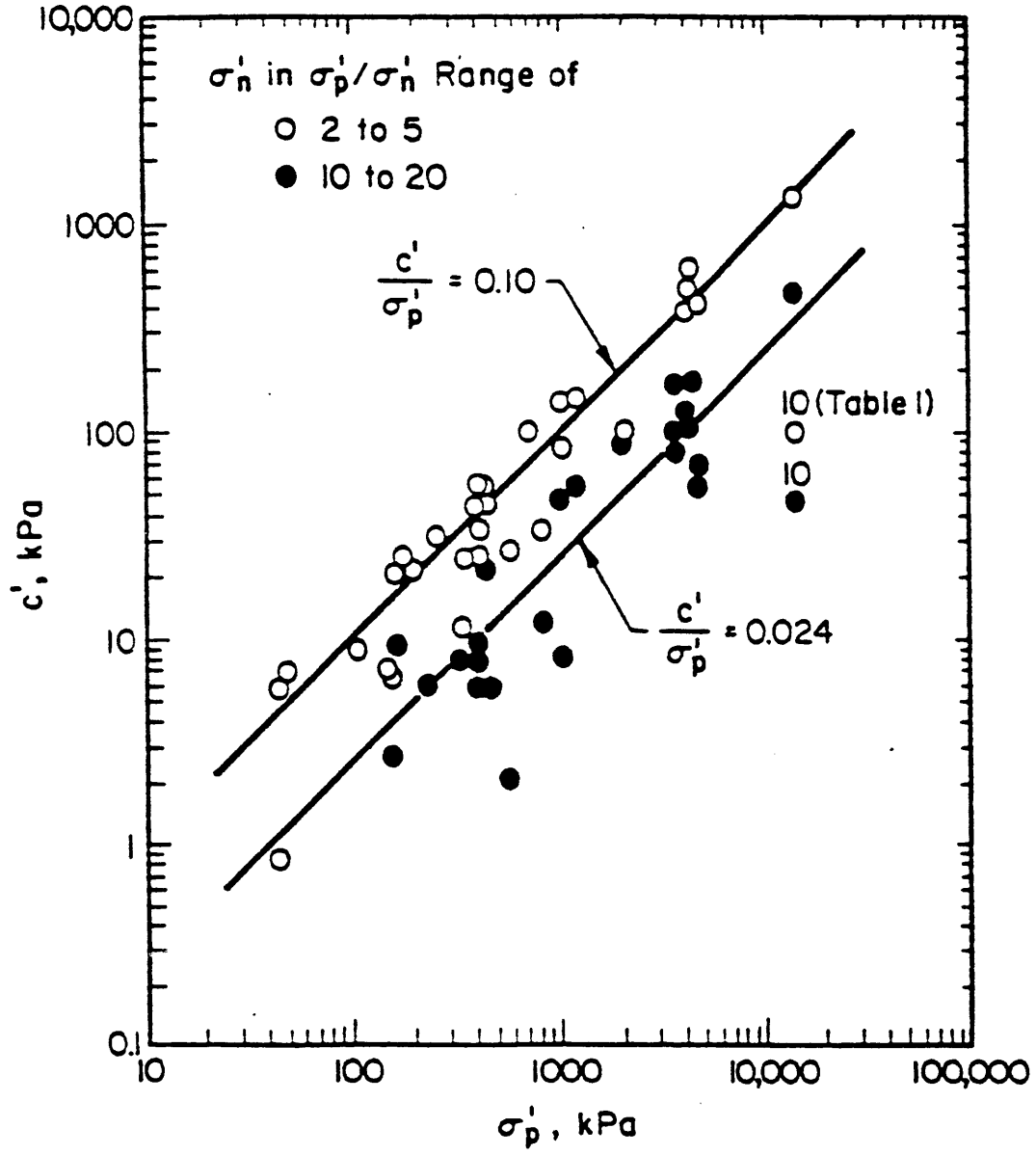

σ'_p = 600 kPa
16 kPa ≤ c' ≤ 60 kPa
c' (average) = 40 kPa

Figure 4.2 Relationship between Cohesion Intercept and Preconsolidation Pressure (Mesri & Adel-Ghaffar, 1993)

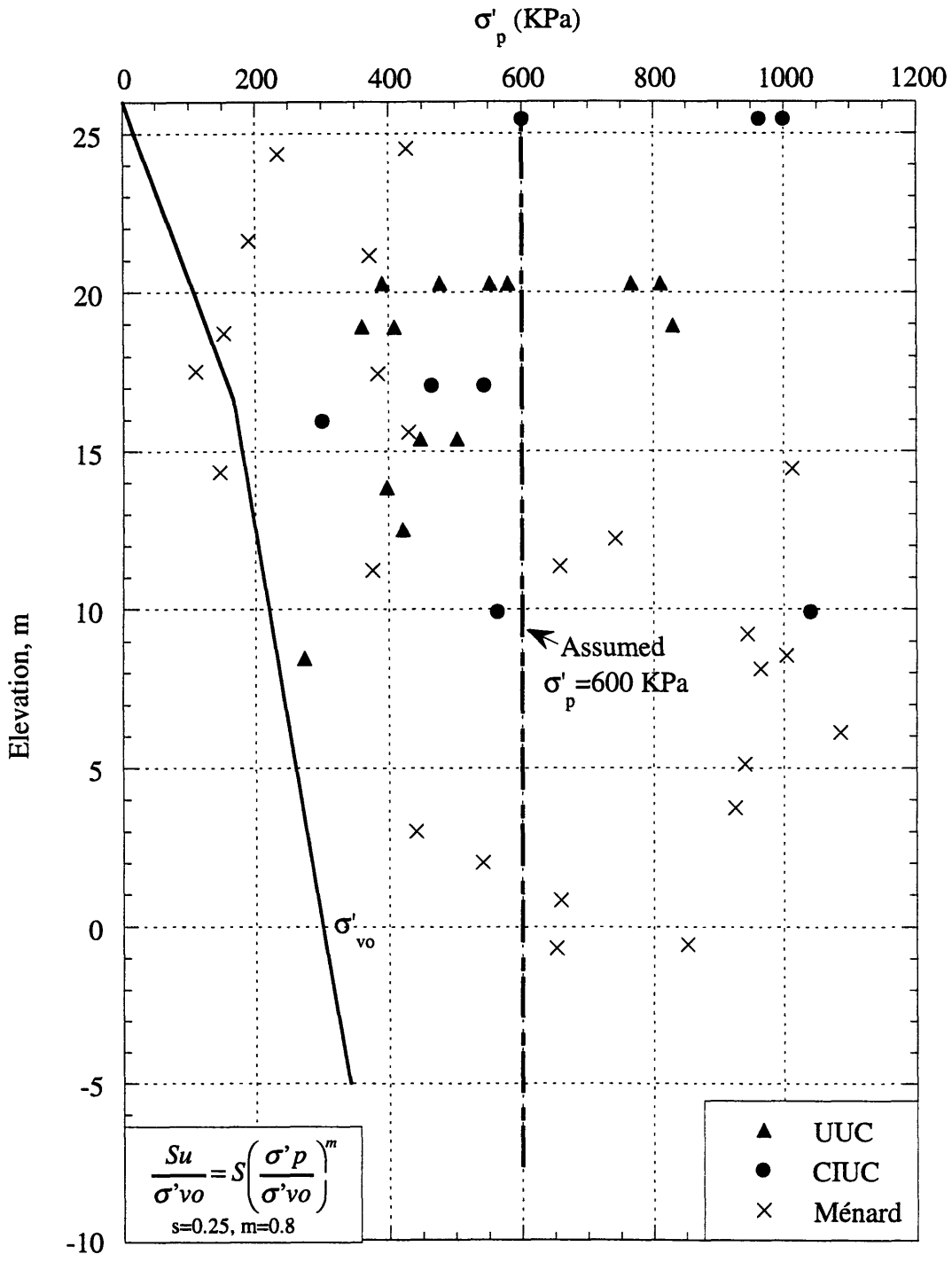

Figure 4.3a Estimation of Stress History for Hato Rey Clays

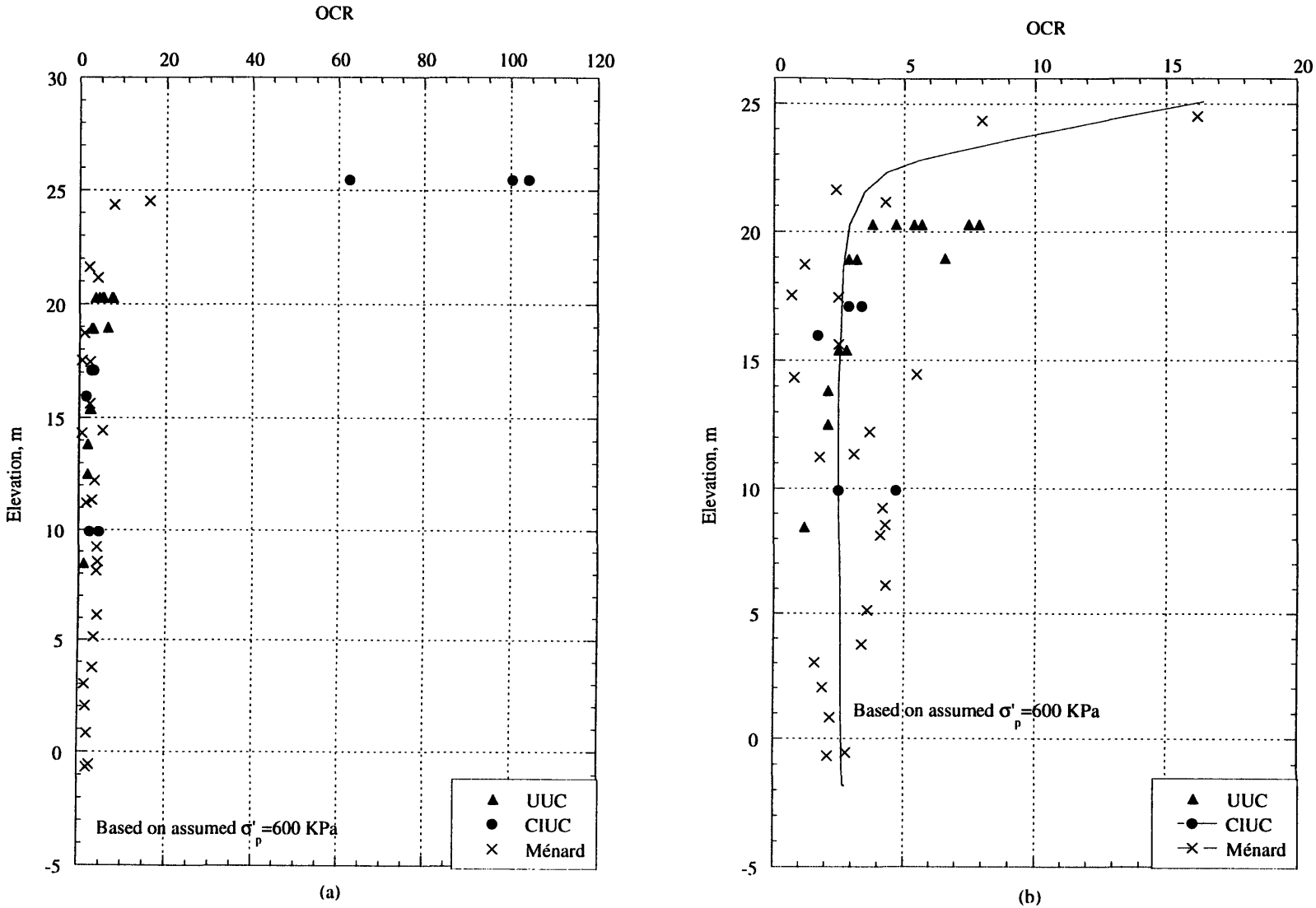

Figure 4.3b Estimation of Stress History for Hato Rey Clays

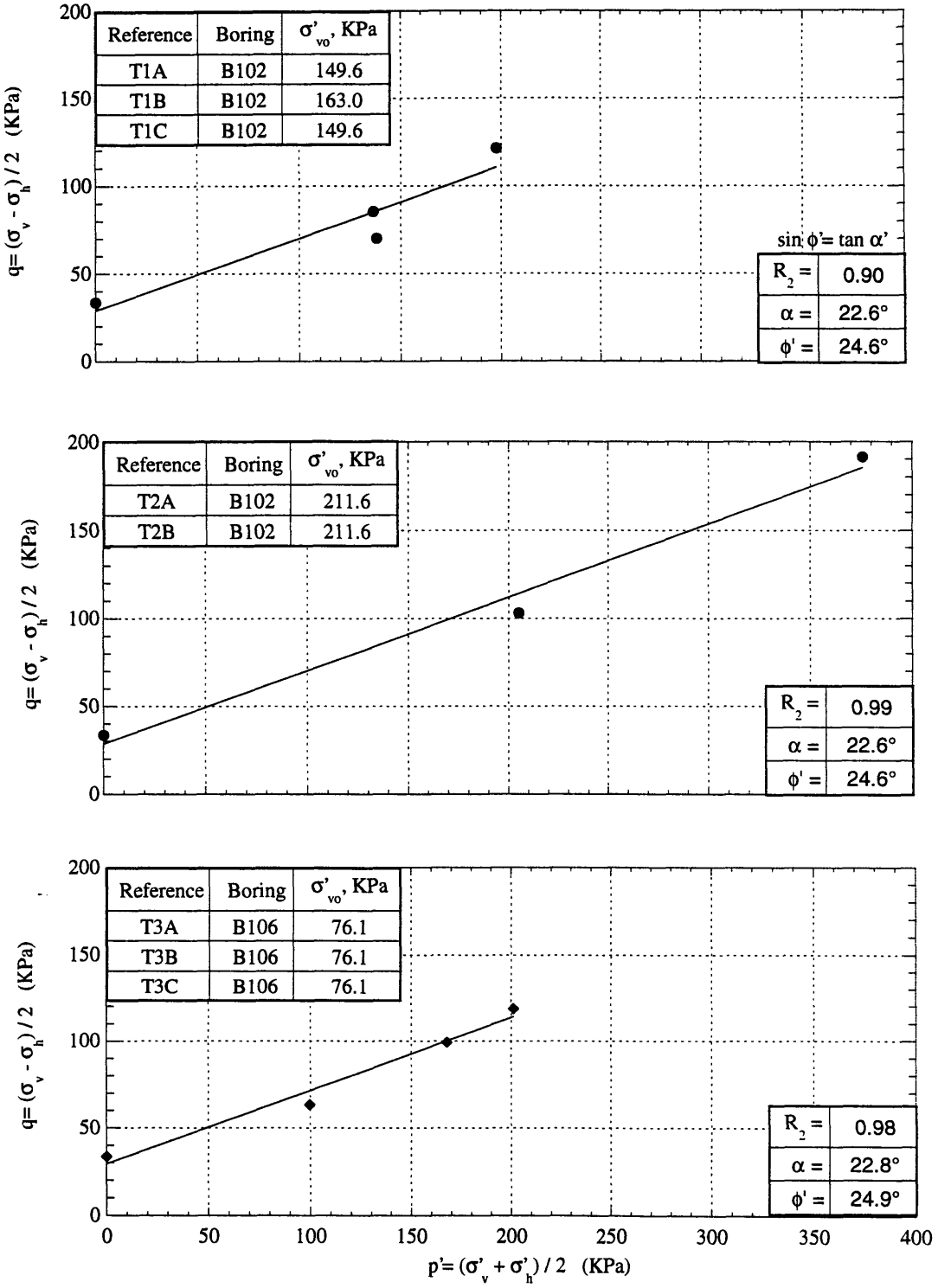

Figure 4.4 Estimation of Friction Angle for Mohr-Coulomb Failure Criterion

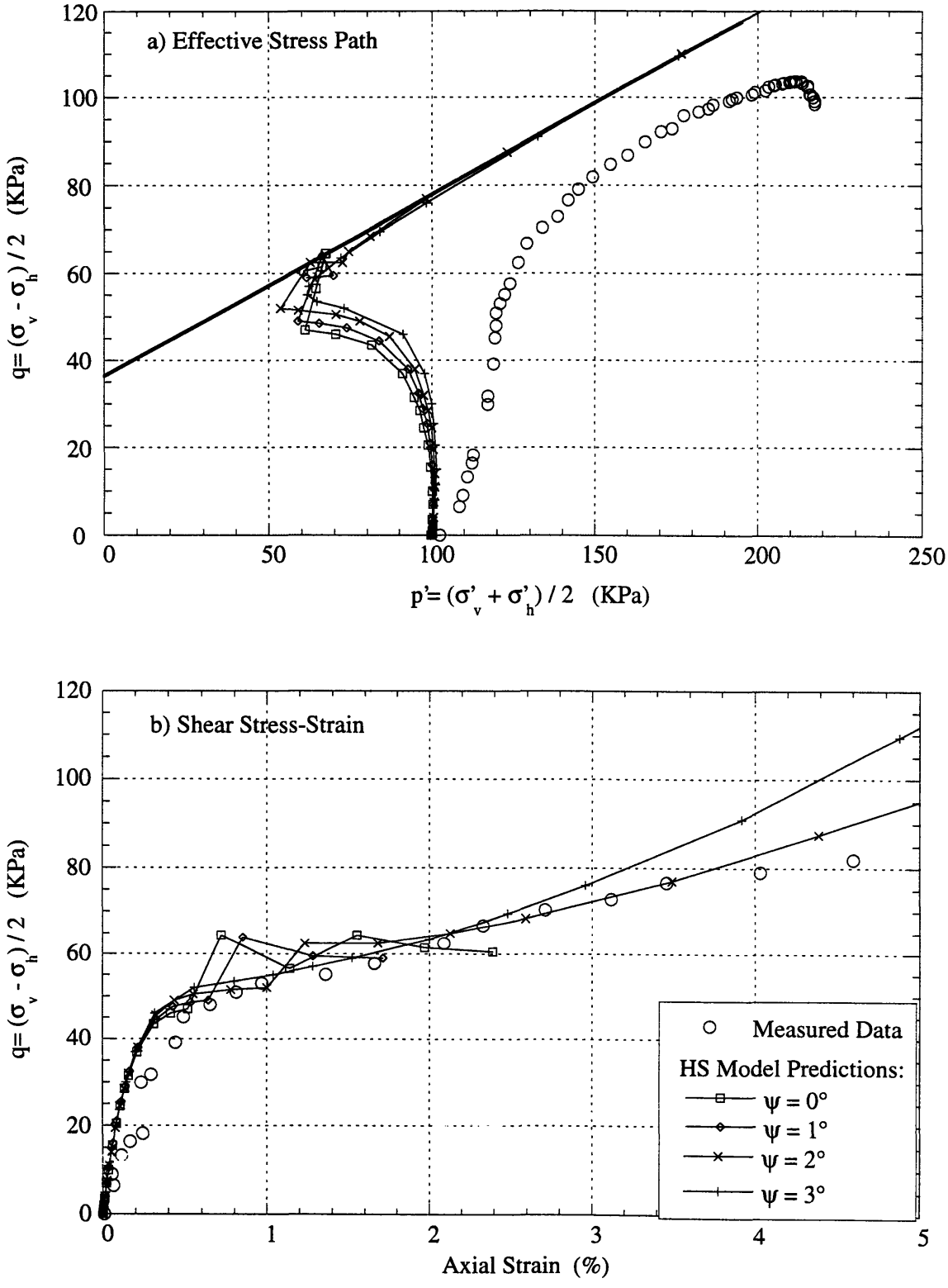

Figure 4.5 Determination of Dilatancy Angle, ψ

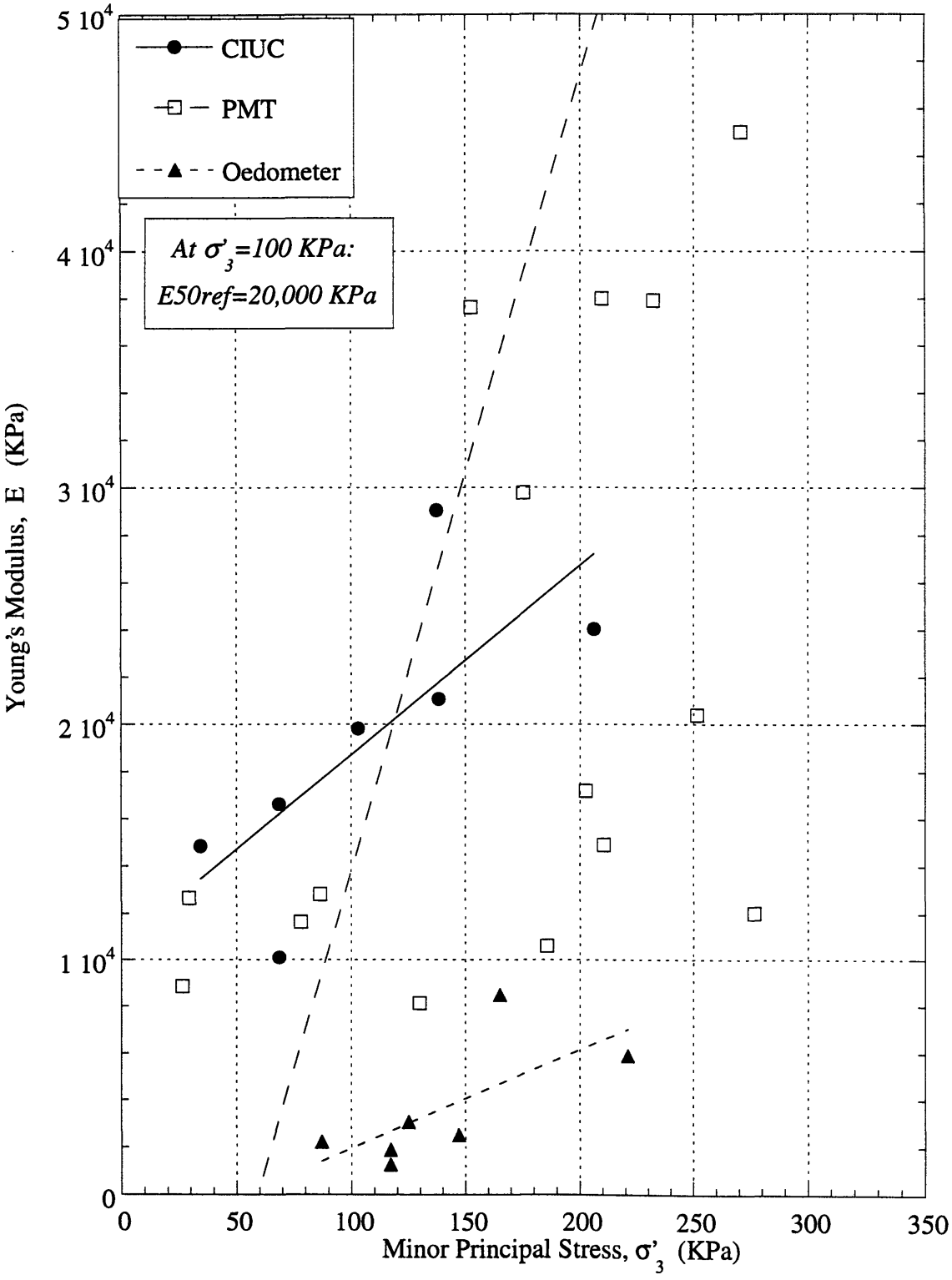

Figure 4.6 Determination of the Primary Loading Stiffness, E_{50}^{ref}

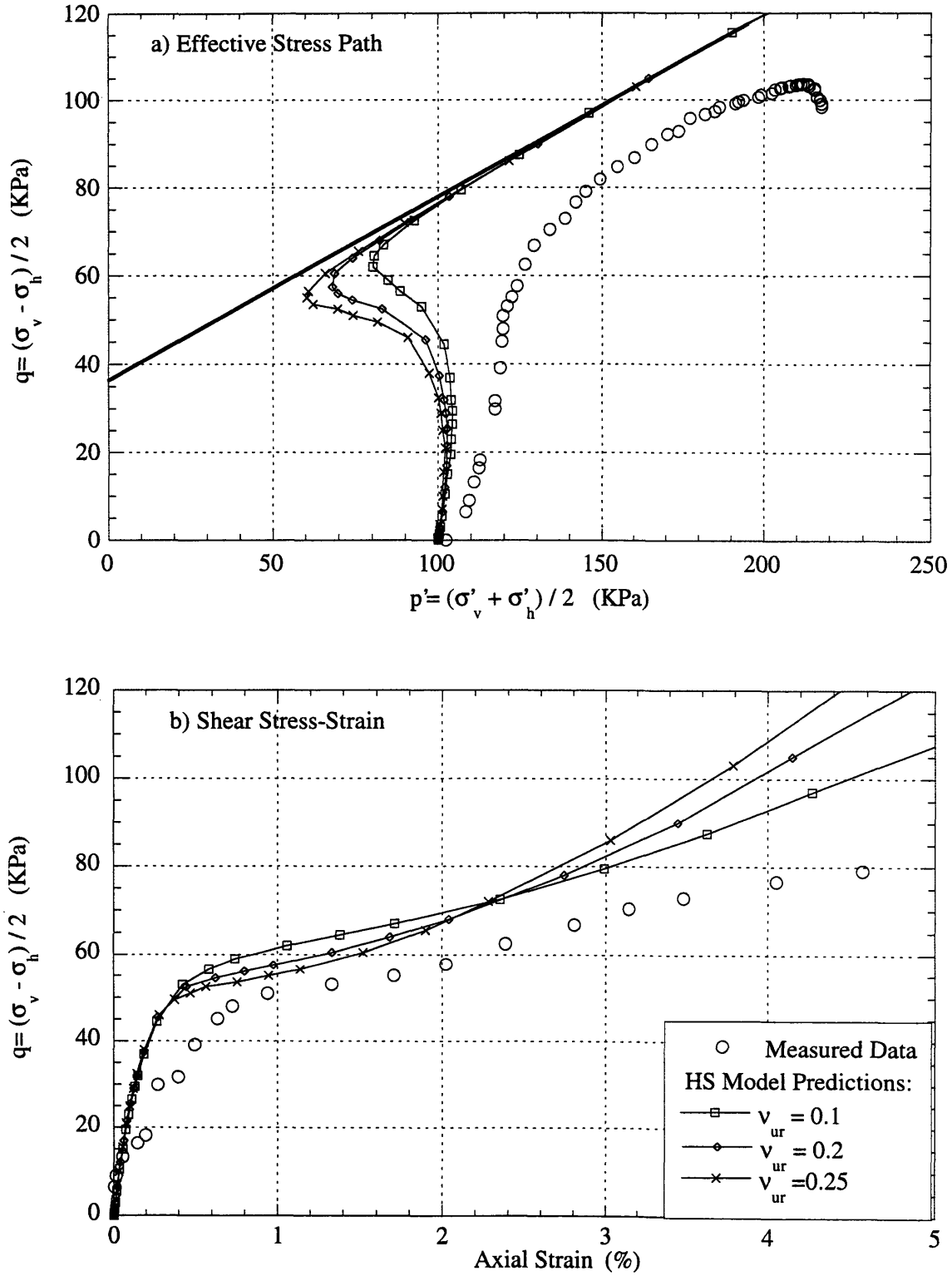

Figure 4.7 Determination of Poisson's Ratio, ν_{ur}

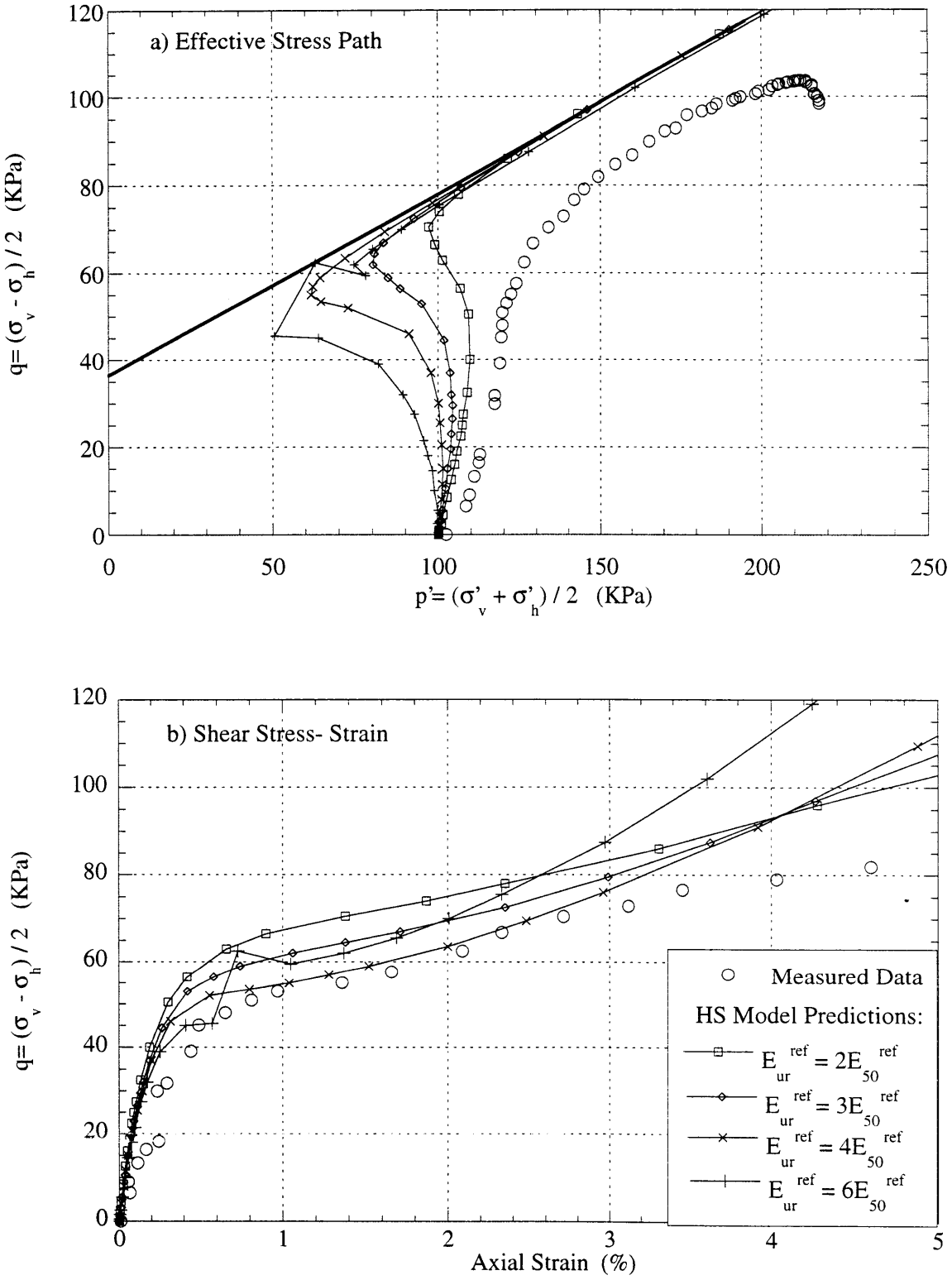

Figure 4.8 Determination of the Unloading/ Reloading Stiffness, E_{ur}^{ref}

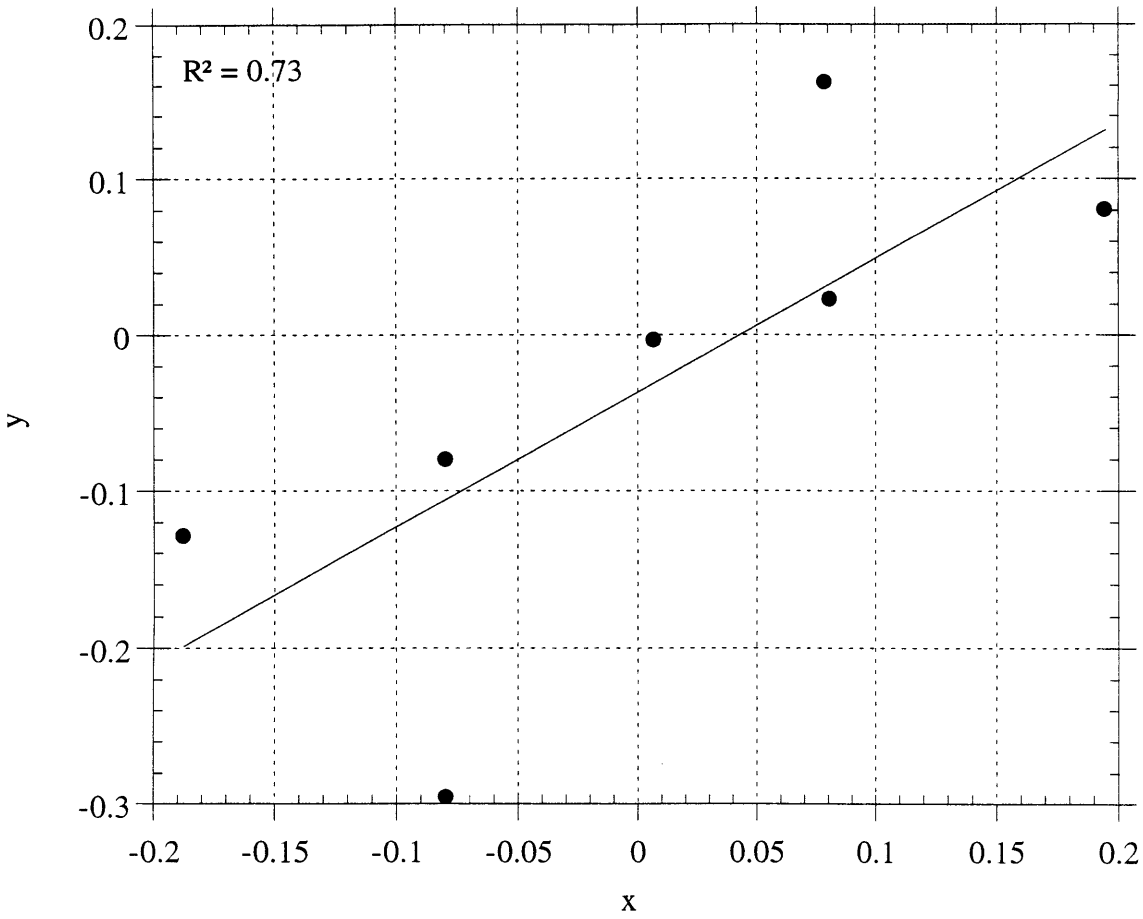

Where:

$$y = \log \frac{E_{50}^{ref}(CIUC)}{E_{50\,ref}} = \log \frac{E_{50}^{ref}}{20{,}000}$$

$$x = \log \frac{\sigma'_3(CIUC) + c'\cot\phi'}{p'_{ref} + c'\cot\phi'} = \log \frac{\sigma'_3(CIUC) + c'\cot\phi'}{100 + c'\cot\phi'}$$

y= mx+b; slope, m=0.86

Figure 4.9 Determination of m Parameter from CIUC Tests

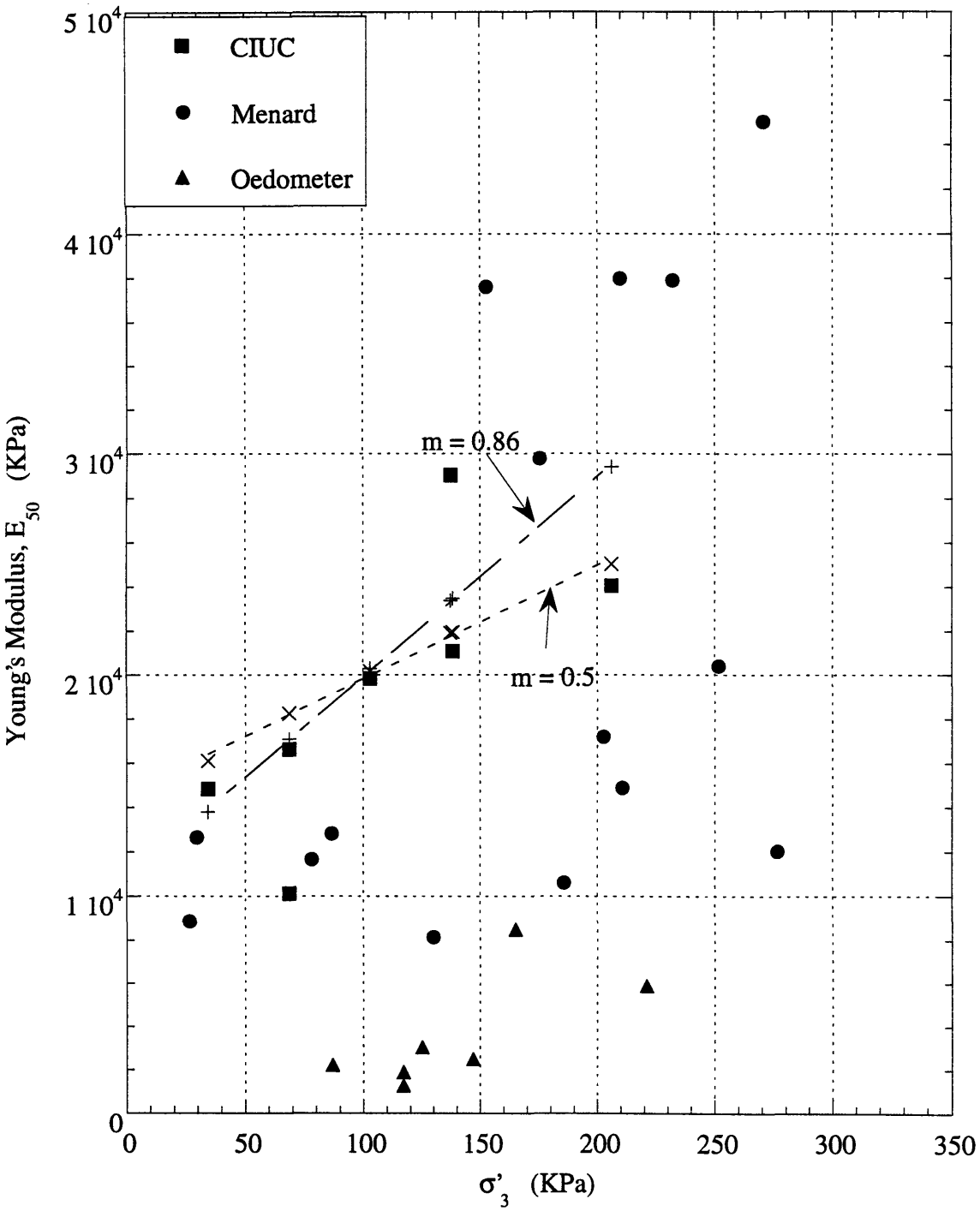

Figure 4.10 Determination of m Parameter

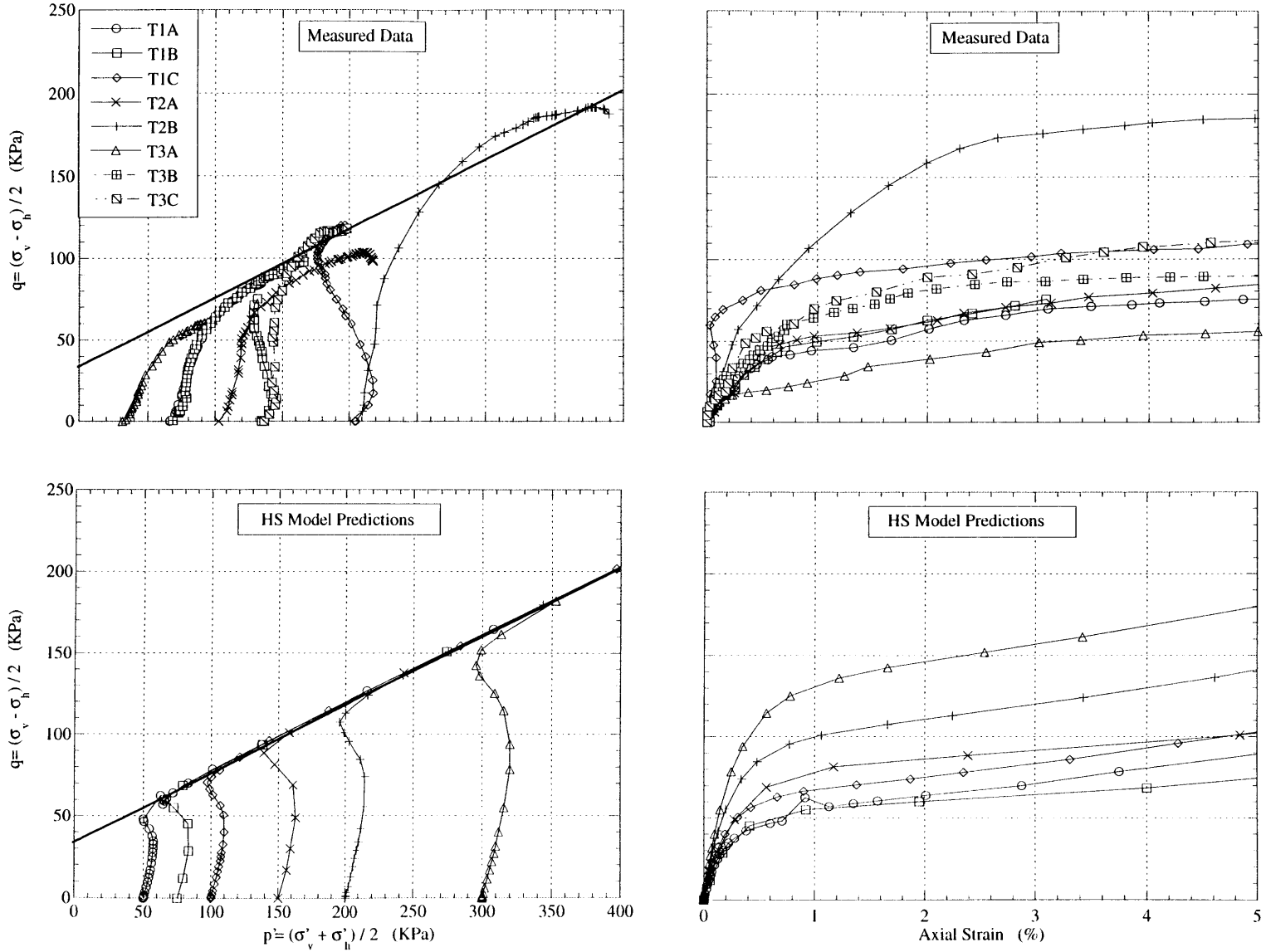

Figure 4.11 Comparison between CIUC Triaxial Tests and Single Element HS Model Predictions

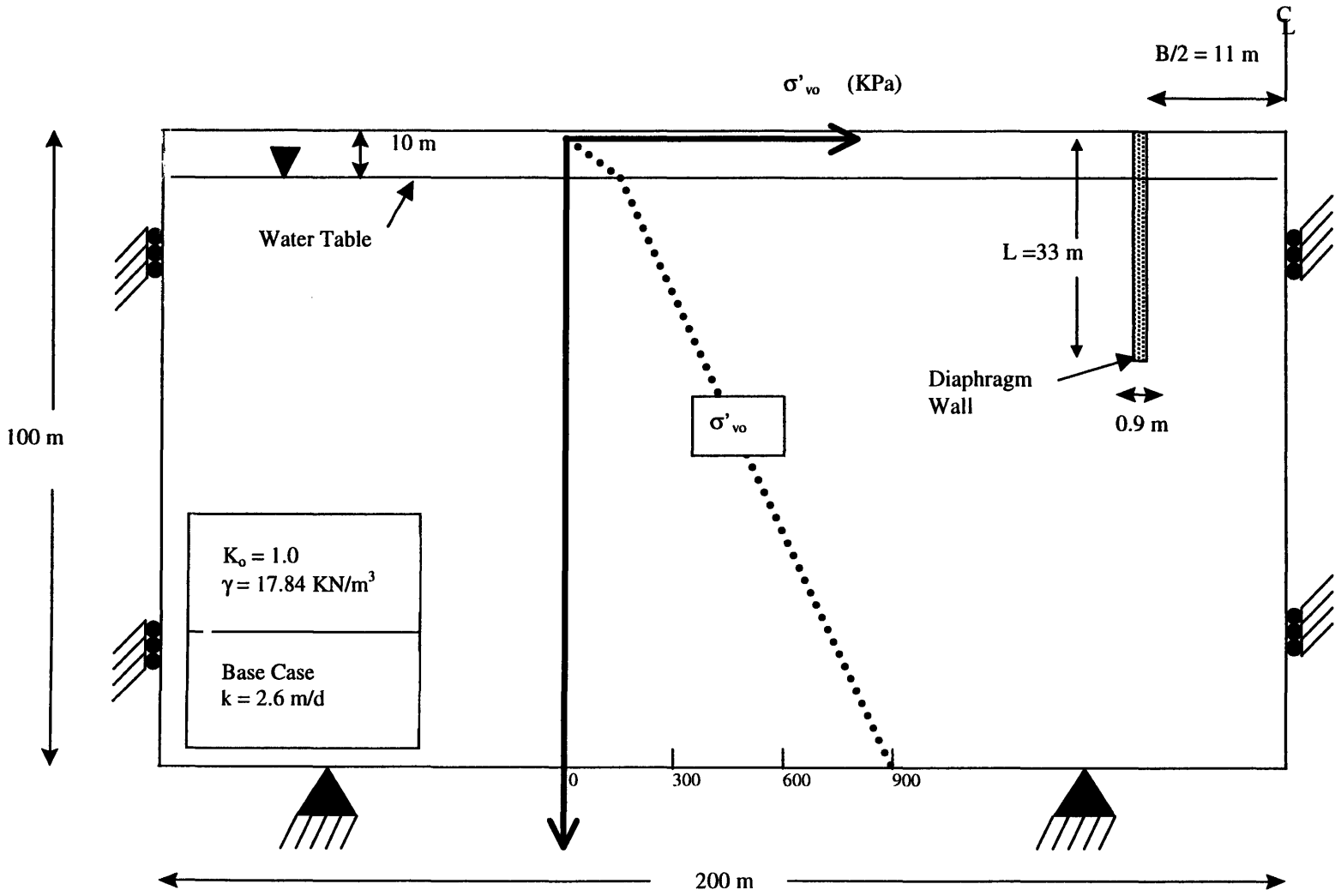

Figure 4.12 Boundary and Initial Conditions for Idealized Excavation

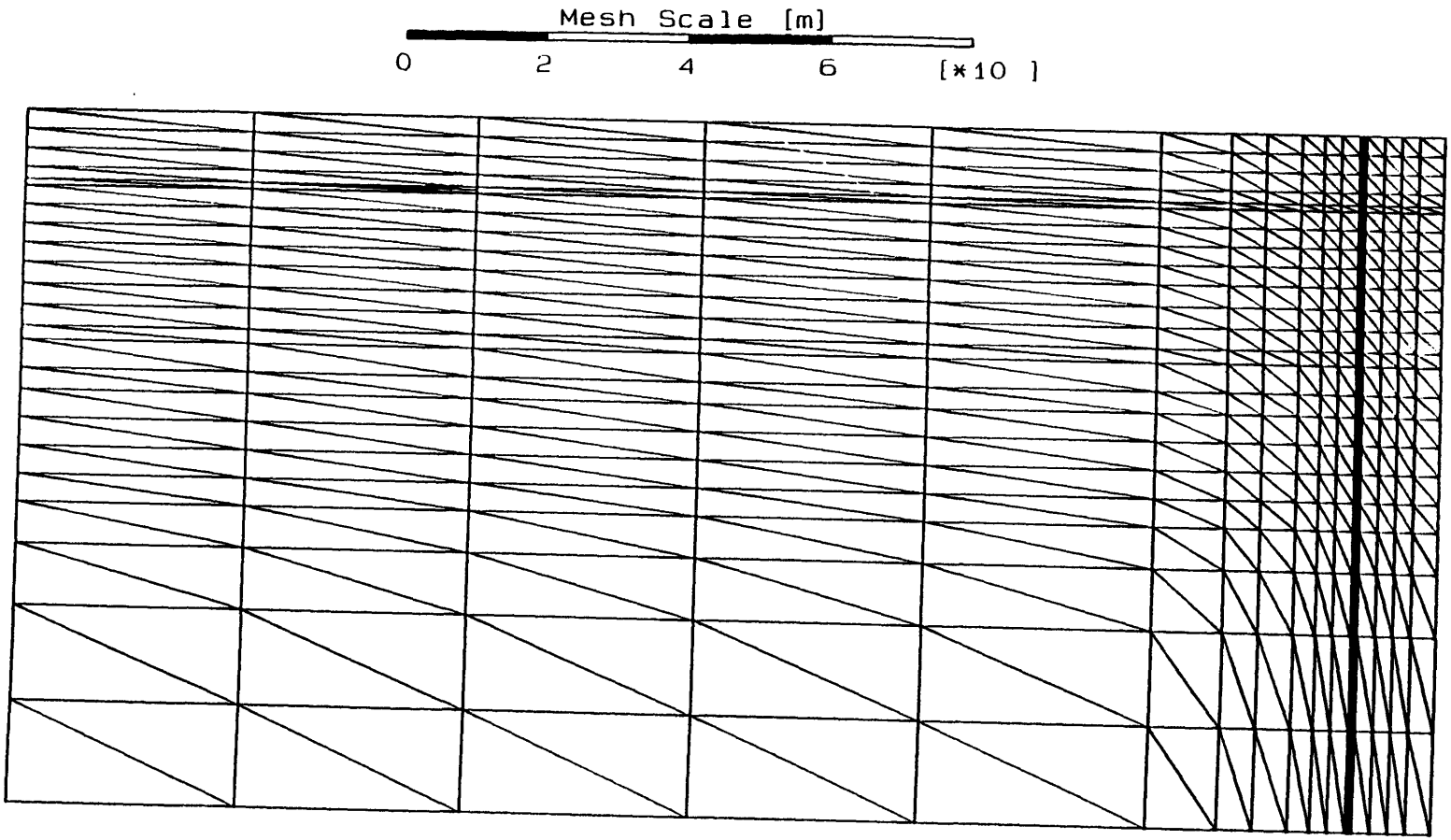

Figure 4.13 Finite Element Mesh

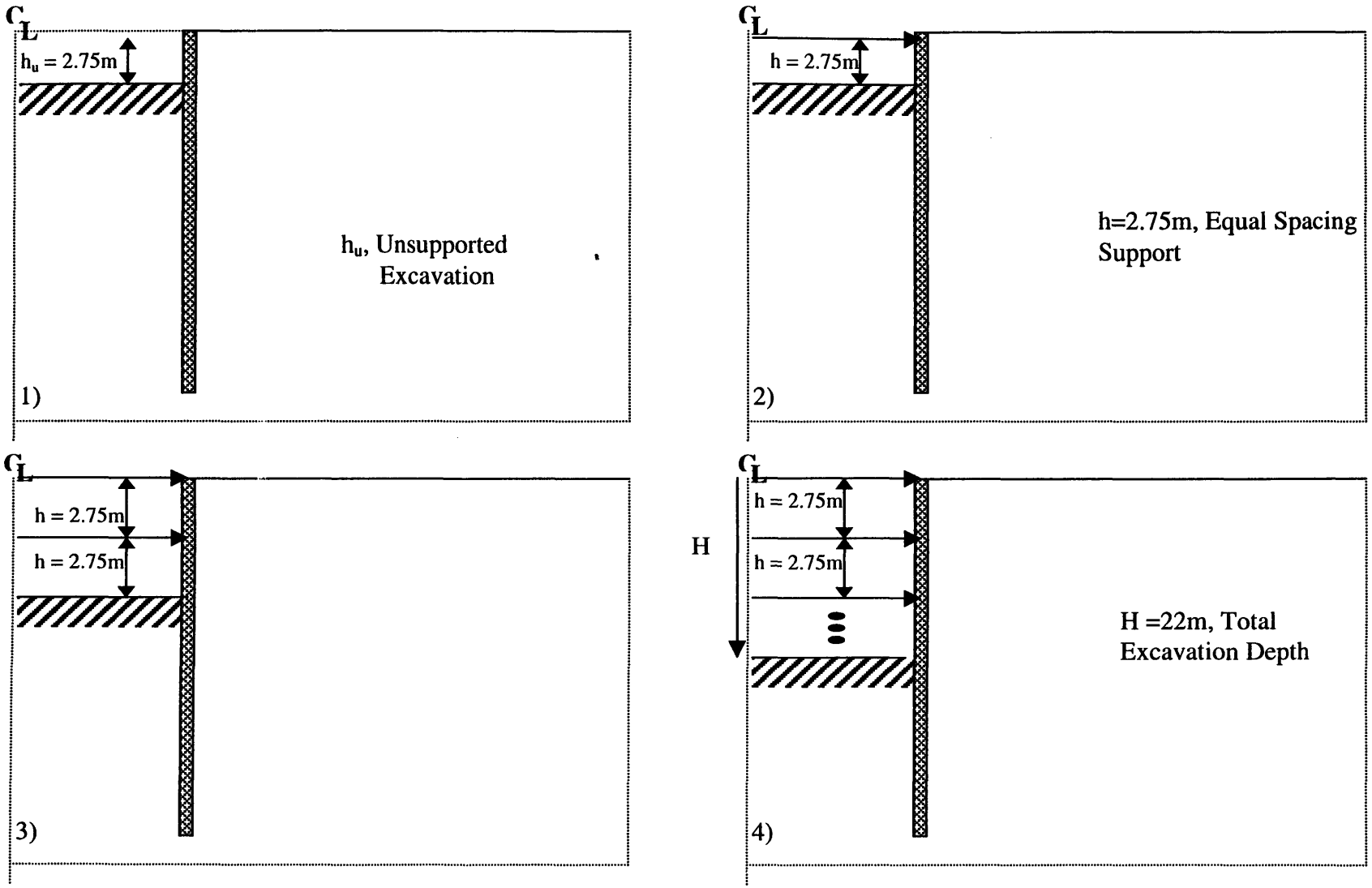

Figure 4.14 Geometry, Support Conditions, and Excavation Sequence

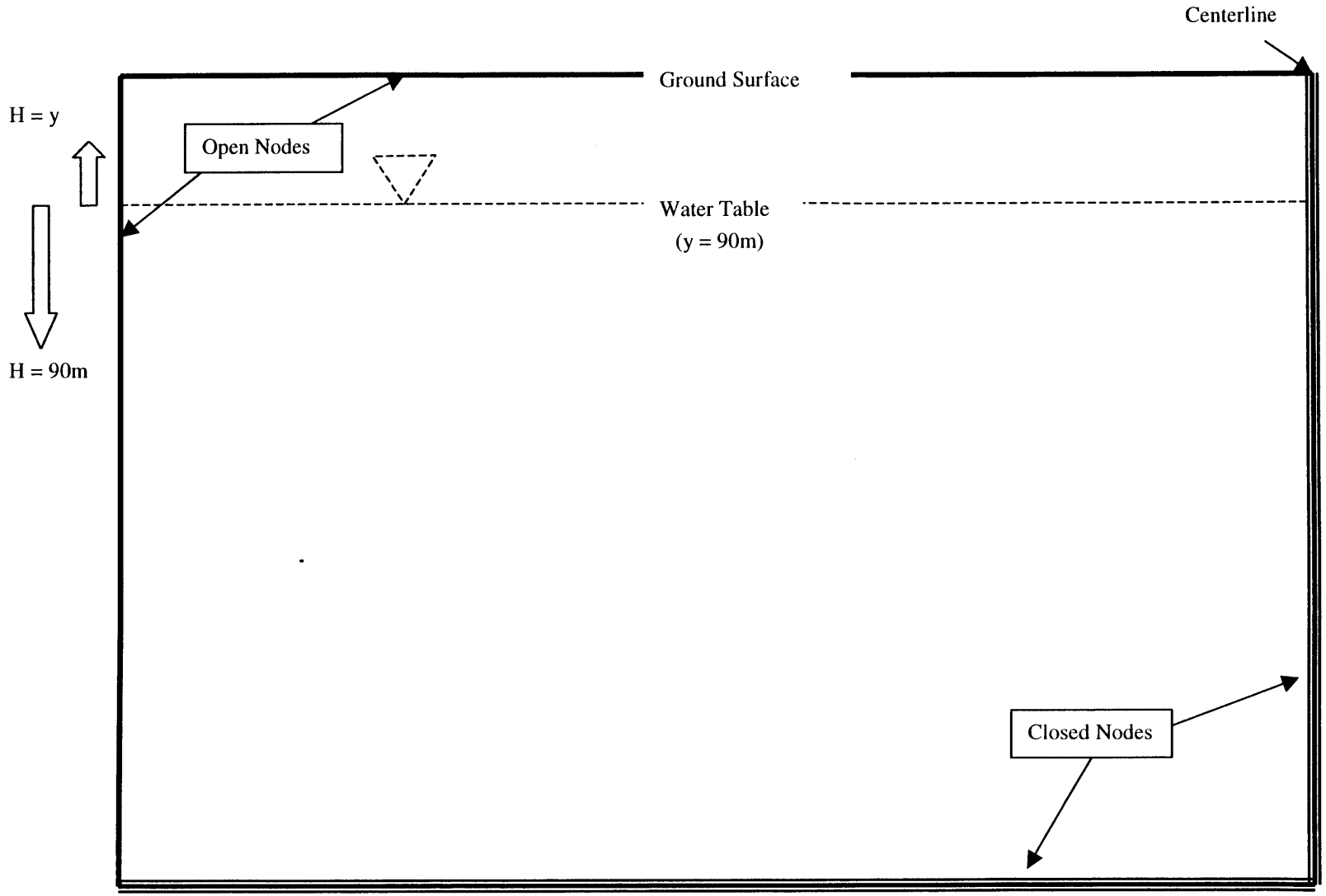

Figure 4.15 Flow Boundary Conditions at each excavation stage

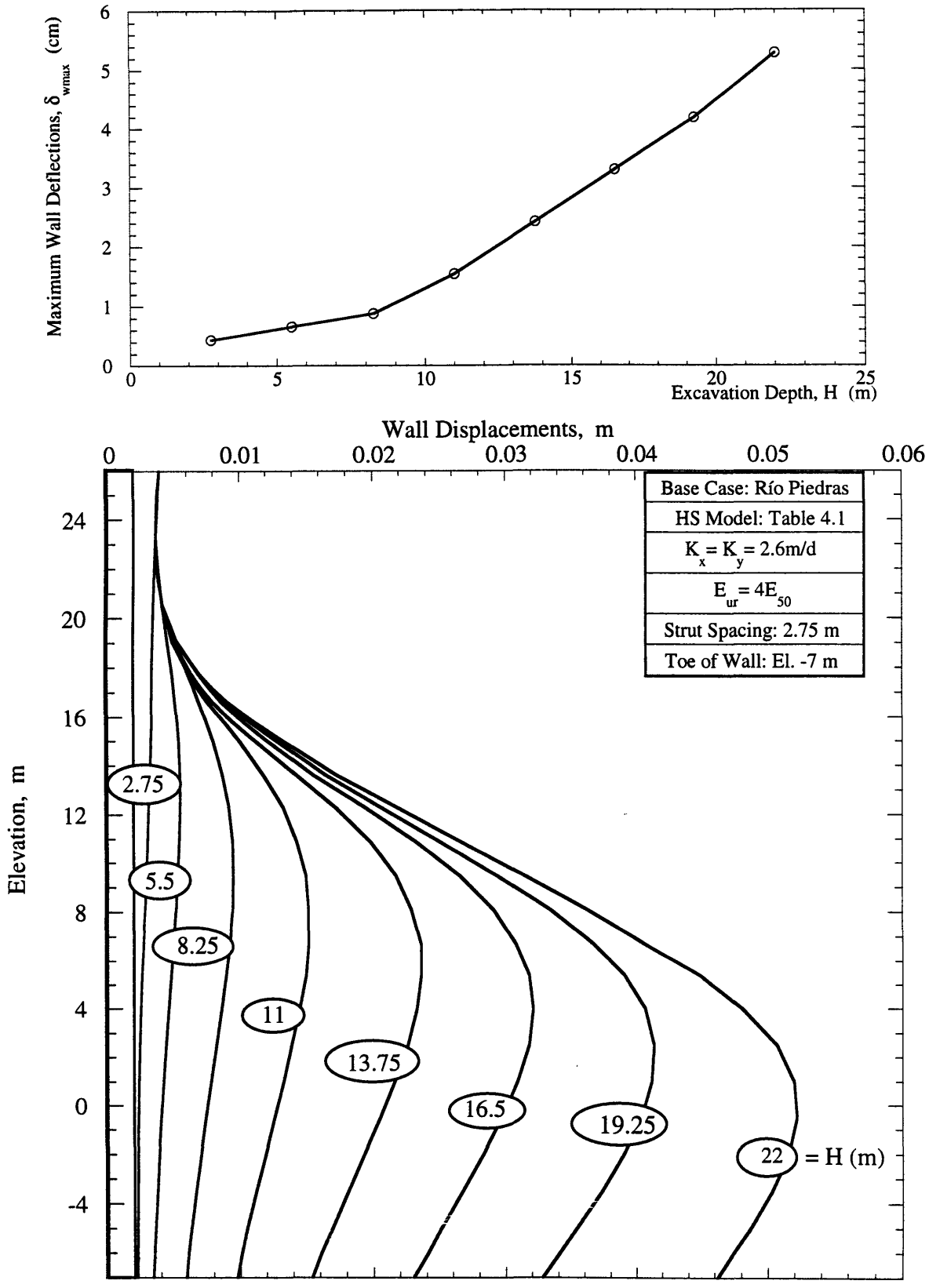

Figure 4.16 Wall Deflections for Base Case Analysis

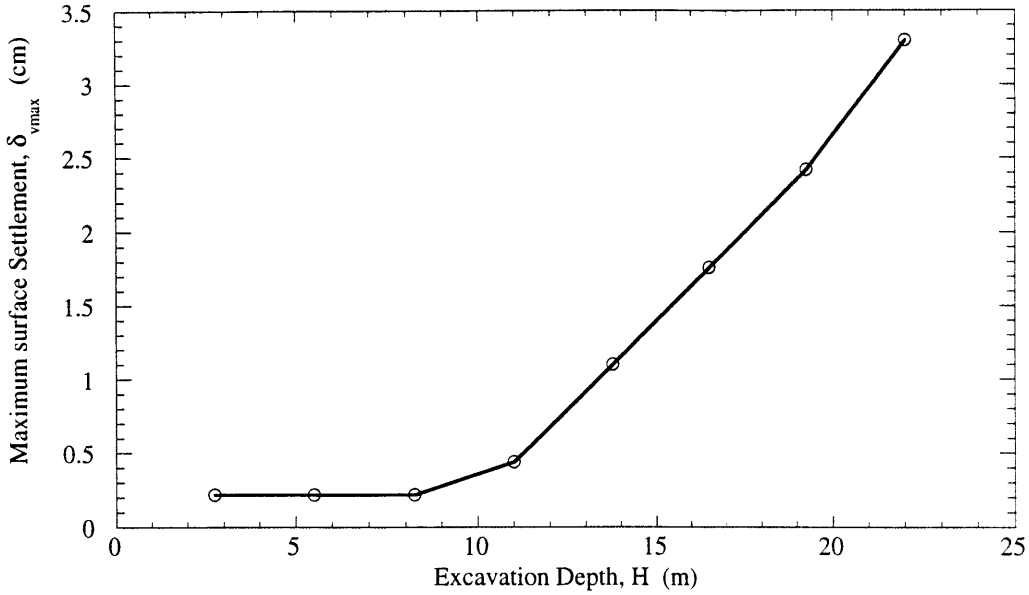

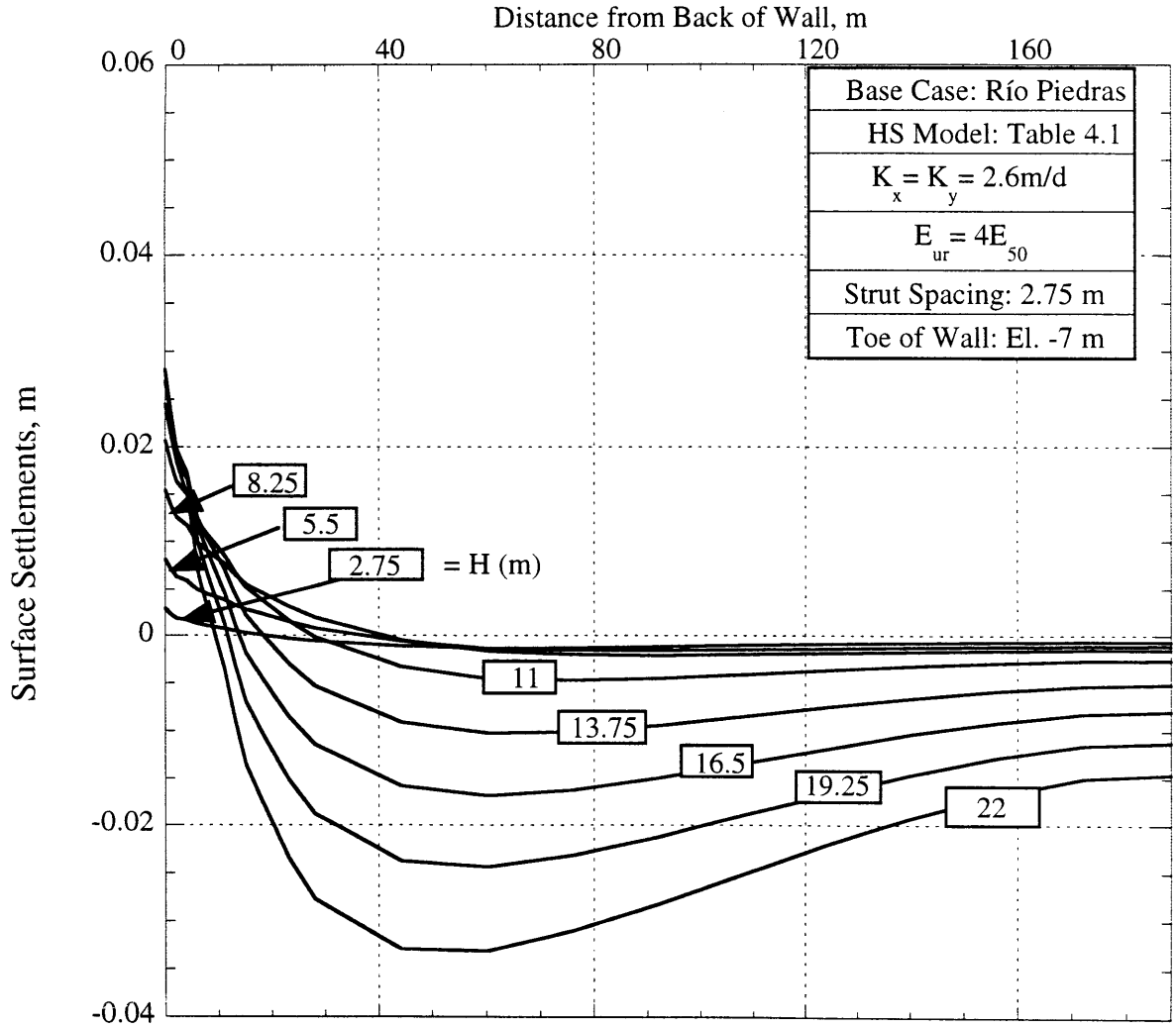

Figure 4.17 Predicted Surface Settlements for Base Case Analysis

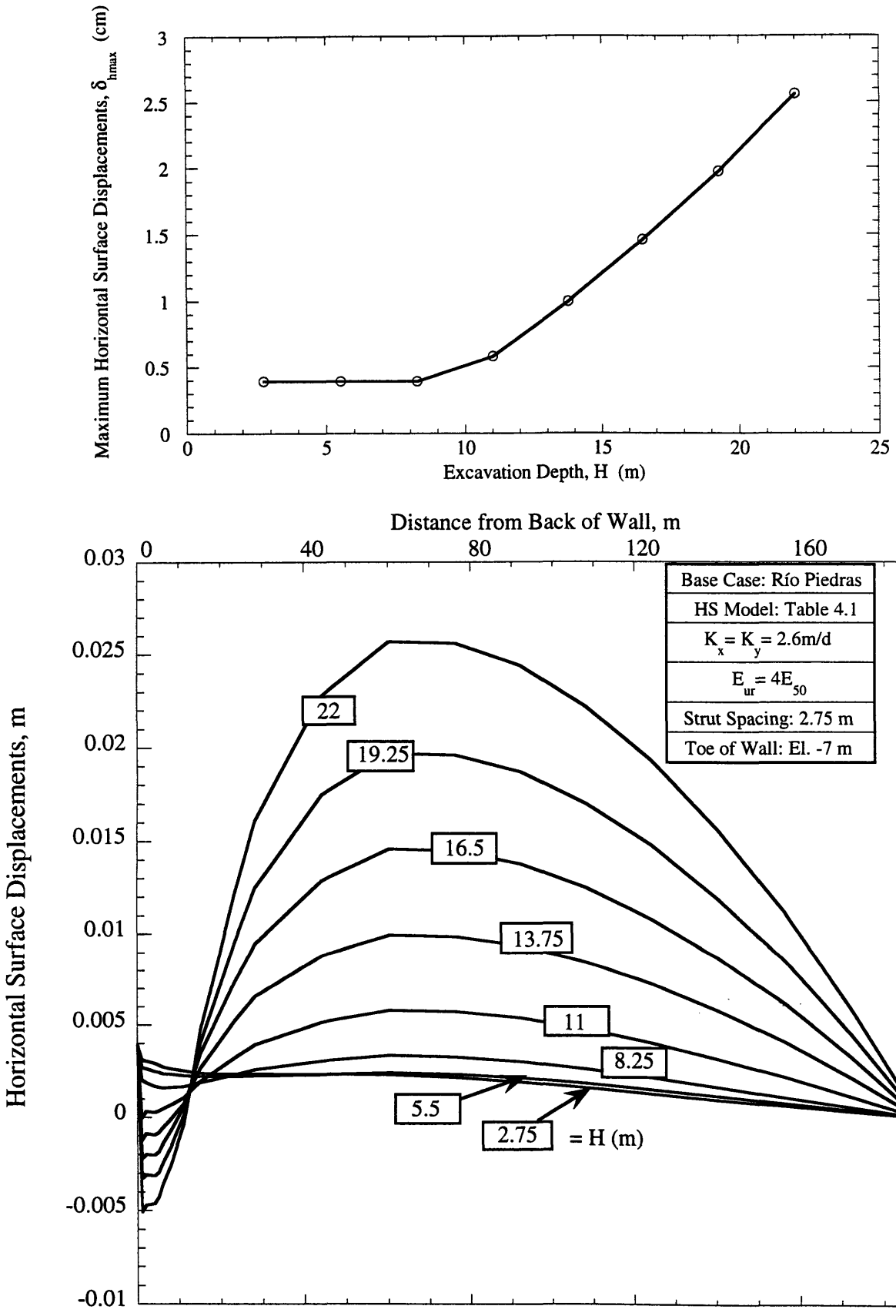

Figure 4.18 Predicted Horizontal Surface Displacements for Base Case Analysis

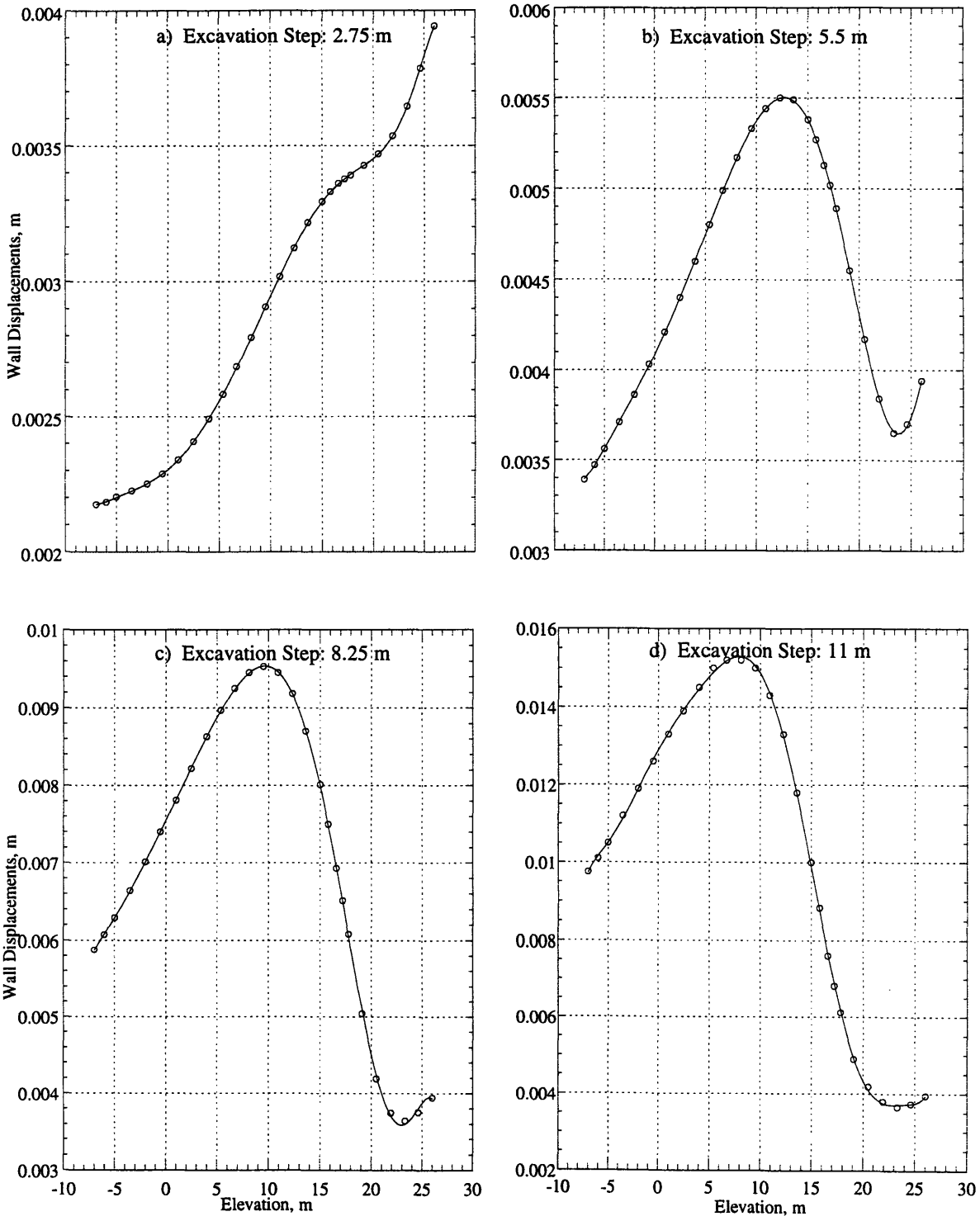

Figure 4.19 Curve Fits for Bending Moment Calculations

(General Expression for Curve Fits: $y = m_0 + m_1 * x + \ldots m_8 * x^8 + m_9 * x^9$)

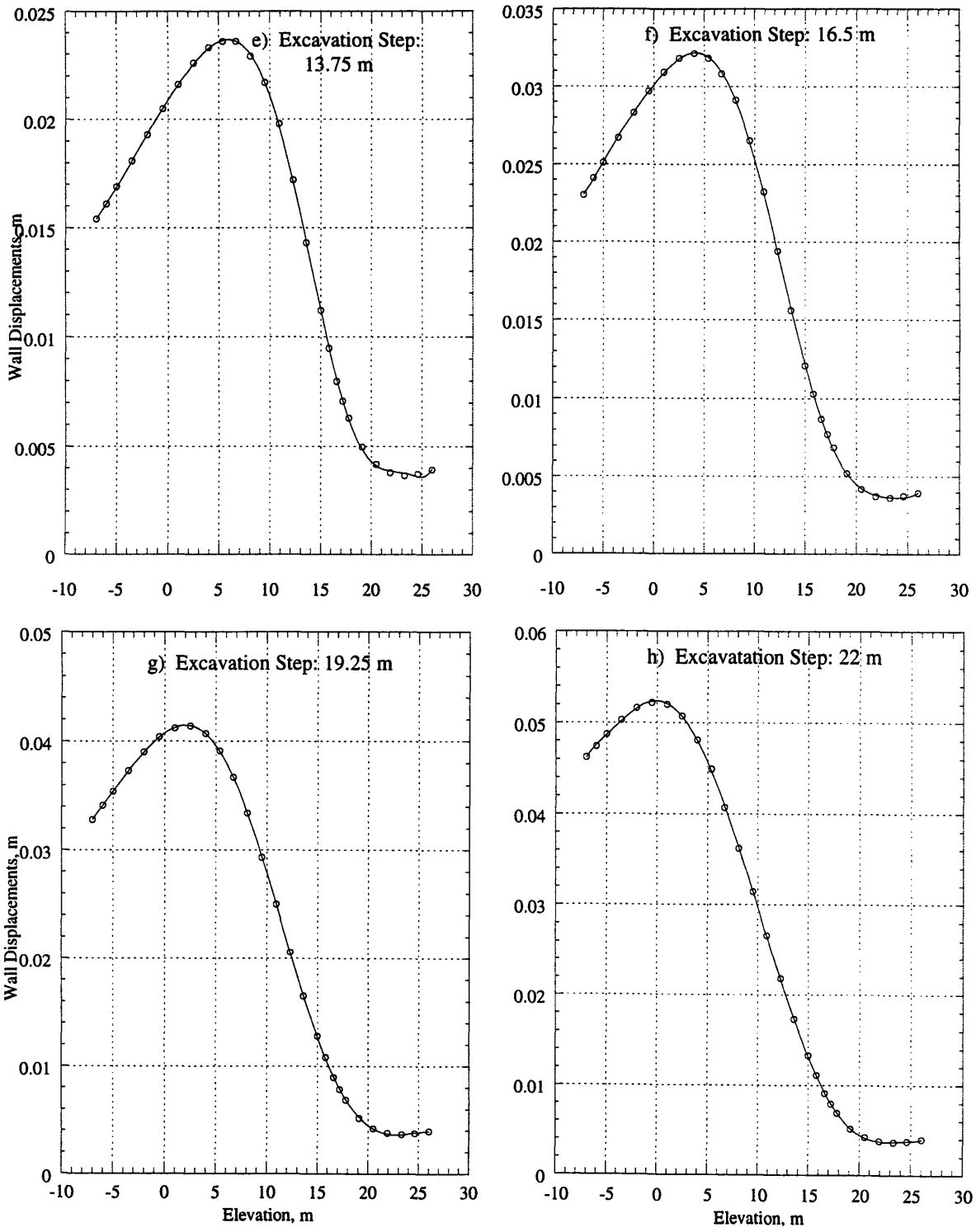

Figure 4.19 Curve Fits for Bending Moment Calculations

(General Expression for Curve Fits: $y = m_0 + m_1*x + \ldots m_8*x^8 + m_9*x^9$)

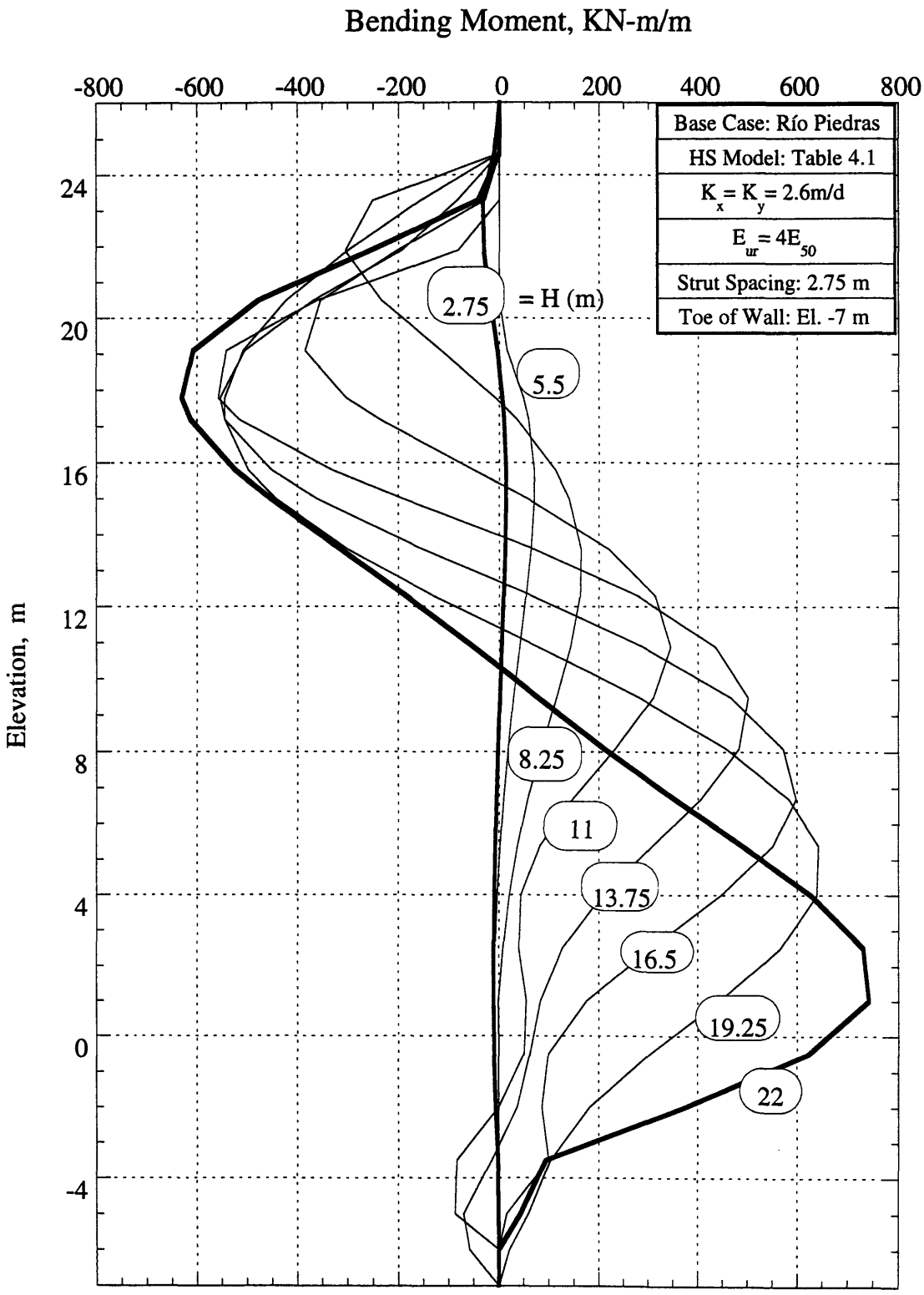

Figure 4.20 Predicted Bending Moments for Base Case Analysis

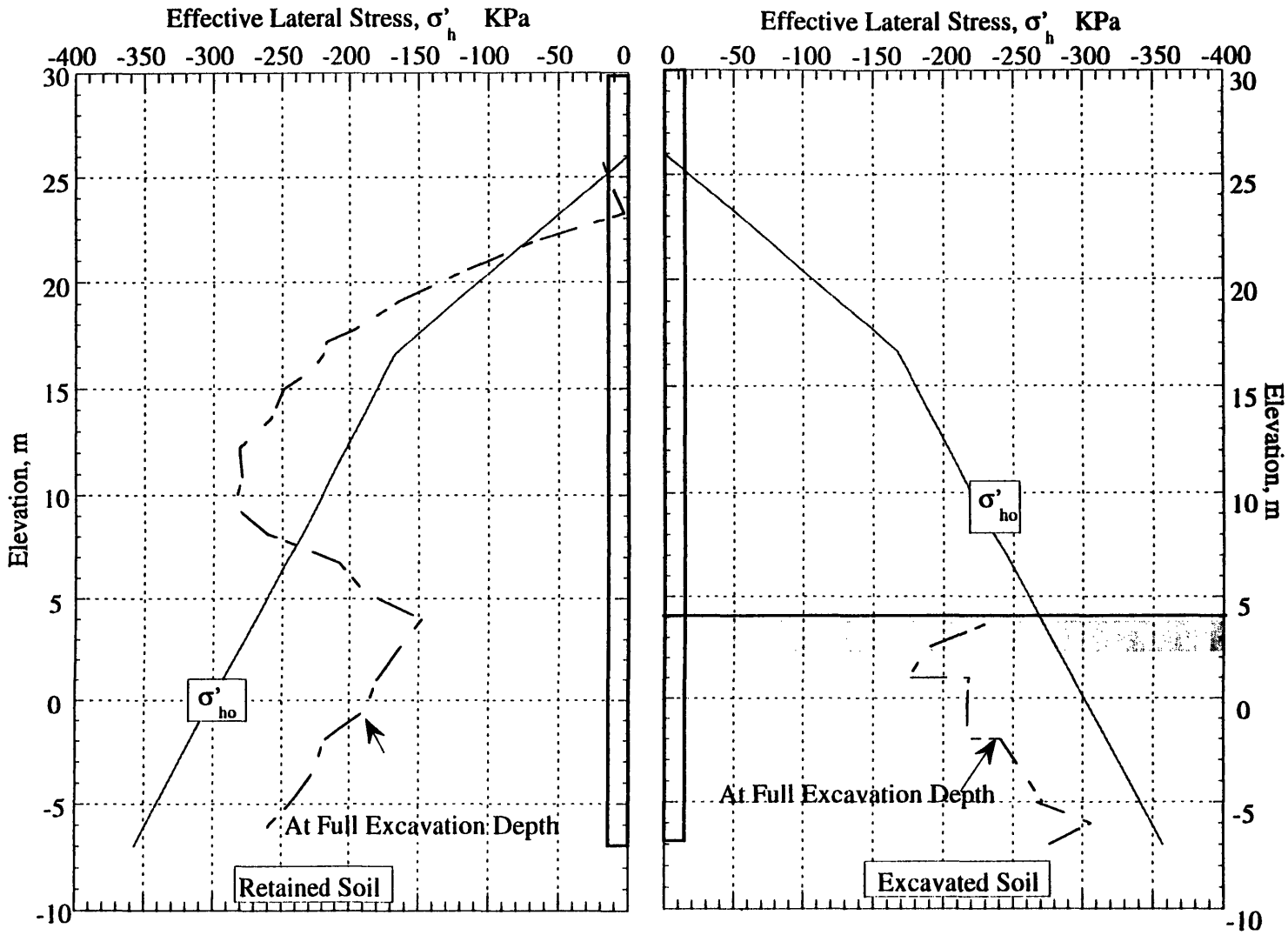

Figure 4.21 Effective Lateral Earth Pressures for Base Case Analysis

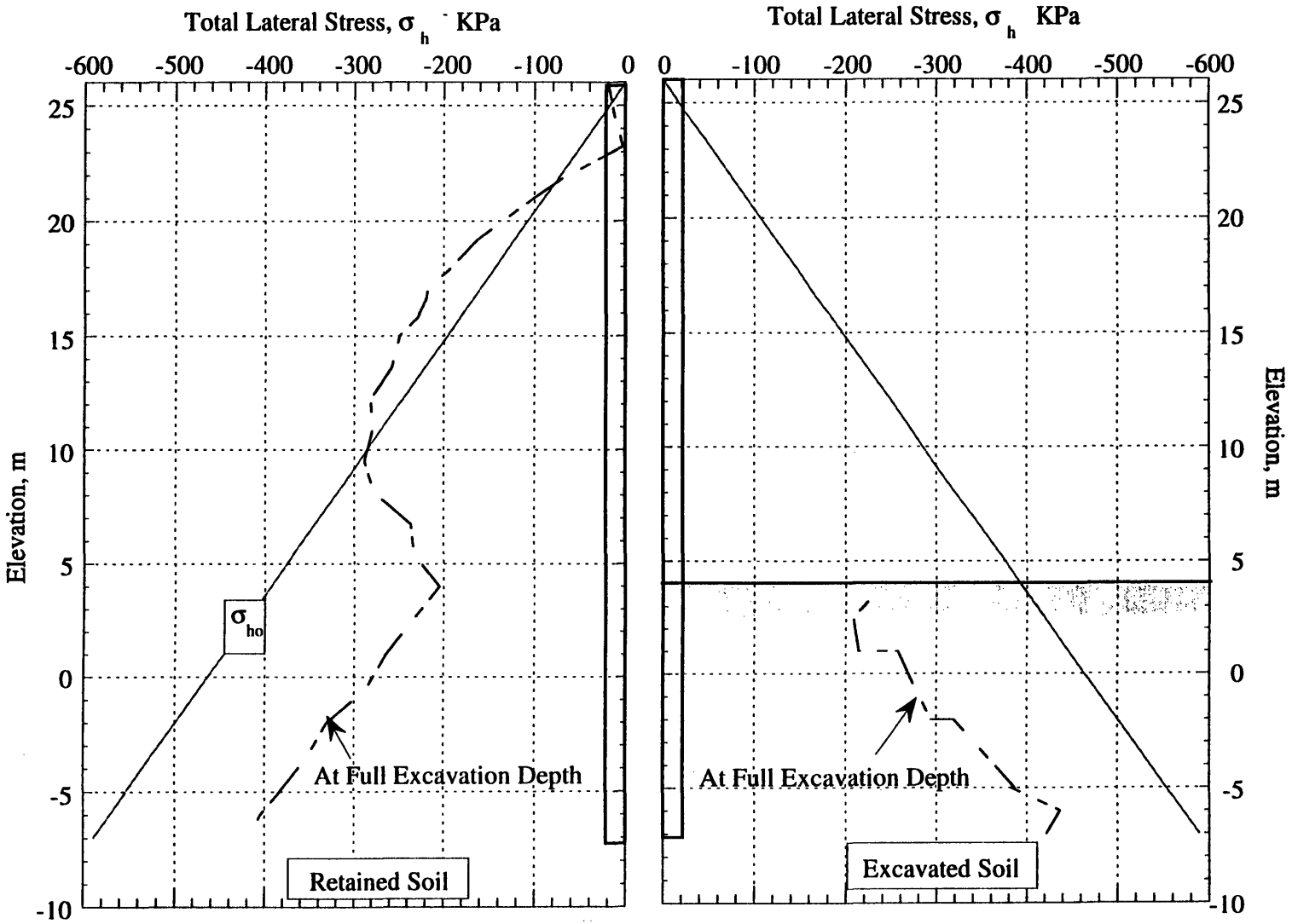

Figure 4.22 Total Lateral Earth Pressures for Base Case Analysis

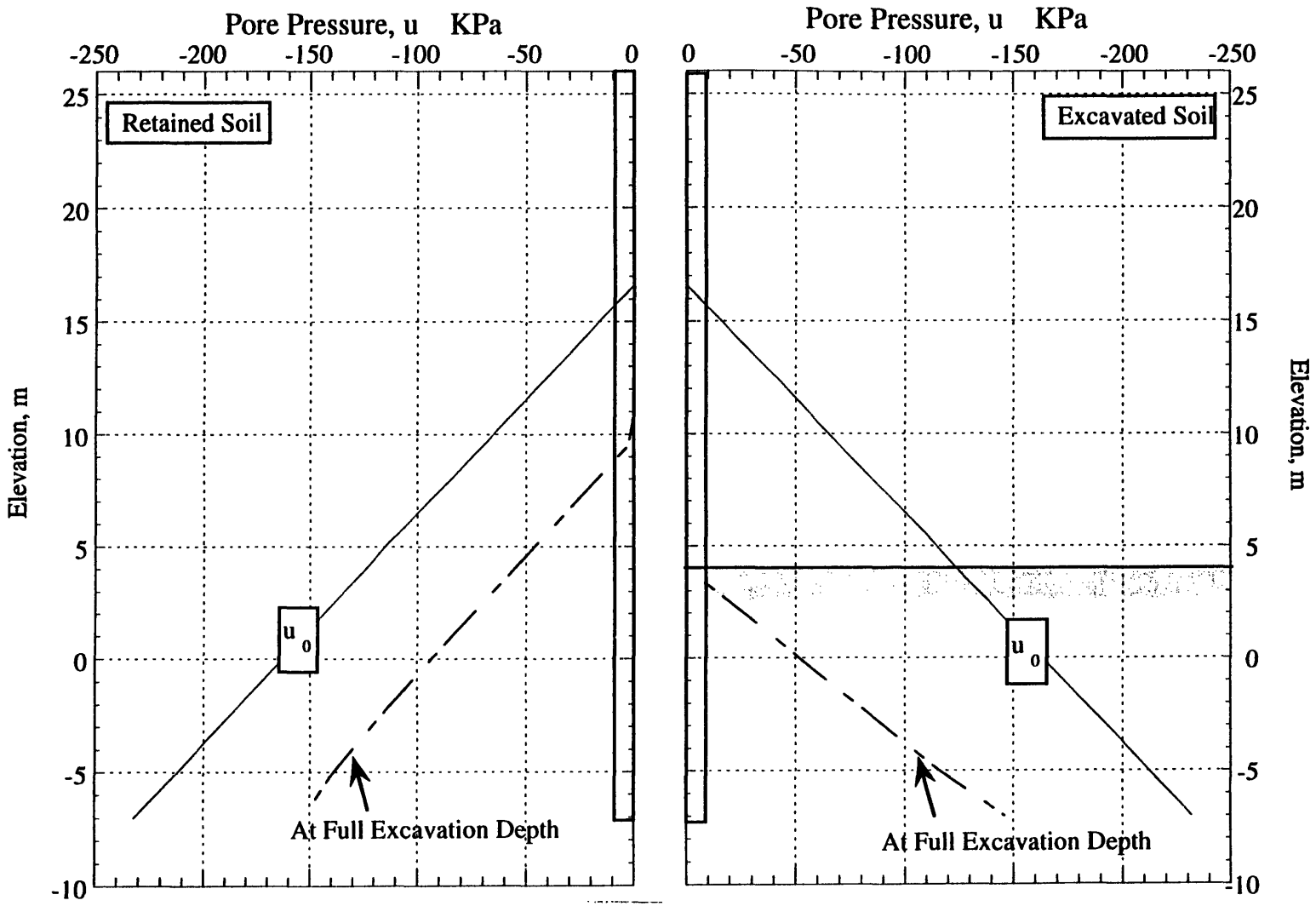

Figure 4.23 Pore Water Pressures on Wall for Base Case Analysis

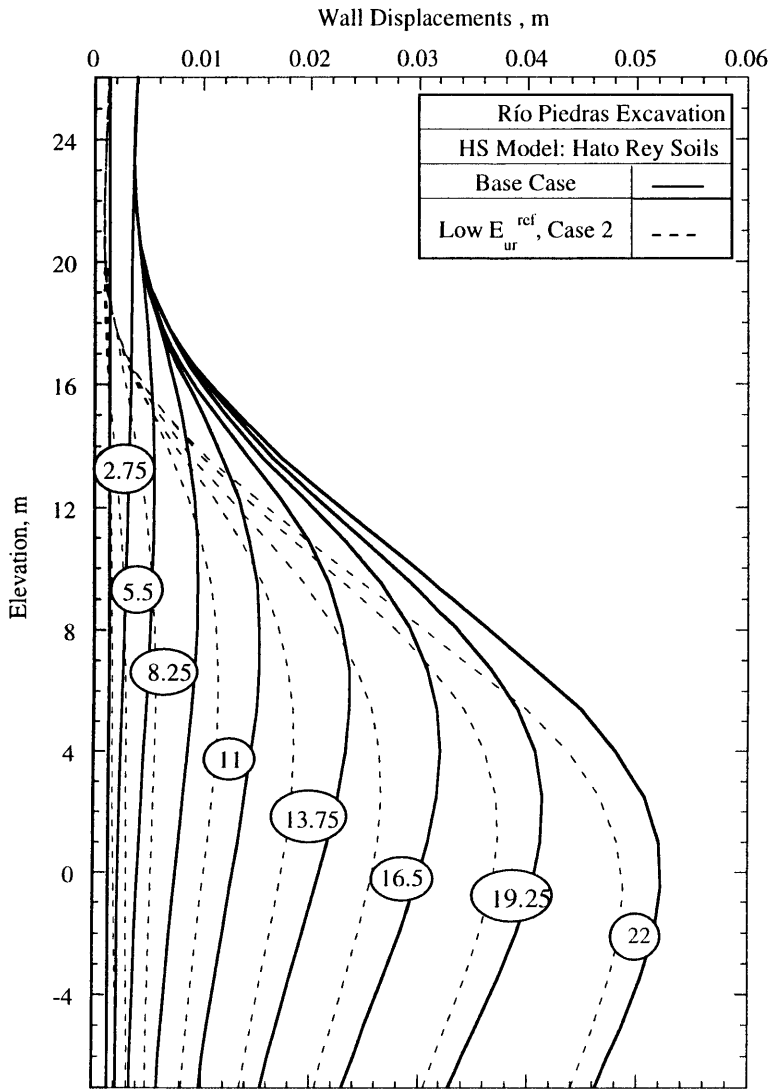

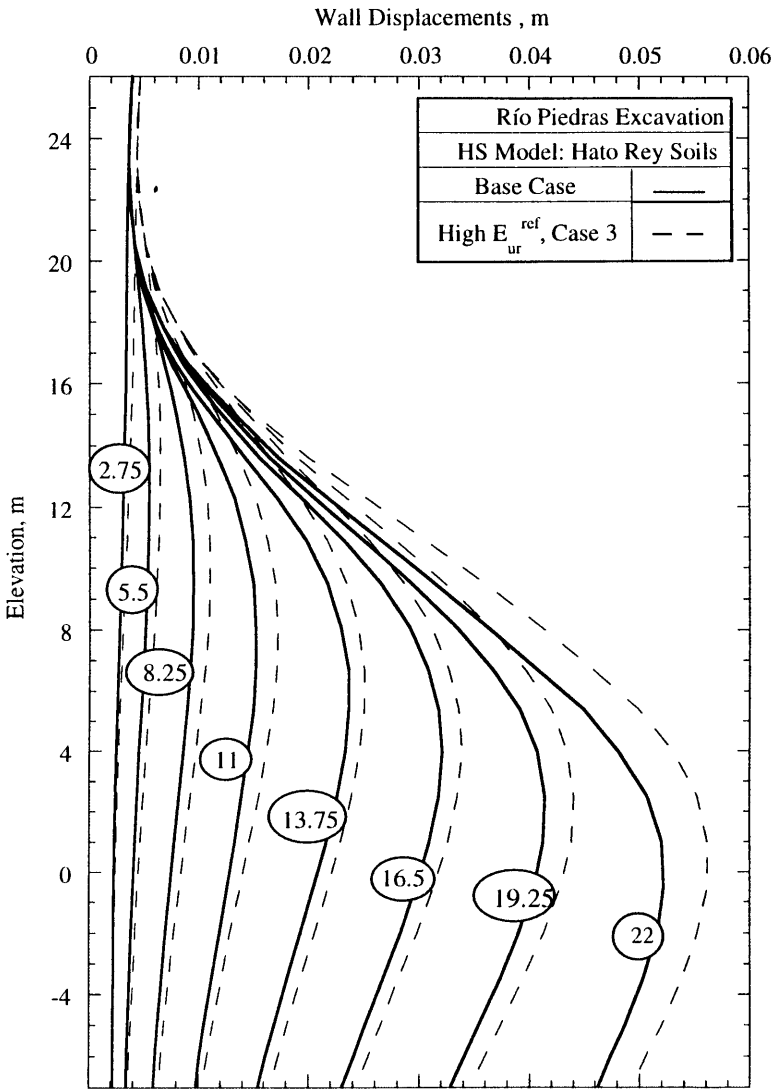

Figure 4.24 Effect of Unloading Modulus E_{ur}^{ref} on wall Displacements

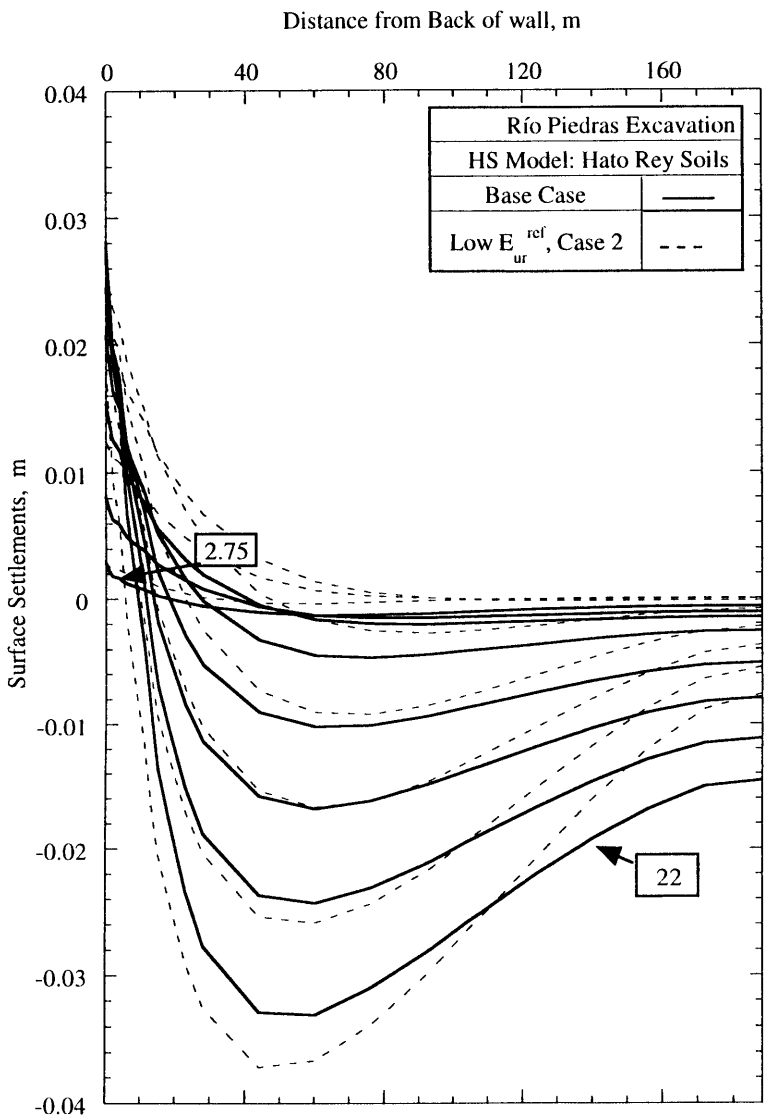

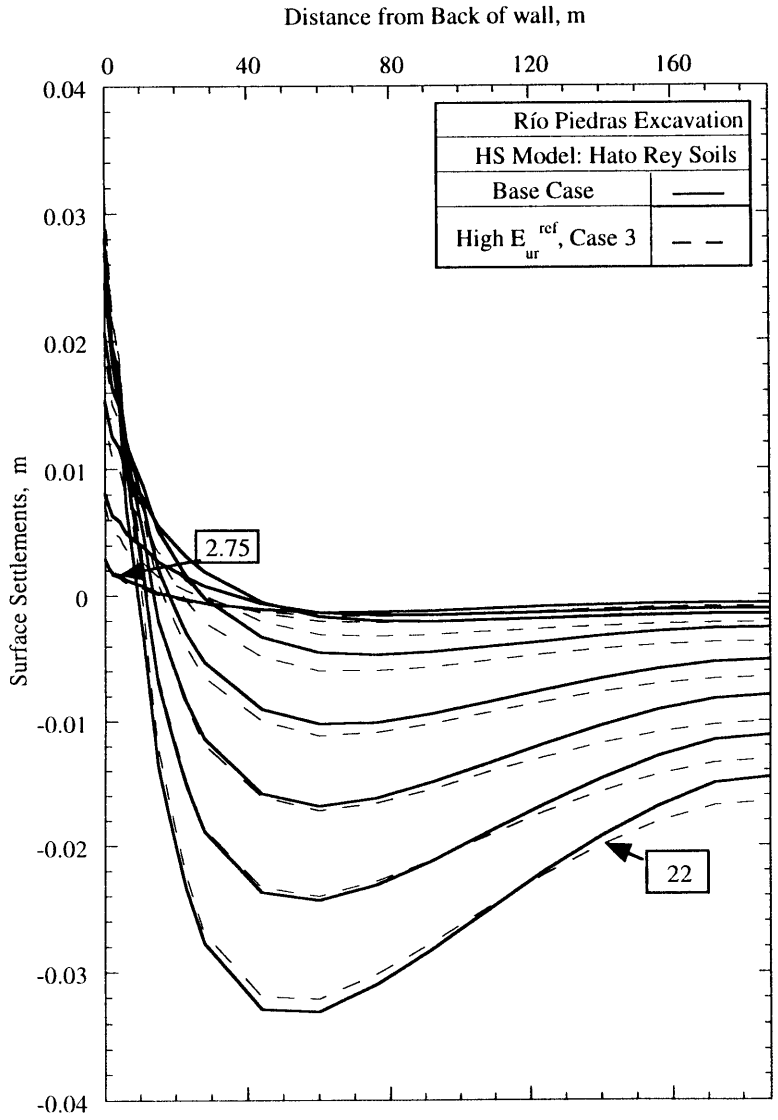

Figure 4.25 Effect of Unloading Modulus E_{ur}^{ref} on Ground Surface Settlements

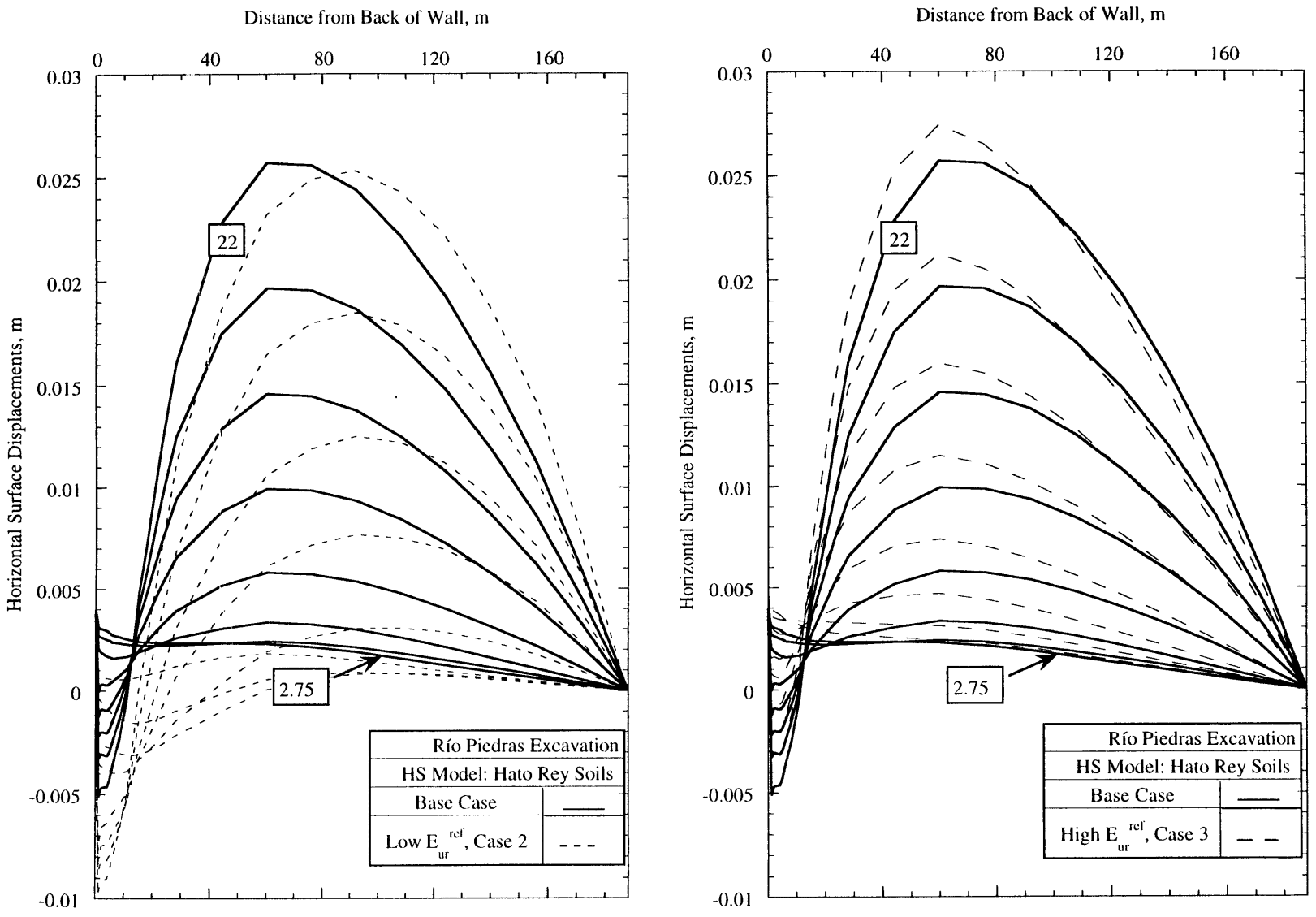

Figure 4.26 Effect of Unloading Modulus on Horizontal Surface Displacements

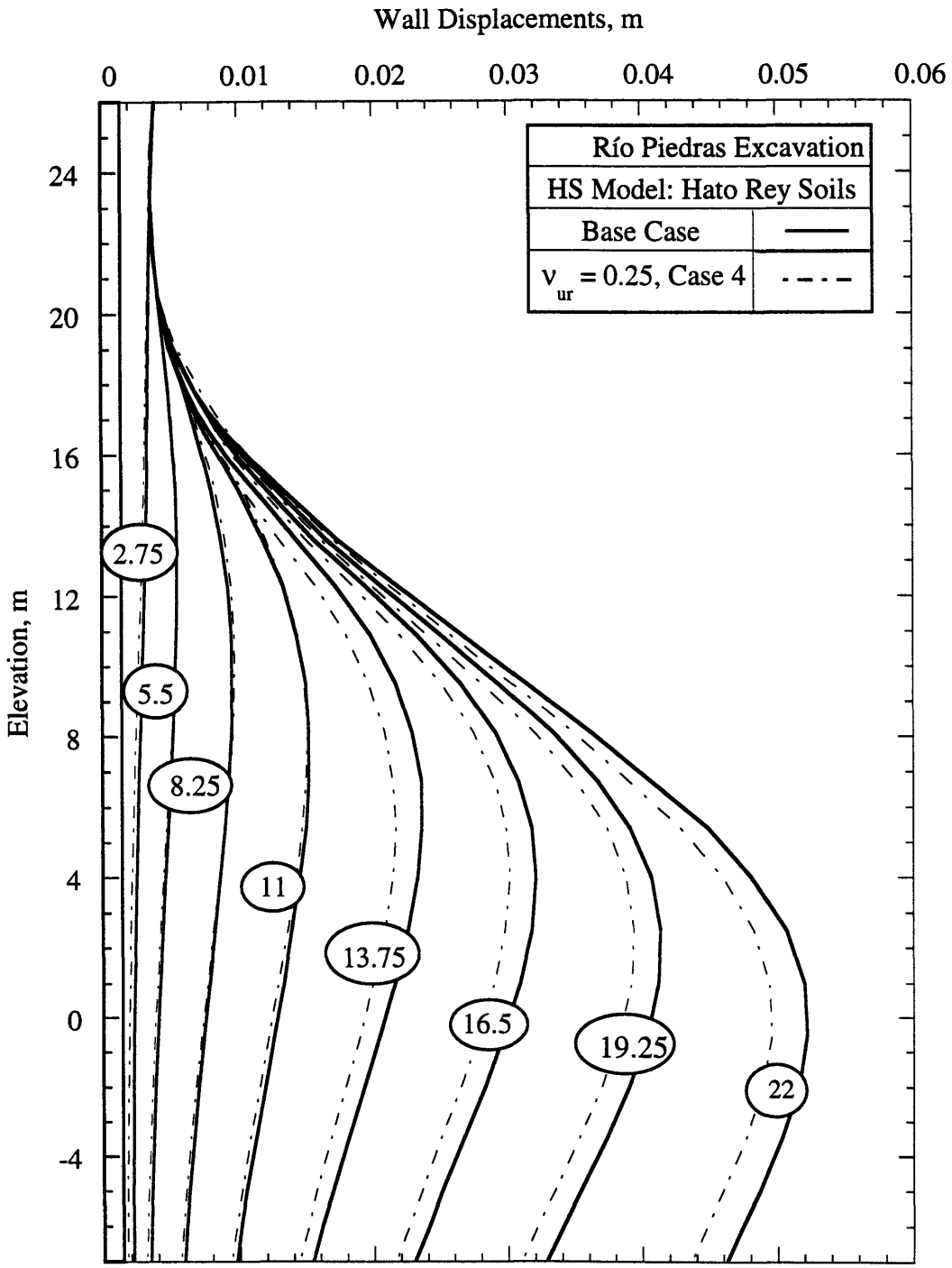

Figure 4.27 Effect of Poisson's Ratio on Wall Displacements

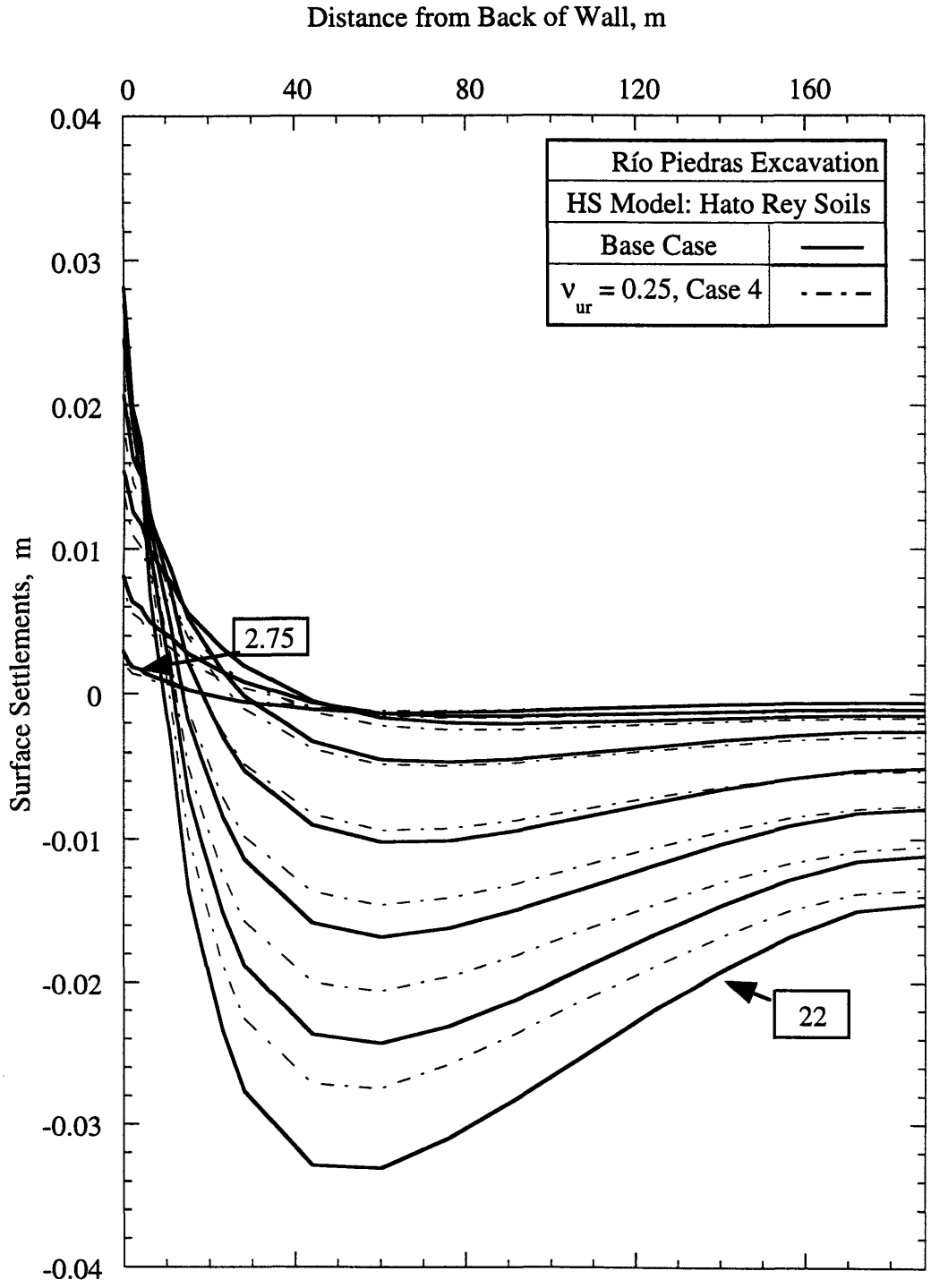

Figure 4.28 Effect of Poisson's Ratio on Ground Surface Settlements

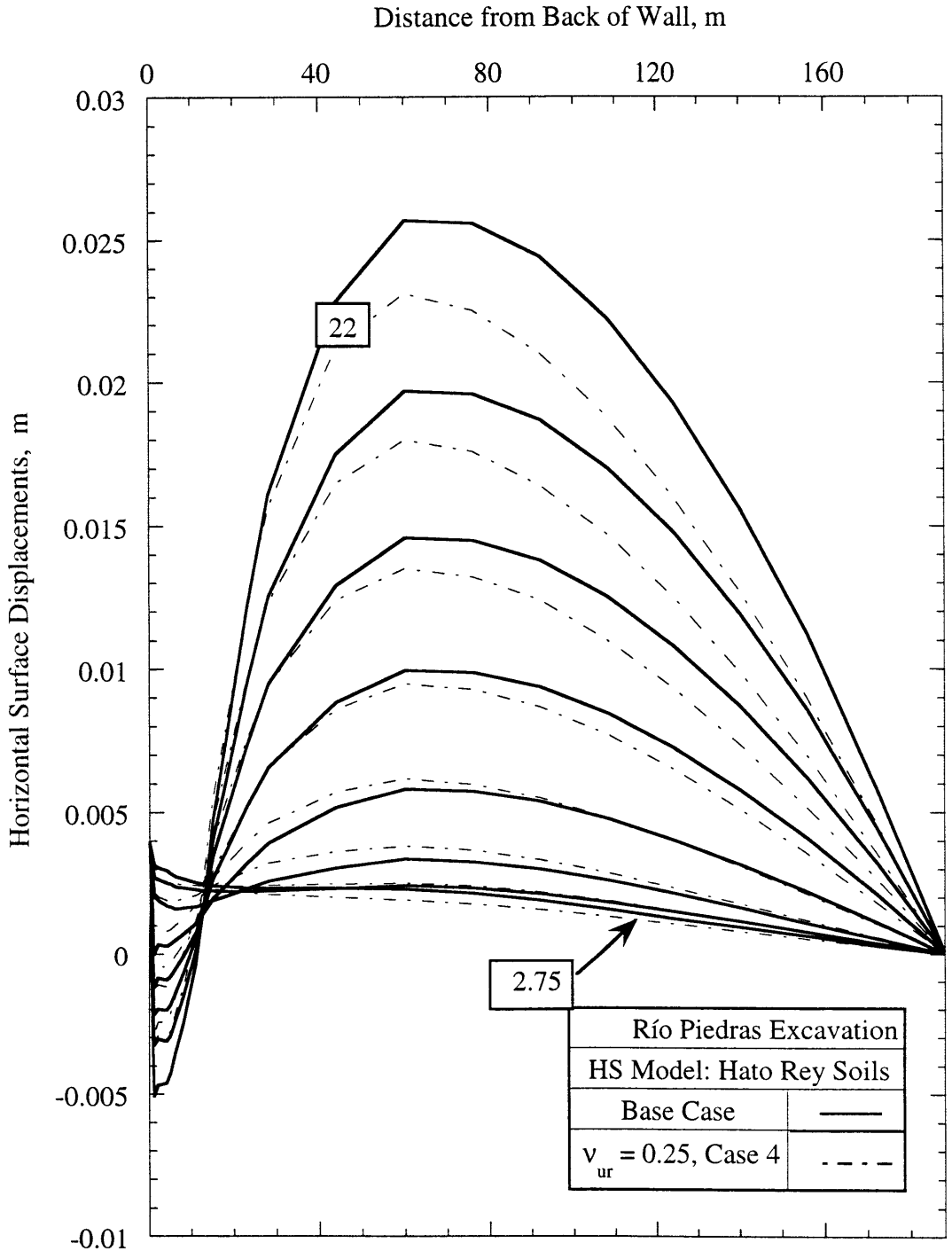

Figure 4.29 Effect of Poisson's Ratio on Horizontal Surface Displacements

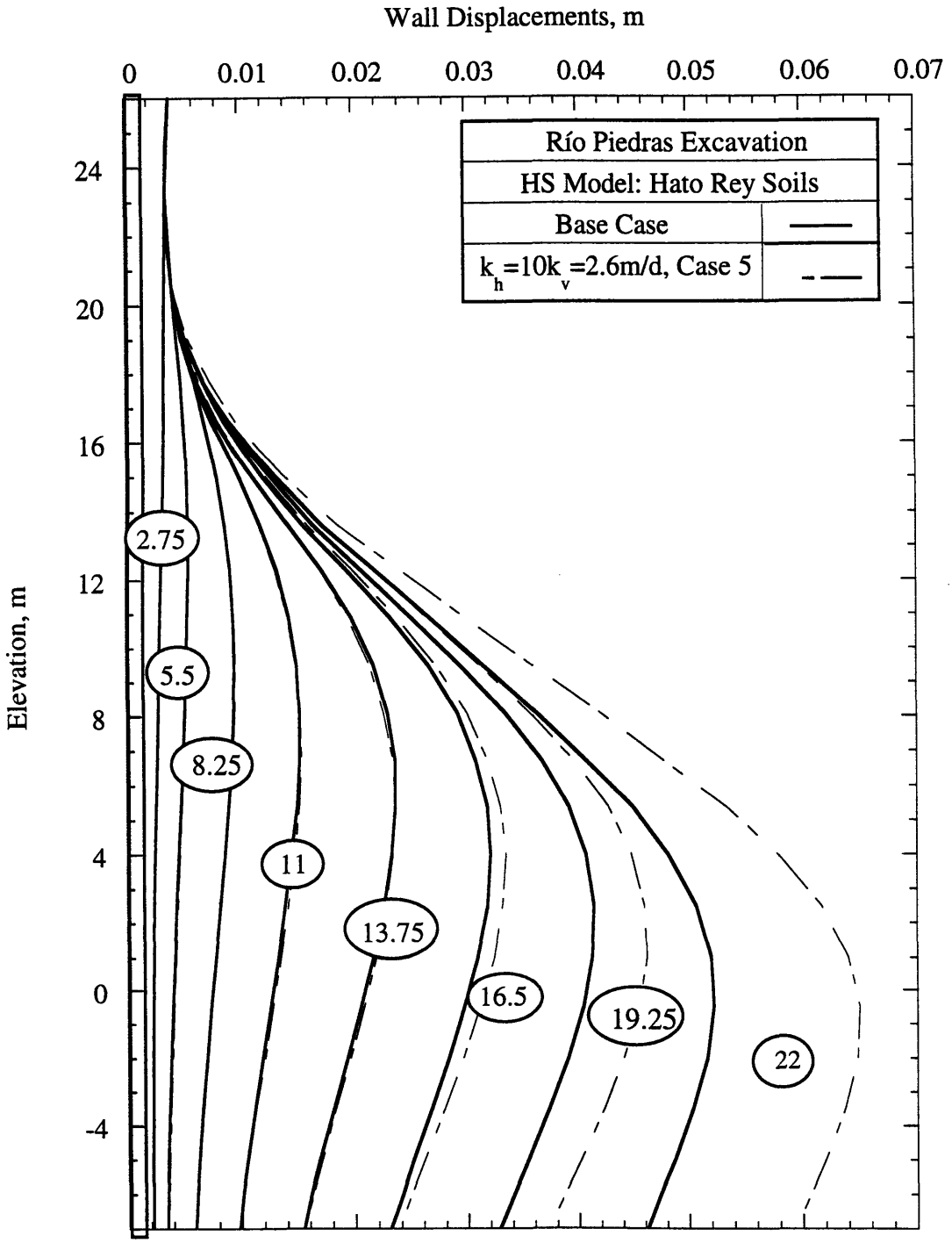

Figure 4.30 Effect of Anisotropic Permeability on Wall Displacements

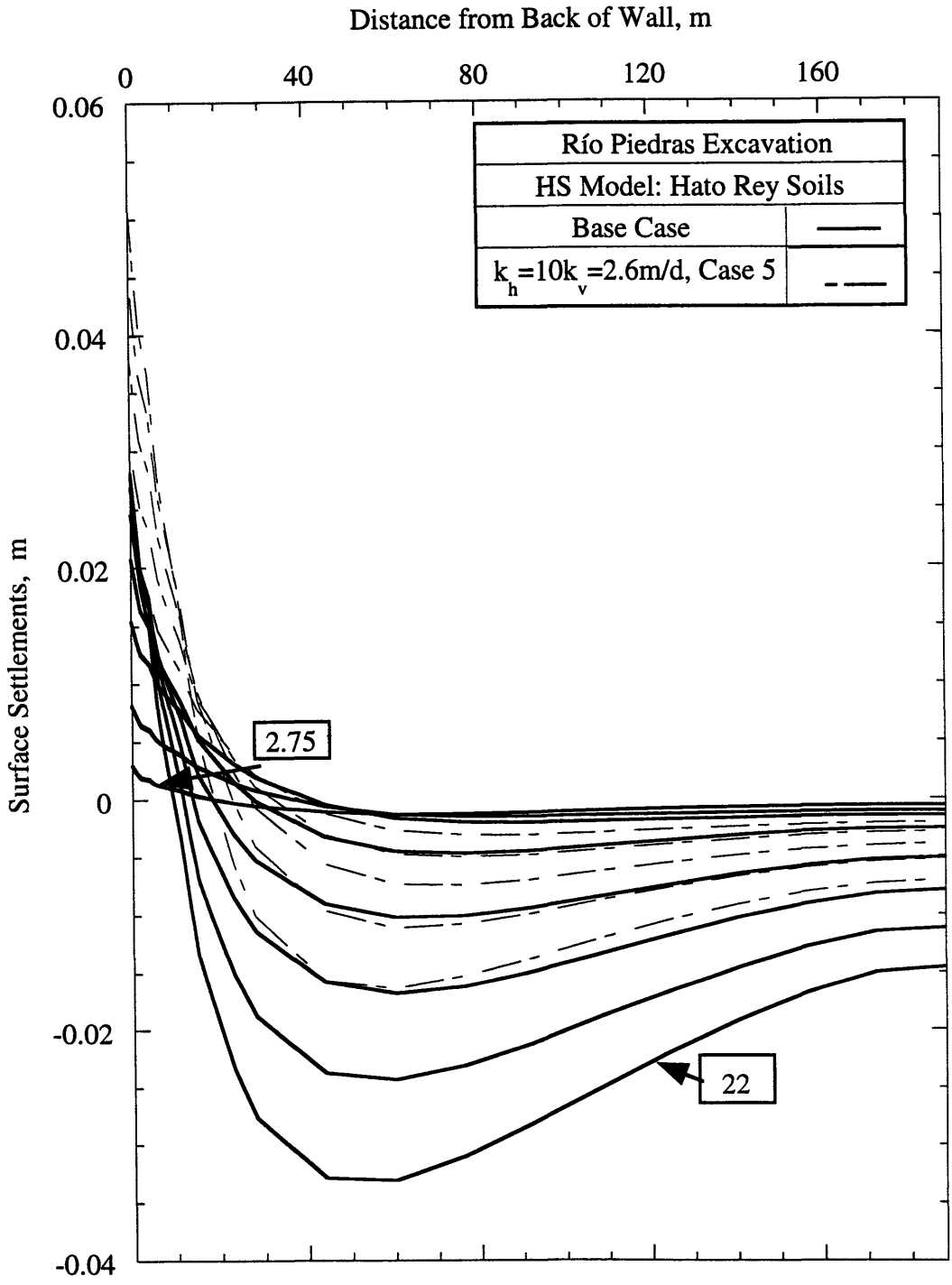

Figure 4.31 Effect of Anisotropic Permeability on Ground Surface Settlements

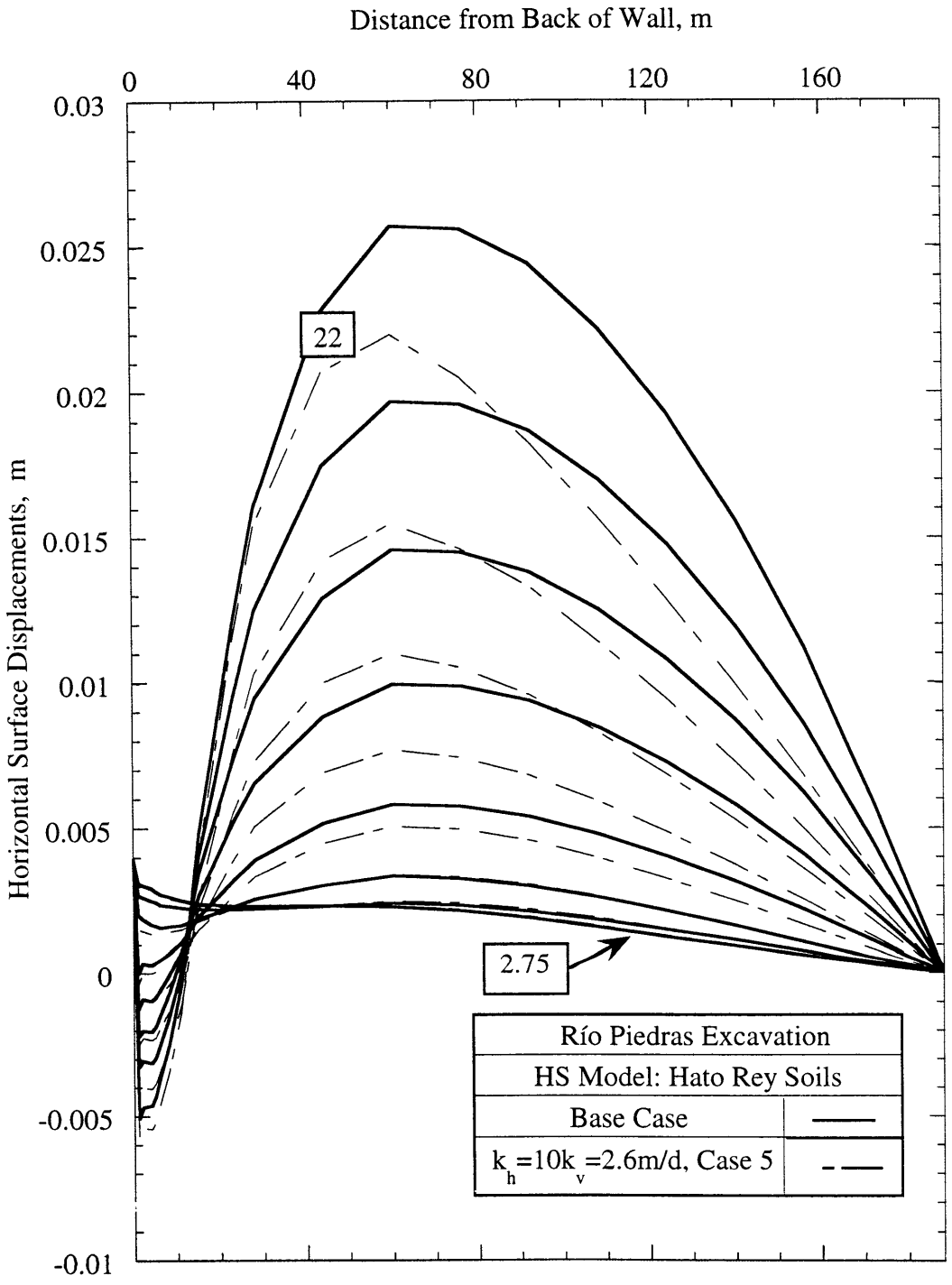

Figure 4.32 Effect of Anisotropic Permeability on Horizontal Surface Displacements

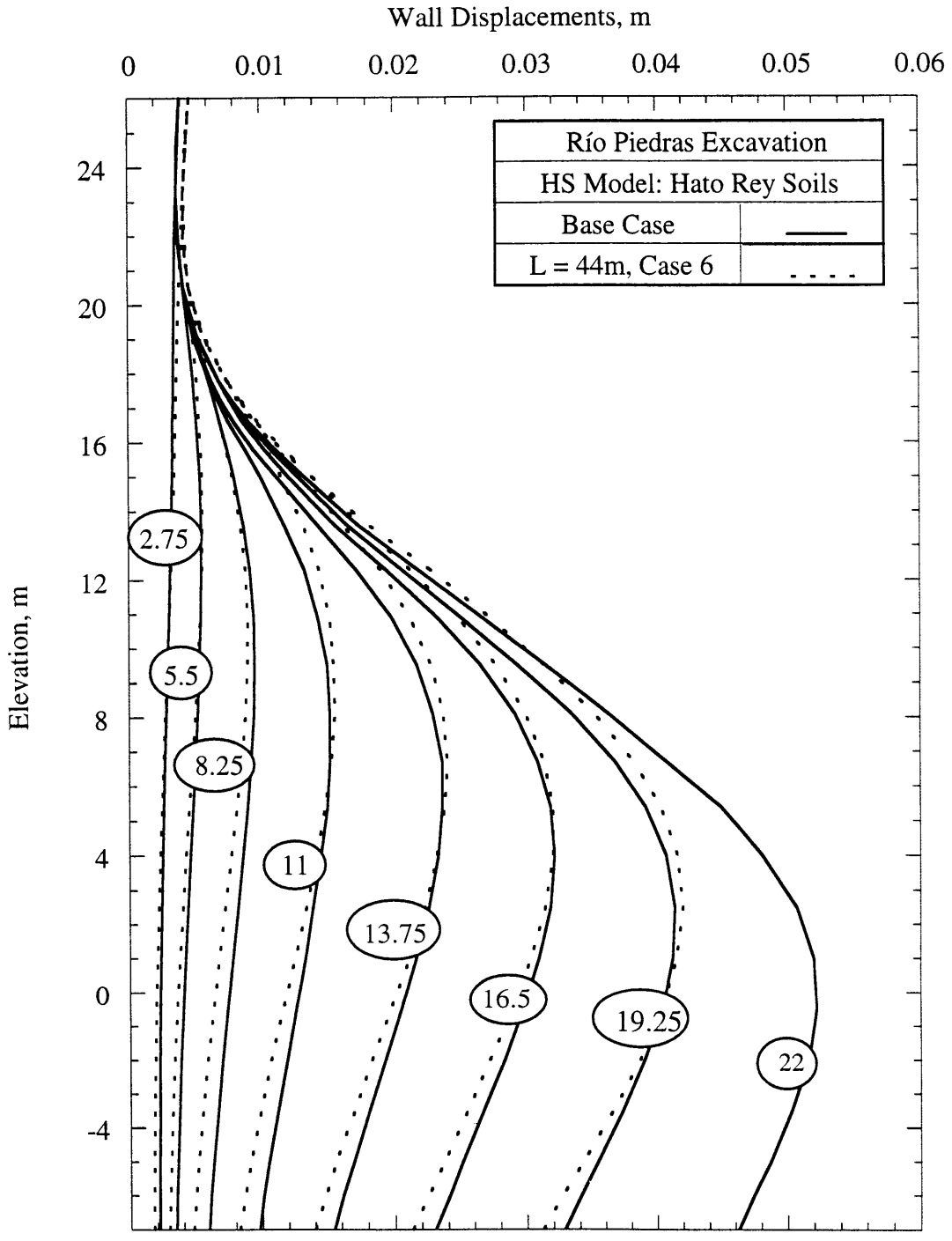

Figure 4.33 Effect of Wall Length on Wall Displacements

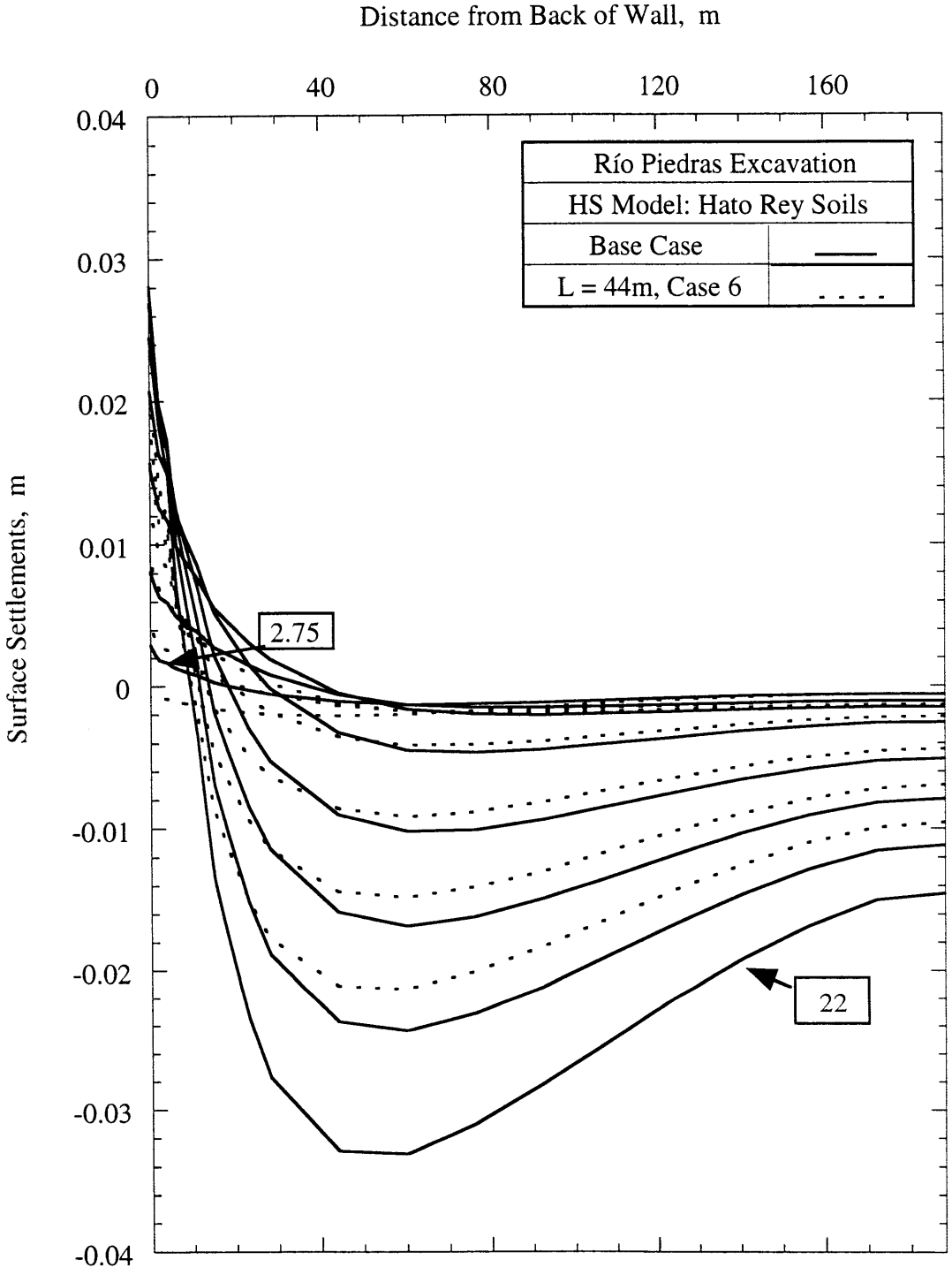

Figure 4.34 Effect of Wall Length on Ground Surface Settlements

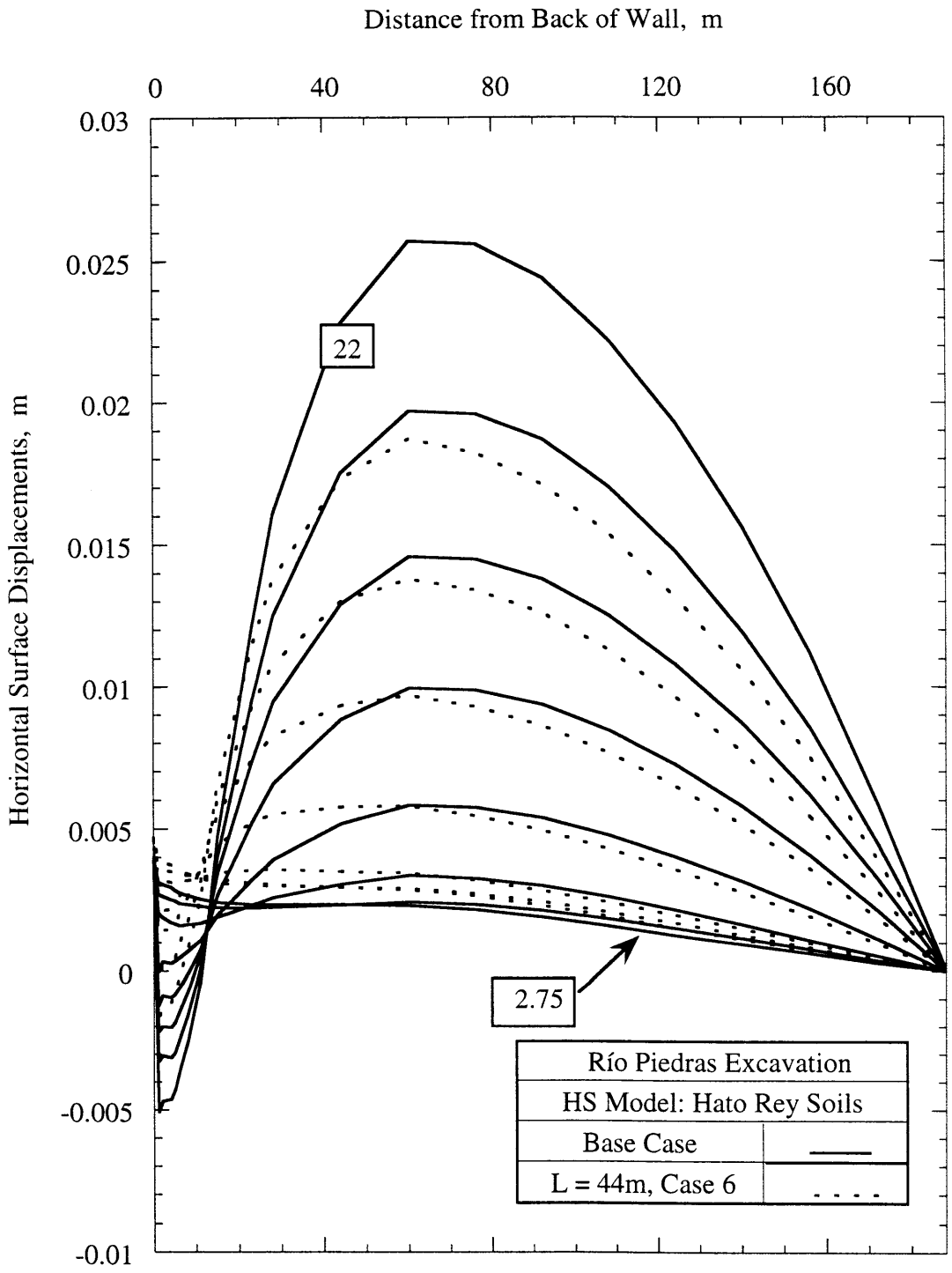

Figure 4.35 Effect of Wall Length on Horizontal Surface Displacements

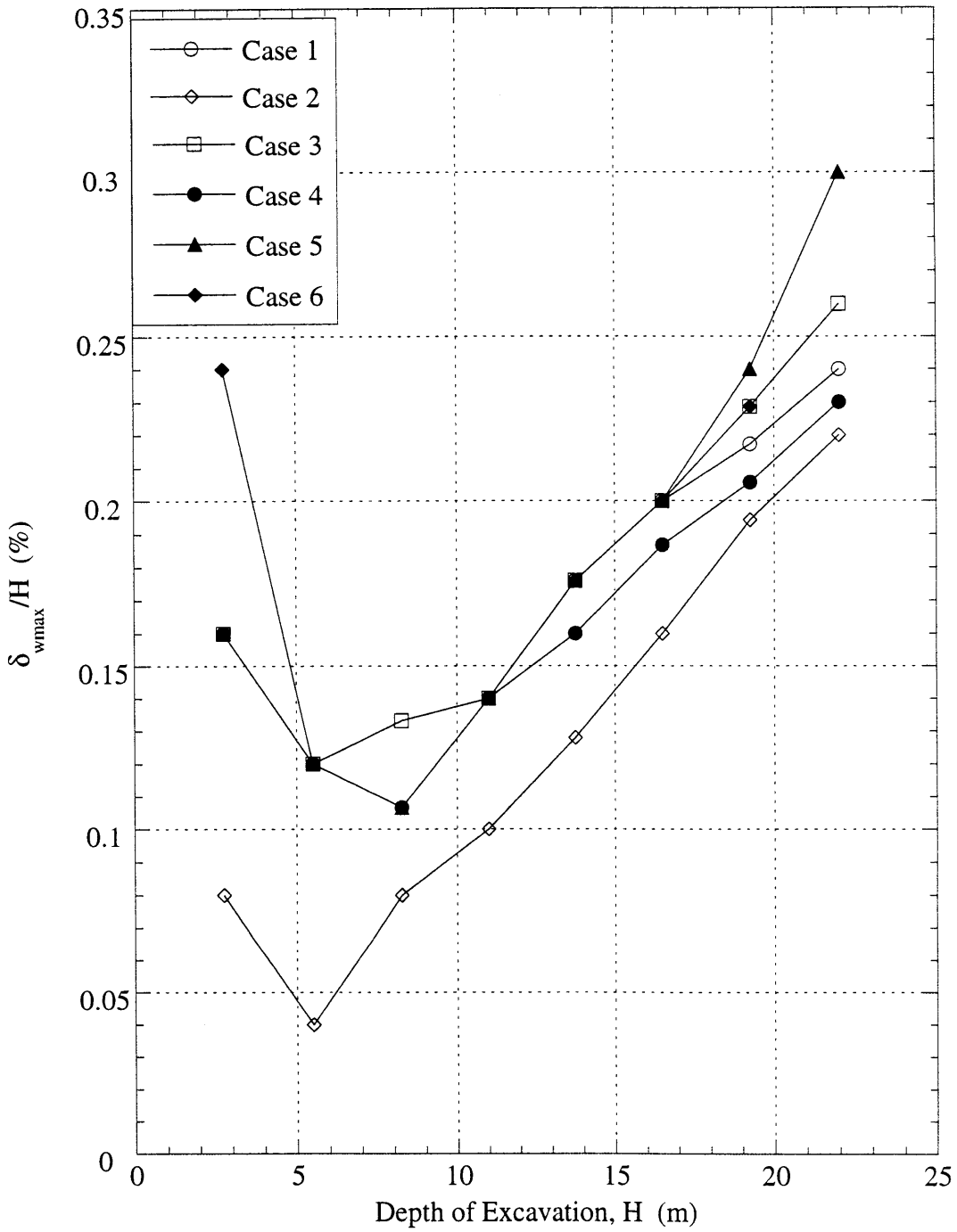

Figure 4.36 Maximum Lateral Wall Deflection Ratios, δ_{wmax}/H

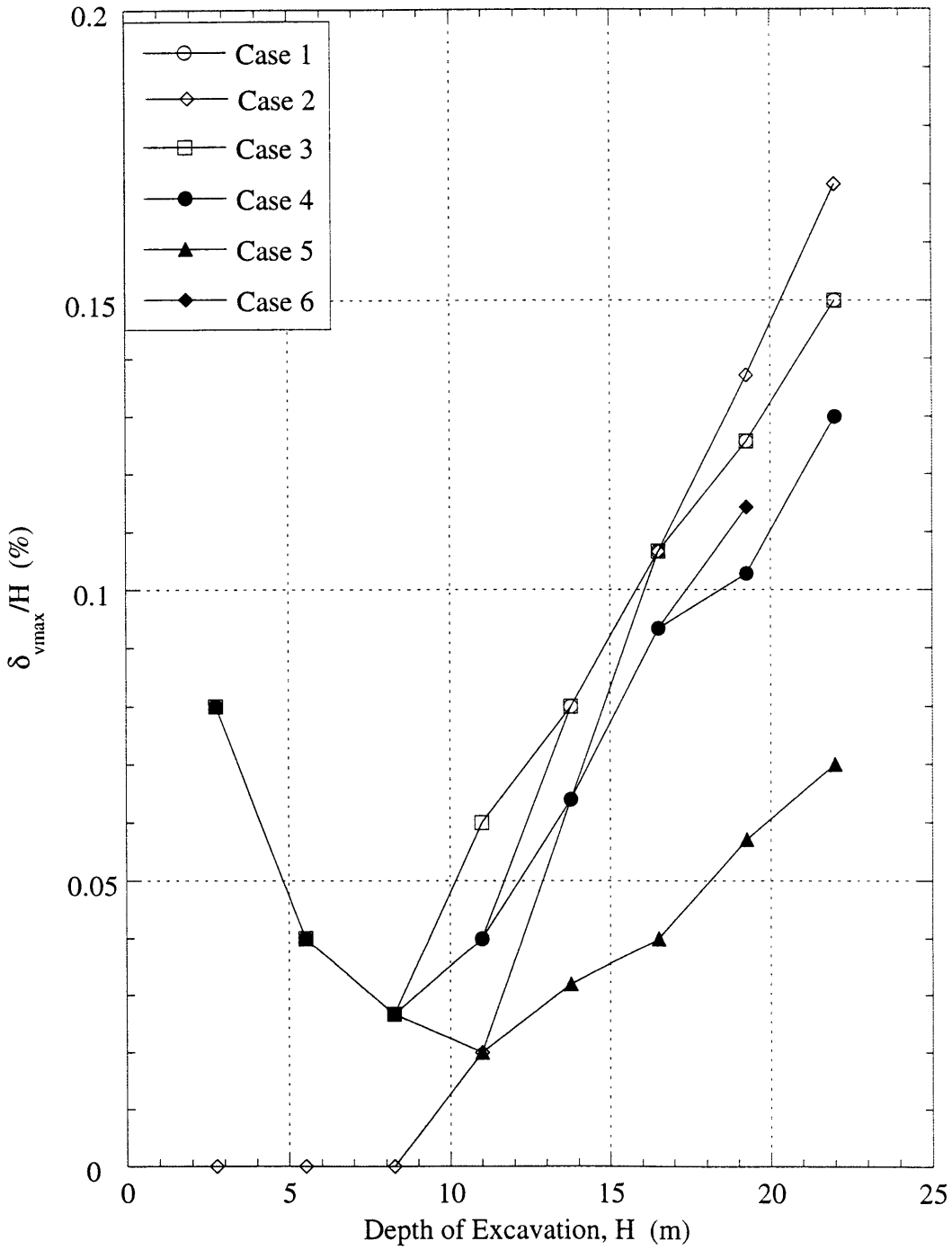

Figure 4.37 Maximum Soil Surface Settlement Ratios, δ_{vmax}/H

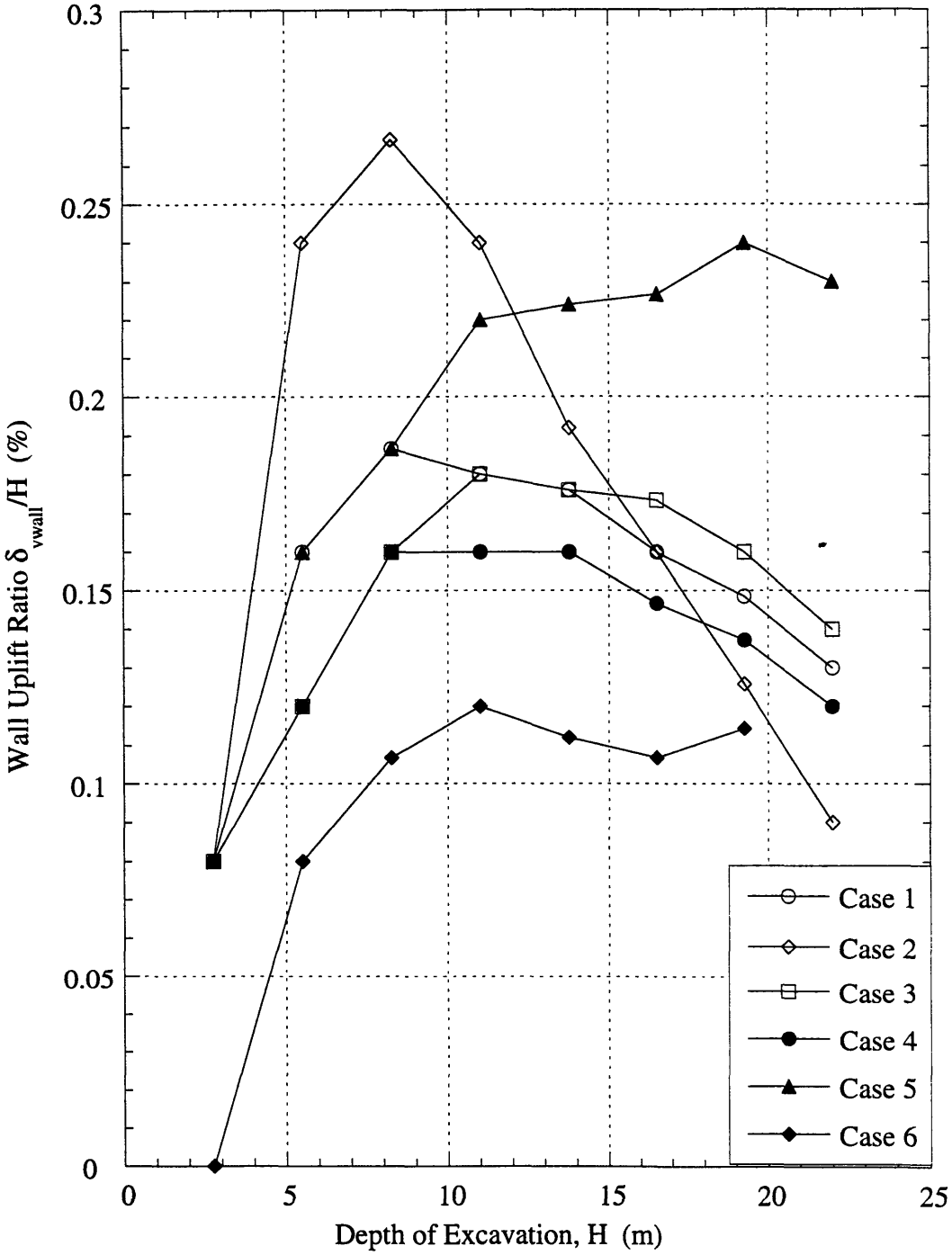

Figure 4.38 Comparison of Wall Uplift Ratios

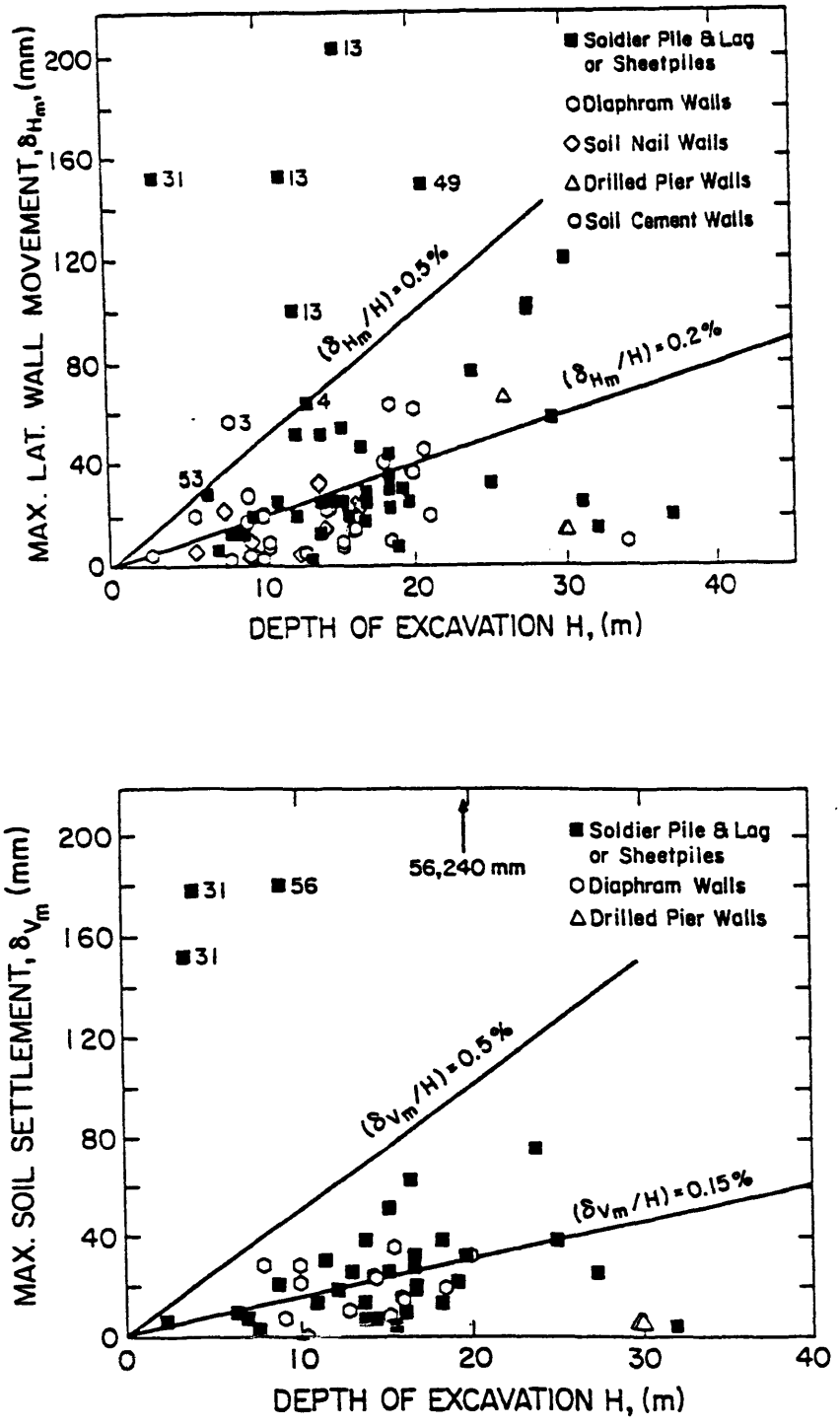

Figure 4.39 Observed Maximum lateral Movements and Soil Settlements reported in Literature (Clough and O'Rourke, 1990).

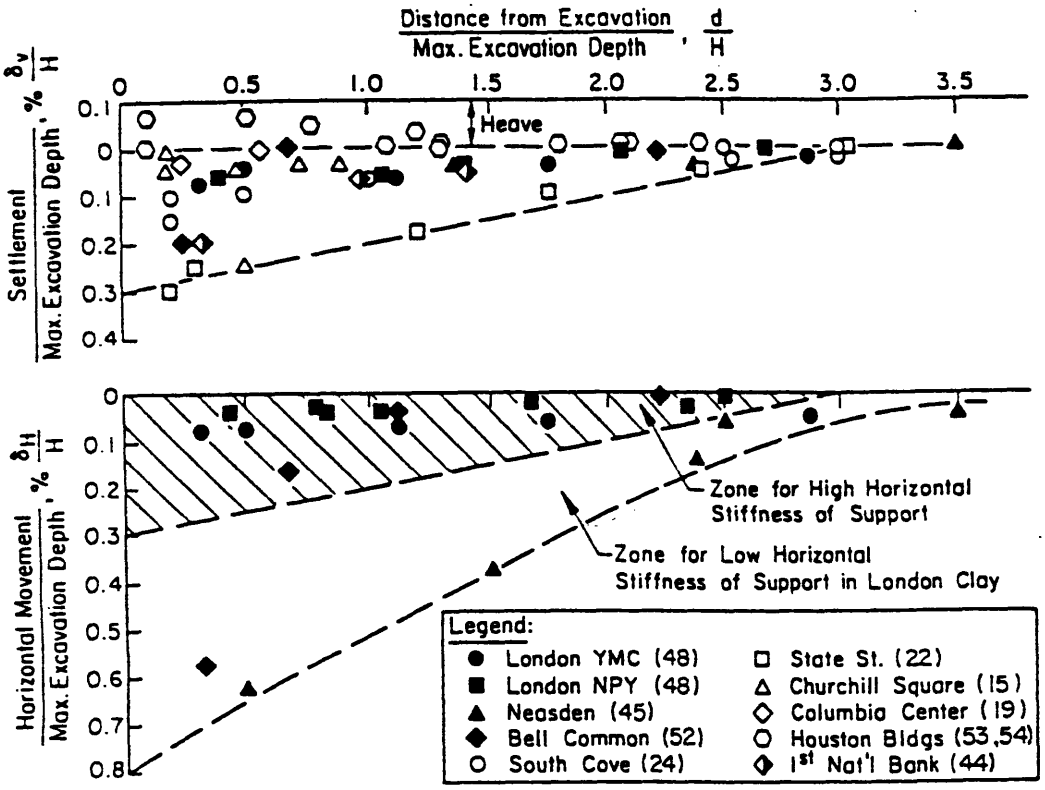

Figure 4.40 Summary of Measured Settlements and Horizontal Displacements Adjacent to Excavations in Stiff to Very Hard Clay (Clough and O'Rourke, 1990).

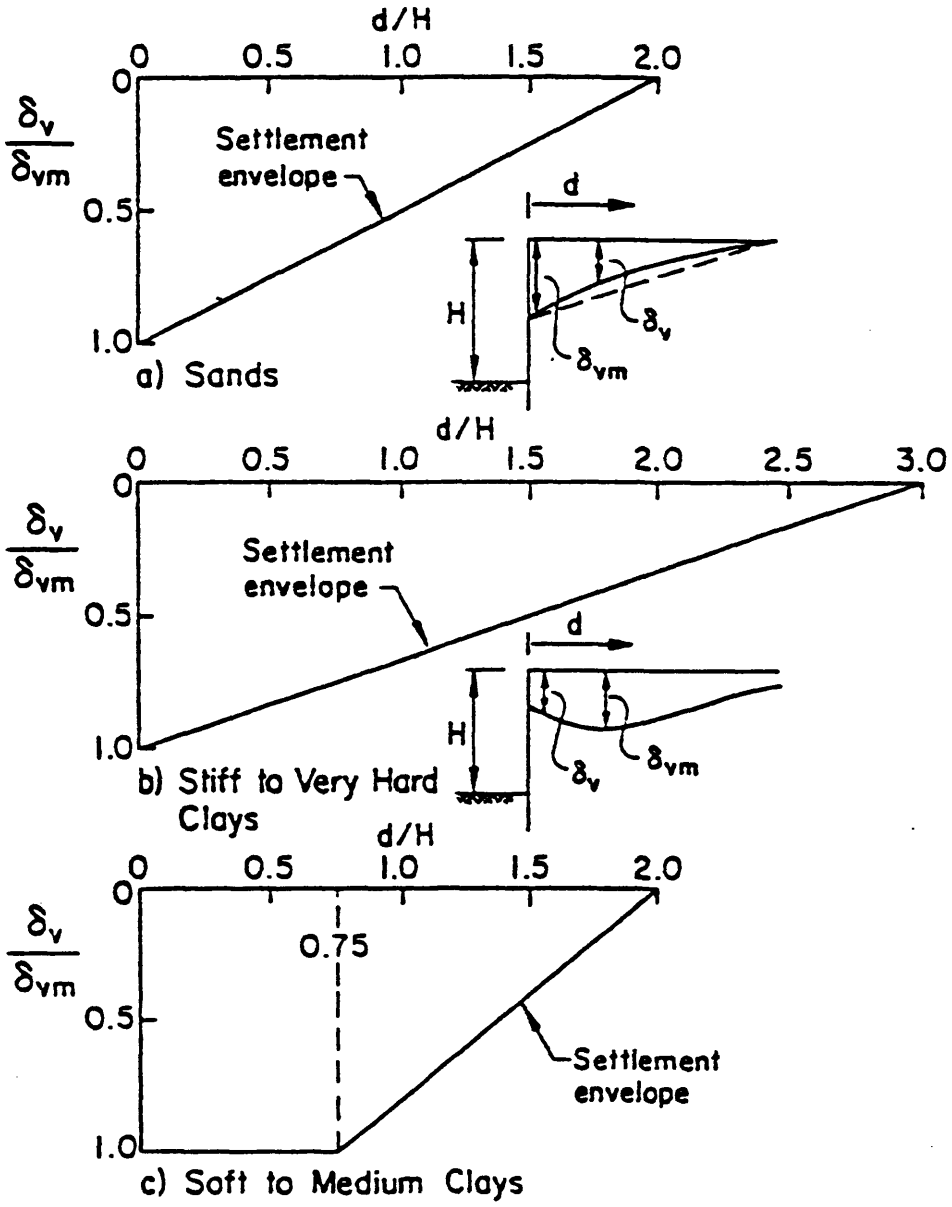

Figure 4.41 Dimensionless Settlement Profiles Recommended for Estimating the Distribution of Settlement Adjacent to Excavations in Different Soil Types (Clough and O'Rourke, 1990).

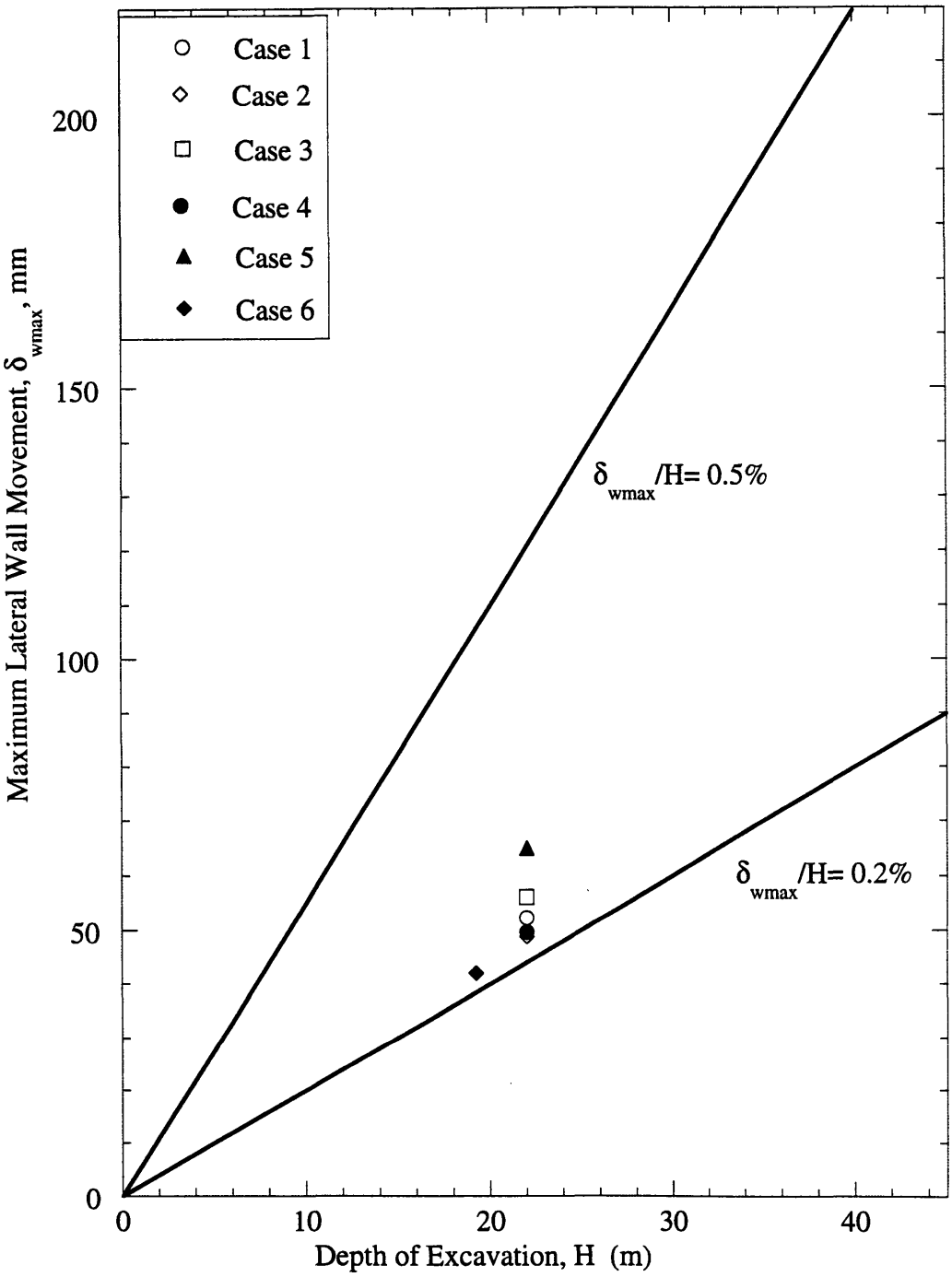

Figure 4.42 Maximum Lateral Movements for Río Piedras Excavation

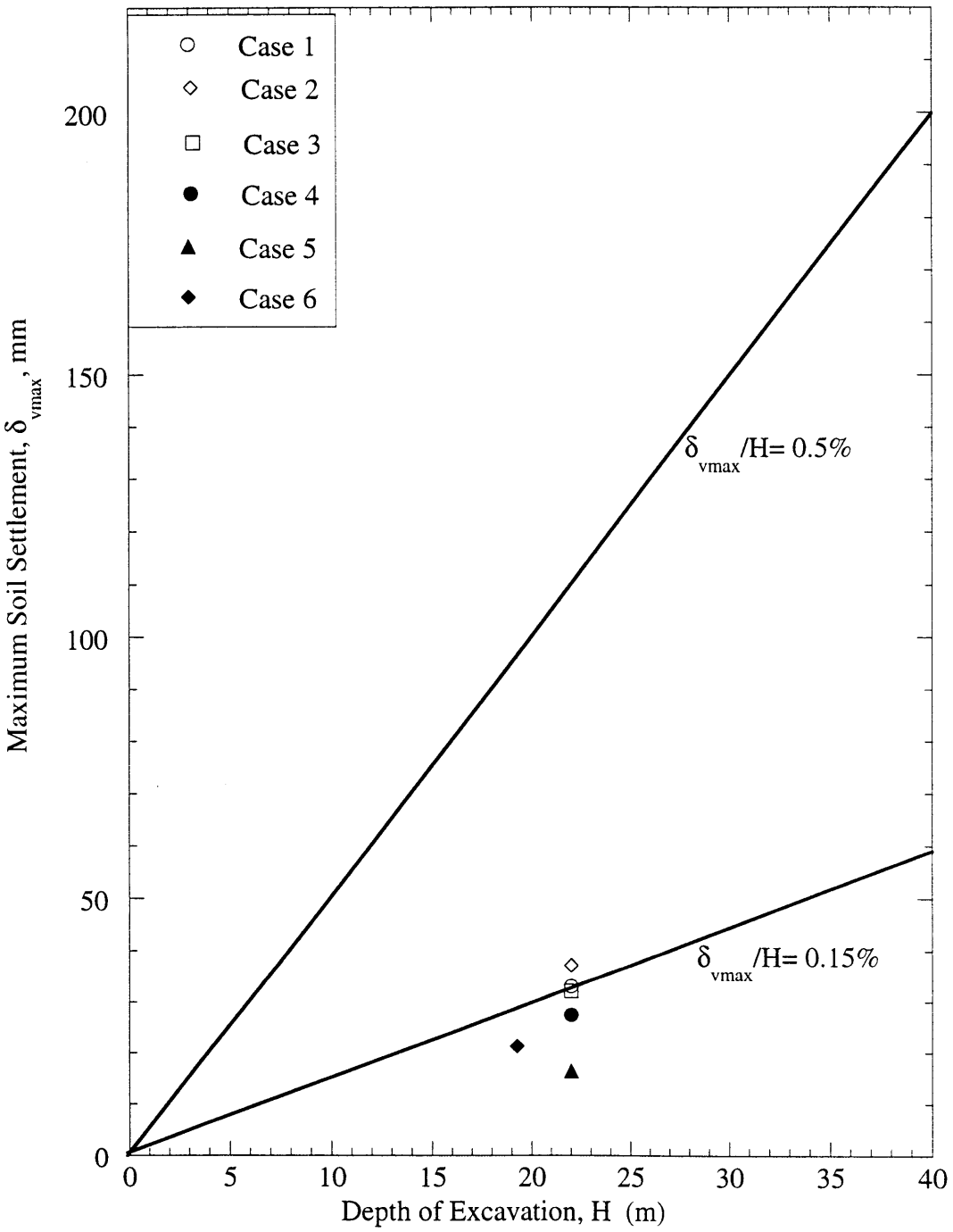

Figure 4.43 Maximum Soil Settlements for Río Piedras

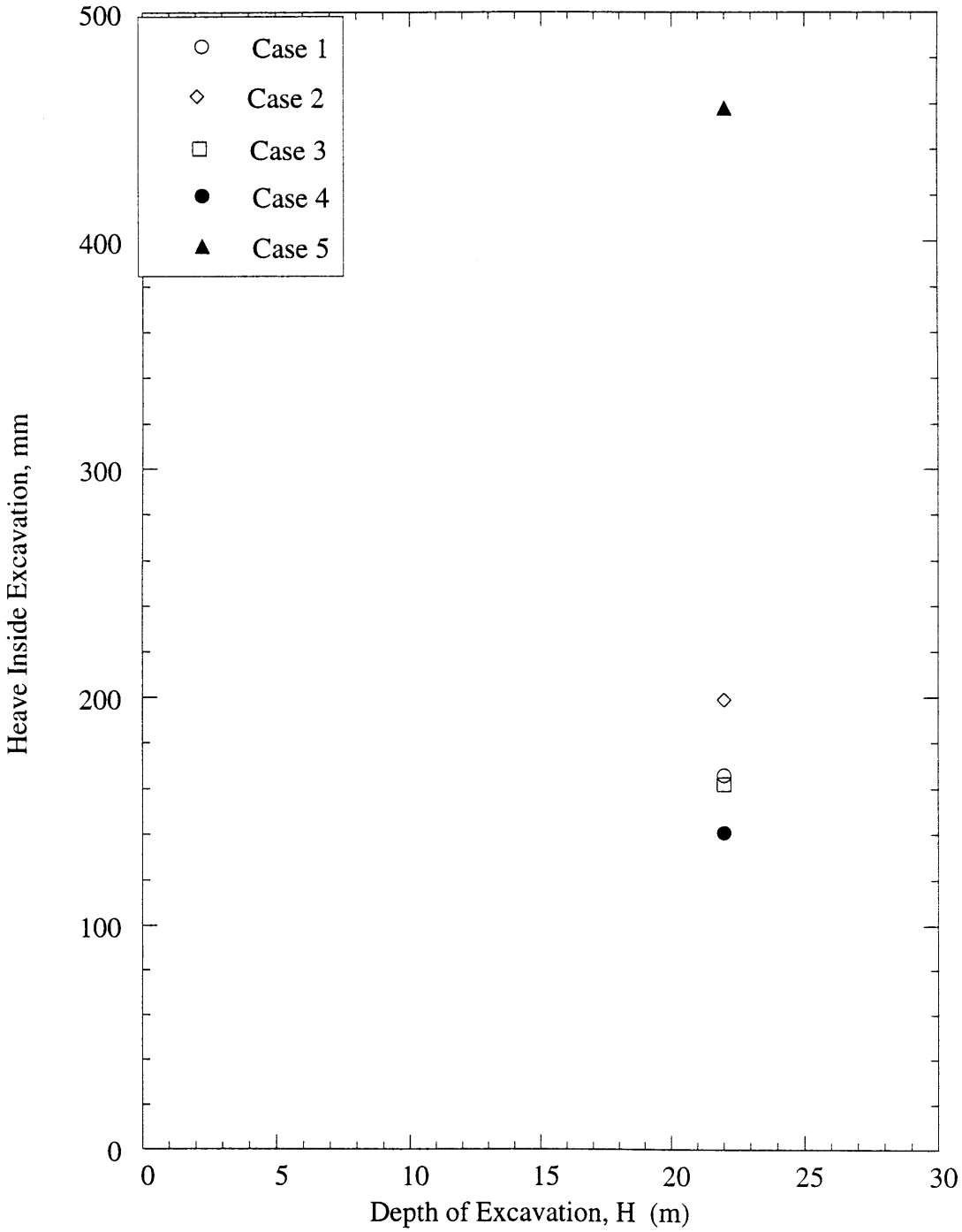

Figure 4.44 Heave Inside Excavation for Río Piedras at H = 22m

5. Summary, Conclusions and Recommendations

5.1 Summary and Conclusions

One of the principal factors affecting the design of deep excavations in cohesive soils is the control of ground deformations, in order to minimize damage to adjacent facilities and mitigate the costs of underpinning. This is especially true for construction in congested areas where the potential for damage to adjacent buildings, utilities, etc., can lead to very expensive remedial measures because of uncertainties in predicted deformations. In a constrained urban environment the influence of movements may be the most significant design issue and may severely impact the support system and construction methods. It is therefore essential to make reasonable predictions of ground deformations prior to construction, and to design lateral earth support systems to constrain the movements within acceptable limits. The goal of this project is to estimate the magnitudes of ground movements for proposed cut-and cover excavations in Section 7 of the Tren Urbano project, and to relate these movements to the stratigraphy of the surrounding alluvial soils.

Chapter 1 presents an overview of the Tren Urbano project, focusing on Section 7 in Río Piedras Section. The fundamentals of finite element analyses and semi-empirical methods for predicting ground movements were described. The main advantage of (non-linear) finite element analyses is their capability to model complex construction sequences and include detailed site-specific properties of the structural system and surrounding soils. This thesis uses Plaxis, a commercially available, PC based, non-linear, finite element program, which is fully capable of simulating the coupled soil deformation and groundwater flow that occurs due to the excavation.

Chapter 2 describes the geology of the San Juan Metropolitan area. The information was obtained from a small number of studies. The entire Río Piedras alignment consists of Older Alluvial deposits (Pleistocene and Pliocene age) comprising silty and sandy clays, with interbedded sands. These Hato Rey sediments are highly pre-consolidated by desiccation, and highly heterogeneous such that continuous units cannot be identified in adjacent boreholes. The soil deposits along this section of the alignment rest unconformably over bedrock at depths varying from about 30 to 100m. Perched ground water conditions are possible within the highly variable, discontinuous, lenticular sand deposits within the mainly clayey alluvium.

Chapter 3 presents information on field and laboratory test results and selected engineering properties. The initial geotechnical site investigations were completed in two phases (ending in February 1996), with a supplemental program (Phase III) in August- September 1996. The strength, flow and compressibility properties of Hato Rey formation were carefully evaluated. For depths up to El.+0m, an average undrained strength, s_u = 150 kPa, was obtained from the more reliable UUC and CIUC triaxial tests. Results from empirical correlations and backanalyses show that drained cohesion, c' = 40 kPa, drained friction angle approximately equal 24.6°. In general the compressibility m_v increases with the insitu water content w (or void ratio e_o) with typical values ranging from m_v= 0.0002m²/kN at e_o= 0.6 to m_v = 0.005m²/kN at e_o= 1.0. Groundwater conditions are hydrostatic with the water table located at El.+16m (near Río Piedras station). Upper and lower bounds of permeability, k = 2.6m/d and k = 0.26m/d, respectively, were estimated form slug and field pumping tests.

Chapter 4 describes the Hard Soil (HS) model selected for the numerical experiments and the modeling procedure used in Plaxis. The input material properties selected for Río Piedras are summarized in Table 4.1. The analyses focus on simplified excavation geometry, soil profile

and construction sequence (see Figures 4.12 - 4.14). The idealized geometry comprises a plane strain excavation with half width, B/2 = 11m supported by a 0.6m thick diaphragm wall. Due to the lack of laboratory test data from which to estimate material properties, a simple elasto-Plastic model, referred to as 'Hard Soil Model' (HS), is used to model soil behavior. In order to understand fundamental mechanisms controlling soil and wall movements, a series of numerical analyses were conducted, to investigate effects of individual parameters including the elastic soil stiffness properties, anisotropic permeability (reducing k_v relative to k_h) and wall embedment. The examination of the effect of these parameters leads to the following main observations:

1. The analyses show maximum wall deflections in the range δ_{wmax} = 4.8 to 6.6cm. The largest movements occur when anisotropic permeability is included in the analyses, while smallest movements occur when the elastic soil stiffness is reduced. All cases follow the same trend with decreasing rate of deflection with increase in excavation depth. The normalized wall deflections, δ_{wmax}/H, vary from 0.22% to 0.30% at the final excavation grade (H = 22m).
2. The analyses predict maximum settlements in the range δ_{vmax} = 1.5 to 3.7cm. Anisotropic permeability causes a reduction in settlements, while the largest settlements occur for the lowest elastic soil stiffness. The normalized ground settlements, δ_{vmax}/H, varies from 0.07% to 0.17% at H= 22m.
3. All of the analyses predict significant upward movement. These predictions are considered unrealistic and arise due to limitations of the HS soil model.

In general, the finite element analyses results on magnitudes of maximum wall deflections, ground settlements and horizontal surface movements have very good agreement with empirical ground movements data from excavation histories (Clough and O'Rourke, 1990). However, the distribution of the settlements and horizontal surface movements is not realistic.

5.2 Main Sources of Uncertainty

The main sources of uncertainty in achieving reliable analytical predictions of soil deformations can be attributed to several factors:

1. Limitations in the site investigation and geometric approximations. The initial conditions in the ground (stratigraphy, initial stress state, and ground water flow regime) can play a significant role in the modes of deformation that occur.
2. Uncertainties in the selection of engineering properties (strength, flow and compressibility properties) as a result of inadequate laboratory and field characterization.
3. Constitutive representation of soil behavior using the HS model in the PLAXIS program.

Soil modeling has an important role in the predictive accuracy of finite element analyses. More realistic distribution of surface settlements and horizontal surface deformations can be achieved by using more realistic soil models to describe soil behavior. However, the use of a sophisticated soil model is only appropriate when high quality input data are available. The complex stratigraphy for Río Piedras brings other problems to the modeling process. The wide variability in texture, composition and appearance of Hato Rey soils makes the selection of model input parameters for an averaged soil profile very difficult.

5.3 Recommendations

Control of ground movements is likely to be a significant issue in Río Piedras since predictions from the simplified analyses are similar in magnitude to the allowable movements. This represents a problem, especially if damage does occur (i.e. cracking of structure, etc.). More refined analyses can be achieved if more reliable data is available. The principal problem is how to determine representative soil behavior given the complex layering of Hato Rey soils.

The borehole data (Figures 3.2 – 3.4) show main layers are clays, sandy clays and clayey sand, all of which can be sampled. Characteristic layers are 1 to 2m thick. By taking almost continuous samples from 1 borehole (and x-raying), 3 or more main horizons can be identified to perform the necessary laboratory tests. The main problem to estimate permeability values, k, is the lack of layer continuity, which already affected previous pumping tests on Río Piedras. This behavior can be modeled by calibrating k more carefully using k_v, k_h, assuming horizontal layering and estimating the bulk k (similar to varved clay).

Additional site investigation is needed primarily to define the deformation (stiffness) properties of the Hato Rey deposits and to select input parameters for advanced constitutive models. The additional tests suggested include:

1. Cross-hole seismic shear wave testing between to boreholes to estimate shear stiffness profile in the field. This tests could be done using conventional equipment (e.g., Stokoe and Woods, 1972) or using seismic cone devices (Campanella et al., 1986).
2. Additional consolidation and triaxial shear tests:

   A. The triaxial shear tests should be performed on samples that are re-consolidated under K_o conditions to the estimated in situ stress state.

   B. A combination of undrained and drained compression and extension shear tests.

   C. Consolidation tests using high pressure triaxial equipment to measure compression and lateral stress (K_o) properties at stress levels exceeding the pre-consolidation pressures, σ'_p. Permeability and consolidation properties should be estimated from Constant Rate of Strain (CRS) consolidation tests.
3. K_o estimated from filter paper suction measurements (Chandler and Gutierrez, 1986) on undisturbed soil samples.

4. A series of K_o-consolidated Direct Simple Shear tests, using a Geonor direct simple shear device, to provide essential independent validation of model predictions.

The main focus, in general, is to perform laboratory testing on high quality soil samples. Undisturbed samples should be obtained using a Denison core barrel (3.5" O.D.) The selection of test specimens should be guided by x-ray inspection of sample quality and uniformity. The x-rays also provide data on desiccation and other features of the macro-fabric.

In addition to improving the available soil data, advanced constitutive modeling is essential to obtain more realistic predictions of ground movements. The MIT-S1 effective stress soil model (Pestana, 1994) is well suited for characterizing the behavior of the stiff Hato Rey alluvial deposits. If the proposed program of laboratory tests are carried out it will be possible to use this type of advanced soil model to refine the predictions describe in this thesis.

References

Bakker, K.J. and Vermeer, P.A. (1986). "Finite Element Analysis of Sheet Pile Walls," *Int. Symposium on Numerical Models in Geomechanics*, NUMOG III, Niagara Falls, Canada, pp. 455-462.

Campanella, R.G., Robertson, P.K. and Gillespie, D. (1986). "Seismic cone penetration test," *Proc. In-Situ '86, Blacksburg, VA, 116-130.*

Capacete, J.L. (1997) Personal Communication

Chandler, R.J. and Gutierrez, C.I. (1986). "The filter paper method of soil suction measurement," *Géothecnique*, 36(2), 265-268.

Christian, J.T. & Wong, I.H. (1973). "Errors in simulating Excavation in Elastic Media by Finite Elements." *Soils and Foundations*, 13(1), 1-10.

Clough, G.W., Smith, E.M. and Sweeney, B.P. (1989). "Movement Control of Excavation Support Systems by Iterative Design." *Foundation Engrg Proceedings Congress,* ASCE, Evanston, Ill., pp.869-884.

Deasi, C.S. (1988). "Case Studies through Material Modelling and Computation," *Case Histories in Geotechnical Engrg*, 2nd Int. Conference, St. Louis, Vol. II, pp. 1551-1565.

Deere, D.E. (1955). "Engineering Properties of the Pleistocene and recent sediments of the San Juan Bay Area, Puerto Rico," *PhD Thesis*, University of Illinois.

Duncan, J.M., and Chang, C.Y. (1970). "Nonlinear Analysis of Stress-Strain in Soil," *ASCE J. of the Soil Mech. And Found. Div.* Vol. 96, pp. 1629- 1653.

Earth Scientific Consultants and McCann, W. (1994). "Seismic Hazard Map for Puerto Rico 1994," The Seismic Safety Commission of Puerto Rico.

FTA and Puerto Rico Highway and Transportation Authority, *Final Environmental Impact Statement, Tren Urbano, San Juan Metropolitan Area*

GDR (1996a). "Geotechnical Data Report, Tren Urbano, Section 7; April 1996", .

GDR (1996b). "Geotechnical Data Report, Tren Urbano, Section 7; October 1996", .

Hashash, Y.M.A (1992) "Analysis of Deep Excavations in Clay," *PhD Thesis*, Massachusetts Institute of Technology, Cambridge, MA.

Head (1980). Manual of "Soil Laboratory Testing", Chapter 14, Wiley

Kaye, C.A. (1959). "Geology of the San Juan Metropolitan Area, Puerto Rico" *USGS* Prof. Paper317-A.

Lambe, T. W. and Whitman, R. V. (1969)."Soil Mechanics" John Wiley and Sons.

McCann, W. and Sykes, L.R. (1984). "Subduction of Aseismic Ridges Beneath the Caribbean Plate: Implications for Tectonics and Seismic Potential of the Northeastern Caribbean," JGR 89 (B6), 4493-4519.

Mesri & Adel-Ghaffar (1993). JGE, ASCE, 119(8).

Meyerhoff, H.A. (1927). "Tertiary Physiographic Development of Porto Rico and the Virgin Islands." *Geol. Soc. America*, Bull, Vol. 38, pp.557-576.

Meyerhoff, H.A. (1933). "Geology of Puerto Rico." University of Puerto Rico Mon., Ser. B., No. 1, 306 p.

Monroe, W.H. (1976). "The Karst Landforms of Puerto Rico." USGS, Professional Paper 899.

Monroe, W.H. and Pease, M.H. (1977). Geologic Map of the San Juan Quadrangle, Puerto Rico; *US Geological Survey.*

O'Rourke, T.D and Clough, G.W. (1990). "Construction Induced Movements of Insitu Walls." *Proc. ASCE: Design and Performance of Earth Retaining Structures,* 439- 470.
Pestana, J.M. (1994) "A unified constitutive model for clays and sands," *PhD Thesis*, Massachusetts Institute of Technology, Cambridge, MA.
Schanz, T. and Vermeer, P.A. (1996). "An Adequate Model for Sand Soil Behavior".
Simpson, B., Calabresi, G., Sommer, H., and Wallays, M. (1979)."Design Parameters for Stiff clays" *Proceedings of the Seventh European Conference on Soil mechanics and Foundation* Engineering, Brighton, UK, Vol. 5, 91- 124.
Stokoe, K.H. and Woods, R.D. (1972). "In-situ shear wave velocity by cross-hole method," *Journal of the Soil Mechanics and Foundations Division*, 98(5), 443-460.
Whittle, A.J. (1996). "Prediction of Excavation Performance in Clays." *To appear BSCE J. of Civil Engineering Practice.*
Whittle, A.J., Hashash, Y.M.A. (1994). "Soil Modeling and Prediction of Deep Excavation Behavior," *Proc. of the International Symposium on Pre-failure Deformation Characteristics of Geomaterials*, Sappore, Japan, Vol. 1,589-594.
Whittle, A.J., Hashash, Y.M.A. & Ladd, C.C. (1993b). "Analysis of excavations in Taipei clay," Research Report R93-12, Department of Civil & Environmental Engineering, MIT, Cambridge, MA, 78p.
Whittle, A.J., Hashash, Y.M.A. & Whitman, R.V. (1993a). "Analysis of a Deep Excavation in Boston," J. *Geotech. Engrg.*, ASCE, 119(1),69-90.

A. Finite Element Analyses Case Studies

Post Office Square, Boston

(Whittle et al., ASCE J. Geotechnical Engineering, 119(1),69-91)

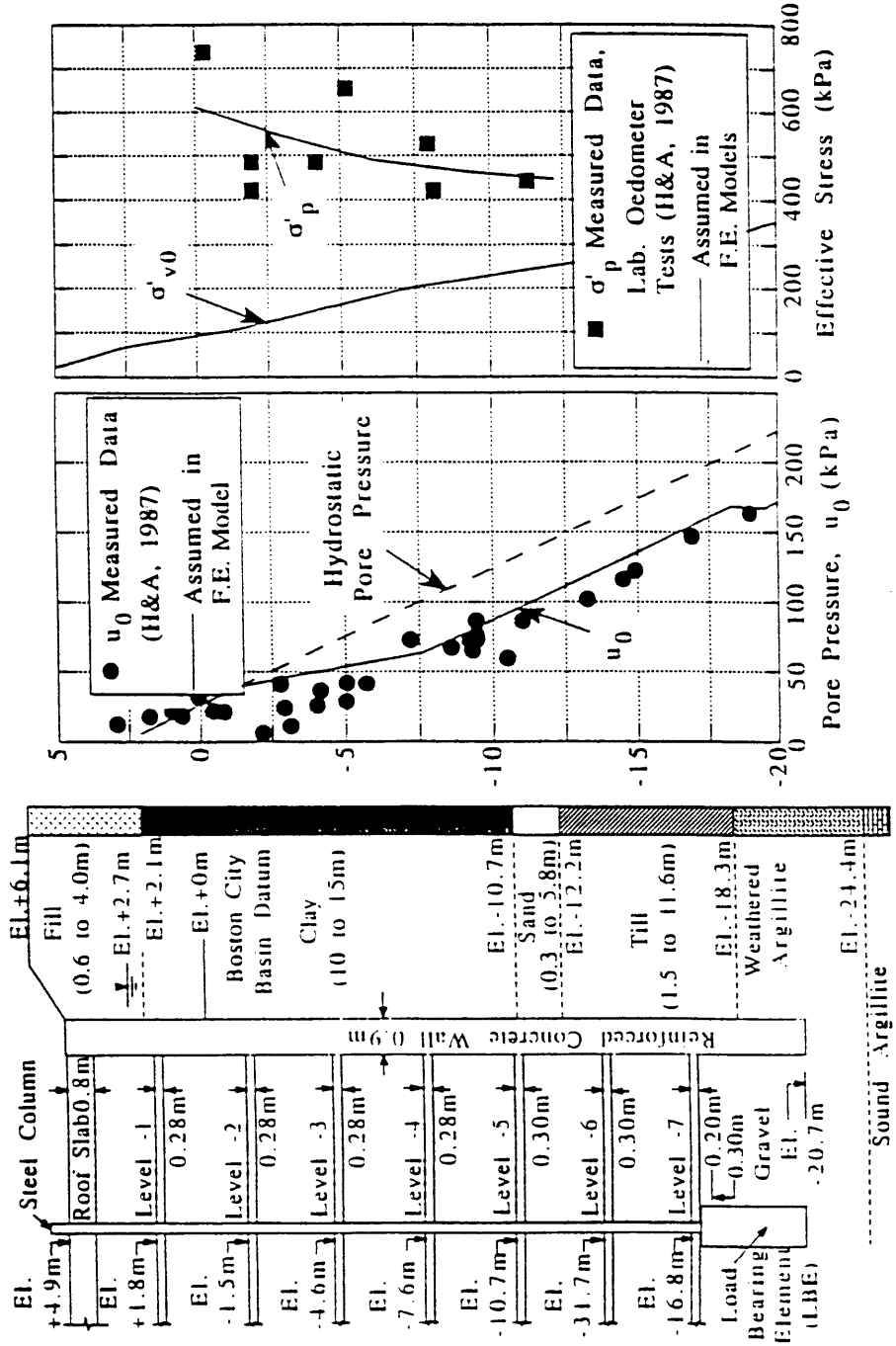

Figure A1 Garage structure and initial soil conditions at Post Office Square, Boston. Principal uncertainties in the ground conditions included the in-situ ground water pressures and engineering properties of the underlying till (glaciomarine) and weathered argillite. The excavation follows a top-down sequence. The perimeter diaphragm wall is braced internally by cast in-situ concrete floor slabs with internal columns supported by load-bearing elements.

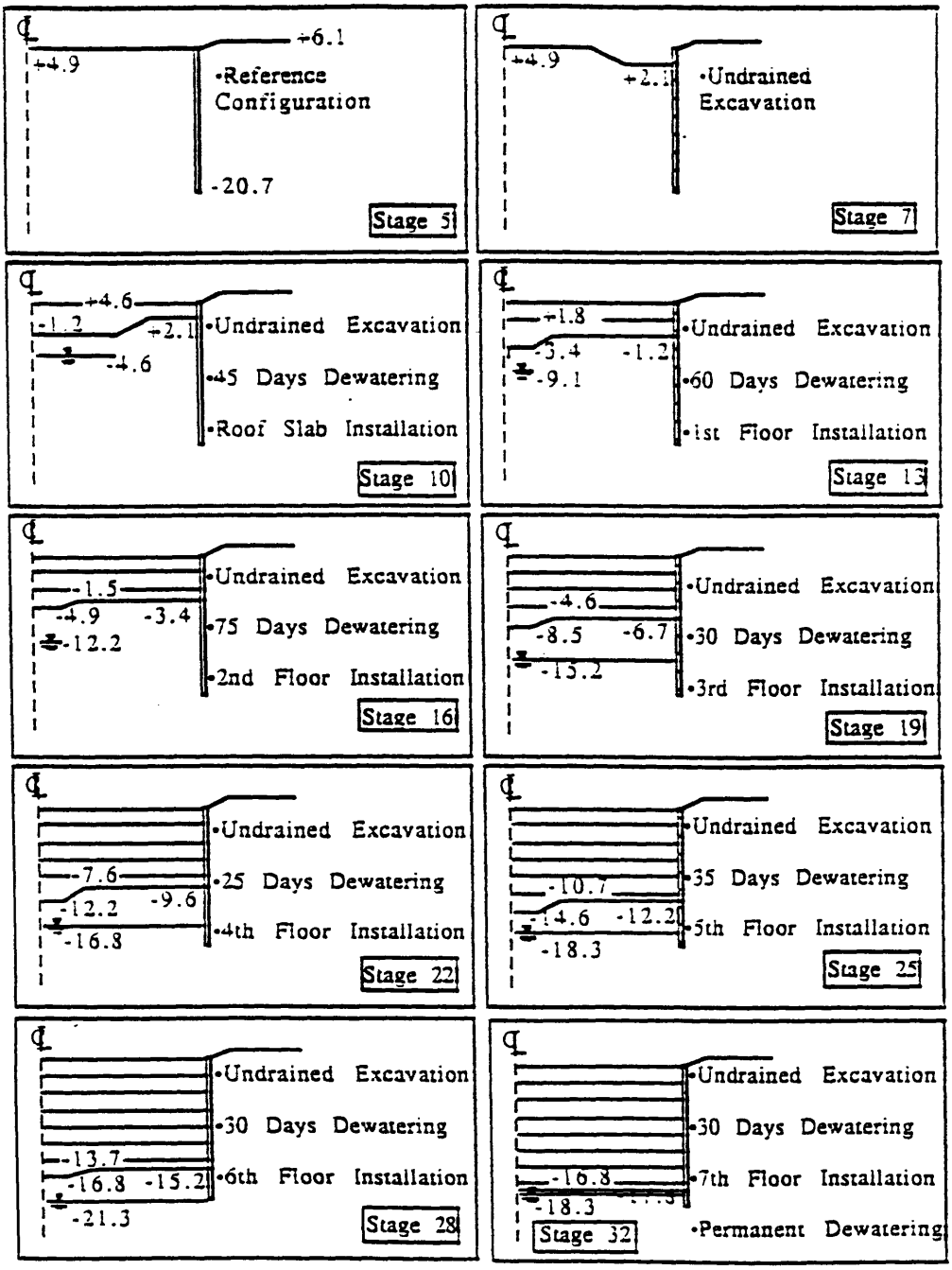

Figure A2 Construction sequence used in finite element model. The simulation includes detailed modelling of construction berms and de-watering schemes based on the actual record of site activities.

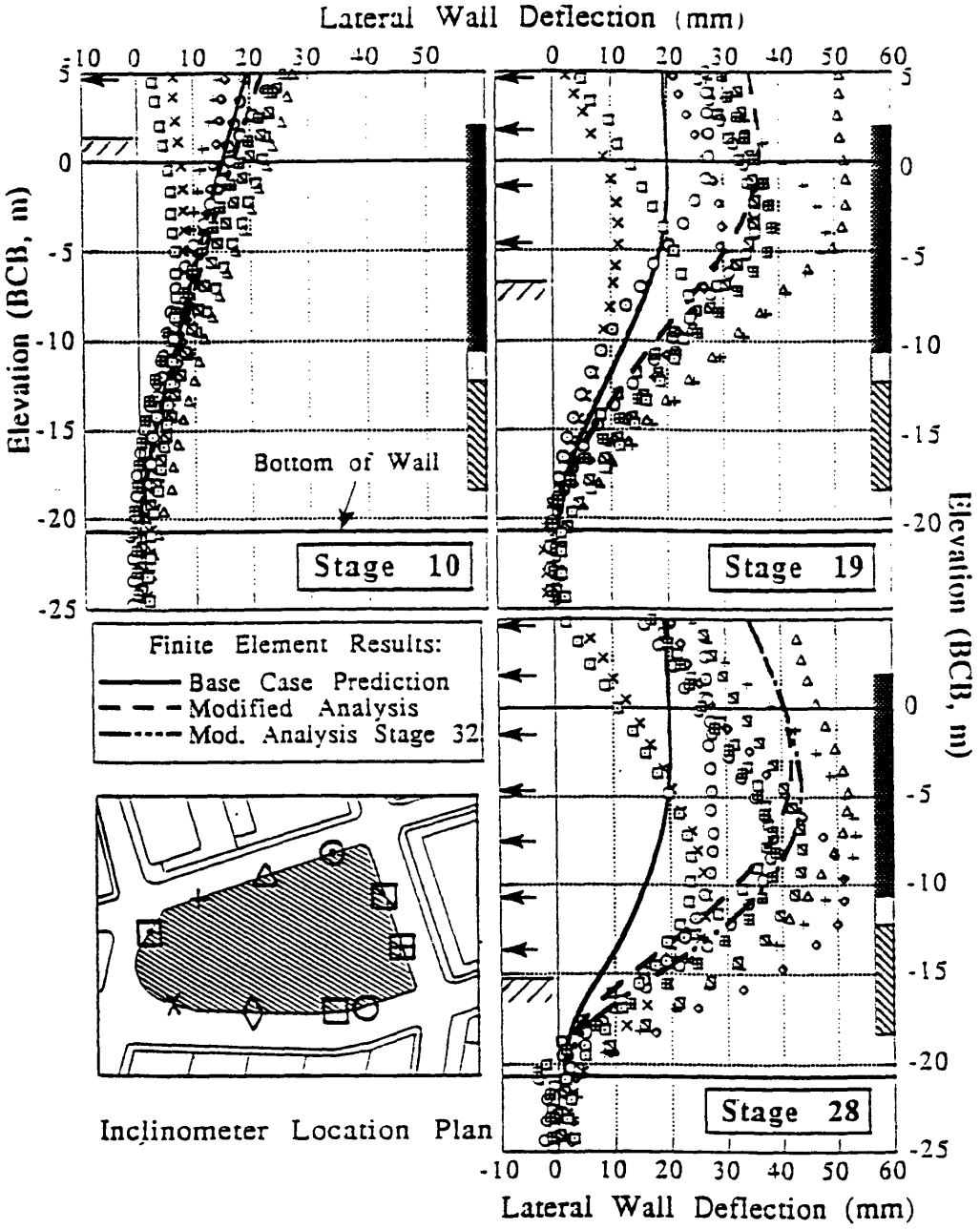

Figure A3 Comparison of predicted lateral wall deflections with inclinometer measurements. The base case analysis showed good agreement with cantilever type movements during the inital excavation, but underpredicted measured wall deflections after stage 10/11. The original (base case) analysis was modified to incoporate two important factors: a) floor slab shrinkage (which controls the support stiffness); and b) improved modelling of flow conditions in the weathered argillite. Results from this modified analysis are generally in very good agreement with the measured wall deflections.

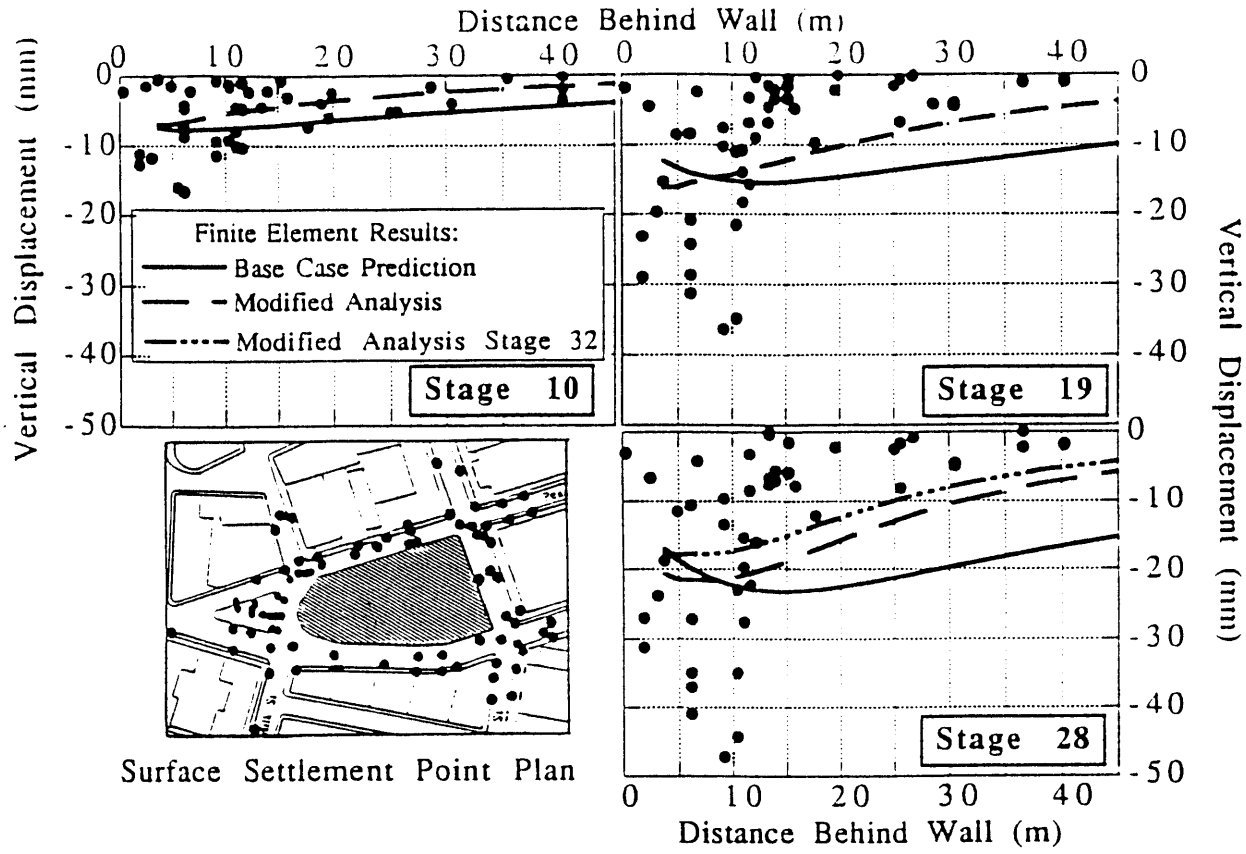

Figure A4 Comparison of predicted and measured surface settlements. Although there is a large scatter in the near field data (within 15m of the wall) the modified analysis gives very reasonable description of the overall settlement trough.

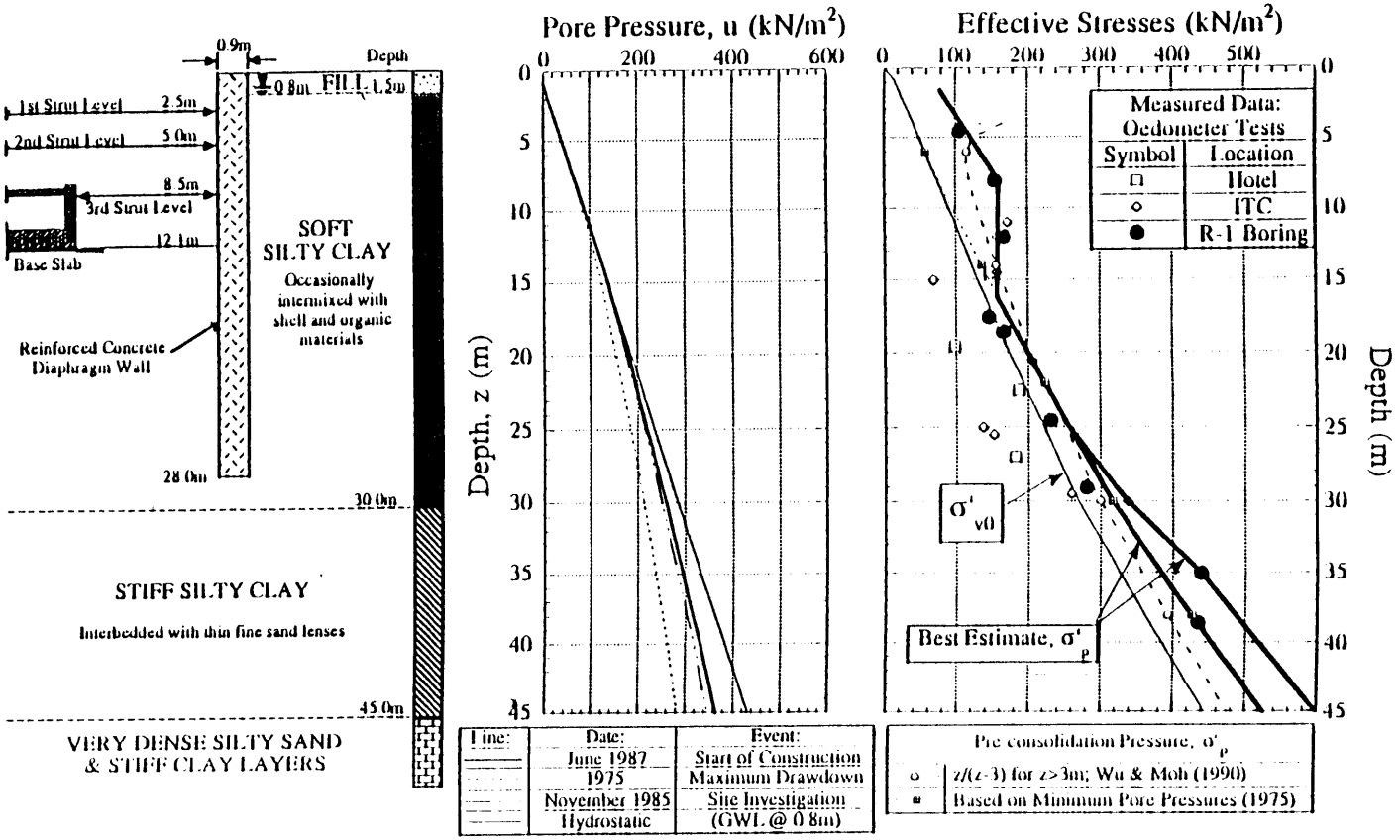

Figure A5 Typical section and site conditions, World Trade Convention Center, Taipei. Soils conditions are typical of K1 Sungshan deposits of soft clay. Principal unknowns are the in-situ pore pressures (which are non-hydrostatic due to past history of groundwater pumping) and engineering properties of the lower clay. Laboratory test data show similar normalized soil properties (strength and deformation) for both clay layers,which are inconsistent with cone resistance measurements.

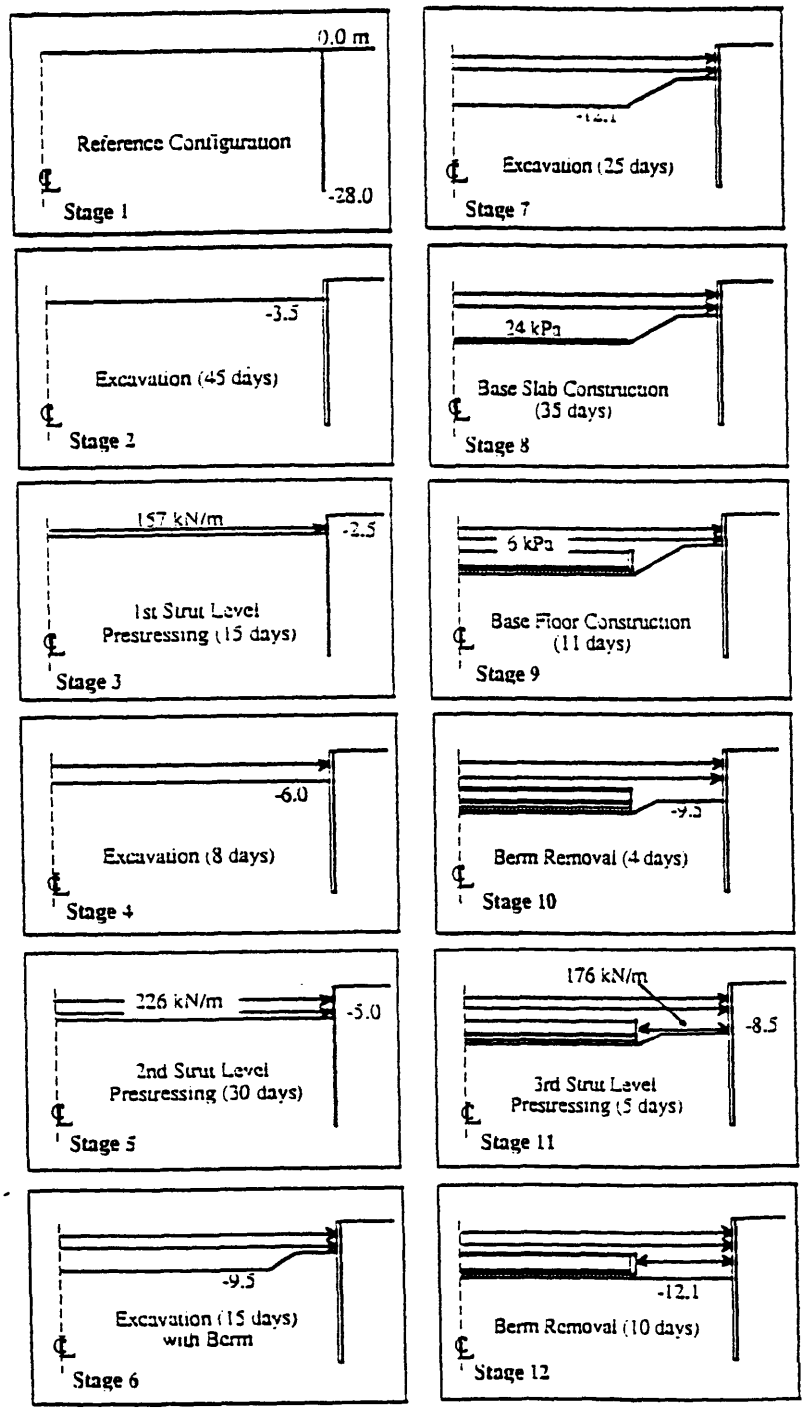

Figure A6 Idealized excavation sequence used in finite element model. The perimeter diaphragm wall is braced by three levels of pre-stressed steel struts.

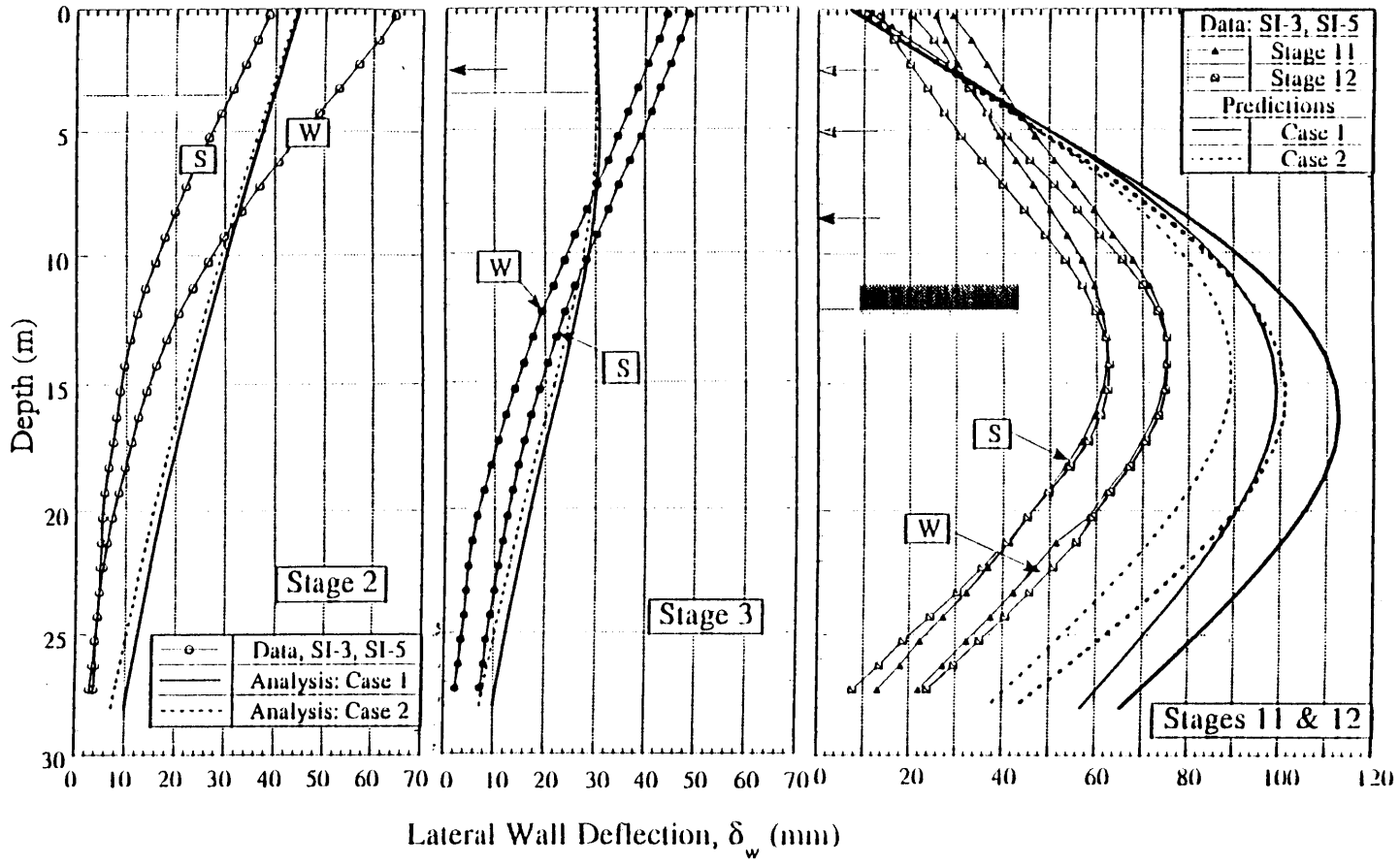

Figure A7 Comparison of predicted lateral wall deflections with inclinometer measurements in the south and west walls. The analysis does not describe accurately the initial cantilever deflection and ultimately overestimates the measured wall deflections by up to 30%. Much of this discrepancy is related to the uncertain properties of the lower 'stiff clays' which was partially demonstrated in the results of modified analysis (case 2).

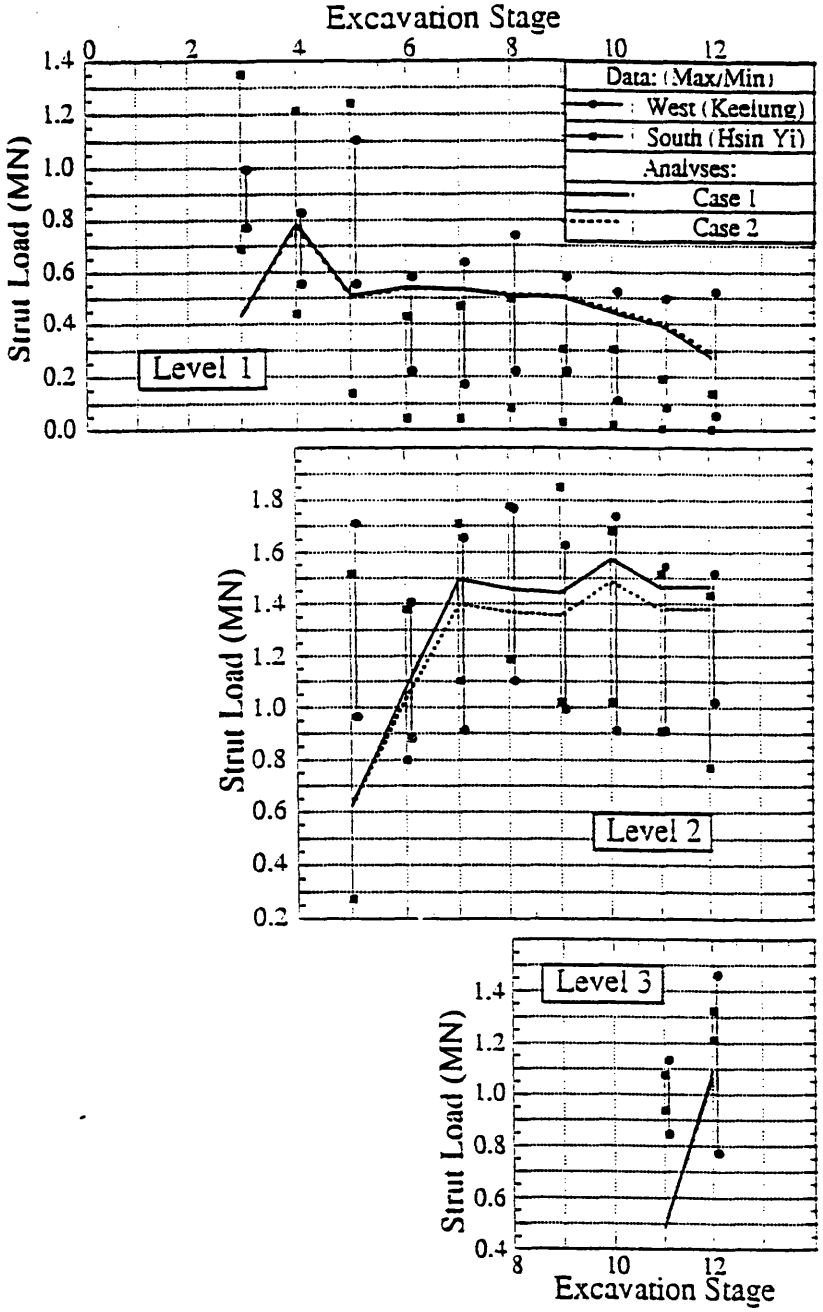

Figure A8 Comparison between predicted and measured strut loads. The analysis gives reasonable predictions of the strut forces measured by pairs of vibrating wire strain gauges at all three levels of bracing.

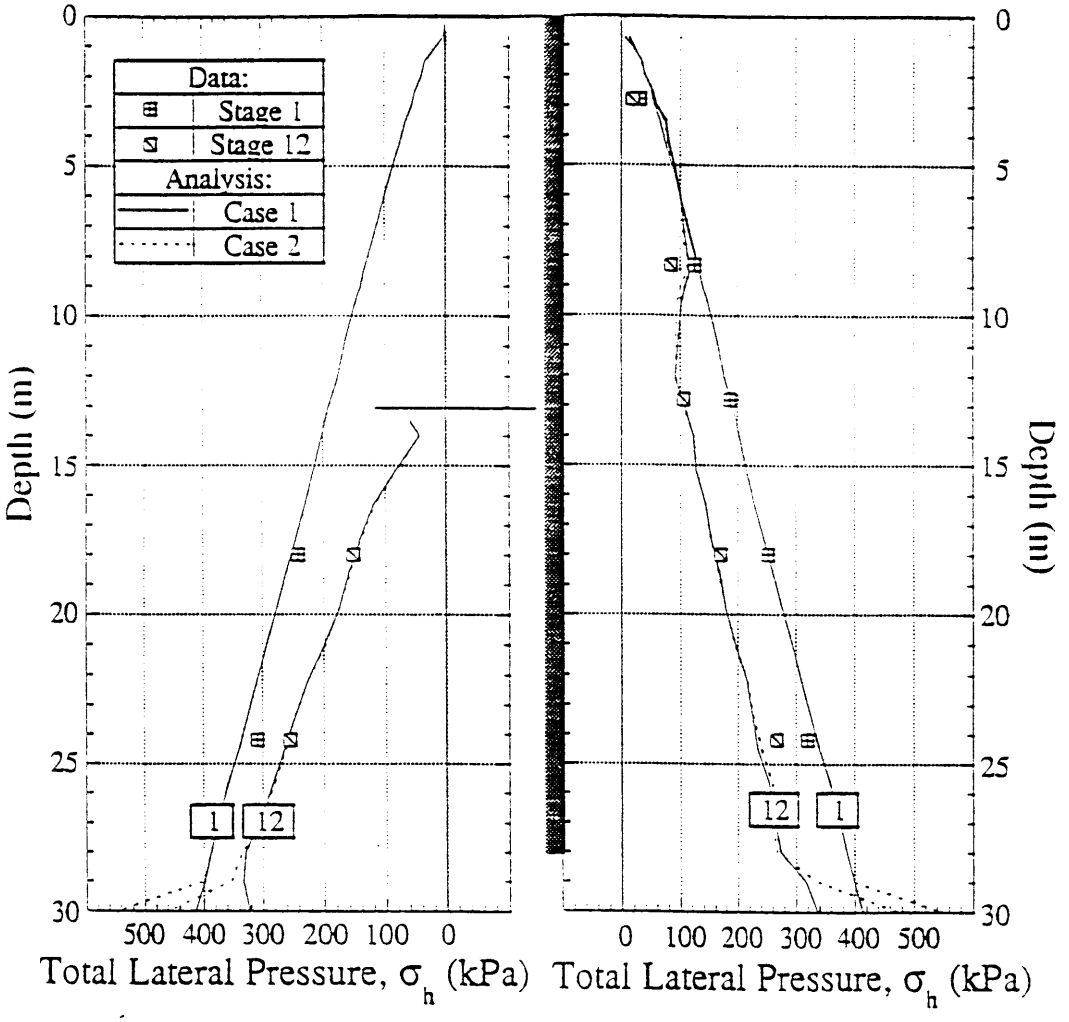

Figure A9 Comparison of predicted and measured total lateral earth pressures. The figure compares total lateral pressures measured on both the inside and outside faces of the diaphragm wall at the beginning and end of excavation. The predictions are in excellent agreement with the measured data. The contrast between these predictions and the wall deflections in figure A2.7 suggests that stiffness properties of the upper soft clay deposit require further investigation.

B. Vertical Coefficient of Consolidation Plots

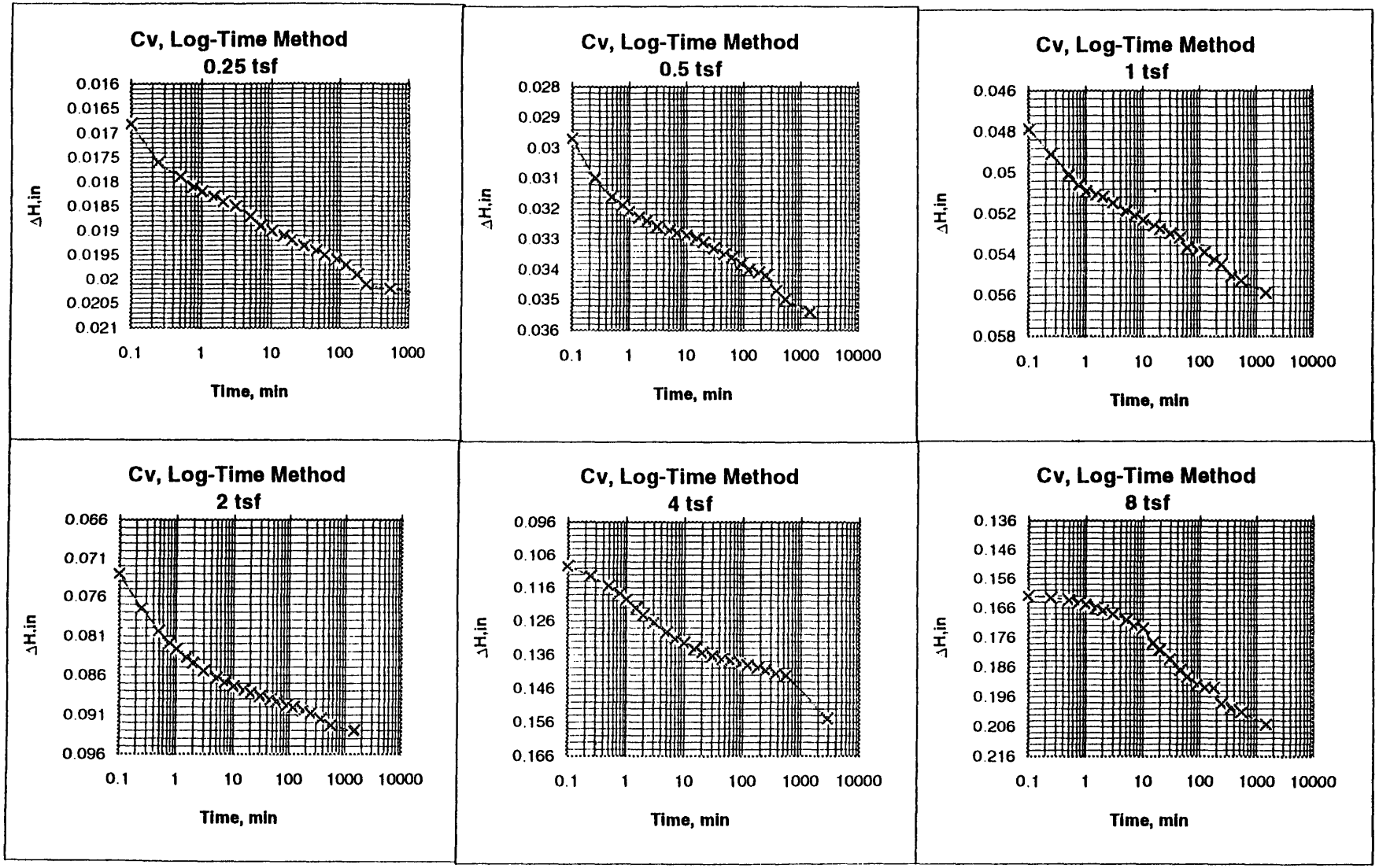

Figure B1 Cv Calculation Using Log-Time Method for Sample C1

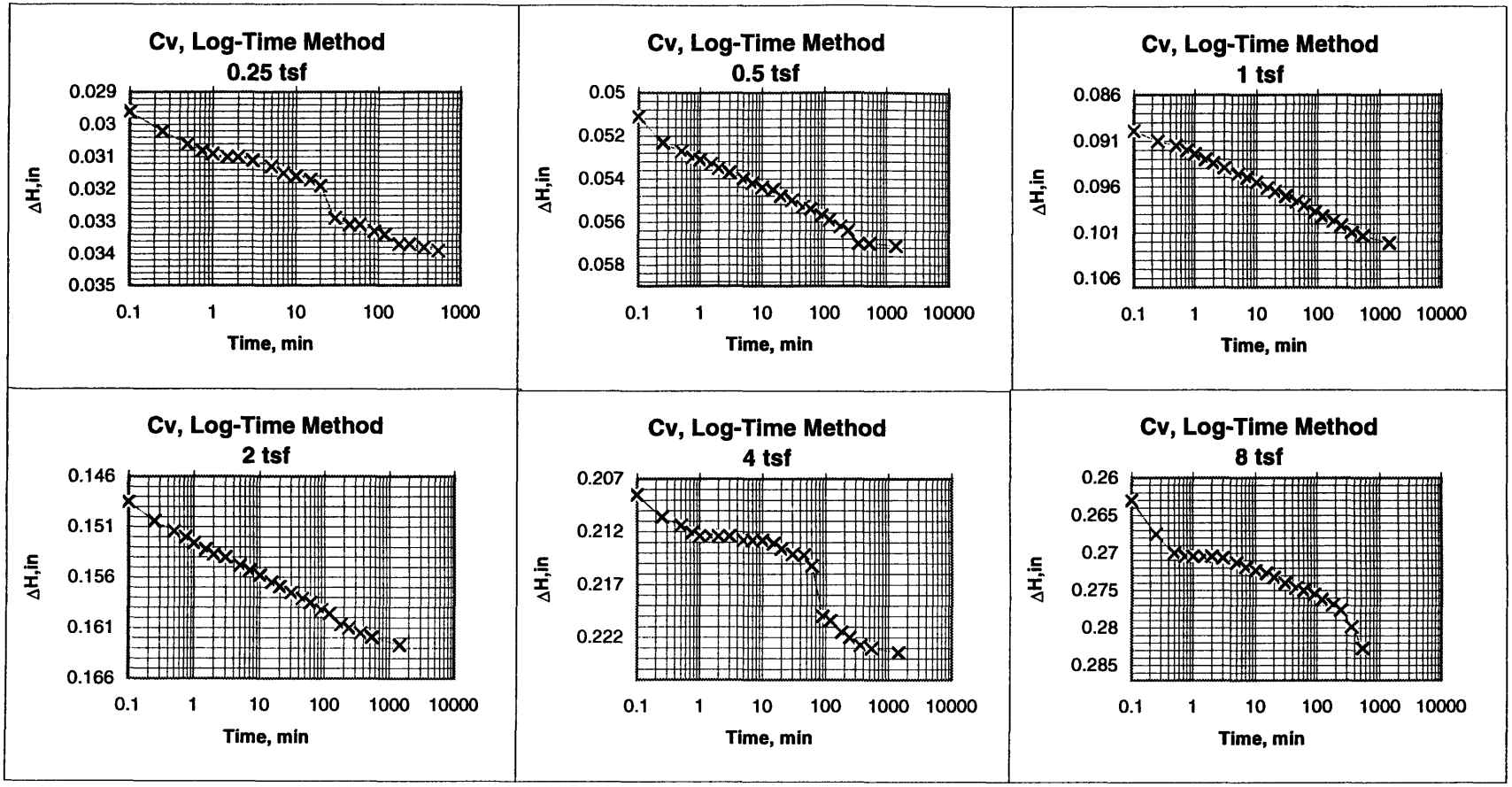

Figure B2 Cv Calculation Using Log-Time Method for Sample C2

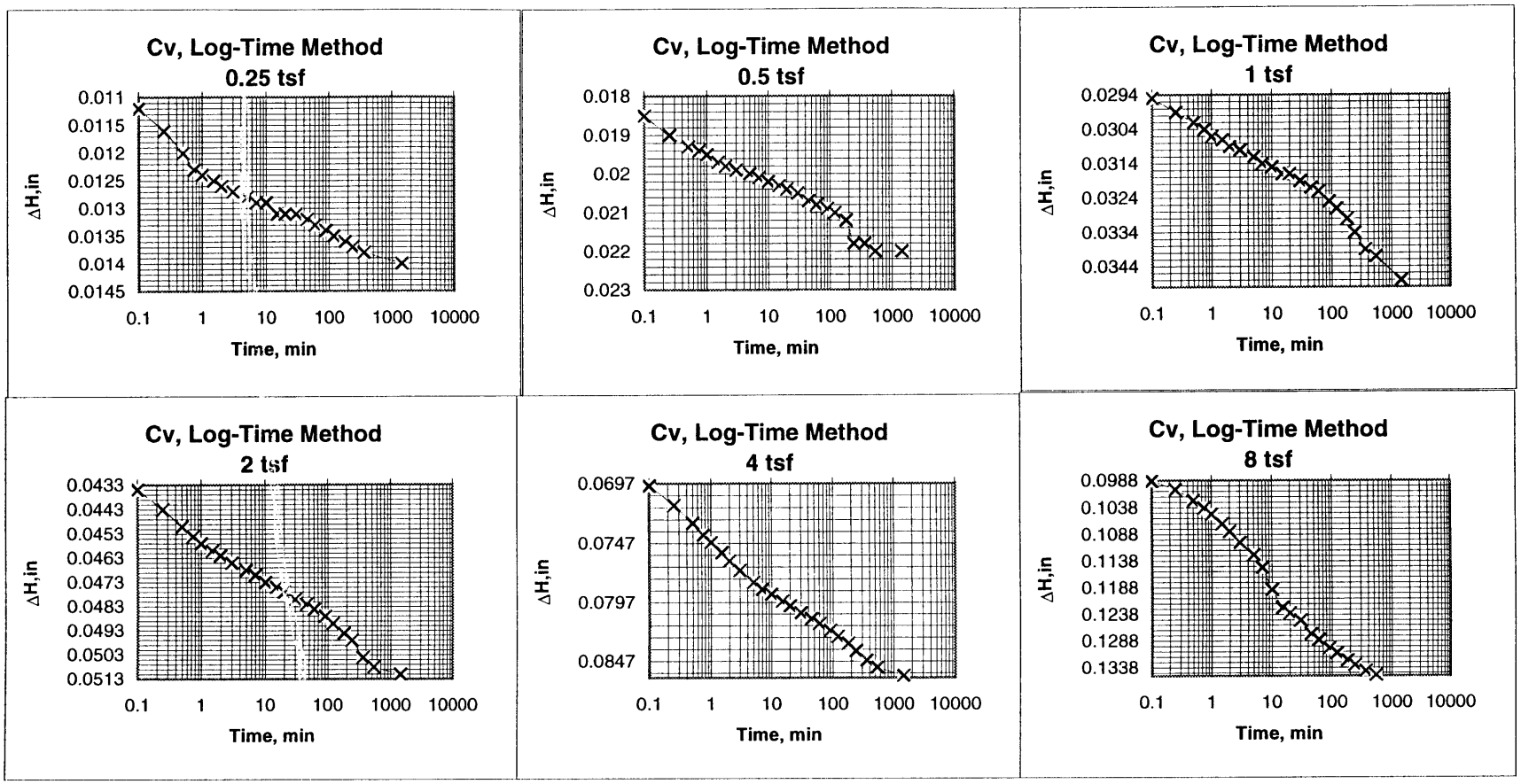

Figure B3 Cv Calculation Using Log-Time Method for Sample C3

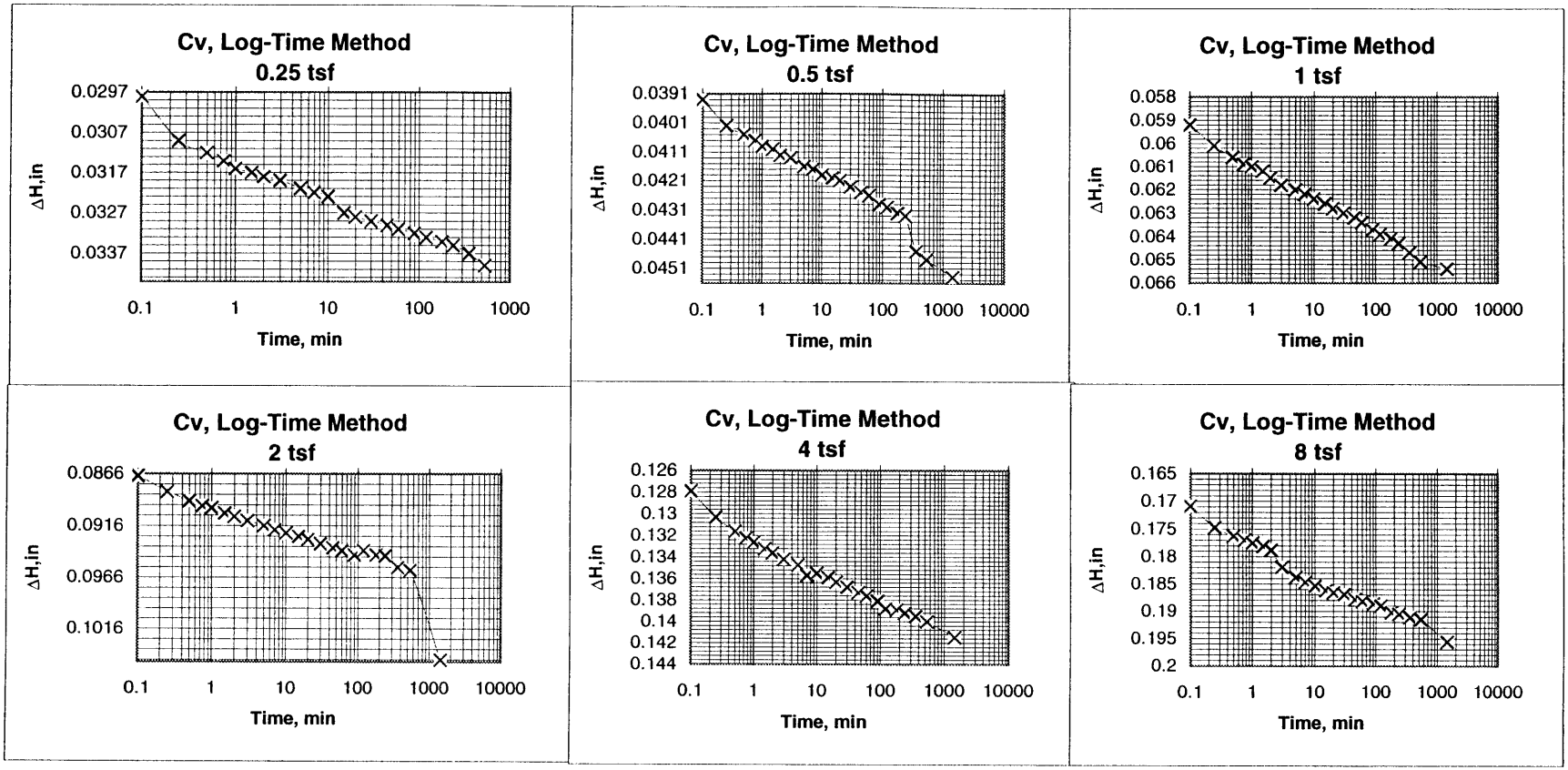

Figure B4 Cv Calculation Using Log-Time Method for Sample C4

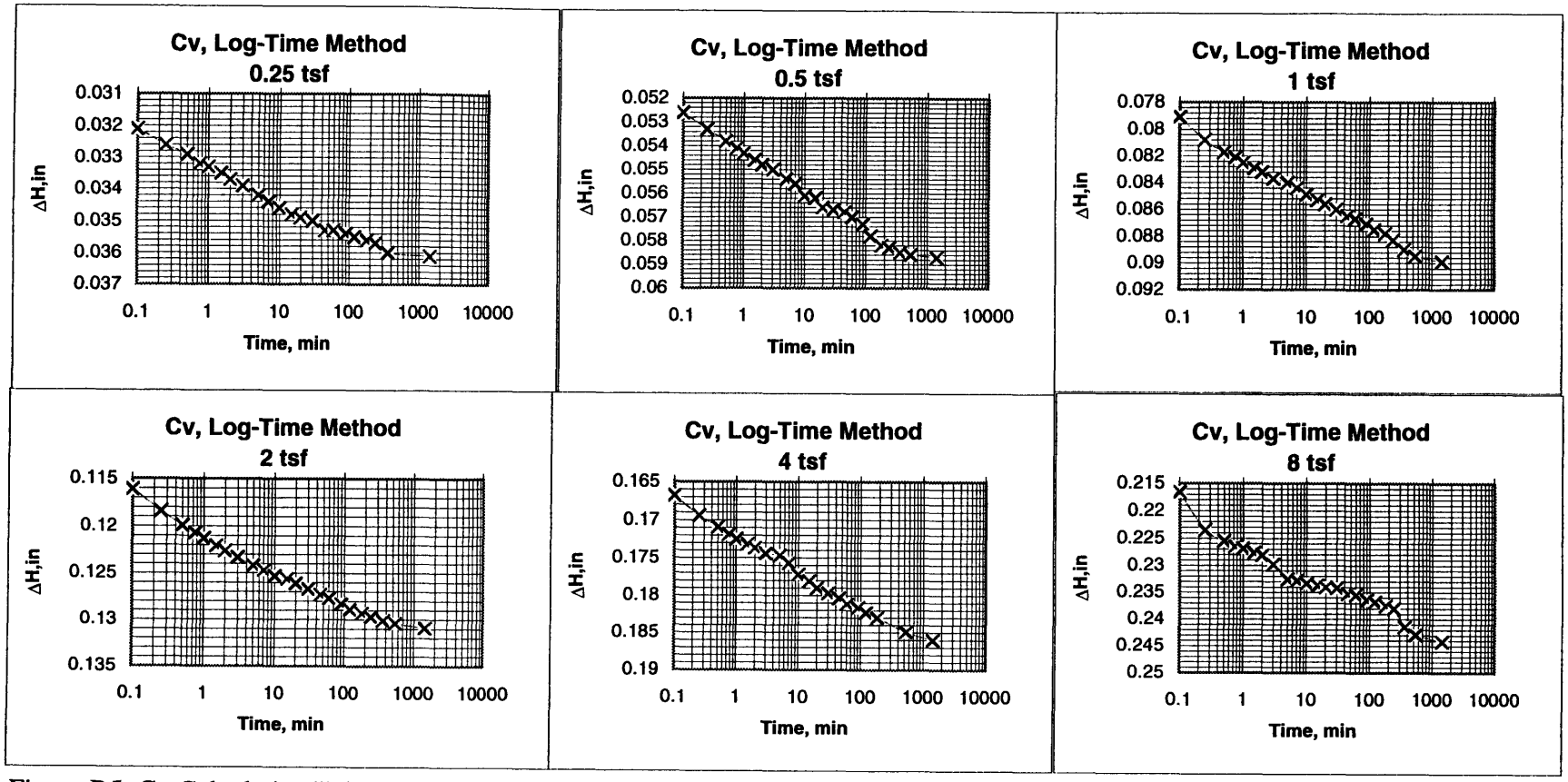

Figure B5 Cv Calculation Using Log-Time Method for Sample C5

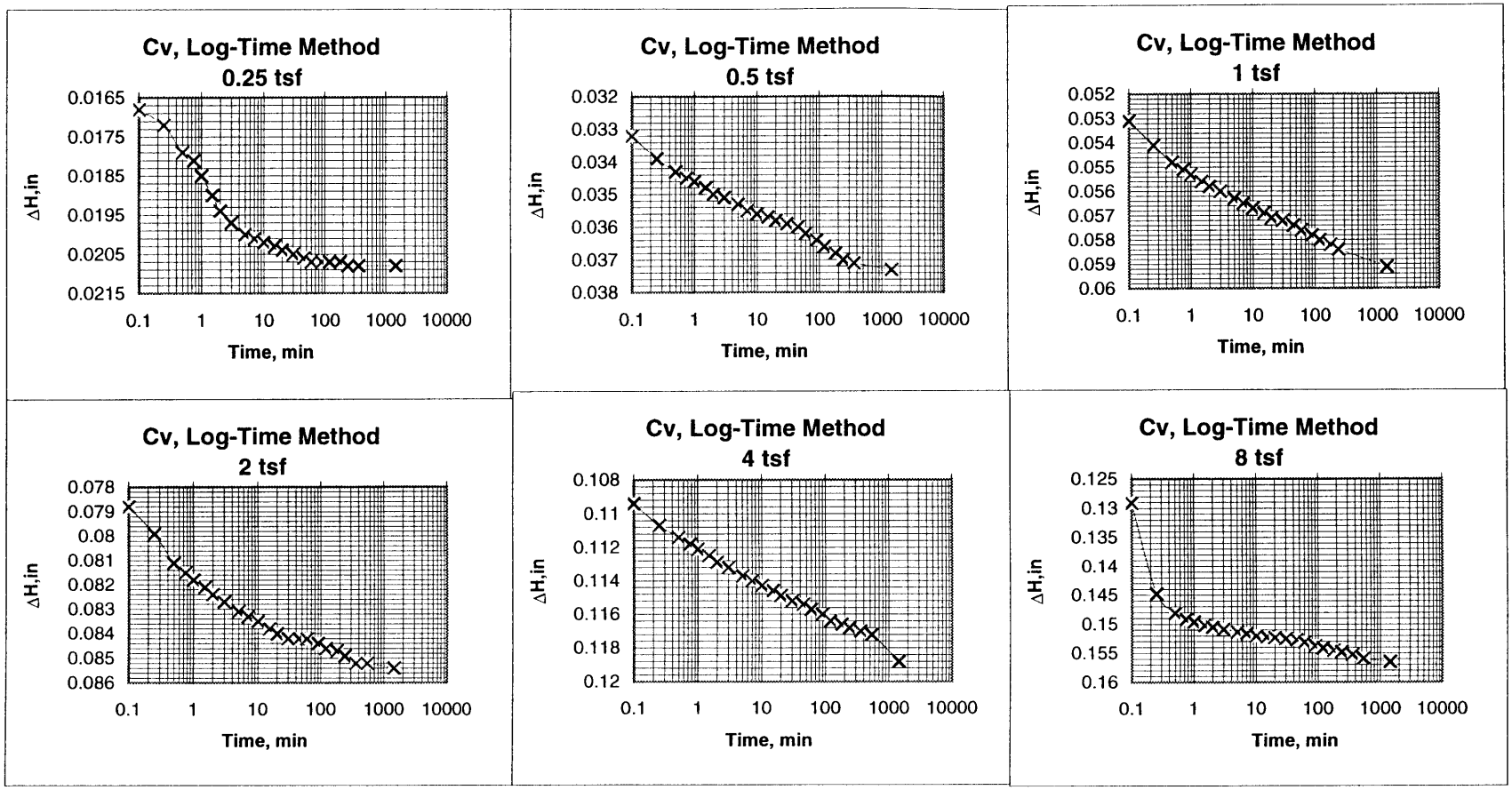

Figure B6 Cv Calculation Using Log-Time Method for Sample C6

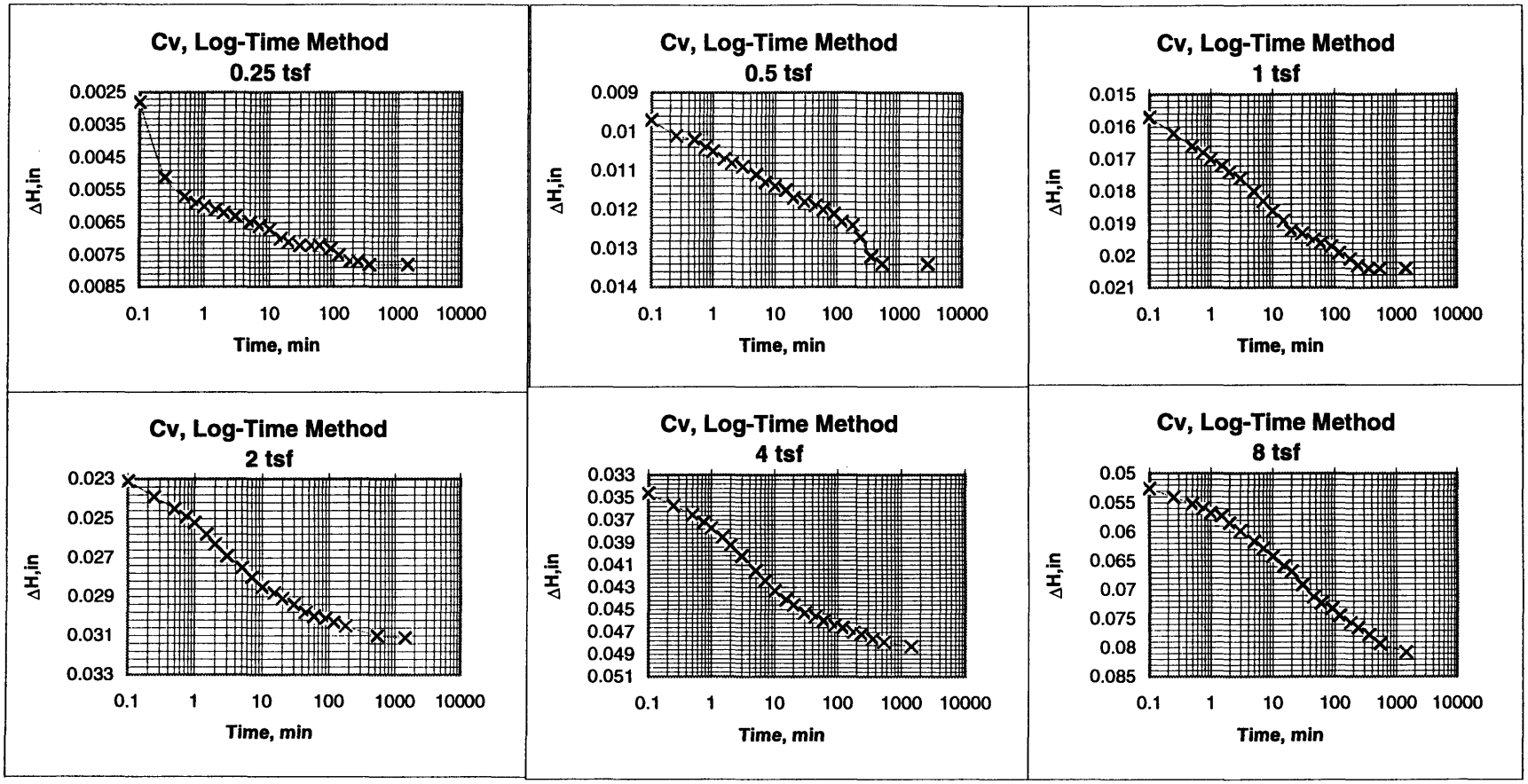

Figure B7 Cv Calculation Using Log-Time Method for Sample C7

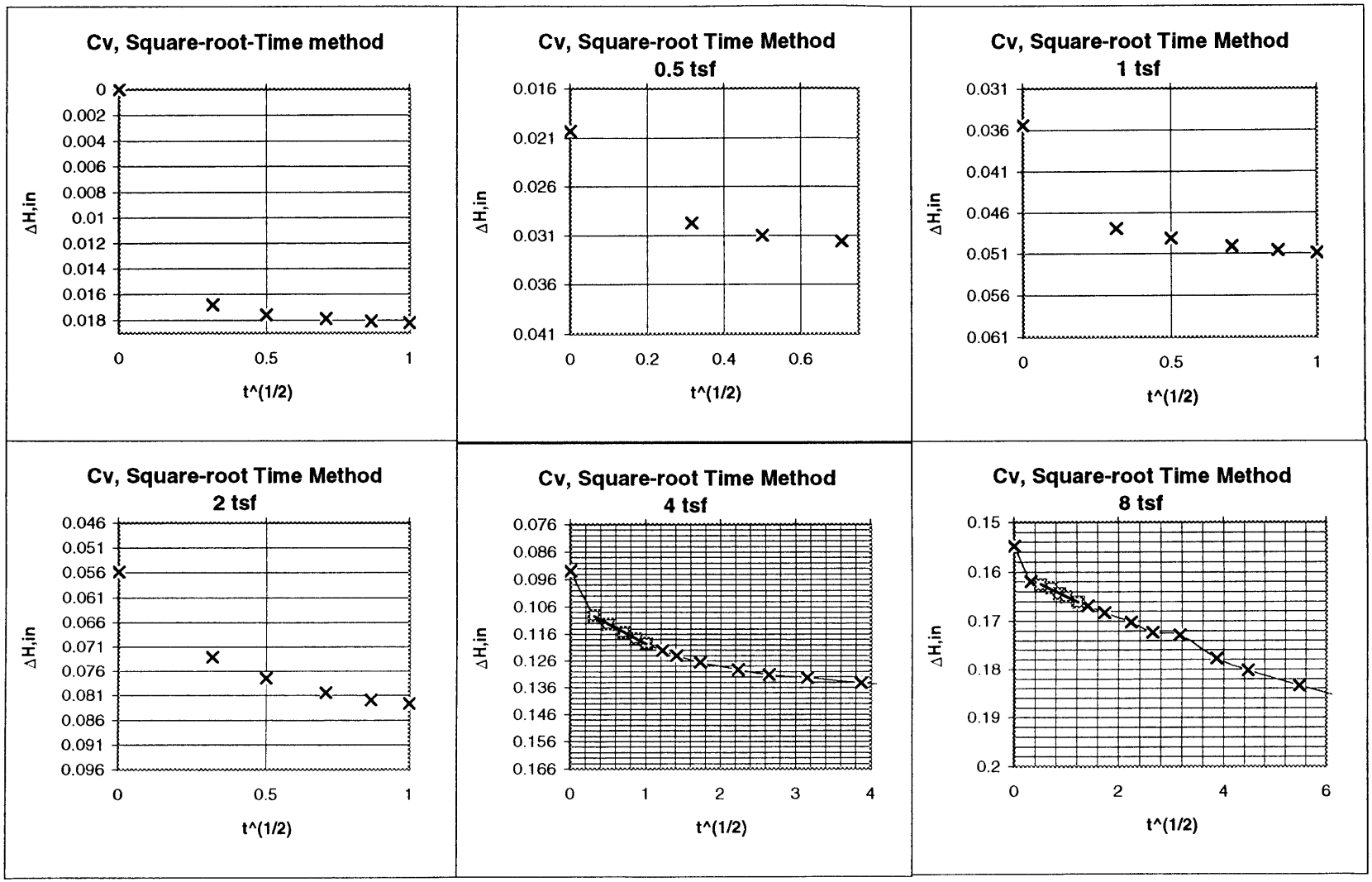

Figure B8 Cv Calculation Using Square Root-Time Method for Sample C1

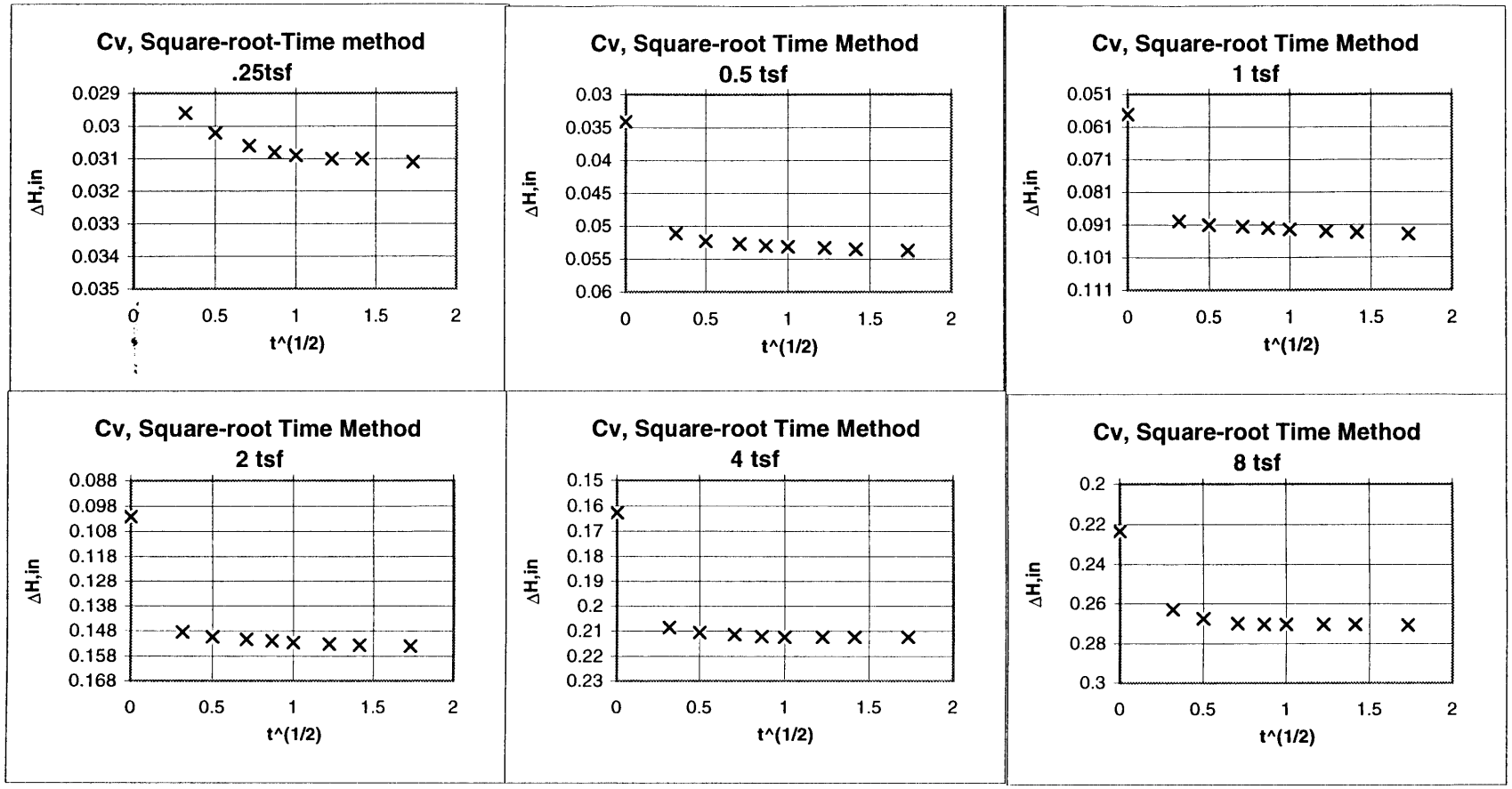

Figure B9 Cv Calculation Using Square Root-Time Method for Sample C2

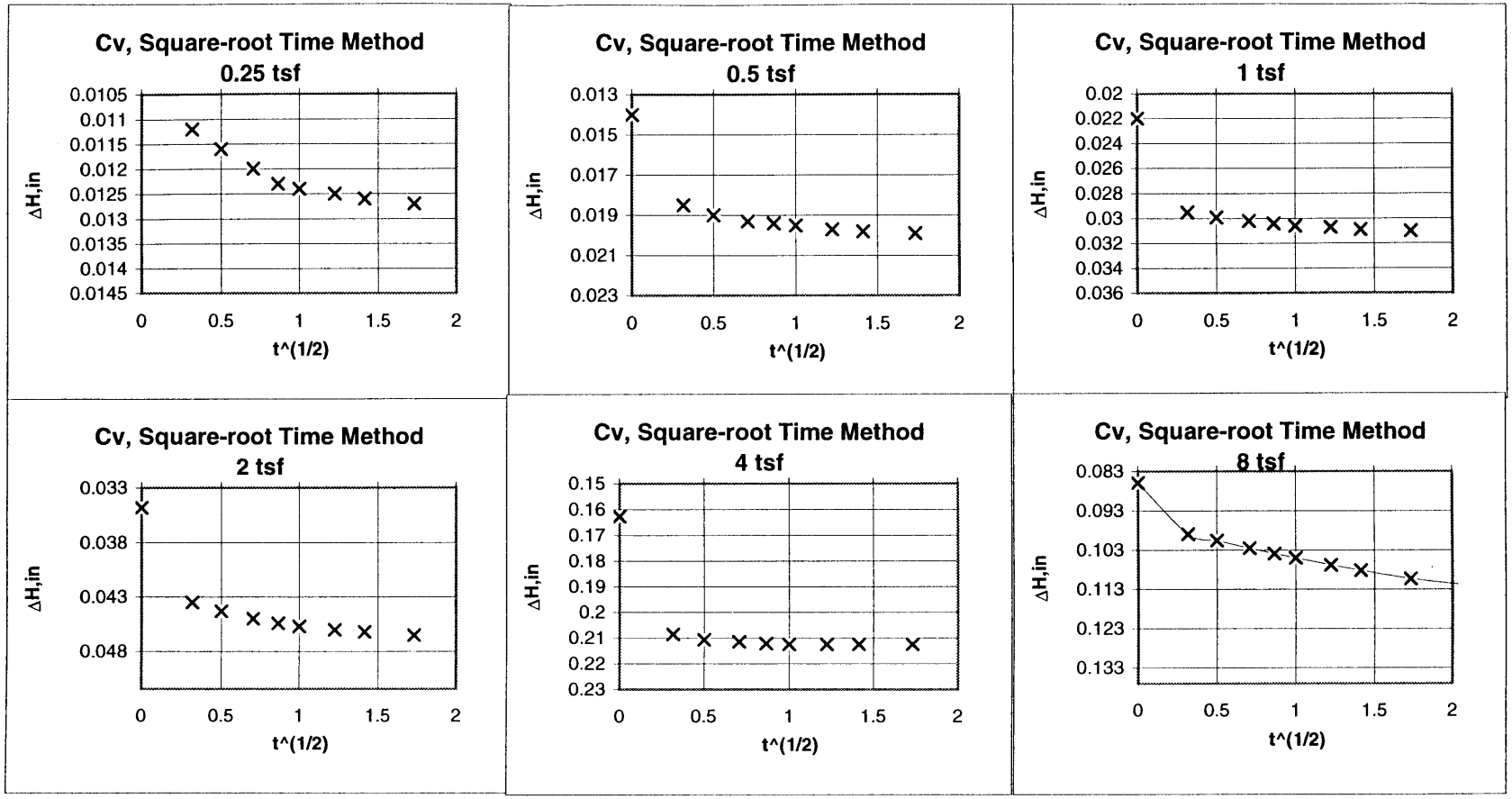

Figure B10 Cv Calculation Using Square Root-Time Method for Sample C3

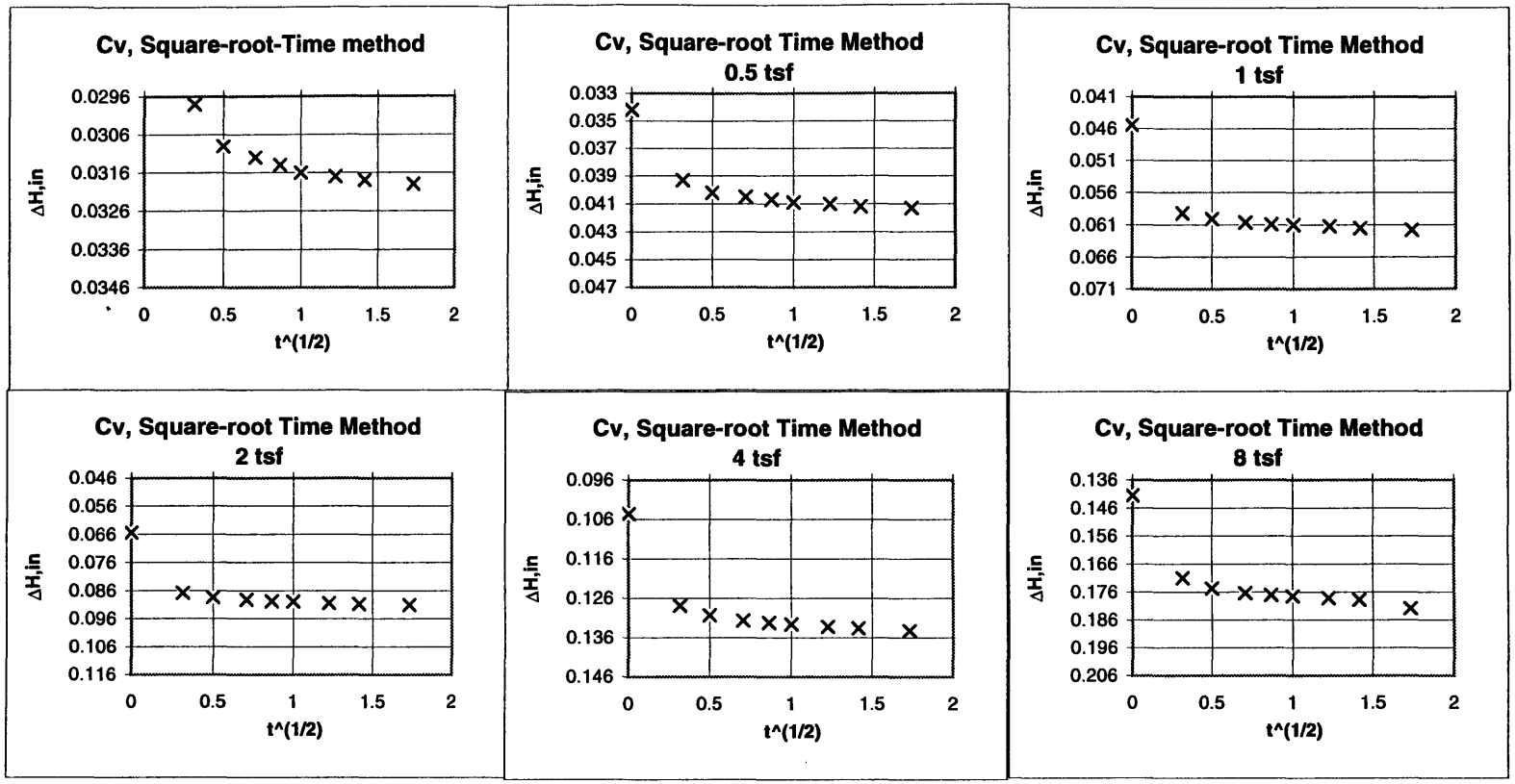

Figure B11 Cv Calculation Using Square Root-Time Method for Sample C4

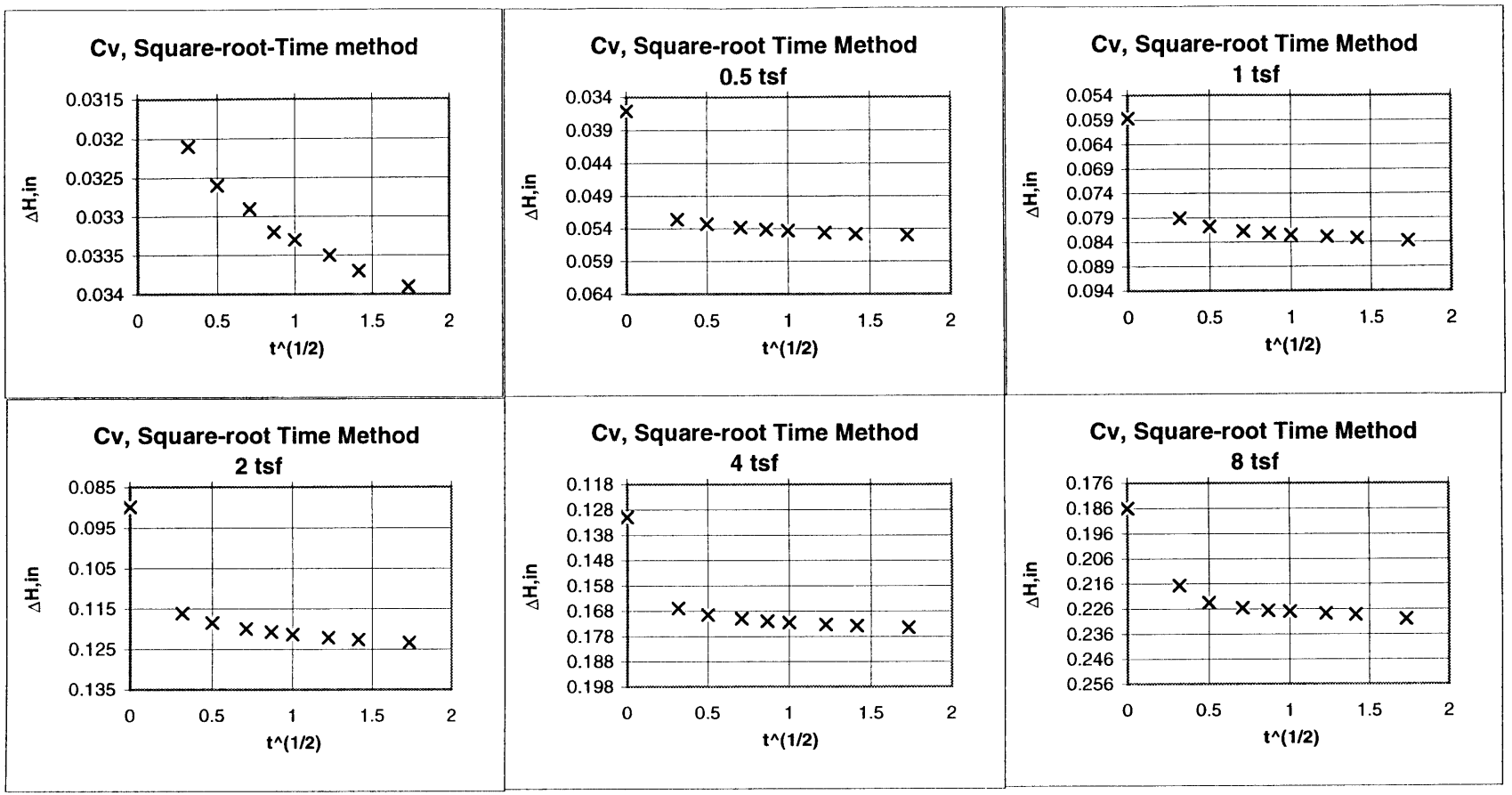

Figure B12 Cv Calculation Using Square Root-Time Method for Sample C5

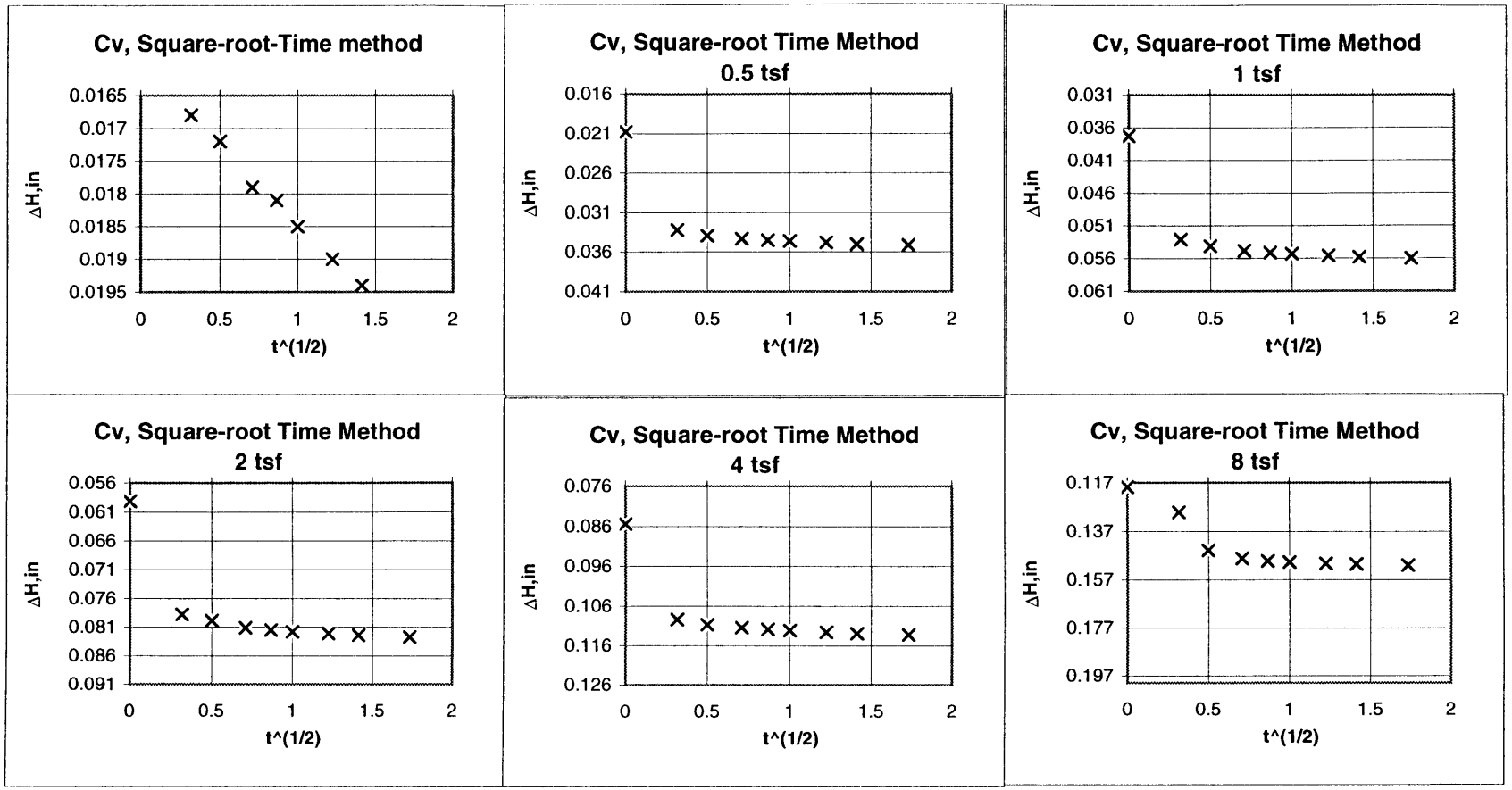

Figure B13 Cv Calculation Using Square Root-Time Method for Sample C6

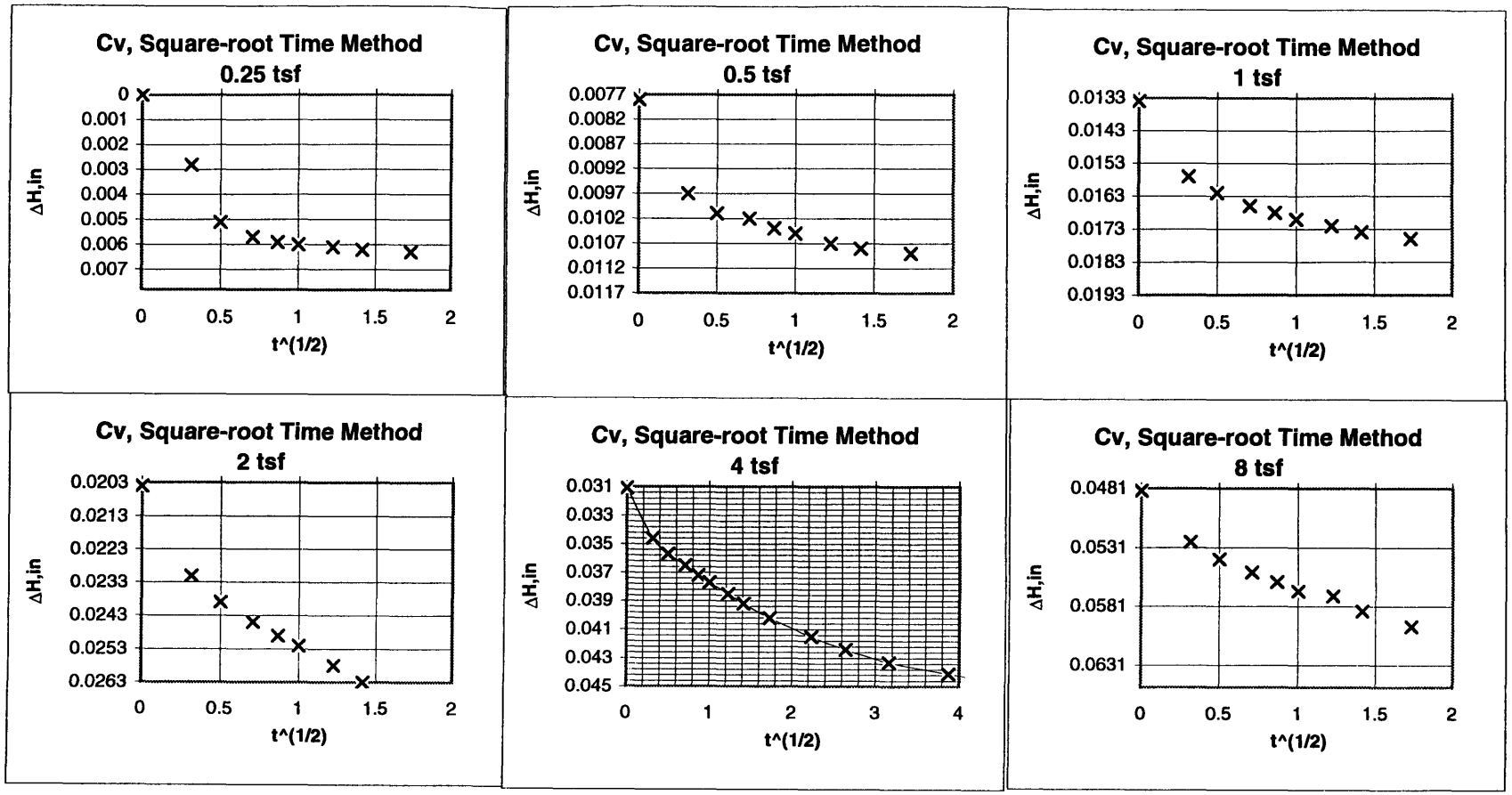

Figure B14 Cv Calculation Using Square Root-Time Method for Sample C7

C. Computations of E' from Oedometer Tests

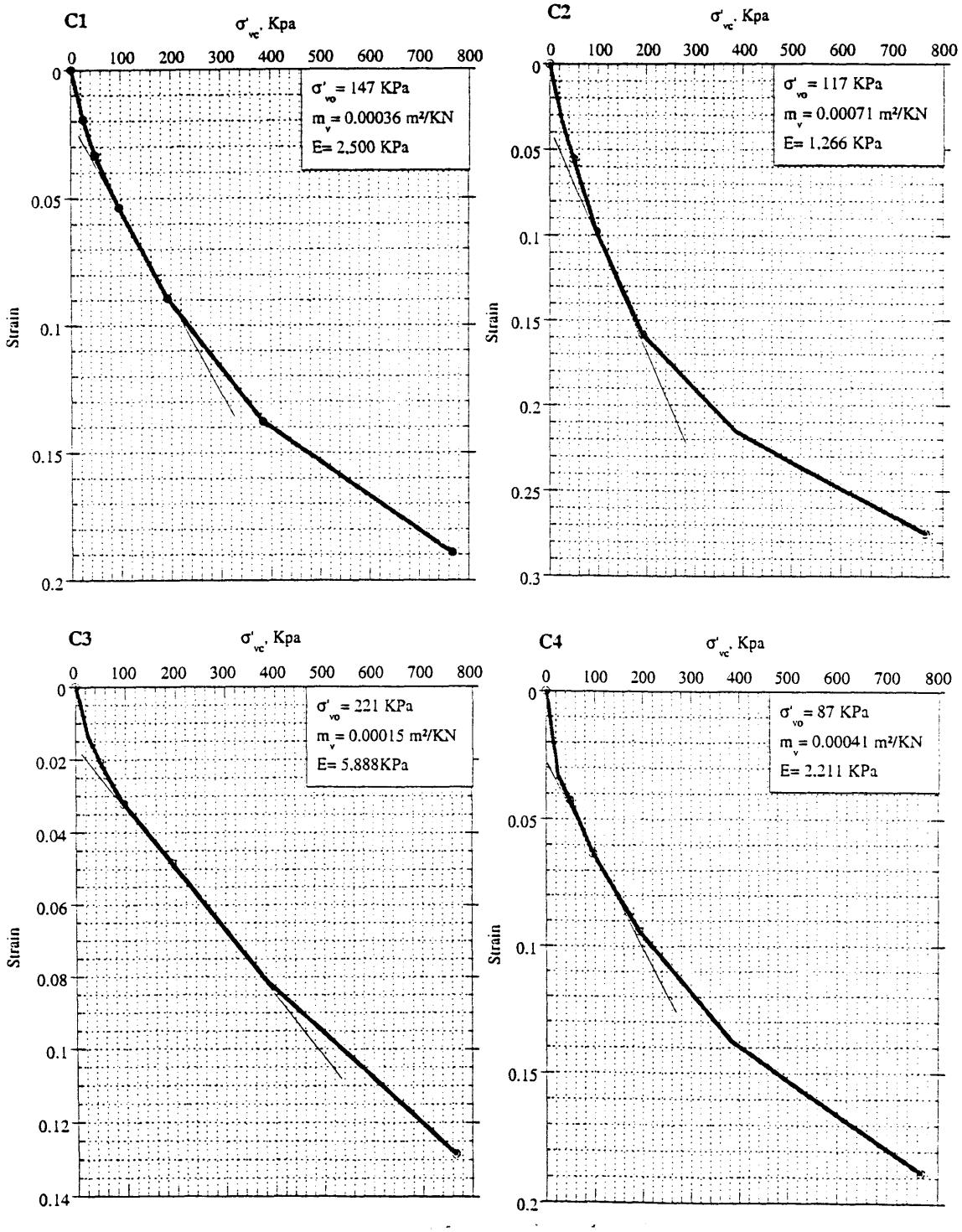

Figure C1 E' Computations from Oedometer Tests

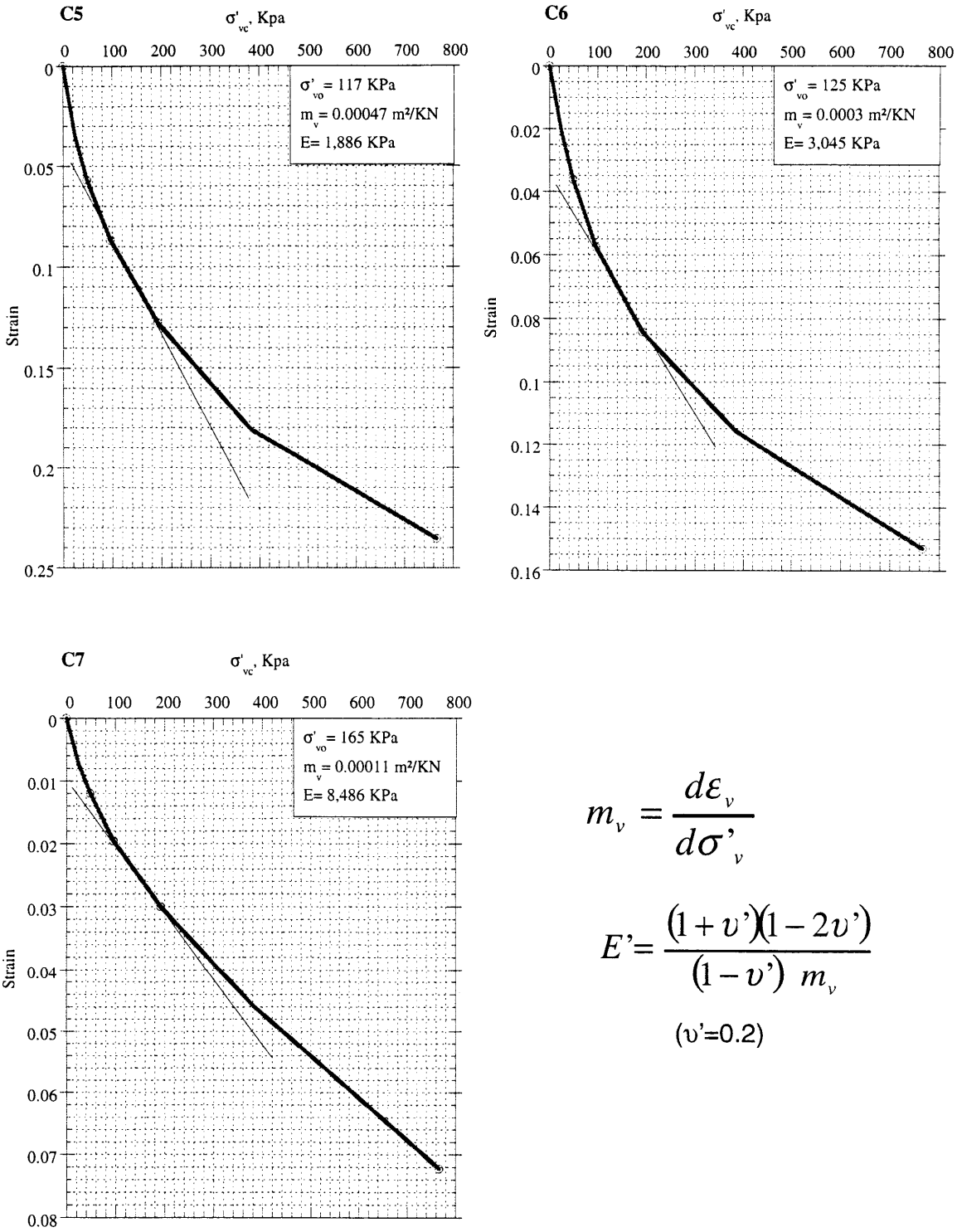

$$m_v = \frac{d\varepsilon_v}{d\sigma'_v}$$

$$E' = \frac{(1+\upsilon')(1-2\upsilon')}{(1-\upsilon')\ m_v}$$

(υ'=0.2)

Figure C2 E' Computation from Oedometer Tests